UNIVERSITY OF SÃO PAULO
SÃO CARLOS SCHOOL OF ENGINEERING

Laura Botero Bolívar

Parametric analysis of the influence of slat geometry on airframe noise by a commercial code

São Carlos

2019

UNIVERSIDADE DE SÃO PAULO
ESCOLA DE ENGENHARIA DE SÃO CARLOS

Laura Botero Bolívar

Análise paramétrica da influência da geometria do slat no ruido de airframe usando um código comercial

São Carlos

2019

Laura Botero Bolívar

Parametric analysis of the influence of slat geometry on airframe noise by a commercial code

Dissertation submitted to the São Carlos School of Engineering - University of São Paulo, for obtaining of a Master of Science degree - Graduate Program in Mechanical Engineering.

Concentration area: Aircraft

Supervisor: Prof. PhD. Fernando Martini Catalano

THIS EXEMPLARY IS THE CORRECTED VERSION.
THE ORIGINAL VERSION IS AVAILABLE ON THE MECHANICAL ENGINEERING DEPARTMENT AT EESC-USP.

São Carlos

2019

Cataloging data reviewed by the Library Prof. Dr. Sérgio Rodrigues Fontes at EESC/USP with information provided by the Author.

Botero-Bolívar, Laura
B748p Parametric analysis of the influence of slat geometry on airframe noise by a commercial code / Laura Botero Bolívar ; Supervisor Fernando Martini Catalano. – São Carlos, 2019.

Dissertation (Master of Science) - Graduate program in Mechanical engineering and concentration area in aircraft – São Carlos School of Enginering, University of São Paulo, 2019.

1. Airframe Noise. 2. Slat Noise. 3. Slat Geometry. 4. Computational Aeroacoustics. I. Catalano, Fernando, supervisor. II. Parametric analysis of the influence of slat geometry on airframe noise by a commercial code .

Eduardo Graziosi Silva - CRB - 8/8907

Laura Botero Bolívar

Análise paramétrica da influência da geometria do slat no ruido de airframe usando um código comercial

Dissertação apresentada à Escola de Engenharia de São Carlos da Universidade de São Paulo, para obtenção do título de Mestre em Ciências - Programa de Pós-Graduação em Engenharia Mecânica.

Área de concentração: Aeronaves

Orientador: Prof. Dr. Fernando Martini Catalano

São Carlos

2019

Ficha catalográfica elaborada pela Biblioteca Prof. Dr. Sérgio Rodrigues Fontes da EESC/USP com os dados inseridos pelo(a) autor(a).

Botero-Bolívar, Laura
B748p Análise paramétrica da influência da geometria do slat no ruido de airframe usando um código comercial / Laura Botero Bolívar ; Orientador Fernando Martini Catalano. – São Carlos, 2019.

Dissertação (Mestrado) - Programa de Pós-Graduação em Engenharia Mecânica e Área de Concentração em Aeronaves – Escola de Engenharia de São Carlos, Universidade de São Paulo, 2019.

1. Ruído de célula. 2. Ruído de Slate. 3. Geometria do Slate. 4. Aeroacústica Computacional. I. Catalano, Fernando, orientador. II. Análise paramétrica da influência da geometria do slat no ruido de airframe usando um código comercial.

Eduardo Graziosi Silva - CRB - 8/8907

FOLHA DE JULGAMENTO

Candidata: Engenheira **LAURA BOTERO BOLIVAR.**

Título da dissertação: "Análise paramétrica da influência da geometria do slat no ruído de airframe usando um código comercial"

Data da defesa: 25/03/2019.

Comissão Julgadora: **Resultado:**

Prof. Titular **Fernando Martii Catalano** APROVADO
(Orientador)
(Escola de Engenharia de São Carlos/EESC)

Prof. Dr. **Odenir Almeida** APROVADO
(Universidade Federal de Uberlândia/UFU)

Prof. Dr. **William Roberto Wolf** APROVADO
(Universidade Estadual de Campinas/UNICAMP)

Coordenador do Programa de Pós-Graduação em Engenharia Mecânica:
Prof. Titular **Gherhardt Ribatski**

Decano da Comissão de Pós-Graduação:
Prof. Titular **Humberto Breves Coda**

To my parents, Diana and Javier, my siblings, Sara and Francisco, and my goddaughter, Paulina.

ACKNOWLEDGEMENTS

First of all, I would like to acknowledge my supervisor, Prof. PhD. Fernando M. Catalano, for his orientations and exigences throughout these two years, which have led to improvements in this research, and the many technical discussions held.

I am also grateful to Danillo Reis and Eduardo Coelho, who lead the SILENCE Aircraft project, for the technical and operational support. My special acknowledgements to Matheus T. de Araujo and Gil Greco for their assistance with the use of PowerFLOW software and availability to solve my questions, and the computational technical personnel from the Federal University of Santa Catarina for their help with the cluster.

Thanks to all the professors I have met during my master's degree program for their technical and personal contributions, which have made me a better professional and researcher. My special gratitude to Prof. PhD. Hernán D. Cerón for his trust in me since I came to Brazil, and for always devoting time to help me, explaining and discussing results, and providing me with his personal support.

I am thankful to the LAE laboratory technician and friend Osnán I. Faria for his every day joy and assistance with the construction of the model; his knowledge and experience have surely led to improvements in the results.

My acknowledgments to the post-graduate program and aeronautical engineering department secretaries Ana Paula Bueno, Iara Olveira and Gisele Poppy for always being willing to help and for their friendly welcome. I would especially like to thank Angela Giampedro and Elena Palloni for checking this dissertation, and my colleagues of the LAE laboratory for their constant support and for making my days better. Special thanks to Lourenço T. Pereira for his teachings of aerodynamics, aeroacoustics and Matlab, challenges posed, which have made me a better researcher and person, and invaluable assistance.

I am thankful to my friends from CEFER USP São Carlos, for their company, friendship, and support, and those from AdS for welcoming me in their group and in their lives. I am also grateful to my Colombian friends in Brazil for being my family in this country. My heartfelt thanks to Daniel Acevedo for his support throughout these 2 years.

Last, but not least, I want to thank my family for always pushing me towards achieving my dreams, always supporting my decisions and giving me unconditional love. My gratefulness to my parents, who are my inspiration, Diana Bolívar and Javier Botero, for all their sacrifices for my being here, my siblings, Sara and Franciso Botero, for teaching me love is bigger than anything else in the world, and my goddaughter, Paulina Acevedo, for always waiting for me with open arms and making me feel I am present in her life.

Special thanks to my grandparents, Gladys Vergara and Jairo Bolívar, for their advice and love, and my grandfather Francisco Botero's memory, which has helped me to carry on. A sincere thank you to my aunt and best friend Sandra Bolívar, for her unconditional support, and all my uncles and cousins, for having shared great moments with me.

I acknowledge the Conselho Nacional de Desenvolvimento Científico e Tecnológico (CNPq) (132539/2017-9 process) and A Financiadora de Estudos e Projetos (FINEP) for the financial support provided to this research.

"Whether you think you can, or that you can't, you are usually right "

Ford (1914)

ABSTRACT

BOTERO-BOLÍVAR, L. **Parametric analysis of the influence of slat geometry on airframe noise by a commercial code** . 2019. 186p. Dissertation (Master of science) - São Carlos School of Engineering, Univeristy of São Paulo, São Carlos, 2019.

Over recent years, airframe noise has become one of the most important research topics in the aeronautic field, due to reductions in engine noise with the development of high-by-pass technology and the necessity to meet the new standards established by regulation entities. It is caused by fluid-structure interaction and pressure fluctuations caused by gaps and discontinuities. Slat is one of the major airframe noise sources due to the complex flow in the gap between it and the wing main element. Although some noise reduction techniques have been applied to the slat, the relation between the slat characteristics and the noise generation has not been completed understood. This study addresses 21 variations in six different parameters of the slat internal geometry for the establishment of their relation with noise generation. Modifications were focused on the cusp and trailing edge regions and their angle, length and thickness were varied. Comparisons between numerical and experimental results of some configurations validated the simulation methodology. Numerical studies were performed by PowerFLOW 5.3® commercial software and the results included transient analysis, as the far-field spectrum, turbulence in the slat cove, power spectra density contours in both flow around the slat and slat surface, and spectra of the pressure fluctuations on the slat surface, and stationary results as pressure coefficient distribution and lift and drag coefficients of the wing. On the other hand, experimental tests were conducted in a closed-section wind tunnel at the Laboratory of Aerodynamics (LAE) of the São Carlos School of Engineering and consisted in measurements of static pressure in the wall model through a ScaniValve and far-field noise through a phased array antenna of microphones, whose post-processing was completed by convectional and CLEAN SC beamforming methodologies. The good agreement in both aerodynamic and aerocoustic results proved the validity of the numerical set-up and the reliability of numerical results. Among all modified parts, the cusp length exerted the major influence on the slat noise and changed significantly the flow characteristics around the slat. However, the angle and thickness of the cusp showed no effect on the aerodynamic and aerocoustic properties of the wing. Some relationships were observed between the slat noise and characteristics of the fluid around the slat, which were constant among all slat modifications.

Keywords: Airframe noise. Slat noise. Slat geometry. Computational aeroacoustics.

RESUMO

BOTERO-BOLÍVAR, L. **Análise paramétrica da influência da geometria do slat no ruido de airframe usando um código comercial**. 2019. 186p. Dissertação (Mestrado) - Escola de Engenharia de São Carlos, Universidade de São Paulo, São Carlos, 2019.

Nos ultimos anos, o ruído de célula tem-se tornado um dos temas mais importantes na indústria aeronáutica, devido às reduções no ruído dos motores com o desenvolvimento da tecnología de alto by-pass e a necesidade de atingir os novos limites impostos pelas entidades de regulação. O ruído de célula é causado pela interação fluído-estrutura e as flutuações de pressão causadas por aberturas e discontinuidades. Uma das mais importantes fontes de ruido é o eslate, devido ao escoamento complexo gerado na abertura entre ele e o elemento principal da asa. Embora algumas técnicas de redução de ruido tem sido aplicadas no eslate, a relação entre as caraterísticas dele e a gereção de ruido ainda não é completamente entendida. Esta pesquisa mostra 21 variações em seis diferentes parâmetros da geometria interna do eslate a fim de estabelecer suas relações com a geração de ruido. As modificações foram focadas nas regiões do bordo de fuga e da cúspide, das quais foram variados o comprimento, ângulo e espesura. Comparações de algumas configurações foram feitas entre os resultados numéricos e experimentais visando a validação da metodologia computacional. Os estudos numéricos foram feitos usando o software PowerFLOW 5.3® e incluem análise não estacionárias como o espectro de ruido de campo distante, contornos do espectro de densidade de potência e espectro das flutuações de pressão na superfíficie do eslate e análise estacionarias como a distribuição do coeficiente de pressão e as variações dos coeficientes de sustentação e arrastro da asa. Por outro lado, os testes experimentais foram executados em um túnel de vento de secção de provas fechada no laboratório de aerodinâmica (LAE) da Escola de Engenharia de Sâo Carlos e consistiram em medições da pressão estática na superfície do modelo através de uma ScaniValve e do ruido através de uma matriz de microfones, cujos dados foram pos-processados utilizando as técnicas de beamforming convencional e CLEAN SC. A boa concordância emtre os resultados demonstraram a validade da metodologia das simulações e a confiabilidade dos resultados numéricos. Entre todas as partes do eslate modificadas, o comprimento da cúspide demostrou um maior efeito no ruído e nas características do escoamento ao redor do eslate. Porém, o ângulo e a espesura da cúspide não mostraram relação nenhuma nas propriedades aeroacústicas e aeordinâmicas da asa. Finalmente, relações emtre o ruido de slate e algumas características do escoamento foram encontradas.

Palavras-chave: Ruído de célula. Ruído de eslate. Geometría de eslate. Aeroacústica computacional.

LIST OF FIGURES

LIST OF TABLES

LIST OF ABBREVIATIONS AND ACRONYMS

ANOPP	Aircraft Noise Prediction Program
AoA	Angle of Attack
ASEL	A-weighted Sound Exposure Level
BGKW	Bhatnagar, Gross, Krook and Welander equation
CFD	Computational Fluid Dynamics
DLR	German Aerospace Center
DNL	Day-night Average Level
DNW	German-Dutch Wind Tunnel
DP	Digital Physics
EASA	European Aviation Safety Agency
EPNL	Effective Perceived Noise Level
ESEL	Equivalent Sound Exposure Level
FAA	Federal Aviation Administration
FAR	Federal Aviation Regulation
FFT	Fast Fourier Transform
FHP	Frisch Hasslacher-Pmeau
FW-H	Ffowcs-William Hawking
ICAO	International Civil Aviation Organization
K-H	Kevin-Helmholtz
LaRC	Langley Research Center
LB	Lattice-Boltzmann
LBM	Lattice-Boltzmann Method
LSB	Laminar Separation Bubble
MD	Molecular Dynamics

MSL	Main Shear Layer
NASA	National Aeronautics and Space Administration
NS	Navier-Stokes
OSPL	Overall Sound Pressure Level
PSD	Power Spectral Density
RMS	Root Mean Square
RNG	Re-normalization Group
ROI	Region of Interest
SCF	Slat Cover Filler
SEL	Sound Exposure Level
SPL	Sound Pressure Level
TKE	Turbulent Kinetic Energy
VLES	Very Large Eddy Simulation
VR	Variable Resolution
WME	Wing Main Element
WT	Wind Tunnel

LIST OF SYMBOLS

α	Angle of slat trailing edge
α_l	Shear-layer length to acoustic path ratio
β	Angle of slat cusp
γ^2	Coherence
ΔZ	Distance in z-direction
δ_{ij}	Kronecker delta
δ_w	Local vorticity thickness
ζ	Numerical constant for Ffowcs William analogy calculation
η	Local strain parameter
η_0	Numerical constant for $\kappa - \epsilon$ model
ι	Slat cusp thickness
κ	Slat cusp length
$\kappa - \epsilon$	Turbulence model
κ_v	Main shear-layer velocity to free-stream velocity ratio
λ	Specific heats of air ratio
λ_j	Most unstable wave in the j direction
μ	Dynamic viscosity
ν	Cinematic viscosity
$\xi(\Delta P)$	Function of pressure gradient
ρ	Density
σ	Inverse of the effective Prandtl number
τ	Turbulent relaxation time scale
τ_{eff}	Effective turbulent relaxation time scale
τ_{ij}	Stress tensor

$\tau_{\mathbf{ij}}$	Lighthill's stress tensor
Φ	Property of the fluid
ϕ	Directivity angle
χ	Slat trailing edge thickness
Ψ	Numerical constant for $\kappa - \epsilon$ model
ψ	Slat trailing edge length
Ω	Collision operator
ω_j	Weighting factor for j direction
a	Acceleration
b	Span
$C_{\epsilon i}$	Numerical constants for $\kappa - \epsilon$ model $(i = 1, 2)$
C_μ	Numerical constant for $\kappa - \epsilon$ model
c	Velocity of sound
c_D	Drag coefficient
c_f	Flap chord
c_j	Velocity of particles in j direction
c_L	Lift coefficient
c_m	Chord of wing main element
c_p	Pressure coefficient
c'_p	Root mean square pressure coefficient
c_s	Slat chord
$d\sum$	Area used for the FW-H analogy integration
E	State of a system
F	Force
$f(\Phi)$	Distribution function of property Φ
f	Frequency

f_n	Frequency of tones obtained analytically
FWH_{length}	Dimension of the FW-H measurement region in the z-direction
FWH_{period}	FW-H sample period
FWH_{start}	Start time of FW-H measurements
$G(i,i)$	Cross spectral power density
k	Boltzmann constant
k_s	Surface roughness length
L_{AE}	Noise measured in A-weighted sound exposure level
L_{Aeq}	Noise measured in equivalent sound exposure level
L_a	Acoustic path
L_{day}	Noise measured in daytime sound level
L_{DN}	Noise measured in day-night sound level
L_{night}	Noise measured in nighttime sound level
L_p	Noise measured in sound pressure level
L_v	Shear-layer length
M	Mach number
M_r	Mach number of sound source
m	Mass
N	Number of molecules
$\vec{n}$	Unit vector in the normal direction
n	Lattice links
n_b	Number of bands
n_h	Number of harmonics
P	Pressure
P_{ref}	Reference pressure
q	Dynamic pressure

R_d	Specific gas constant of the air
Re	Reynolds number
$\vec{r}$	Unit radiation vector
r	Particle position
S	Local velocity gradient
s	Position along the shear layer
SL	Shear-layer
St	Strouhal number
T	Temperature
t	Time
TKE	Turbulent kinetic energy
TKE'	Root mean square turbulent kinetic energy
U_∞	Free-stream velocity
u'	Root mean square x-velocity
V	Volume
v_j	Velocity component in j direction
v'	Root mean square y-velocity
w'	Root mean square z-velocity
x	Observer position
y	Source position
y^+	Dimensionless wall distance

CONTENTS

1 INTRODUCTION

The exponential growth of the global population and development of large metropoles worldwide have increased the number of individuals affected by the operation of large airports. One of the most important perturbations caused by airports is the high noise levels related to take-off and landing procedures of airplanes. As a result, over the past years, more and tighter regulations about aircraft noise and several programs for its reductions have been developed towards keeping the life quality of the neighboring communities. An example is the last chapter of the International Civil Aviation Organization (ICAO), responsible for noise levels (chapter 14), reduced in 7 dB the standard limits in relation to the previous chapter (chapter 4) (ICAO, 2016).

Aircraft noise is comprised of engine noise and airframe noise, which are related to the aircraft propulsion components and the noise produced by the fluid-structure interaction, respectively. Formerly, aircraft noise was attributed to engines, however, with the development of high-by-pass-ratio engines and new technologies in their materials and components, engines have become significantly quieter and airframe noise has been the focus of aircraft noise reduction.

Airframe noise is generated by the interaction between turbulent flow and aircraft structure and incremented by discontinuities and gaps. Its main sources are high-lift systems (flap and slat) and landing gear, of which the slat is one of the most important. The slat is a high-lift device located upstream the wing main element (WME), which is deflected during the take-off and landing procedures for increasing the maximum lift coefficient of the wing (C_L) and stall angle of attack. It is usually attached to the WME through brackets and join the WME enfolding. The noise in the slat is caused by unsteady loads located in the slat cove and by the interaction between the fluid troughout the gap and the downstream elements (slat trailing edge and WME leading edge), and this complex flow causes a typical slat spectra composed of mid-frequency tones, a broadband component and a single high-frequency tone. The slat noise spectrum behavior has been described under different conditions of Mach number, angle of attack and slat deflection, nevertheless, the slat noise mechanism has not been completely understood.

Some slat noise reduction techniques consist in filling the cove, setting seals on the upper internal surface of the slat and modifying the cusp geometry. However, the relation between slat geometry and noise has not been analyzed to date.

This research focuses on the numerical and experimental analysis of the effect of slat internal geometry on the slat noise generation. For the analysis, parametric modifications (only one characteristic was modified per time) of a real slat of a convectional medium range

aircraft were accomplished: 5 modifications in the cusp length, 5 in the angle of the trailing edge, 3 in the trailing edge length, 2 in the trailing edge thickness, 2 in the cusp thickness, and 2 in the cusp angle. Both, numerical and experimental analysis were achieved using a three-element wing, i.e., slat, wing main element and flap, and only the slat was modified in each case. All modifications were simulated using the PowerFLOW 5.3b software, and two modifications of the cusp length and baseline were tested experimentally in the LAE-1 closed-section wind tunnel at the São Carlos School of Engineering - University of São Paulo. The studies were conducted at 34 m/s free stream velocity, which corresponds to a 1.1×10^6 Reynolds number based on the stowed chord of the wing and 0.098 Mach number based on the atmospheric conditions at the wind tunnel location. There is a limitation in Reynolds and Mach numbers due to the limitations of the wind tunnel power and dimensions. Numerical and experimental results were compared for validating establishing an appropriate simulation methodology.

The main contributions of this work are: the analysis of the effect of the slat geometry in the noise, which can be implemented in the design process of a slat, the proper establishment of aeroacoustic simulations set-up, which can use for future studies and finally and probably the most important contribution is the relations found between some characteristics of the flow around the slat and the far-field spectra, once with these relations, comparisons of the noise generated by different slat configurations could be achieved by simple aerodynamic and stationary simulations.

1.1 Objectives of the research

1.1.1 Main objective

Analyze parametrically the effect of the slat geometry on the generated noise and relate the acoustic phenomenon with slat-flow.

1.1.2 Specific objectives

- Simulate the baseline configuration and compare the results with wind-tunnel experimental tests.

- Make aeroacoustics and aerodyamics experiments in a wind tunnel of the baseline and other configurations.

- Simulate different slat configurations modifying some parameters of its internal geometry for detecting their influence with slat noise.

1.2 Structure of the dissertation

This dissertation is divided into four main sections. The first part (chapter 2) reports on a literature review of the main researches and concepts of airframe noise, specifically regarding slat noise, and some slat noise reduction techniques.

Chapter 3 is devoted to the methodology applied in the research, the numerical and experimental set-ups and the validation case. The numerical set-up consists in a revision of PowerFLOW program and the basic theory of Lattice-Boltzmann method and Ffowcs William-Hawking acoustic analogy. The experimental set-up section describes the experimental processes, wind tunnel, model and post-processing analysis. Finally, the validation case includes a comparison between numerical and experimental results of the baseline configuration.

Chapter 4 addresses the slat geometry modifications. Chapter 5 provides the results of the research - the first part is an analysis of the slat noise and a characterization of the flow around the slat; it then describes the results of the aerodynamic and aeracoustic effect of each slat modified parameter. The last chapter reports the concluding remarks and suggests future works.

2 LITERATURE REVIEW

2.1 Programs and regulations

Concerns about the noise generated by aircraft, mainly around airports, have been the focus of recent researches and tighter regulations, since aircraft noise reductions promote increments in the airplane traffic with no negative effects on neighboring communities (DOBRZYNSKI et al., 1998). Figure 1 shows the area around the airports established by the International Civil Administration Organization (ICAO) in each chapter of noise, whose maximum noise level allowed is 80 dB and how it was reduced over the years. In 40 years the area was reduced a 93%.

Figure 1: 80 dB Sound Exposure Level (SEL) contours

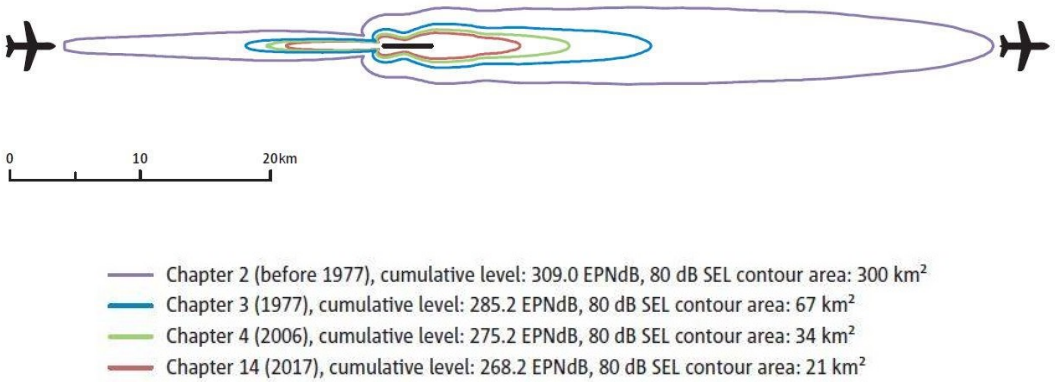

Reference: EASA (2016)

Aircraft noise is regulated by aircraft certifying entities through international standards applied when the aircraft is requesting its airworthiness certification (FEDERAL AVIATION ADMINISTRATION, 2017). Such standards are established in conjunction with International Civil Aviation Organization (ICAO). Airplane acoustic certification involves measurements of the aircraft noise level in Effective Perceived Noise Level (EPNL) scale, which indicates the noise intensity heard by humans that depends on both Sound Pressure Level (SPL) and sound frequency, at three reference points:

- Fly-over: 6.5 km from the brake release point, under the take-off flight path;
- Sideline: highest noise measurement recorded at any point 450 m from the runway axis during take-off.
- Approach: 2 km from the runway threshold, under the approach flight path.

The maximum values depend on the maximum take-off weight (ICAO, 2016).

Apart from EPNL, specific metrics have been developed to measure the aircraft noise level. In general, noise is defined as pressure field fluctuations, which are used for the calculation of the SPL (Equation 2.1). The logarithm scale reduces the range of values and the reference pressure (P_{ref}) is the threshold of human hearing, i.e., $2 \times 10^{-}5\ Pa$ for a 1000 Hz frequency. The Noise measured in SPL is identified by L_p. The A-weighted sound exposure level (ASEL) scale, identified by L_{AE} scale, captures all the energy of single events, characterized by the rise and fall of the noise level over a minute. For multiple events, their average, called equivalent sound exposure level (ESEL) and denoted by L_{Aeq}, is used. Daytime and nighttime sound levels can also be distinguished by metrics L_{day} and L_{night}, respectively. The day-night average level (DNL), denoted by L_{DN}, is used when additional sensitivity to nighttime operations is considered (ICAO, 2016; SPERRY, 1968).

$$SPL = 20 * Log_{10}(P/p_{ref}) \tag{2.1}$$

The Federal Aviation Regulation (FAR) has implemented several programs towards reducing the number of individuals exposed to significant noise levels, defined as 65 dB on the DNL scale. Figure 2 shows the reduction in the exposed individuals and the air traffic growth between 1975 and 2012. The individuals exposed were reduced an approximately 90%, whereas the landings were more than doubled increased. The graph indicates a new quieter generation of aircraft is in development.

Figure 2: Individuals exposed to significant noise and air traffic variation between 1975 and 2012

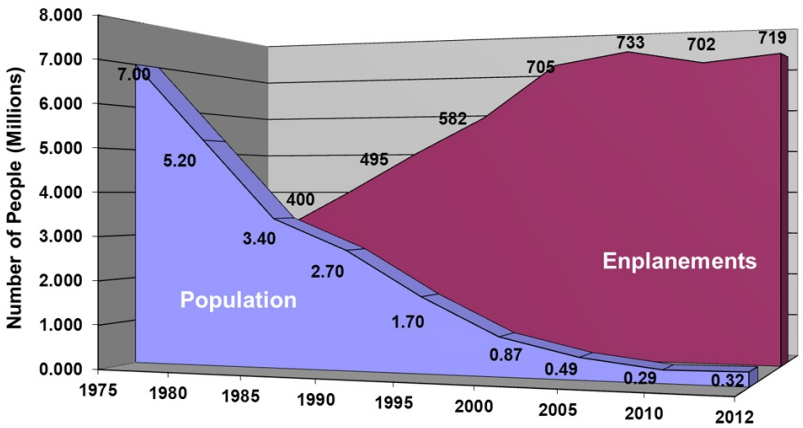

Reference: Federal Aviation Administration (2017)

In 1995, the European Union proposed reduce to half the noise impact until the year 2020. Concomitantly, more stringent requirements were established on Advanced Subsonic Transport and Quiet Aircraft Technology research programs in the United States

of America. Nowadays, most regulatory and research entities, as FAA and NASA, and also private companies have programs for reductions in the aircraft noise (DOBRZYNSKI, 2010).

2.2 Aircraft noise

The main sources of aircraft noise are located where the the flow instabilities play an important role and it is increased by gap and discontinuities. Figure 3 shows the noise sources in a typical commercial aircraft. In all cases, the flow conditions were profoundly changed by either discontinuities, or the junction of the wake of different aircraft components.

Figure 3: Aircraft noise sources

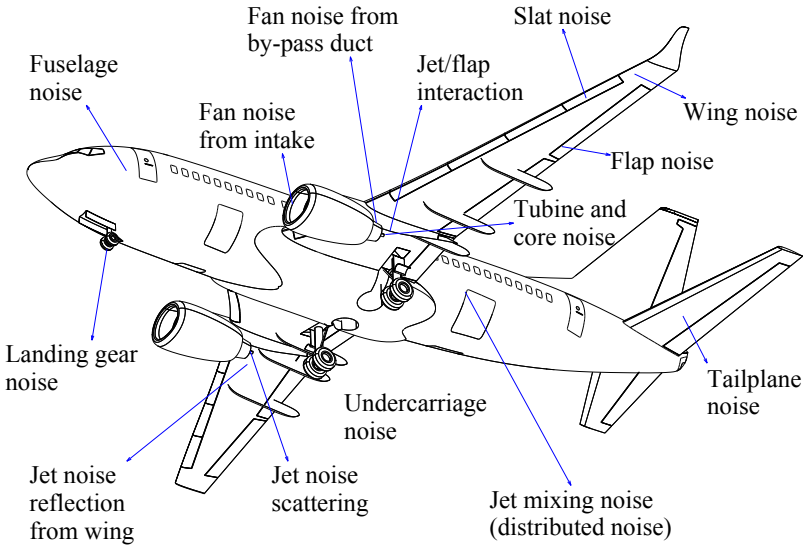

Reference: Modified from Chow, Lempereur and Mau (1999) and Morgan and Hardin (1975)

Despite the number of noise sources showed in Figure 3, aircraft noise can be divided into two main components, namely engine noise and airframe noise. Engine noise refers to the noise generated by all components of aircraft propulsion system, and airframe noise is the noise from the airframe moving through the air. When aircraft noise was considered an important issue, engines were its main source and the focus of noise reduction. However, over the past few decades, they have become significantly quieter, mainly in long-range aircraft, due to technical advances in the components and materials used (CHOW; MAU; REMY, 2002) and the incorporation of high-by-pass technology. As a consequence, airframe noise has become the main source of aircraft noise and nowadays, approximately half of the total noise during landing approach is caused by engines, while the other half is generated

by the aircraft structure (GLEINE; MAU; CARL, 2002). Figure 4 shows an estimate of aircraft noise per component performed by Airbus (2015) in a typical Twin-engine long range transport aircraft in the approach flight stage.

Figure 4: Noise from aircraft components in approach stage

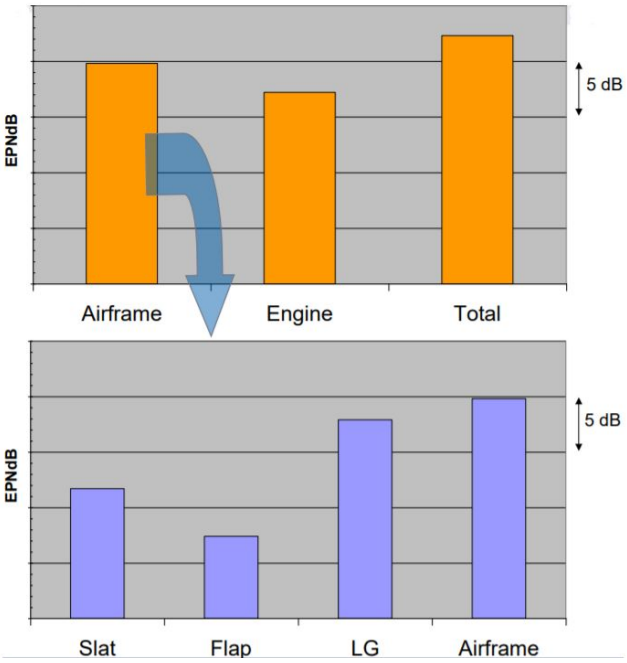

Reference: Airbus (2015)

Airframe noise is generally caused by fluctuations in the flow field near surfaces with discontinuities (STREETT et al., 2006), as high-lift devices. According to Dobrzynski (2010), a wing in a high-lift configuration is 10 dB noisier than a wing in cruise configuration. During landing approach and take off, when high-lift devices and the landing gear are deployed, the following six mechanisms are identified as main airframe noise sources. The rank of airframe noise sources highly depends on the geometry and operational conditions of each aircraft (CASALINO et al., 2008):

- Wing trailing-edge scattering of boundary-layer turbulent kinetic energy into acoustic energy;
- Vortex shedding from slat/main-body trailing-edges and the possible gap tone excitation through nonlinear coupling in the slat/flap coves;
- Flow unsteadiness in the recirculation bubble behind the slat leading-edge;
- Roll-up vortex at the flap side edge;

- Landing-gear multi-scale vortex dynamics and consequent multi-frequency unsteady force applied to the gear components; and
- Parasitic noise, due to joints and hollow pins

In general, airframe noise can be divided into landing gear, flap and slat noise. Landing gear noise is characterized by a low-frequency noise (between 0.5 and 3 kHz) related to more bulky gear components, such as tires and large struts and cavities, and high-frequency noise, due to the small components attached to the main structural components. Flap side-edge noise is attributed to the combination of trailing-edge noise, interaction of the vortex flow with the flap upper surface and the noise originated from accelerated free turbulence in the vortex flow (DOBRZYNSKI, 2010). The slat noise is explained in detail in the next subsection.

2.3 Slat noise

Figure 5 shows the flow around a typical deployed slat. The fluid through the gap formed between the slat and the main element is accelerated due to the slat concave geometry and the curvature of the wing main element leading edge. Such an acceleration generates an additional lift, however, it also causes the formation of an entrapped eddy vortex along the concave rear surface of the slat by the turbulent separation of the airflow along the lower rear edge of the slat. Furthermore, the vortex is continuously supplied with more energy from the adjoining gap airflow. Therefore, turbulence cells are formed along the boundary between the eddy vortex and the gap-flow and pulled along with and into the accelerated gap-flow. Such a phenomenon generates and radiates aerodynamic noise along the entire span of slat, especially when the turbulent cells separate and flow over the upper rear or trailing edge of the slat (MAU; DOBRZYNSKI, 2004). The boundary between the eddy vortex and the gap-flow is called slat main shear layer (MSL) and the point on which the main shear layer impinges the slat surface is called reattachment point.

Figure 6 shows a typical slat spectrum in SPL versus strouhal number (St), characterized by low/mid-frequency tones, broadband at medium frequencies, which decrease in function of the frequency, and high-frequency hump (PAGANI; SOUZA; MEDEIROS, 2016). Tonal peaks are attributed to the cavity resonance in the slat cove in combination with the adjacent wing leading edge; the more accepted theory is tonal peaks are generated due to a feedback loop between the cusp and the reattachment point in the upper slat internal surface, which is supplied with the vortex generated in the cusp and acoustic waves generated when the main shear layer impinges on the slat surface (TERRACOL; MANOHA; LEMOINE, 2015). The relation between mid-frequency tones with Reynolds number has not been completely understood. Experiments with different tripping devices have shown low-frequency tone effects could be attenuated or eliminated

through tripping at the slat hook (DOBRZYNSKI, 2010). However, other results have shown mid-frequency tones are present even with the use of tripping devices (KOLB et al., 2007a; POTT-POLLENSKE; ALVAREZ-GONZALES; DOBRZYNSKI, 2003). Although broadband noise does not have a specific definition, Dobrzynski and Pott-Pollenske (2001) modeled it as an acoustic dipole normal to the slat surface near the trailing edge. High-frequency tones are usually caused by the vortex shedding behind blunt trailing edge and it is usually not presented in fligth conditions (IMAMURA et al., 2007).

Figure 5: Flow around slat

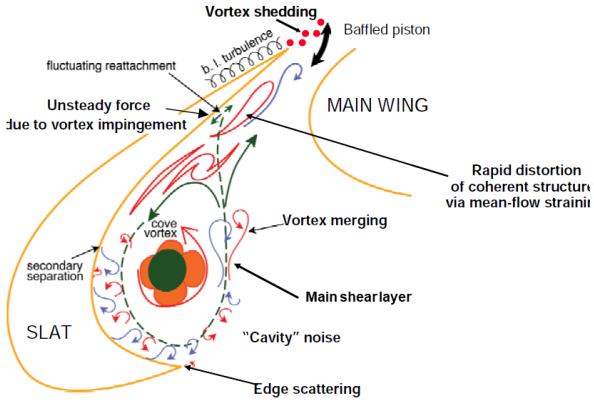

Reference: Mau and Dobrzynski (2004)

Figure 6: Typical Slat spectra

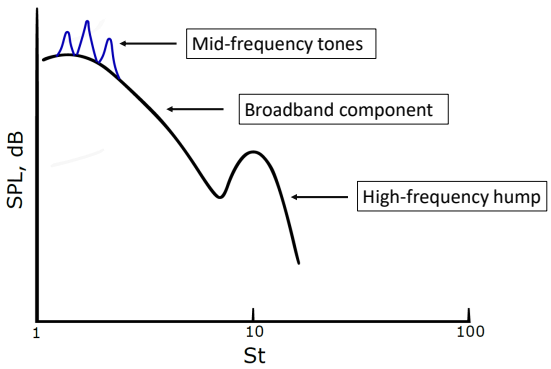

Reference: modified from Khorrami and Lockard (2006)

Terracol, Manoha and Lemoine (2015) characterized the slat main shear layer in slat cove and identified 2D Kevin-Helmholtz instabilities near the cusp of the slat. Such 2D flow transition to 3D turbulent flows along the shear layer and finally impinges on the upper slat wall. The authors also used the distance between the reattachment and the cuspid and the distance traveled by the main shear layer to analytically estimate the frequencies of the discrete low-frequency tones, as will be addressed in subsection 4.2.4

Previous research on slat noise has found several typical characteristics of slat spectra. Dobrzynski et al. (1998) observed peaks are significant only for angles of attack above 8^o i.e., if there is a significant mass flow through the gap (however, this is against other researches (PAGANI; SOUZA; MEDEIROS, 2016; PEREIRA et al., 2018b)). The tones increase in function of the flow speed and slat trailing edge bluntness and their frequencies also increase linearly with flow speed and decrease with slat chord, i.e., the Strouhal number is almost constant ($St = fU_\infty/c_s$). Chow, Mau and Remy (2002) established some *"noise generation velocity laws"*, U^6, for landing gears and slats, U^8 for flaps and $U^{5.5}$ for combined high-lift devices (flap and slat). Pagani, Souza and Medeiros (2016) described the slat noise spectra behavior in function of angle of attack as follows: when the angle of attack increases, the tonal peaks decrease and the high-frequency hump shifts toward higher frequencies and their magnitude is weakly affected for up to 8^o angles of attacks.

Choudhari et al. (2002) observed slat noise is independent of Reynolds number for values higher than 7×10^6. Kolb et al. (2007b) identified slat stagnation points through surface flow visualization and studied the laminar separation bubble (LSB) on the upper surface. Such an LSB reattaches upstream the slat trailing edge and generates a multiplicity tonal frequency in a high-frequency range (from 5 to 10 kHz).

2.3.1 Techniques of slat noise reduction

Slat noise is generated mainly by its surface discontinuities and recirculation in the gap, therefore, several solutions have focused on the mitigation of the eddy vortex and interruption of recirculation through the gap.

The design of low-noise high-lift devices requires the analysis of several constraints, e. g., certification requirements set the maximum lift coefficient to the minimum landing speed. Therefore, if the maximum lift coefficient is reduced, the minimum speed must be increased, which increases the airframe noise and might compromise the benefits achieved with the reduction by the high-lift device (DOBRZYNSKI, 2010).

Dobrzynski (2010) considered constraints and divided them into the following three groups: I. Operational constraints: maintenance of maximum lift and sufficient lift for moderate angles of attacks; II. Safety constraints: reliability, i. e., malfunctioning of low-noise treatments must not affect the aircraft performance and handling quality, and no changes in lift/moments with activation of control devices; and III. Operational cost constraints: weight, structural stress, system complexity, and maintenance.

Slat cover filler (SCF), a concept introduced by Gleine, Mau and Carl (2002), is one of the most common noise reduction solutions, since it eliminates the complex flow in the cove region of the slat, hence, the associated acoustic source. Streett et al. (2006) evaluated the SCF (Figure 7) and found a 3 to 5 dB noise reduction through the spectrum. They performed aerodynamic tests to evaluate the reduction wing performance and found SCF caused the wing stalls two grades of angle of attack before and reduced 0.001 the maximum lift coefficient. Chow, Mau and Remy (2002) implemented an SCF on an original A320 full-scale wing and conducted experimental tests in the German-Dutch wind tunnel (DNW). They found an average 0.8 dB reduction in each microphone. On the other hand, Kolb et al. (2007b) compared two SCFs, of which the first was the traditional SCF and the second was designed according to the trajectory of the separation streamline. Although both significantly reduced the slat noise, the second showed lower noise emissions. According to this technique, there is an optimal SCF for each angle of attack (since the shear layer varies with the AoA). The results are shown in Figure 8.

Despite the benefits offered, SCF has not been implemented in real airplanes because the slat cover must be rigid to be functional and impede the retraction of the slat. Scholten et al. (2015) designed an SCF using a highly deformable material. However, the

solution involved other implications, which will not be discussed in this dissertation.

Figure 7: Slat cover filler

Reference: Streett et al. (2006)

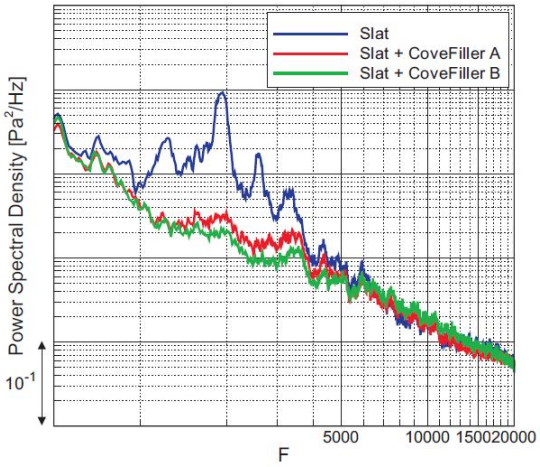

Figure 8: Cover fillers and Baseline spectra

Reference: Kolb et al. (2007b)

Chow, Mau and Remy (2002) proposed a row of brushes attached to the upper and lower slat trailing edges, as shown in Figure 9. The solution reduced approximately 5 dB at low frequencies and 1% the maximum lift coefficient.

Figure 9: Row of brushes

Reference: Chow, Mau and Remy (2002)

Smith, Chow and Molin (2006) measured the slat noise reduction installing acoustic liners at the slat cove and wing main element (WME) leading edge (see Figure 10) towards attenuating the noise generated in the gap. The results indicated a 2.5 dB broadband noise reduction for all angles of attack in a 2 to 8 kHz frequency range and no effect of acoustic liners on the aerodynamic performance. Acoustic liners consist of a single layer of air-filled cavities separated from the duct airflow by a porous facing sheet designed to absorb acoustic energy as an acoustic wave passes through the sheet and into the cavities (BAUER, 1977).

Figure 10: Acoustic Liners

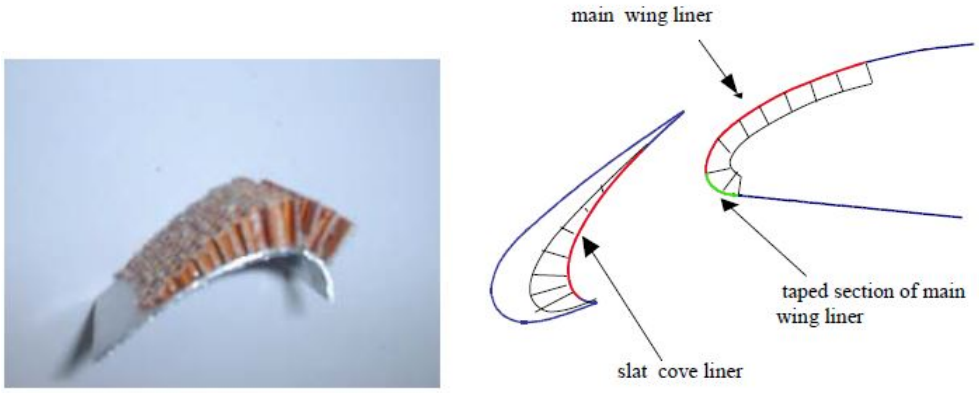

Reference: Smith, Chow and Molin (2006)

Mau and Dobrzynski (2004) designed a noise-reduction technique according to which flexible bristles are distributed along the lower and upper rearward edges in the span direction. As the bristles are flexible, they are self-adjusting due to the aerodynamic forces exerted by the respective prevailing airflow conditions. They form a smoothly contoured separation between the entrapped eddy vortex and the smooth gap airflow through the slat gap. When the slat is retracted, the bristles deform and adapt to the leading edge wing. Figure 11 shows a schematic view of the solution. A reduction of up to 15 dB was achieved.

Gleine, Mau and Carl (2002) projected a hollow expandable and contractible displacement element to fill-out the slat gap. It is secured on the concave rear slat surface and faces the leading edge of a wing. Engine bleed air flows through the hollow element and expands and contracts it. When the slat is extended, the displacement element is expanded to fill-out the concave cavity, and when it is retracted, the element is contracted to be accommodated between the slat and the leading edge of the wing main element (see Figure 12).

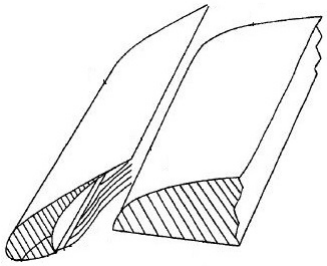

Figure 11: Bristles solution

Reference: Mau and Dobrzynski (2004)

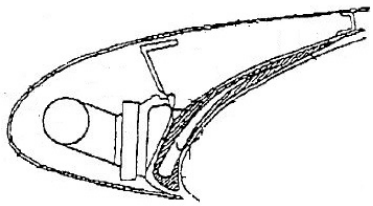

Figure 12: Hollow displacement element

Reference: Gleine, Mau and Carl (2002)

2.4 Aircraft noise prediction models

Due to the importance of aircraft noise, concerns about methods that predict noise have also played a fundamental role in the aeronautic science. However, this acoustic field reached a relatively modest progress in comparison to other branches of aerospace engineering, as CFD and wind tunnel testing. Actually, they still rely on empirical data for at least some aspects (FILIPPONE, 2014). The objective of prediction methods is to reliably predict sound emissions by a convectional aircraft without expensive simulations or high-fidelity wind tunnel tests and incorporate the results in the design process.

The first studies on airframe prediction models were lead by Fink (2002) in the 1970's and NASA in its ANOPP (NASA Langley's aircraft noise prediction program). After ANOPP, NASA developed an improved version, called ANOPP2, and currently has the FOOTPR/RADIUS code, focused on high speed jets with complex engine geometry and complex jet interaction (FILIPPONE, 2014). On the other hand, the German Aerospace Agency (DLR) developed the PANAM code, for comparison of the noise generated by different aircraft configurations - precision in this program is not the main focus, but the behaviour of each aircraft (BERTSCH, 2013). Private companies have also developed their own codes towards an approximation of aircraft noise in both military and commercial industries.

The assumptions of prediction models depend on the noise generation phenomenon, and the mathematical model used for each case is different, i. e., a prediction model used for fan noise or jet noise is different from that used for airframe noise. The Ffowcs William (WILLIAMS; HAWKINGS, 1969) and Ligthill (LIGHTHILL, 1952) theories about the sound aerodynamically generated are commonly used for modeling the airframe noise, combined with experimental, numerical and flight test results. The most complete slat noise prediction model is the one established by Guo (2012), since it combines the Ffowcs william-hawking model and the green's function for modeling the source and propagates the noise.

2.5 Lattice-Boltzmann method - PowerFLOW

Lattice Boltzmann Method (LBM) is a new technique for solving fluid dynamic problems. It is based on the resolution of the Boltzmann equation in a discrete lattice with appropriate symmetries. The Lattice-Boltzmann equation is essentially the kinetic equation resulted from the ensemble-averaging of the discrete dynamics of the Frish-Hasslacher-Pmeau (FHP) cellular automation supplemented with the assumption of molecular chaos (SUCCI; BENZI; HIGUERA, 1991).

Conventional numerical schemes, e. g. Navier-Stokes (NS) equations, are based on the discretization of macroscopic continuum, however, LBM incorporates the physics

of microscopic processes. The method is different from the others, since its convection operator in the phase space is linear and uses a minimal set of velocities (CHEN; DOOLEN, 1998). Such characteristics enable LBM to accurately capture the aerodynamics of high Reynolds number flows, pressure fluctuations due to separated and reattached flows (main airframe noise source), and multiphase flows. Furthermore, LBM solve complex geometries without grids defined by complex analytical functions, since it calculates the interaction between the surface and fluid particle by particle (CROUSE et al., 2006; HE; DOOLEN; CLARK, 2002).

PowerFLOW software resolves fluid dynamic problems, focusing on acoustic problems. It is based on LBM to resolve the fluid properties and uses the Ffowcs William-Hawking model to propagate and calculate the noise in the far-field using the pressure fluctuation on the surface.

Several studies have been developed with commercial software PowerFLOW; Crouse et al. (2006) demonstrated the capability of LBM to reproduce acoustic phenomena through four canonical acoustic problems with PowerFLOW. Fares, Casalino and Khorrami (2015) evaluated some noise reduction techniques in flap and landing gears applied to a Gulfstream aircraft model using PowerFLOW. The results were validated through the comparison of wind tunnel tests conducted at NASA Langley Research Center (LaRC) $14 - by - 22\ ft$ Subsonic Tunnel and showed agreement between experimental and numerical data. The details of simulations can be found in Khorrami, Fares and Casalino (2014). Casalino et al. (2014) also studied landing gear noise through powerFLOW code and compared the results with two types of wind tunnel, i. e., one acoustic and another aerodynamic, and with flight tests (CASALINO et al., 2012, 2014). Differences in the simulations set-up were established for the comparison of results with each wind tunnel.

3 METHODOLOGY

The methodology used in this research includes two approaches, numerical and experimental. The project could be divided into four parts; the first is related to the understanding and analyses of PowerFLOW code and the physics behind the software; the second is composed by experimental test; third comprehends simulations of the baseline configuration at different angles of attack and comparisons of the results with experimental ones for the validation and establishment of proper simulation parameters; comparisons of different fluid characteristics and far-field spectra will be accomplished; finally, the last part refers to the simulation of geometry variations and their analyses. Therefore, this chapter describes PowerFLOW program, Lattice-Boltzmann method and Ffowcs-William Hawking acoustic analogy formulation and the experimental and computational setup. The values of the Y-axis in the result graphs are not exhibited due to confidentiality issues.

3.1 Computational approach

3.1.1 PowerFLOW program

The information given in this subsection of the dissertation were taken from the PowerFLOW's guide user manual.

PowerFLOW is a software developed by Exa for computational simulations of fluid-flows. It focuses on aerodynamic, thermal and aeroacoustic simulations and provides solutions of transient or steady-state flows. It uses a particle-based method using the DIGITAL PHYSICS (DP)®, which is a technology also patented by Exa.

DP simulates a discrete fluid represented by particle densities in discrete space and time, rather than discretized partial differential equations, as Navier-stokes, as in traditional CFD methods. It is based on a discrete form of kinetic energy theory and uses an extended Lattice-Boltzmann model, in which particles exist at discrete locations in space and move in discrete directions at discrete speeds and time intervals.

The computational domain is discretized into cubic lattice (3D cells) with symmetry properties necessary for artifact-free fluid simulations. Such 3D cells are called voxels in DP and their intersections with the body are called surfels, as shown in Figure 13. The time unit in the simulations is called timestep and, at each timestep, the particles move from one to another neighboring voxel.

As in real fluids, DP (using the LBM) considers three microscopic processes, namely particle/particle interaction, particle/surface interaction and particle movement (advection).

Figure 13: PowerFLOW space discretization

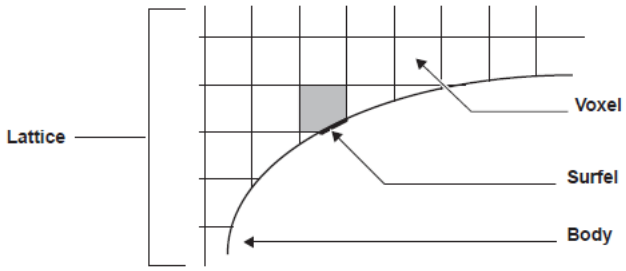

Reference: PowerFLOW user's guide (DASSAULTSYSTEMS, 2015)

A particle/particle interaction occurs at each timestep in two phases, namely movement, and collision. In the movement phase, PowerFLOW considers particle densities moving only in discrete directions and speeds, whereas in the collision phase, particles can change speed and/or direction while maintaining total mass, momentum, and energy in the voxel. The kinetic theory used sets the equilibrium for each direction.

The particle/surface interaction is divided into voxel to surfel and surfel to voxel advection. In the former, particles that would hit a surfel within a timestep are gathered by the surfel. The collision process applied is subject to the conservation of mass, and exchange momentum and energy with surfaces, through the application of the specific boundary condition. The amount of momentum changed corresponds to pressure and friction in the fluid and surface, respectively. In the second step, the gathered particles are reflected. The boundary condition is a direct discrete analog of a process for a true continuous fluid system, which enables PowerFLOW to accurately and automatically handle complicated surface geometries.

PowerFLOW uses the direct simulation method for low Reynolds number (Re) (<10000), whereas a turbulence model is used for high Re (>10000). However, the program enables the user to select the mathematical model.

When configured as a direct simulation, the program resolves the Kolmogorov length scale in the bulk fluid (approximately $Re^{-\frac{3}{4}}$ to the length scale mean flow) and achieves a $y^+ \approx 1$ in the boundary layer.

As a turbulence model, PowerFLOW uses the $\kappa - \epsilon$ RNG equations with extensions, which are equivalent to Very Large Eddy Simulations (VLES) time-accurate physics. The effects of the unresolved (sub-grid) scale-flow properties on the resolved large scale are extended via eddy viscosity and turbulent Prandtl numbers. PowerFLOW also uses the universal Law of the Wall velocity profile to assume the velocity in the voxels closest to the surface and, coupled with the wall model pressure gradient extension, determines the

local skin friction.

The mesh is generated through Variable Resolution regions (VR), which are regions of different mesh element sizes. They are identified by levels: the highest level has the smallest elements, which increase by twice their size at each VR level. PowerFLOW recommends the use of 8 to 11 levels of VR for aerodynamic simulations. For establishing the minimum element size, PowerFLOW uses a variable named resolution, defined as the number of cells along the char length. Higher resolution requires higher time discretization.

For establishing the simulation time and time discretization, the user can set total time in timesteps or in physical time. For cases that the user enter the physical time, PowerFLOW uses the resolution for determining the simulation time in one timestep. The calculation depends on the Mach number regime and the turbulence model. For the option of Mach number "same of experiments", Equation 3.1 shows how PowerFLOW discretize simulation time, where k is 0.028224 for turbulence model or 0.0288 for direct simulations.

$$simulated\ time\ in\ one\ timestep = \frac{k}{\sqrt{Temp_{char}} \times resolution/length_{char}} \tag{3.1}$$

The boundary conditions define the surface behavior in a PowerFLOW simulation and can be divided into wall boundary conditions, which prevent the fluid from passing through the wall, and driving boundary conditions, which force the fluid to conform to one or more constraints on pressure, velocity, mass flux or mass flow.

The possible wall boundary conditions in PowerFLOW are:

- standard wall, which is a regular wall,
- frictionless wall, which is an idealized wall, also called free slip wall,
- selectable wall, which behaves like a standard wall in some places and a frictionless wall in others, according to the spatially varying equation,
- sliding wall, which moves at a uniform velocity parallel to itself without changing shape.
- rotating wall, which rotates around an axis without changing shape, and
- velocity wall, which is a standard wall of prescribed velocity.

PowerFLOW enables the user to select the boundary layer regime between laminar, turbulent or automatic in all walls; in the automatic option, the program calculates the transition point. The flow can be also forced to be laminar or turbulent and in the automatic option, the program calculates the turbulence in the free stream flow.

Driving boundary conditions can be used as inlets or outlets and the user can select among velocity, pressure and velocity, mass flux, mass flow, static pressure and total pressure.

PowerFLOW enables different types of measurements during a simulation and, according to the necessities, users can select among:

- standard measurement by region and face, which records fluid, fan and porous media variables in a volume or faces defined,
- sampled face measurement, which collects fluid data in non-solid faces,
- composite measurement by region or face, which records integrated values of measurement variables in volumes or faces defined,
- probes, which measure fluid or surface variables at a specific location.

The type of measurement influences both simulation time and storage.

To calculate the far-field noise, PowerFLOW uses the pressure-history in a surface and propagate it to the far-field through the Ffowcs William-Hawking analogy, which considers the aerodynamic noise as a source of stress tensor strength.

A simulation is divided into three steps, namely discretization, decomposition, and simulation. During discretization, the continuous geometry is converted to a discrete collection of voxels and surfels. In the decomposition phase, a case is split according to the multiprocessor server or cluster used to run the simulation. Finally, measurement files are created during simulation.

The program includes additional components for completing the post-processing. The modules used in the current study are PowerDELTA, which converts CAD files, meshes the geometry and improves the quality of faceted geometry, PowerCASE, which prepares the case to be simulated, PowerACOUSTICS, which achieves the far-field analysis, and PowerVIZ, which exhibits the fluid flow properties and fluid structures.

3.1.2 Lattice-Boltzmann method

This subsection briefly describes the Lattice-Boltzmann method and the kinetic theory focused on the DP principles. More information can be found in Mohamad (2011)

LBM was introduced by McNamara and Zanetti in 1988 as a method to solve fluid dynamic problems. It is known as an explicit method, once it aims at being an intermediate method between the conventional CFD solvers and the molecular dynamic (MD) solvers. Convectional CFD solvers establish the fluid as a continuous medium and MD analyzes the fluid particle by particle. In LBM, the fluid is replaced by fraction particles according

to a distribution function that considers the behavior of a collection of particles as a unit. Particles stream only in given directions (lattice links), collide at lattice sites and are represented by a distribution function. LBM is also called mesoscale (MOHAMAD, 2011).

3.1.2.1 Kinetic theory

The concept of the kinetic theory of gases, which analyzes small particles with constant movement, must be reviewed for the understanding of LBM. This theory considers particles perfect spheres with the same mass in constant and rapid motion. It also takes into account a large number of particles, therefore, a statistical analysis determines the fluid behavior, and the distance between particles is larger than their size. The particles interact only during collision (no chemical reactions are considered), which is instantaneous and perfectly elastic. The kinetic theory resolves three variables of particle position and three variables of velocity vector.

The kinetic gas theory used in PowerFLOW involves five possible boundary conditions. The first is a perfect reflection, i. e., the velocity magnitude is conserved with the reflected direction. The second conserves the velocity magnitude with the opposite direction. The third is an infinite boundary condition, under which the body acts as a toroidal wall. The fourth boundary condition is a solid boundary in which the particle reflects in a random direction. Finally, the fifth is a thermal source or thermal sink, which adds or removes energy, respectively (EXA COMPANY, 2009).

The gas kinetic theory calculates the density through Equation 3.2, where N is the number of molecules, m is the mass and V is the volume. The pressure is calculated as the change of momentum generated by the collision of particles with the surface, and the kinetic energy (KE) of a gas is calculated through Equation 3.3, where k is the Boltzmann constant and T is the temperature in Kelvin.

$$\rho = \frac{Nm}{V} \tag{3.2}$$

$$KE = \frac{3}{2}kT \tag{3.3}$$

3.1.2.2 Distribution function

Maxwell (1959) introduced the distribution function concept, which is a parameter that characterizes the effect of the molecules, i. e., the percentage of molecules in a certain location of a container whose velocities are within a certain range at a given instant of time. Once the particles can have different velocities, when they collide faster particles transfer momentum to slower particles and the total momentum is maintained.

For a gas of N particles, the number of particles whose velocities range between c_x and $c_x + dc_x$ (c is the velocity vector and its subscript indicates direction) is $Nf(c_x)dc_x$, where $f(c_x)$ is the distribution function and represents the fraction of particles of velocities in that interval at any instant of time (this applies to all direction). The probability of the velocity ranging between $c_x + dc_x$, $c_y + dc_y$ *and* $c_z + dc_z$ is $Nf(c_x)f(c_y)f(c_z)$. If this equation is integrated over all possible velocity values, the result is one, as shown in Equation 3.4

$$\int\int\int f(c_x)f(c_y)f(c_z)dc_xdc_ydc_z = 1 \tag{3.4}$$

The distribution function does not depend on the direction, but only on the speed particles, as showed in Equation 3.5 , where Φ is another function to be determined. Once a function distribution is a fraction of particles, its value must range between 0 and 1.

$$f(c_x)f(c_y)f(c_z) = \Phi(c_x^2 + c_y^2 + c_z^2) \tag{3.5}$$

3.1.2.2.1 Maxwell-Boltzmann distribution function

The left hand in Equation 3.6 shows the kinetic energy per particle and the right hand shows the mean kinetic energy of a particle established by the kinetic theory (Equation 3.3). If an exponential function distribution is $f(c) = A^3e^{-Bc^2}$, Equation 3.7 is obtained from Equation 3.6.

$$\frac{\int_0^\infty \frac{1}{2}mc^2f(c)dc}{\int_0^\infty f(c)dc} = \frac{3}{2}kT \tag{3.6}$$

The value of B can be obtained from Equation 3.7, hence, $f(c) = A^3e^{\frac{-mc^2}{2kT}}$. Constant A is found through the integration of the distribution function overall speeds and equaled to 1, as shown in Equation 3.4.

$$\frac{3m}{4B} = \frac{3}{2}kT \tag{3.7}$$

Finally, the Maxwell-Boltzmann distribution function is obtained replacing constants A and B in the distribution function initially established and is shown in Equation 3.8.

$$f(c) = 4\pi(\frac{m}{2\pi kT})^{\frac{3}{2}}c^2e^{\frac{-mc^2}{2kT}} \tag{3.8}$$

3.1.2.2.2 Boltzmann distribution function

Boltzmann generalized the Maxwell-Boltzmann distribution function for arbitrarily large systems and established, for any system in thermal equilibrium, the probability of

a system being in a particular state E is proportional to $\epsilon^{\frac{-E}{kT}}$, i. e., $f(E) = Ae^{\frac{-E}{kT}}$. A is obtained through the integration of the distribution function proposed by Boltzmann over all possible values (Equation 3.9).

$$\int_{-\infty}^{\infty} Ae^{\frac{-E}{kT}} = 1 \tag{3.9}$$

Finally, Equation 3.10 indicates the Boltzmann distribution function in 3D, which can be expanded to each direction. Such a function is the Maxwell-Boltzmann distribution function integrated over a surface of sphere and the base of LBM.

$$f(c) = (\frac{m}{2/\pi kT})^{\frac{3}{2}} e^{\frac{-mc^2}{2kT}} \tag{3.10}$$

3.1.2.3 Boltzmann equation

As addressed in subsections 3.1.2.2.1 and 3.1.2.2.2, a system can be characterized by a distribution function $f(r, c, t)$, which is the fraction of particles positioned between r *and* $r + dr$ with velocities between c *and* $c + dc$ at a specific time t.

If an external force is applied, collisions occur between particles and cause a net difference between the number of particles in the $drdc$ interval. The rate of change between the final and initial status of the distribution function is called collision operator (Ω). Equation 3.11 provides the number of molecules in a system.

$$f(r + cdt, c + Fdt, t + dt)drdc - f(r, c, t)drdc = \Omega(f)drdcdt \tag{3.11}$$

If Equation 3.11 is divided by $drdcdt$, it is reduced to $\frac{df}{dt} = \Omega(f)$. Distribution function f depends on r, c and t; therefore, it can be rewritten as partial derivatives, as shown in Equation 3.12.

$$\frac{df}{dt} = \frac{\partial f}{\partial r}\frac{dr}{dt} + \frac{\partial f}{\partial c}\frac{dc}{dt} + \frac{\partial f}{\partial t} \tag{3.12}$$

Once $dr/dt = c$ and $dc/dt = a = \frac{F}{m}$, Equation 3.11 can be rewritten, as shown in Equation 3.13, and in a vectorial form, as shown in Equation 3.14.

$$\frac{\partial f}{\partial t} + c\frac{\partial f}{\partial r} + \frac{F}{m}\frac{\partial f}{\partial c} = \Omega \tag{3.13}$$

$$\frac{\partial f}{\partial t} + \overrightarrow{c} \bullet \nabla f + \frac{1}{m}\overrightarrow{F} \bullet \nabla f = \Omega \tag{3.14}$$

Equation 3.14 is the Boltzmann transport equation. The first term is the variation in time, the second is the variation from the flux of particles in the physical space, the

third is the variation from the flux of particles in the velocity space and the right-hand side term is the variation from collisions.

3.1.2.4 BGKW equation

Ω is a function of f to be determined, so that Boltzmann equation can be solved. However, Bhatnagar, Gross and Krook (BGK) and Welander (W) established an approximation for the collision operator without introducing a significant error to the outcome solution (Equation 3.15), where f^{eq} is the local equilibrium distribution function, which is the Maxwell-Boltzmann distribution function, ω is the collision frequency and τ is the relaxation factor.

$$\Omega = \omega(f^{eq} - f) = \frac{1}{\tau}(f^{eq} - f) \tag{3.15}$$

Whit the BGKW approximation, Boltzmann equation can be rewritten as shown in Equation 3.16. Such an equation can be expanded in each direction (linkages in LBM) and is the settlement of LBM, equivalent to Navier-Stocks equation in convectional CFD simulations.

$$\frac{\partial f}{\partial t} + \overrightarrow{c} \bullet \nabla f + \frac{1}{m}\overrightarrow{F} \bullet \nabla f = \frac{1}{\tau}(f^{eq} - f) \tag{3.16}$$

Boltzmann equation is a linear partial differential equation that resembles an advection equation with a source term. Its right-hand side represents the advection (streaming) and the lef-hand side represents the collision process. The local equilibrium distribution function with a relaxation time determines the type of problem to be solved.

3.1.2.5 Discretization of Boltzmann equation

Equation 3.16 can be discretized in time and spatially. Equation 3.17 shows the LB equation discretized in time in a specific j direction.

$$f_j(r + c_j\Delta t, t + \Delta t) = f_j(r, t) + \frac{\Delta t}{\tau}[f_j^{eq}(r, t) - f_j(r, t)] \tag{3.17}$$

Two factors are taken into account for the spatial LB equation discretization, namely dimension of the problem and number of linkage (direction in which the particle can move). Each case has a different discretization. As addressed in subsection 3.1.1, PowerFLOW divides the computational domain into 3D-cells, and the particles can move in 18 directions to neighboring cells (see Figure 14). Such a discretization is named D3Q19 (3-dimensions and 19-velocity directions, including the 0-vector). Only this type of discretization will be explained.

Figure 14: Lattice arrangement for 3D problems and 19 velocity vectors

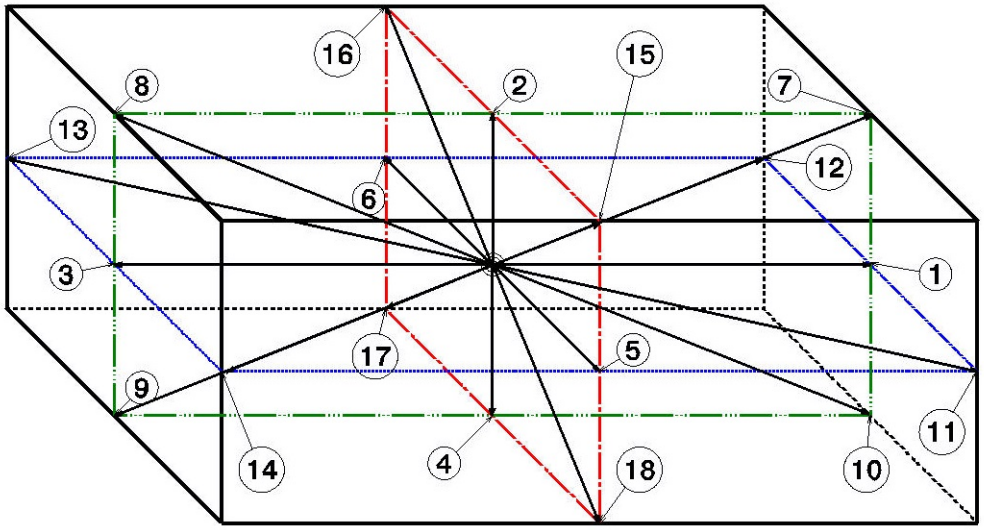

Reference: modified from Mohamad (2011)

Figure 14 shows the 3D lattice arrangement with 19 velocity vectors, including the central vector of zero speed.

- Nodes 1, 2, 3 and 4 are in the center of the eastern, northern, western and southern faces, respectively.
- Nodes 5 and 6 are in the center of the front and back faces, respectively.
- Node 7 is in the intersection of the eastern and northern faces.
- Node 8 is in the intersection of the western and northern faces.
- Node 9 is in the intersection of the western and southern faces.
- Node 10 is in the intersection of the eastern and southern faces.
- Node 11 is in the intersection of the front and eastern faces.
- Node 12 is in the intersection of the back and eastern faces.
- Node 13 is in the intersection of the western and back faces.
- Node 14 is in the intersection of the western and front faces.
- Node 15 is in the intersection of the northern and front faces.
- Node 16 is in the intersection of the northern and back faces.
- Node 17 is in the intersection of the southern and back faces.

- Node 18 is in the intersection of the southern and front faces.

The 19 velocity vectors for the distribution functions of f_o to f_18 are c(0,0,0), c(1,0,0), c(0,1,0), c(-1,0,0), c(0,-1,0), c(0,0,1), c(0,0,-1), c(1,1,0), c(-1,1,0), c(-1,-1,0), c(1,-1,0), c(1,0,1), c(1,0,-1), c(-1,0,-1), c(-1,0,1), c(0,1,1), c(0,1,-1), c(0,-1,-1), c(0,-1,1), c(-1,0,-1), c(0,0,0). Each direction is a linkage in LBM. The weighting factors (ω_i) are $\frac{12}{36}$ for f_0, $\frac{2}{36}$ for f_1 to f_6 and $\frac{1}{36}$ for f_7 to f_18.

3.1.2.6 Equilibrium distribution function

The general form of the equilibrium distribution function is showed in Equation 3.18, where U_∞ is the macroscopic flow velocity vector, A,B,C and D are constants to be determined according to the conservation principle, and Φ denotes a scalar parameter, as density, temperature or species concentration, which is equal to the summation of all distribution functions, as in Equation 3.19, where n is the number of lattice links.

3.1.2.7 Very large eddy simulations model

As addressed elsewhere, PowerFLOW uses the Very Large Eddy Simulation (VLES) turbulence model based on the Reynolds Average Navier-Stokes (RANS) methodology and formulation of $\kappa - \epsilon$ two-equation turbulence model RNG. This turbulence model basically introduces two additional equations and variables, κ, which is the turbulent kinetic energy, and ϵ, which is the kinetic energy dissipation rate, and resolves them at each voxel.

$$f_i^{eq} = \Phi\omega_i[A + Bc_i + C(c_i \bullet U_\infty)^2 + DU_\infty^2] \tag{3.18}$$

$$\Phi = \sum_{i=0}^{i=n} f_i^{eq} \tag{3.19}$$

According to Pope (2001), the three basic categories of turbulent scales of motion are dissipative, inertial and anisotropic ranges. The dissipative and inertial ranges of turbulence can be modeled by a theoretical description. The turbulence theory is based on the description of such universal aspects. The anisotropic turbulence contains the largest scales of turbulent motion; it is not universal in nature, and the application of the turbulence theory to that range is much more complex.

Methodologies as RANS ignore the time-dependent nature of the flow and the turbulence theory is applied towards defining the eddy viscosity on all scales of turbulent motion, including anisotropic scales. The application of the turbulence theory necessarily leads to an empirical tuning of the turbulence model parameters for accounting for the effect of anisotropic scales, and the turbulent dissipation results in a time-steady behavior. However, PowerFLOW harnesses the fact it is a transient solver of high 3D resolution

and resolves the anisotropic turbulence scales (or very large eddies) directly. It uses the turbulence theory to model only the dissipative and inertial turbulence ranges. The dynamics of the sub-grid scale turbulence is represented by two additional equations derived from an extended Renormalization Group (RNG) theory. This approach is known as Very Large Eddy Simulations, or VLES. On the other hand, VLES is self-consistently coupled to the LBM for the resolved flow dynamics.

Turbulence models are employed within PowerFLOW as follows: a local effective relaxation time based on local and instantaneous flow field information is introduced in the Lattice Boltzmann collision operator to account for the unresolved universal scales of turbulent motion, similarly to the concept of eddy viscosity in a Navier-Stokes solver. This relaxation time is locally determined for each cell in the simulation domain for each timestep via the supplementary two equations. The LBM-VLES model is more applicable to situations encompassing turbulence, since large and small (sub-grid) scales are not well separable.

Equation 3.20 and 3.21 show the modified $\kappa-\epsilon$ RNG equations used by PowerFLOW (CHEN et al., 2003; KOTAPATI et al., 2009).

$$\rho\frac{D\kappa}{Dt} = \frac{\partial}{\partial x_j}[(\frac{\rho\nu_0}{\sigma_{\kappa_0}} + \frac{\rho\nu_T}{\sigma_{\kappa_T}})\frac{\partial\kappa}{\partial x_j}] + \tau_{ij}S_{ij} - \rho\epsilon \tag{3.20}$$

$$\rho\frac{D\epsilon}{Dt} = \frac{\partial}{\partial x_j}[(\frac{\rho\nu_0}{\sigma_{\epsilon_0}} + \frac{\rho\nu_T}{\sigma_{\epsilon_T}})\frac{\partial\epsilon}{\partial x_j}] + \Omega_{\epsilon 1}\frac{\epsilon}{\kappa}\tau_{ij}S_{ij} - [\Omega_{\epsilon 2} + C_\mu\frac{\overline{\eta}^3(1-\frac{\overline{\eta}}{\eta_0})}{1+\Psi\overline{\eta}^3}]\rho\frac{\epsilon^2}{\kappa} \tag{3.21}$$

Parameter $\nu_T = C_\mu\kappa^2/\epsilon$ is the eddy viscosity in the RNG, and all dimensionless coefficients are the same of the original model (KOTAPATI et al., 2009) ($C_\mu = 0.0845$, $\sigma_\kappa = 0.7194$, $\sigma_\epsilon = 0.7194$, $C_{\epsilon 1} = 1.42$, $C_{\epsilon 2} = 1.68$, $\eta_0 = 4.398$, $\Psi = 0.012$ (LI; JAMMALAMADAKA, 2015)), where σ is the inverse of the effective Prandtl number and S is a measure of the local velocity gradient. $\overline{\eta}$ is a combination of a local strain parameter $\eta = \kappa S/\epsilon$, local vorticity parameter $\eta_\omega = \kappa\Omega/\epsilon$ and local helicity parameters.

LBM is extended towards modeling the turbulent fluctuations through the replacement of its molecular relaxation time scale with an effective turbulent relaxation time scale, i.e., $\tau \longrightarrow \tau_{eff}$, where τ_{eff} can be derived from RNG. as shown in Equation 3.22 (EXA COMPANY, 2009).

$$\tau_{eff} = \tau + C_\mu\frac{\kappa^2/\epsilon}{T(1+\overline{\eta}^2)^{\frac{1}{2}}} \tag{3.22}$$

Furthermore, a hybrid wall function models the boundary layer on solid surfaces towards reducing the resolution requirements near the wall. The wall function used by

PowerFLOW, shown in Equation 3.23, is an extension of the standard log law of the wall, which includes the effect of favorable and adverse pressure gradient and accounts for surface roughness through a length parameter. u_t is the local tangential component of velocity, k_s is the surface roughness length and $\xi(\nabla p)$ is the function that accounts for pressure gradients.

$$\frac{u_t}{u_T} = f(y^+, k_s, \xi(\nabla p)) \tag{3.23a}$$

$$\kappa = \frac{u_T^2}{\sqrt{C_\mu}} \tag{3.23b}$$

$$\epsilon = \frac{u_T^4}{\nu \kappa y^+} \tag{3.23c}$$

3.1.3 Ffowcs-William analogy

Lighthill (1951) proposed a theory of aerodynamic noise to identify noise sources and established the aerodynamic noise as an acoustic analogy, in which turbulence provides a quadrupole distribution in an ideal atmosphere in rest. The author also described the general properties of the induced field and developed the dominant effect of steady low-speed solenoidal source convection. In 1963, Ffowcs Williams extended this theory to account for high-speed steady solenoidal convection (WILLIAMS; HAWKINGS, 1969).

The theory of aerodynamic sound is based on the equations of mass and momentum conservation of a compressible fluid, which are valid outside any closed internal surfaces that may be present and can be combined to provide an inhomogeneous equation that governs the generation and propagation of sound waves in that region (LIGHTHILL, 1952).

3.1.3.1 Lighthill's analogy

The theory developed by Lighthill for the control of the noise of jet-propelled aircraft has been extended for the calculation of the airframe noise through the noise generated by turbulence. The author defined the source of sound as the difference between the exact statements of natural laws and their acoustical approximations. The exact statement of mass is given by Equation 3.24 and the exact momentum density is given by Equation 3.25, where $p_{ij} = p'\delta_{ij} - \tau_{ij}$; δ_{ij} is Kronecker δ function ($\delta_{ij} = 1$ if $i = j$ and $\delta_{ij} = 0$ if $i \neq j$) and τ_{ij} is the viscous stress tensor.

$$\frac{\partial \rho}{\partial t} + \frac{\partial}{\partial x_i}(\rho v_i) = 0 \tag{3.24}$$

$$\frac{\partial}{\partial t}(\rho v_i) + \frac{\partial}{\partial x_j}(p_{ij} + \rho v_i v_j) = 0 \tag{3.25}$$

The subtraction of $\frac{\partial}{\partial x_i}$ (Equation 3.25) from $\frac{\partial}{\partial t}$ (Equation 3.24) yields equality 3.26.

$$\frac{\partial^2 \boldsymbol{\rho}}{\partial t^2} = \frac{\partial^2 \boldsymbol{\rho'}}{\partial t^2} = \frac{\partial^2}{\partial x_i \partial x_j}(\rho v_i v_j + p_{ij}) \tag{3.26}$$

The subtraction of Equation 3.26 from Equation 3.27 provides the Lighthill's equation (Equation 3.28), where $\mathbf{T_{ij}}$ is the Lighthill's stress tensor, given in Equation 3.29, where c is the velocity of sound and the bold letters represent a 3D vector.

$$c^2 \bigtriangledown^2 \rho' = c^2 \frac{\partial^2 \rho' \delta_{ij}}{\partial x_i \partial x_j} \tag{3.27}$$

$$\frac{\partial^2 \boldsymbol{\rho'}}{\partial^2 t} - c^2 \bigtriangledown^2 \boldsymbol{\rho'} = \frac{\partial^2 T_{ij}}{\partial x_i \partial x_j} \tag{3.28}$$

$$\mathbf{T_{ij}} = \rho v_i v_j + p_{ij} - c^2 \boldsymbol{\rho'} \delta_{ij} \tag{3.29}$$

Equation 3.28 is known as Lighthill's analogy and no approximation is made. Real material motion can be considered an acoustic field in which waves propagate at constant speed c. The source field for such waves is a quadrapole distribution. The strength of the quadrapole in volume is the Lighthill's stress tensor (T_{ij}). The quadrupole field can be assumed as the divergence of a dipole, or the double divergence of a monopole. The solution of Equation 3.28 is given in Equation 3.30, where $\mathbf{x}$ is the observer position (the microphone location in the case of PowerFLOW) and $\mathbf{y}$ is each point in volume V (quadrupole source). Every quadrupole element at $\mathbf{y}$ generates a field that travels at the sound speed to reach the observer, located in $\mathbf{x}$ with a $\frac{|\mathbf{x}-\mathbf{y}|}{c}$ delay.

$$\rho'(\mathbf{x}, t) = \frac{\partial^2}{\partial x_i \partial x_j} \int_V \frac{T_{ij}(\mathbf{y}, t - \frac{|\mathbf{x}-\mathbf{y}|}{c})}{a\pi c^2 |\mathbf{x} - \mathbf{y}|} \tag{3.30}$$

More information on Lighthill's analogy can be found in Dowling and Williams (1983) and Lighthill (1952)

3.1.3.2 Ffowcs-William Hawking formulation

The equations in this subsection were taken from Williams and Hawkings (1969).

As addressed in the previous section, aerodynamic noise is equivalent to a quadrupole source of strength density T_{ij}. In the Ffocws William-Hawking (FW-H) analogy, the source is assumed coherent within spatial and temporal scales corresponding to the correlation length and lifetime of a turbulent eddy (typically l/bcM). No surface is present and the

convection velocity is uniform throughout the source. Equation 3.31 shows the density fluctuations in the sound field.

$$4\pi c^2(\rho-\rho_0)=\int[(\frac{\zeta}{((1-M_r)^2+\zeta^2)^{\frac{1}{2}}}\frac{\partial}{\partial\vec{n}})+\frac{\partial}{c\partial r}(\frac{1-M_r}{(1-M_r)^2+\zeta^2})]^2T_{rr}\frac{d\sum}{r((1-M_r)^2+\zeta^2)^{\frac{1}{2}}} \tag{3.31}$$

The magnitude of density fluctuations depends on the measurement of area $d\sum$, which is the surface area of source volume V and varies in function of the orientation and shape of the source, which vary with the convection velocity. However, $d\sum$ is always of magnitude l^3, regardless of the orientation or shape of the source.

In Equation 3.31, M_r is the Mach number at which the source approaches the field point, $\vec{n}$ is a unit vector normal to the surface, T_{rr} is $T_{ij}\vec{r}_i\vec{r}_j$ and $\tilde{\mathbf{r}}$ is the unit radiation vector. ζ is an arbitrary constant for the adequation of the time scale and the spatial scale of the intersection area ($d\sum$) and is given by Equation 3.32.

$$\zeta=(\frac{l}{2c}|\frac{\partial\mathbf{M}}{\partial\tau}\cdot\hat{\mathbf{r}}-\frac{c(M^2-1)}{r}|)^{1/2} \tag{3.32}$$

If the source is in steady rectilinear motion (PowerFLOW simulations), the only relevant value of ζ in the far field is the one based on eddy lifetime. For this model, the density fluctuations are given by Equation 3.33

$$4\pi c^2(\rho-\rho_0)\simeq\int\frac{\zeta^2}{((1-M_r)^2+\zeta^2)^{\frac{2}{3}}}\frac{\partial^2T_{rr}}{\partial N^2}\frac{d\sum}{r} \tag{3.33}$$

The measurements of $d\sum$ and normal derivative $\frac{\partial}{\partial N}$ are proportional to l^3 and l^{-1}, respectively. Turbulence stress tensor T_{ij} can be approximated by its first term $\rho u_i u_j$, which is proportional to ρc^2M^2. Therefore, the mean square density fluctuation (which is proportional to the sound intensity) for this case is given by Equation 3.34, where z is a small numerical constant.

$$\overline{(\rho-\rho_0)^2}\sim\overline{\rho^2}\frac{l^2}{r^2}\frac{z^2M^8}{((1-M_r)^2+z^2M^2)^3} \tag{3.34}$$

According to the equation, at low speeds, the sound intensity varies following the eighth power of the convection speed coupled with a directional factor $|1-M_r|^{-6}$. At high speeds, near Mach wave condition ($1-M_r=0$), the eighth power law is replaced by a second power variation at a much higher overall level, since z is small.

Apart from the Ffowcs-Williams Hawking analogy, PowerFLOW uses formulation 1A, presented in (FARASSAT, 2007), which is a solution of the FW-H equation with

surface sources only when the surface moves at subsonic speed. The formulation uses analytically the observer time derivative.

3.2 Computational set-up

3.2.1 Model

The model used for numerical studies was a 2D three-element wing, comprised of a slat, the wing main element, and a flap. In all simulations, the flap and slat were fully extended with 30^o flap and slat deflections. The angle of attack (AoA) was 0^o for all slat modifications. Simulations at other angles of attack were performed for the baseline configuration for comparisons with experimental results. The wing was simulated as an infinite wing for avoiding 3D effects in the model tips.

The model has 500 mm stowed chord and 1300 mm span in both experiments and simulations of the baseline configuration; the span was reduced for the modifications in the slat.

3.2.2 Computational domain

The computational domain, shown in Figure 15, was 6.5 $m \times 1.65$ $m \times 1.3$ m (where X and Z are in the streamwise and spanwise directions, respectively) for replicating wind-tunnel working section dimensions (3 $m \times 1.65$ $m \times 1.3$ m) and avoiding future corrections for the effective AoA. It measures upstream and downstream the model 3 and 10 times the model stowed chord, respectively, for enabling a complete development of the flow.

Figure 15: Computational domain dimensions [m]

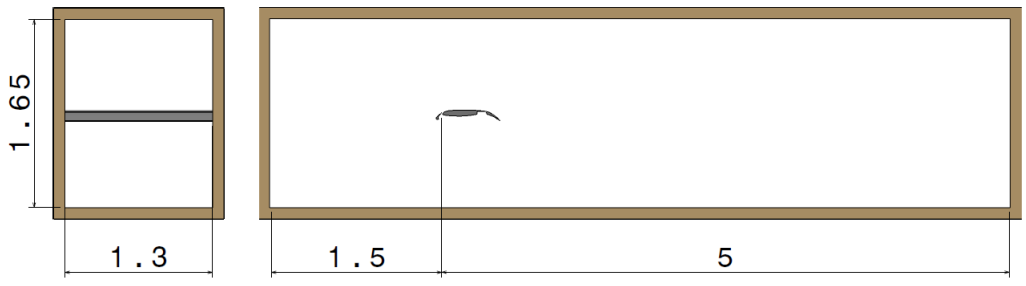

Reference: Author

In simulations of slat modifications, the computational domain in the Z-direction was reduced to 0.25 m for reducing computational costs; however, the 2.5D condition was maintained. The Baseline configuration was also simulated in this computational domain for comparisons with the slat modifications.

3.2.3 Boundary conditions

The velocity inlet was set at 34 m/s and the outlet was imposed with no pressure gradient in all configurations. The turbulence intensity was set at 0.21%, which is the wind tunnel turbulence level at the working section at 34 m/s, according to Santana et al. (2014), and 1×10^{-3} m turbulence length scale.

The atmospheric conditions were $P = 91455$ Pa, $\rho = 1.052$ kg/m^3, $\nu = 1.497 \times 10^{-5}$ m^2/s and $T = 303$ K, which correspond to 1.135×10^6 Reynolds number based on the stowed chord and 0.098 Mach number.

The walls of the computational domain (wind-tunnel walls) were solid (see Figure 15) and modeled as frictionless walls. Simulations under other wall conditions were conducted, however, no changes were observed in the results. The wing walls were set as standard walls with no forced boundary layer transition (the option automatic in powerFLOW). Studies were carried out in modified boundary-layer regimes (model and wind tunnel walls) and no significant changes were detected in the aerodynamics and aeroacoustics reuslts. On the other hand, the boundary layer of the slat was imposed as laminar and turbulent in different parts according to the trip set in the experimental model, however, the pressure gradient in the slat is highly favorable and complete the transition is difficult.

The outermost fluid region was modeled as high viscosity fluid or anechoic layer for the absorption of acoustic waves. Such a condition is necessary for simulations even if the wind tunnel has no anechoic region, since, otherwise, simulations would take long and their completion would not be viable. This region is inside the computational domine.

3.2.4 Refinement studies

Simulations were conducted with ten refinement regions (VR0 to VR9), where the coarsest and finest elements were in the VR0 and VR9 regions, respectively. VR0 to VR5 regions are different boxes within the computational domain and whose sizes decrease, as the VR increases. VR 6, 7 and 8 are offsets of the three elements (slat, wing main element, and flap) and VR9 is located inside the FW-H measurement region. Two types of VR9 region were used, i.e., a box that involved the slat and the suction region of the wing main element, and an offset in the same region. Figure 16 shows the refinement regions in a generic high-lift wing and the two types of VR9 tested. In the figure, the name of each region is located outside them.

Four minimum element sizes (δx_{min} = 0.18, 0.20, 0.25 and 0.28 mm) were used in each mesh configuration. According to Terracol, Manoha and Lemoine (2015), a good indicator of the adequacy of the grid for properly resolving the main shear layer dynamics is based on the local ratio between the characteristic lengths of the shear layer and the local grid resolution in each flow direction.

Figure 16: Refinement regions and different mesh configurations

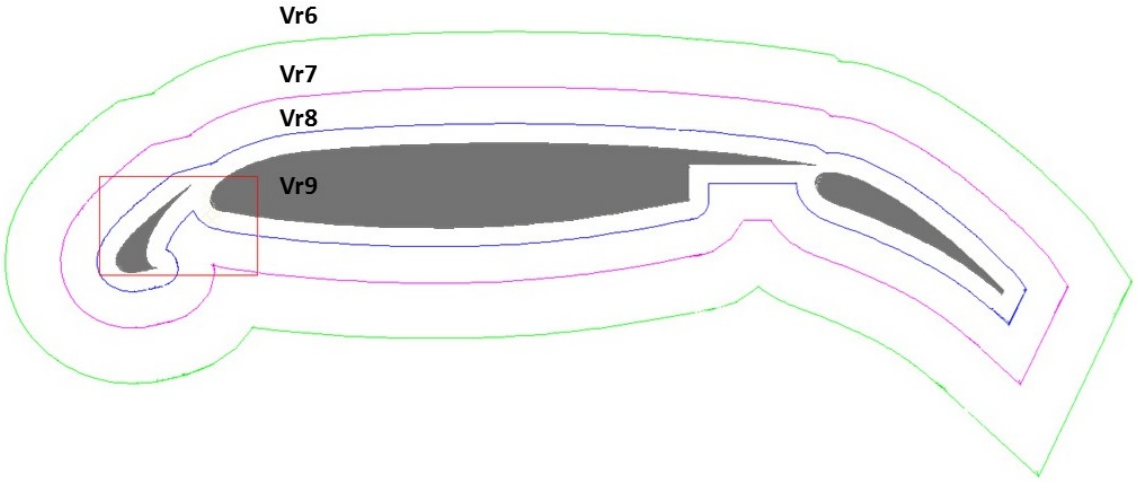

(a) Type 1 of VR 9

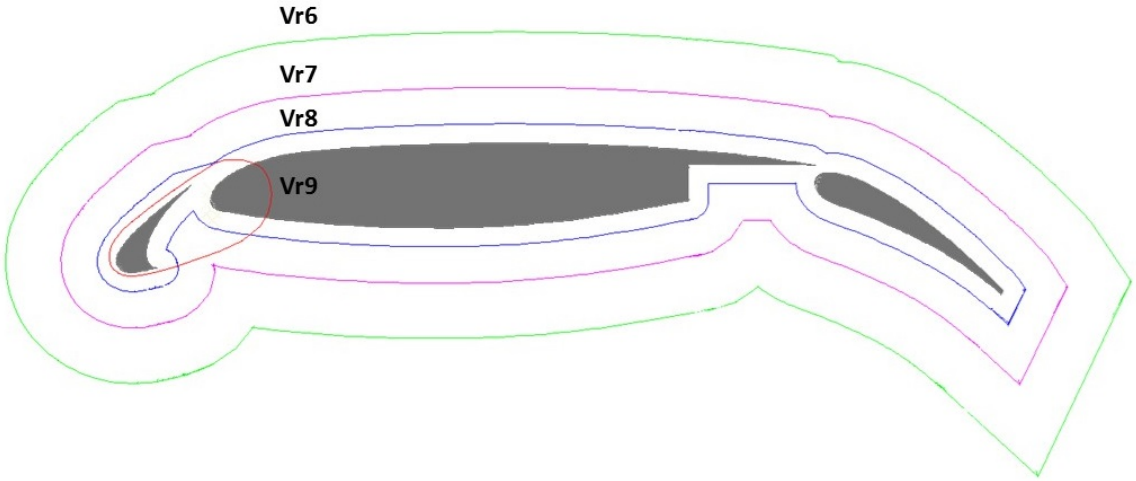

(b) Type 2 of VR 9

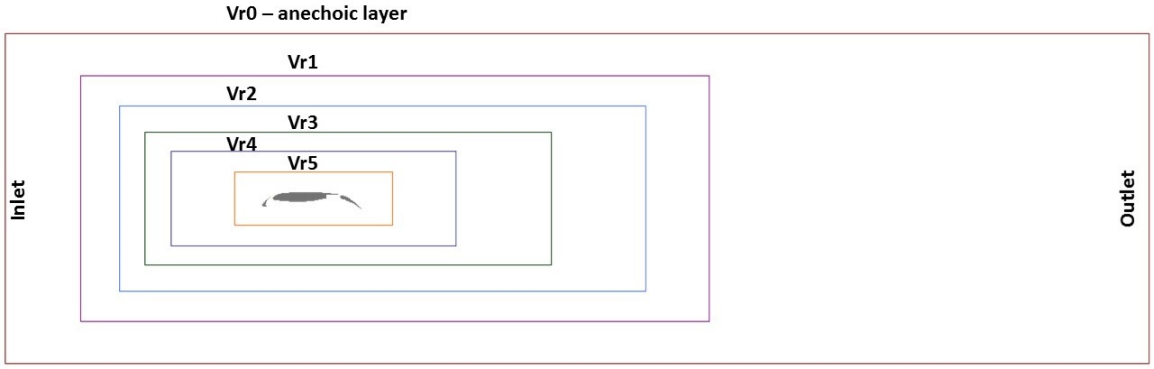

(c) VR 5 to 0 for all mesh configurations

Reference: Author

In a mixing layer between two parallel flows of velocities U_1 and U_2 (the main shear layer of the slat can be considered a mixing layer), the most-unstable wavelengths in the stream-wise (X-axis), span-wise (Z-axis) and shear (Y-axis) directions are $\lambda_x = 7\delta_w$,

$\lambda_z = \frac{14}{3}\delta_w$, and $\lambda_y = \delta_w$, where δ_w is the local vorticity thickness calculated by Equation 3.35 and $\vec{n}$ is the shear-normal direction.

$$\delta_w = \frac{|U_1 - U_2|}{max(\frac{dU}{d\vec{n}})} \tag{3.35}$$

Terracol, Manoha and Lemoine (2015) also demonstrated the vorticity thickness increases along the shear layer, therefore, it was calculated for the 0.18 mm minimum element size case, at the beginning of the shear layer (the most critical case), i. e., $\frac{s}{SL} = 0.1$, for the determination of the grid resolution.

Initially, the shear-normal angle was calculated with the velocity components in the shear layer and was equal to 58.44^o for the baseline configuration. Once the mesh is a square-grid, the angle was approximated to 56.03^o and the velocity components were acquired and derived in that direction. Figure 17 shows the velocity profile around the shear layer and its normal-shear derivative. The values of U_1, U_2 and $max(\frac{dU}{d\vec{n}})$ shown in the graph lead to a 7.4×10^{-4} m vorticity thickness, which corresponds to a $\frac{\lambda_x}{\delta x_{min}} = 29, 26, 21$ *and* 18, for the minimum element sizes tested.

Figure 17: Tangential velocity profile and associated normal shear derivative at $\frac{s}{SL} = 0.1$

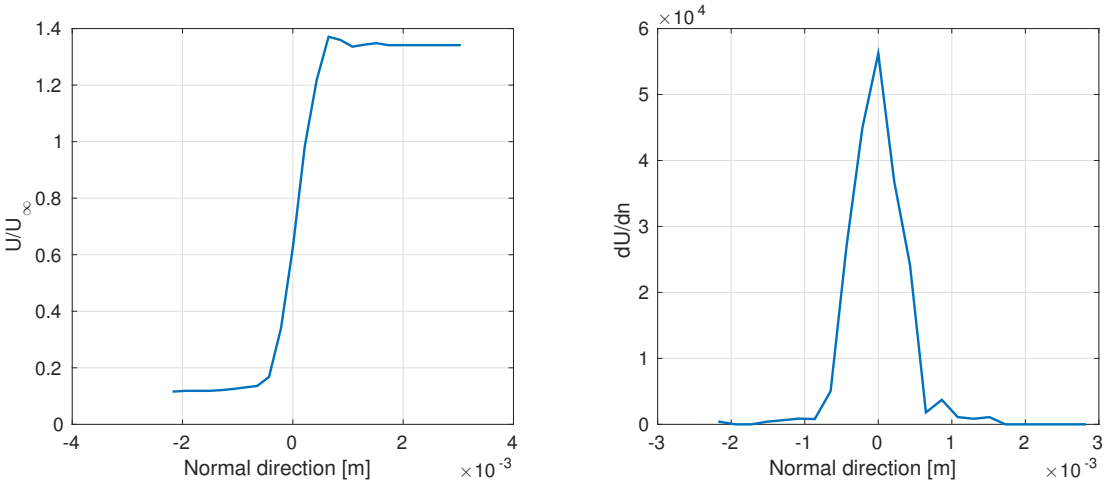

Reference: Author

Figure 18 shows the Power Spectral Density (PSD) obtained for both cases of mesh configuration and different minimum element sizes. For all cases, pressure fluctuations are propagated to the central microphone of the antenna array of the wind tunnel for future comparisons. All meshes captured the same mid-frequency peaks and were in agreement regarding frequency and magnitude. Some differences were detected in the slope of the broadband noise meshes with $\frac{\lambda_x}{\delta x_{min}} = 29$ for St above 40 (high frequency). Table 1 shows the OSPL for each mesh configuration integrated between St 1.6 and 100. The major difference was 2 dB between the mesh types and $\frac{\lambda_x}{\delta x_{min}} = 29$ and 18.

Figure 18: PSD for different minimum element size

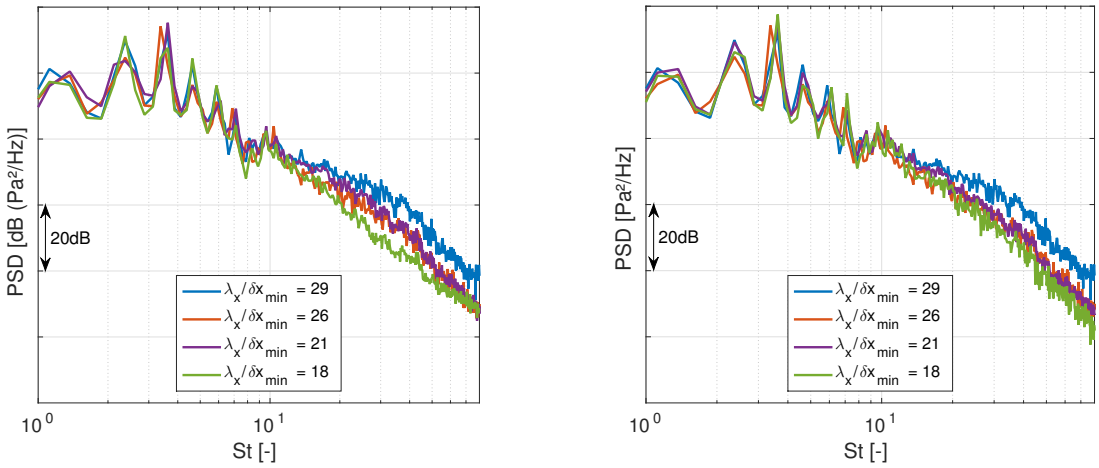

(a) First type of mesh (box) (b) Second type of mesh (offset)

Reference: Author

Table 1: OSPL for acoustics fluctuations between St 1.6 and 100 with different meshes

$\frac{\lambda_x}{\delta x_{min}}$	OSPL [dB]	
	Type 1 (box)	Type 2 (offset)
29	0	1.1
26	-0.3	0.4
21	-0.3	1.4
18	-0.8	1.0

Reference: Author

Figure 19 displays the pressure coefficient distribution for the different minimum element sizes simulated. The pressure distribution in the slat and main wing element is not sensitive to the element size. Some differences were found in the predicted separation in the flap, however, they are not significant for the flow in the slat region. No variation was found in the lift and drag coefficients for different minimum element sizes.

Slat modifications were simulated with the first type of VR9 region, which exhibited a smaller variation in the OSPL when the minimum element size was changed. The minimum element size used was 0.25 mm equivalent to $\frac{\lambda_x}{\delta x_{min}} = 21$, $\frac{\lambda_y}{\delta y_{min}} = 3$, $\frac{\lambda_z}{\delta z_{min}} = 14$ and a resolution of 2000, which is sufficient for the capture of the main shear layer dynamics. Approximately 3.2×10^8 elements were created for the full-span baseline configuration and simulations were completed in 30240 CPU hours for 851000 timesteps (0.34 s in real time). Simulations of slat modifications (reduced span) have 8.5×10^7 voxels and took 9035 CPU hours for 851000 timesteps.

Figure 19: Pressure coefficient distribution for different minimum element size

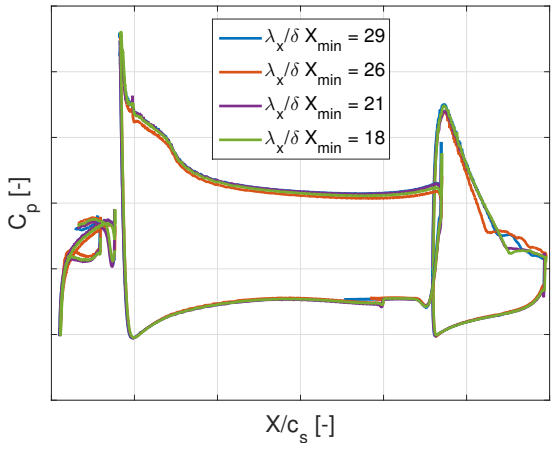

Reference: Author

3.2.5 Far-field measurements

The calculation of the far-field was based on the FW-H acoustic analogy (WILLIAMS; HAWKINGS, 1969), included in PowerACOUSTICS 3.1b post-processing tool. The analogy uses the pressure fluctuation in the near-field to calculate noise in the far-field. The noise is propagated to the microphones and the spectrum in each of them is calculated by a Fast Fourier Transformation (FFT). The values of the calculated spectra are converted to dB using $2 \times 10^{-5}\ Pa$ as reference value.

The original time signal is divided into one or several parts for the calculation of the FFT. The window width specifies the number of such divisions and is calculated by PowerACOUSTICS as a product of powers of two, three, and five, and less than the number of available frames.

There are several window types that segment the original time signal for the FFT calculation. The smoothing from the FFT windowing is highly enhanced by the application of a window function that tapers the original time signal within the FFT window according to a function that is zero at both endpoints and one at the center point. The algorithm subtracts the mean value for the time segmentation prior to the application of the window function. The window function not only promotes smoothing, but also reduces numerical artifacts, called Gibbs (or leakage) error in the spectrum, by forcing the function to be zero on the segment ends. Leakage is a common problem with FFT calculations and affects the spectrum adversely when one or more FFT windows on the time series shows a large jump in the value between its starting and ending points. As a consequence, a discontinuity is created in the periodic representation of the signal and contaminates the spectrum with large amplitude values at high frequencies. After the application of the

window function to a time segment, the signal starts and ends with zero, which eliminates the discontinuity. PowerACOUSTICS enables the user to choose the window type among none, Welch, Hanning, Bartlett and end taper 5%. A Hanning window type was used for all simulations in this study, since it smoothes the signal using a limited length-time signal to better predict the power spectrum to be obtained over much larger time. Equation 3.36 shows the Hanning window equation, where x_h ranged from 0 to 1 and $f_h(x_h) = 0$ when $x = 0$ *or* 1 and $f_h(x_h) = 1$ when $x_h = 0.5$.

$$f_h(x_h) = \frac{1}{2}(1 - cos(2\pi x_h)) \tag{3.36}$$

A 100 Hz constant-width band was used for the calculation and the minimum and maximum frequencies were 400 and 40000 Hz, respectively.

Power spectrum values were normalized by the frequency (f) by Equation 3.37, where n is the number of Fast Fourier Transformation (FFT) bands that contribute to the target band for a standardization of the comparison of spectra at different bandwidths.

$$PSD = \sum_{i=0}^{n_b} \frac{P_i}{\Delta f \times n_b} \tag{3.37}$$

The solid surface pressure measurements were taken from a $3.5c_s \times 4.7c_s \times Z$ (Figure 20) crop in the middle of the span. Measurements are taken only in the surface of the model, the crop is used for determine the region of the model in wich the measurements are taken and any shape could be used. A study of convergence was conducted for the establishment of the appropriate dimension in the span-wise direction of the FW-H measurement region. $0.95c_s$, $2.35c_s$ $3.5c_s$ and $4.7c_s$ distances were simulated and the results are shown in Figure 21. The PSD values were standardized adding Equation 3.38 for each FW-H length case. A significant variation in the mid-frequency peaks and broadband noise intensity was observed between FW-H lengths of $0.95c_s$ and $2.35c_s$, and no variations were detected between $2.35c_s$, $3.5cs$ and $4.7cs$, which indicates a convergence of the FW-H length.

$$10log(\frac{b}{FWH_{length}}) \tag{3.38}$$

A study of the pressure fluctuations coherence on the trailing edge for $AoA = 0^o$ determined the length in which a correspondence is associated with the noise. The coherence was calculated for each point (i) by Equation 3.39, where $G(1, i)$ is the cross-spectral power density for non-dimensional frequency (St) between signals at points 1 and i, separated by a distance of Δz. The points used were spaced $\Delta z = 0.06c_s$ from each other until $z = 7c_s$ and $\Delta z = 0.01c_s$ until $z = 1c_s$. Figure 22 shows the coherence for the Strouhal numbers of the peaks observed in the slat spectra and for a Strouhal number of broadband noise

Figure 20: FWH measurement region

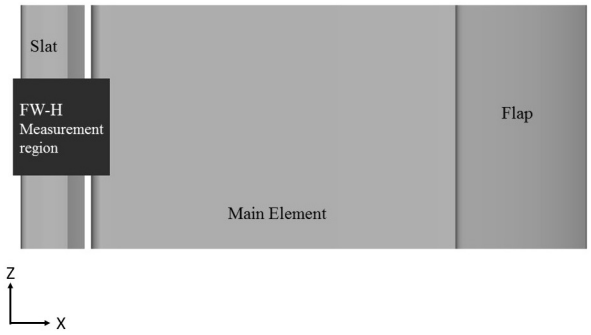

Figure 21: Influence of the span-direction dimension of the FW-H measurement region ($\delta x_{min} = 0.25\ mm$)

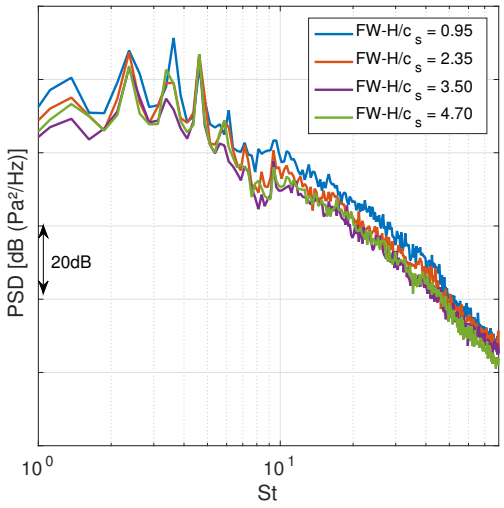

Reference: Author

($St = 97.5$); in this case, the coherence was calculated from each point i respect the first point. An average of the coherence at each distance for same Strohual numbers is also provided, i.e., the coherence between all points located at each distance was calculated. The frequency of the third peak ($St = 4.7$) shows a higher coherence than that of the first peak ($St = 2.4$) in a shorter distance. However, for longer distances, the coherence at the third peak rapidly decays, which suggest different loops generate peaks at different frequencies and have different coherence lengths.

Regarding coherence for the largest distance, the first peak exhibited a cyclic behavior, also related to the loop created between the cusp and the trailing edge responsible for the tonal noise. The first peak ($St = 2.4$), which is the maximum value in the far-field spectrum, shows the highest coherence for longer distances. It is minimum at $z = 3.5c_s$ and the mean at a $z = 2.35c_s$, which indicates a distance between 2.35 and 3.5 times the slat chord is sufficient for the analyses of the noise generation phenomena, without the negative effect of periodicity.

The low capacity of a $0.95c_s$ FW-H length to predict the noise is probably due to the coherence length related to the noise reaches values greater than the FW-H domain, as shown in Figure 22 (a), where the coherence is high and constant along the distance for the first and third peaks, including $z = c_s$. The broadband noise does not correlate between the points for any Δz, as expected. A $FWHlength = 2.35c_s$ was used for all

simulations, since such a distance can capture the noise generation phenomena.

$$\gamma^2 = \frac{(G(1,i))^2}{G(1,1) \times G(i,i)} \tag{3.39}$$

Figure 22: Span-wise coherence (left) and mean coherence (right) in the slat trailing edge of the baseline configuration

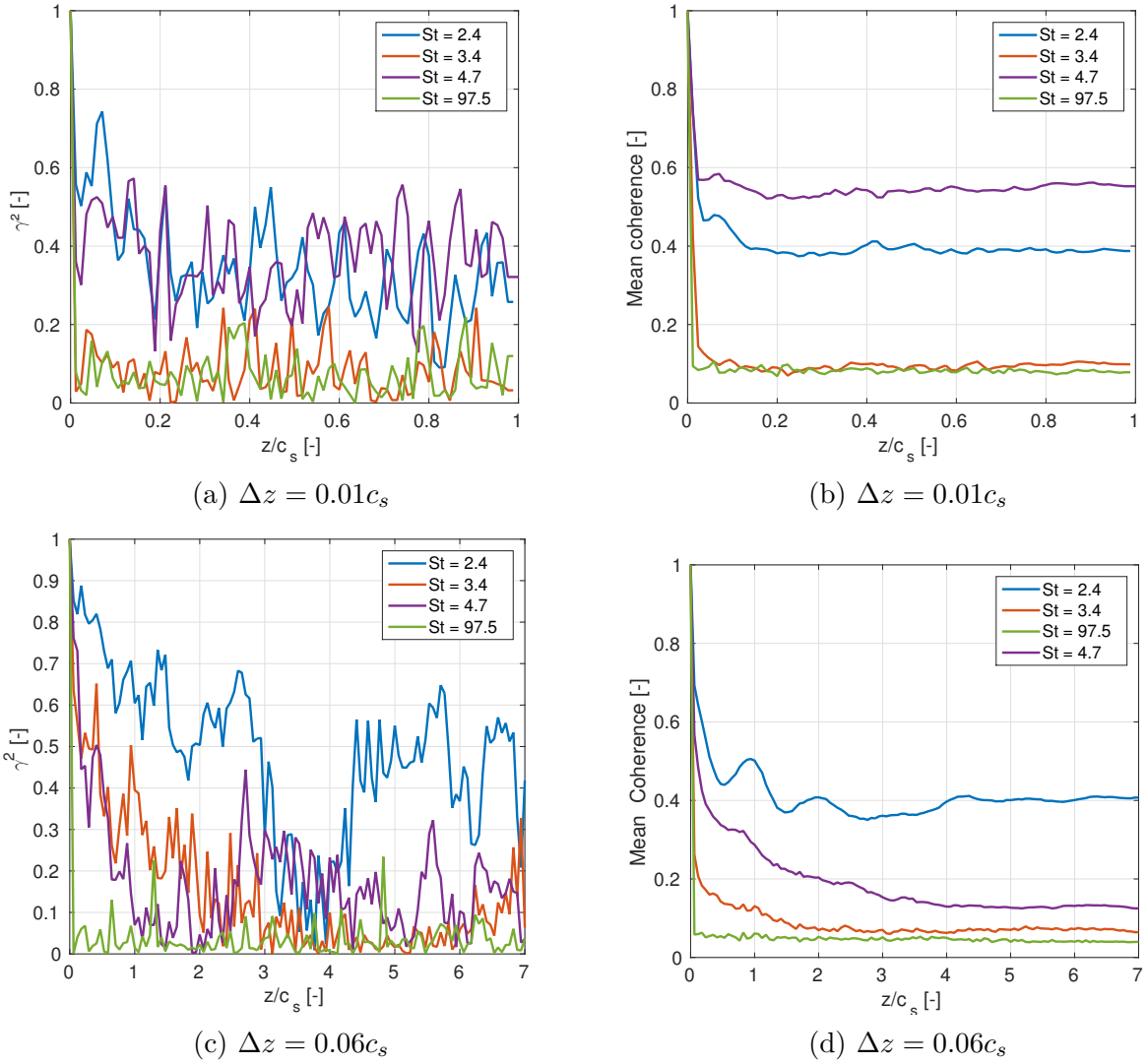

(a) $\Delta z = 0.01c_s$

(b) $\Delta z = 0.01c_s$

(c) $\Delta z = 0.06c_s$

(d) $\Delta z = 0.06c_s$

Reference: Author

For comparisons with experimental results, surface pressure fluctuations were propagated to 61 microphones in a spiral array located on the simulation wall at approximately 835 mm from the pressure side of the model, which is equivalent to the wind tunnel array. The pressure fluctuations were propagated to 72 microphones equal spaced in a 30 m radius circle array located in the Z-plane at mid-span of the model for the analysis of slat directivity. Figure 23 shows the microphones arrays and their plane regarding the model. Differently from the directivity array figure, the figure of the wind tunnel array (a) is on scale with a 1300 mm model span.

Figure 23: Microphones arrays and their plane regarding the model

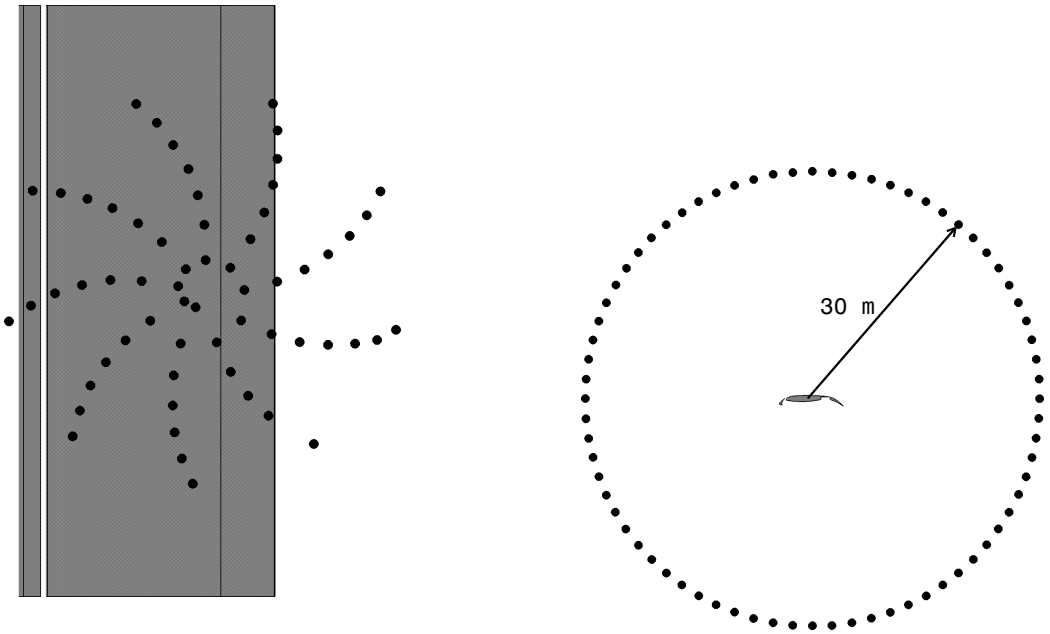

(a) Wind tunnel array (d) Directivity array

Reference: Author

The FW-H measurements started at 0.147057 s, calculated by Equation 3.40, where the characteristic length is the stowed chord and the characteristic velocity is the inlet velocity. The FW-H sampling period was calculated by Equation 3.41, where the maximum frequency is 40 kHz. The calculated sampling frequency was 81.68 kHz (30 timesteps).

$$FWH_{start} = 10\frac{Char.length}{Char.velocity} \tag{3.40}$$

$$FWH_{period} = \frac{1}{2 \times f_{max}} \tag{3.41}$$

3.2.6 Near-field measurements

Fluid measurements were taken after the convergence of lift and drag coefficients for avoiding the initial transient effects (Figure 24). Therefore, the time-average measurements of the fluid were taken from 0.277 s until the end of the simulation at 71 Hz sampling frequency in each 3D cell. Instantaneous measurements started at 0.277 s at 10 kHz sampling frequency in each 3D cell.

Instantaneous values were taken from a crop in the slat region for the baseline configuration at a higher sampling frequency (88 kHz) for the analysis of the main shear layer spectra.

Figure 24: Aerodynamic coefficients convergence

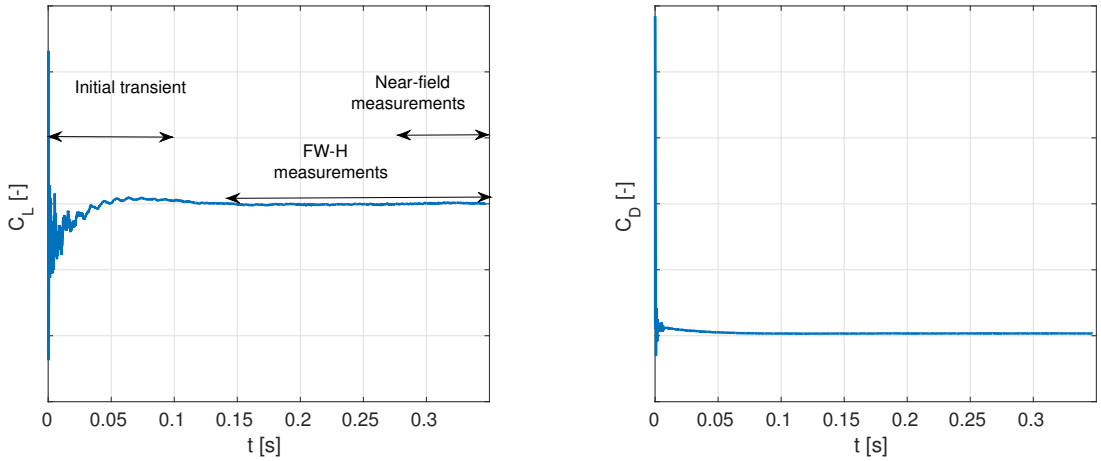

(a) Lift coefficient (b) Drag coefficient

Reference: Author

3.3 Experimental set-up

This subsection describes the facilities and model used for the experiments, as well as the methodology employed for aerodynamic and aeroacoustic tests.

3.3.1 Wind tunnel facility

LAE-1 wind tunnel (CATALANO, 2004), located at the Laboratory of Aerodynamics (LAE) of São Carlos School of Engineering, University of São Paulo (EESC-USP), was used for the tests. It is a closed-circuit wind tunnel of 1.3 $m \times 1.67\ m \times 3\ m$ height, width, and length working section, respectively. It has an 8-blade fan driven by a 110 HP electrical motor, with seven straighteners located downstream the fan and two 54% porosity screens located before the contraction cone for turbulence reduction. Such conditions enable the wind tunnel to reach velocities of up to 45 m/s with a 0.21% turbulence level at the working section (SANTANA et al., 2014). Figure 25 shows its top and isometric views.

Initially, the wind tunnel was designed for aerodynamic tests, however, it has been recently adapted for aeroacoustic measurements through two acoustic treatments applied on the walls and fan. The first process consisted in the application of melamine foam on walls A and B (Figure 26), which promoted a 1.5% velocity reduction at 31 m/s. In the second treatment, a baffle (element D in Figure 26) was installed along wall A and polyurethane foam was applied in regions where the gap between the fan blade and the wall was longer than 3 mm (Region C in Figure 26). Figure 27 shows the region of larger gap with and without the trip treatment.

Figure 28 displays the wind tunnel background noise spectra of the baseline configuration and after each treatment at 37 m/s velocity. The first treatment reduced

Figure 25: LAE-1 Wind tunnel

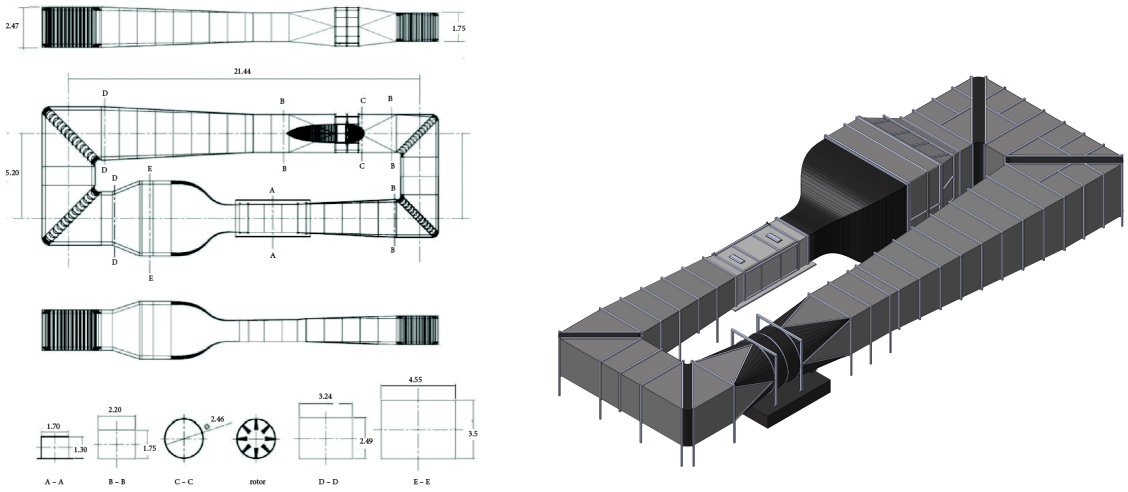

Reference: Santana et al. (2014)

the background noise at low frequencies and the second reduced it at high frequencies.

Figure 26: Regions of acoustic treatments

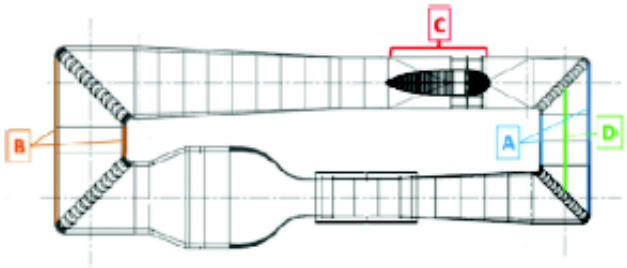

Reference: Santana et al. (2014)

Figure 27: Tip treatment

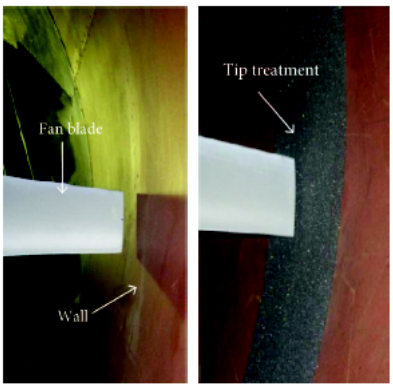

Reference: Santana et al. (2014)

Figure 29 shows the overall sound pressure level (OSPL) as a function of flow speed. The first treatment reduced approximately 4 dB in all velocity range, however, the second reduced the noise only at velocities below 20 m/s. The acoustic treatments reduced the turbulence level from 0.25% to 0.21% in all velocity range. Refer to Santana et al. (2014) for more information on such acoustic treatments.

3.3.2 Atmospheric conditions and free-stream flow

Atmospheric conditions were measured at the beginning of each test for the establishment of non-dimensional parameters to be compared. The atmospheric pressure was measured by a 1 $mmHg$ precision calibrated mercury barometer and the temperature

Figure 28: Background noise spectra. $U_\infty = 37m/s$

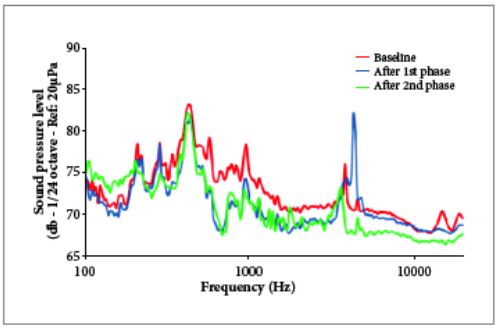

Reference: Santana et al. (2014)

Figure 29: Overall sound pressure level reduction

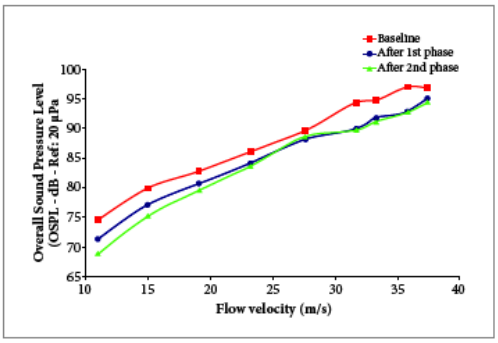

Reference: Santana et al. (2014)

was measured inside the wind tunnel by a 0.1^oC precision thermocouple. Relative humidity was measured in percentage by a 0.1% precision hygrometer that corrects the calculation of air density. The ideal gas law for dry air and water vapor was used for the calculation of the humid air density ($\rho_{humidair}$). This procedure involved saturation pressure, relative humidity, atmospheric pressure, temperature, molar masses and the universal gas constant.

The Mach number was computed from Equation 3.42, where U_∞ is the free-stream velocity and λ is the relation between specific heats at constant pressure and constant volume, equal to 1.4 for air under normal pressure and temperature conditions. R_d is the specific constant for dry air and T is the atmospheric temperature in K.

$$M = \frac{U_\infty}{\sqrt{\lambda \times R_d\, T}} \tag{3.42}$$

The air viscosity was calculated according to Sutherland viscosity law, shown in Equation 3.43, where T is the atmospheric temperature in K, and C_1 and C_2 are specific constants for each gas. For the air, C_1 is 1.458×10^{-6} $[\frac{Kg}{m-s-K^{1/2}}]$ and C_2 is 110.4 $[K]$.

$$\mu = \frac{C_1 \times T^{3/2}}{C_2 + T} \tag{3.43}$$

The free-stream velocity was computed from the dynamic pressure (q) by Equation 3.44 and the dynamic pressure was measured by a pitot-static probe located at the working section wall. The probe measures both total and static pressures and is connected to a micro-manometer (DP-CALC 8702), whose digital output is the difference between the pressures (dynamic pressure). The instrument has 0.1 Pa precision and is connected to the computer to acquire the data automatically at each angle of attack.

$$U_\infty = \sqrt{\frac{2q}{\rho_{humidair}}} \tag{3.44}$$

3.3.3 Experimental model

A 2D wing section with a conventional transport aircraft airfoil (Figure 30) manufactured in aluminum alloy was used for the experiments. The wing section was composed of three elements, namely slat, wing main element and flap and exhibits the following three possible configurations: fully-stowed, fully-extended and flap side edge; for all tests of the current study the used configuration was fully-extended, in order to slat noise does not be contaminated with flap side edge noise. Slat and flaps are attached to the wing main element (WME) by four steel brackets equally spaced along the span, starting at the model's ends. It has 500 mm stowed chord and 1300 mm span (wind tunnel height) and is mounted vertically on the wind tunnel working section by a turn-table that enables variations in the angle of attack at a 0.1^o precision.

The model has a zig-zag trip in the slat at 35% of slat chord and in the flap at 15% of flap chord. For this campaign, the brackets were covered by foam, in order to avoid the interference of the brackets noise in the slat noise.

The wind tunnel has a suction system at the model's borders for improving the two-dimensional flow and measurements uniformity. It is installed in the wind-tunnel turn tables and communicates with the wind tunnel test section through a 22% perforated plate, which is sealed and only specific parts of the model chord are opened. For the experiments, the suction was applied at: Slat leading edge (10 mm length and 70 mm wide), wing main element suction side (10 mm height and from $0.33c_m$ to $0.9c_m$) and flap suction side (10 mm height and from $0.33c_f$ to $0.9c_f$). The suction system is driven by a 9.2 kW electrical motor and a 8 blade fan and for all experiments, the suction system was set at 50% of total potency.

3.3.4 Aerodynamic measurements

Aerodynamic measurements were taken by 101 pressure taps located on the model surface and distributed as follows: 57 taps along the WME chord, 28 taps along the flap chord and 16 along the WME span. The span-wise distributed taps checked the flow uniformity and analyzed wind tunnel wall effects.

The taps are connected to a ZOC33/64PxX2 SCANIVALE®, which has 128 channels that measure the static pressure at a 45 kHz frequency. The accuracy of such facility after calibration is ± 0.15% full scale (FS)(SCANIVALVE CORPORATION, 2003).

The ScaniValve ZOC33/64PxX2 pressure sensors are arranged in 8 blocks of 8 sensors. Each block has its own calibration valve and four modes to operate: operate, calibrate, purge and isolate. Then, the calibration is completed through selecting the option calibrate, in which the valve connects all the pressure sensors to the calibration input.

3.3.5 Aeroacoustic measurements

G.R.A.S 46BD (G.R.A.S, 2018) microphones were used for acoustics measurements. They included a 26 CB preamplifier and their frequency ranged from 4 Hz to 70 KHz ($\pm$2 dB), with a 1.5 mV/Pa sensitivity. Their dynamic lowest and highest limits are 44 $dB(A)$ and 166 dB, respectively. The acquisition data are performed through a PXI-1042Q chassis connected to microphones.

Microphones are flush-mounted on the side-wall wind tunnel in a spiral array of 61 points, shown in Figure 31 at 835 mm from the center of the model. The spiral array, of 850 mm diameter, was optimized according to Fonseca et al. (2010) for achieving a high-frequency range with minimum beam-width and side-lobe contamination. Figure 32 shows a G.R.A.S 46 BD microphone and its dimensions.

Figure 30: Model mounted in the wind tunnel

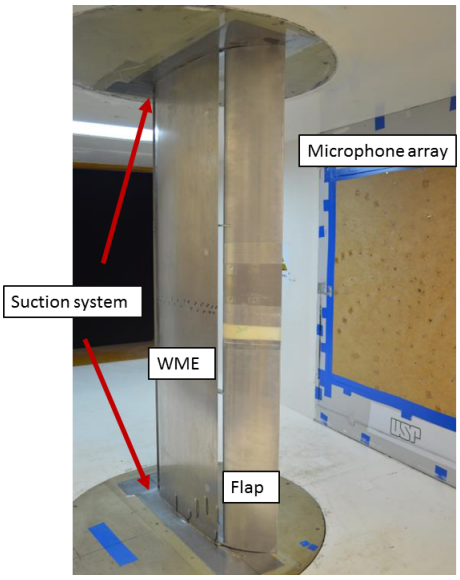

Reference: Author

Figure 31: Microphones array

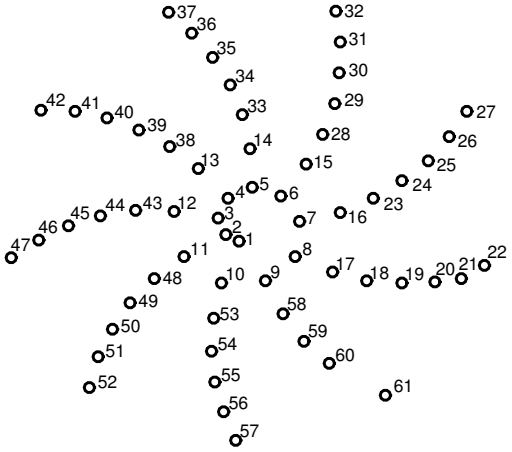

Reference: Author

The calibration of microphones prior to each test is important because the noise perceived by them and the delay between the signals will be fundamental in the beamforming calculation. The calibration was performed for each isolated microphone and used an NC-74 sound calibrator (RION CORPORATION, 2003) with 94 $dB \pm 0.3\ dB$ sound pressure level, 1 $kHz \pm 2\%$ frequency and 1.0 Pa reference pressure fluctuation for the microphone adapter. The NC-74 is a compact and lightweight unit that incorporates a sensor that detects atmospheric pressure and requires no atmospheric pressure compensation. Based on the information provided by the sensor, a CPU controls the signal amplitude. The unit always provided the correct output for achieving constant sound pressure level, regardless of fluctuations in atmospheric pressure (RION CORPORATION, 2003). Microphone data was acquired during the calibration and a digital band-pass filter creates data used for

Figure 32: Schematic view and dimensions (in mm) of a microphone

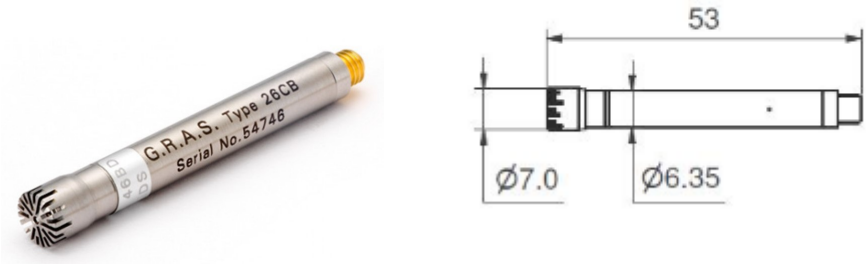

Reference: G.R.A.S (2018)

the calculation of microphones sensitivity that ranges from 1.45 to 2.60 mV/Pa for all microphones of the array.

3.3.6 Post-processing analysis

The main purpose of wind tunnel tests is the identification and quantification of noise sources. The microphones used record the pressure fluctuation over time for further calculating power spectra. Once microphones cannot reject interfering sources and quantify noise, a technique, called beam-forming, is used for post-processing the acquired data. The method, developed by Boeing Company in 1994, creates a full array cross-spectral matrix for each frequency of interest using the microphones data. A grid of a potential source location is then defined and a complex array steering vector is computed for each grid point, which takes into account the non-uniform flow, microphone imperfections and installation effects. Beam-forming combines the cross-spectral matrices and steering vector to produce maps of the model acoustic distribution, and successively focuses the phased array for each point on a grid and measures the apparent source strength distribution. Such a calculation depends on a mathematical model for the acoustic propagation from each grid point to each microphone. The mathematical model is based on the high-frequency wave propagation theory.

According to the beam-forming method, an imaging system that spatially separates the true source from the image reflected from the remote sides of the wind tunnel walls must be applied. The wall boundary layer adjacent to the microphones creates a signal typically 10-20 dB higher than the acoustic radiation from the model. However, this interference can be eliminated through the processing of only the correlated sound between pairs of array microphones, i. e., the diagonal of the array cross-spectral matrix is deleted. More information on the mathematical model of beam-forming can be found in Allen et al. (2013).

3.3.6.1 Beam-forming CLEAN - SC

Beam-forming CLEAN SC (CLEAN based on spatial Source Coherence) (SIJTSMA, 2007) is a technique based on the traditional CLEAN (used in astrology)(HOGBOM; BROUW, 1974) that post-processes the results achieved by the convectional beam-forming. CLEAN SC eliminates the secondary lobes coherent with the main lobe of the dominant source on the beam-forming map and identifies aerodynamic noise sources of levels lower than the secondary lobes of dominant sources.

In the present study, a Beam-forming CLEAN SC developed at LAE Laboratory was the post-processing tool that identified the noise sources and levels. The Region of Interest (ROI), i. e., the surface region of the source power integration, used for the comparison with numerical results was a crop of same dimensions of the FW-H measurement region. Figure 33 shows the ROI delimited by red lines (flap, wing main element and slat, from left-to-rigth). Beamforming CLEAN SC does not produce a continuous spectrum, since it concentrates the spectral energy of the coherent noise sources into a single point, which sometimes produces pronounced peaks that change the levels in the spectrum.

Figure 33: Region of interest used for the comparison with numerical results

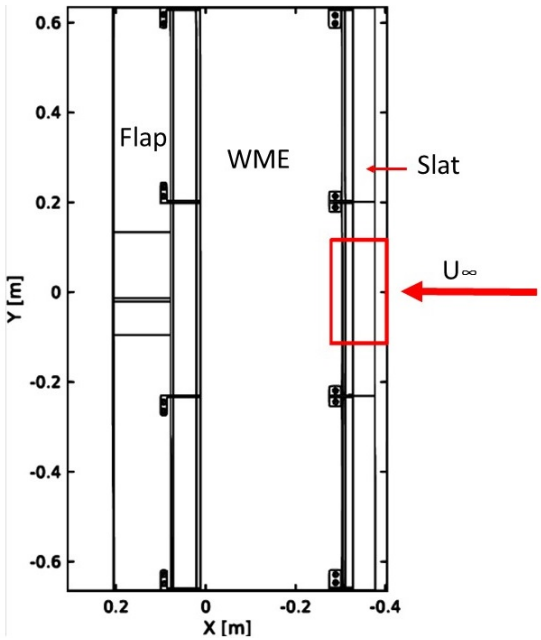

Reference: Author

3.4 Geometry variations

This study aims at modifications in some characteristics of the internal geometry of the slat for detecting their influence on the slat noise generation. Some aspects were taken into account for the design of the different geometries. The same gap and overlap were

maintained for keeping the same aerodynamic slat properties and only one characteristic was modified at each time. Modifications were accomplished through offsets (for changing distances) or rotations (for changing angles) of the slat and the new part of the geometry was adapted to the slat baseline configuration. Hence, other parameters, as curvatures or angles, were not changed.

The following six slat internal geometry parameters were modified: cusp length (κ in Figure 34), angle of the trailing edge (α in Figure 34), angle of the cusp (β in Figure 34), trailing edge thickness (χ in Figure 34), cusp thickness (ι in Figure 34) and trailing edge length (ψ in Figure 34)

Figure 34: Modified Parameters of the slat geometry

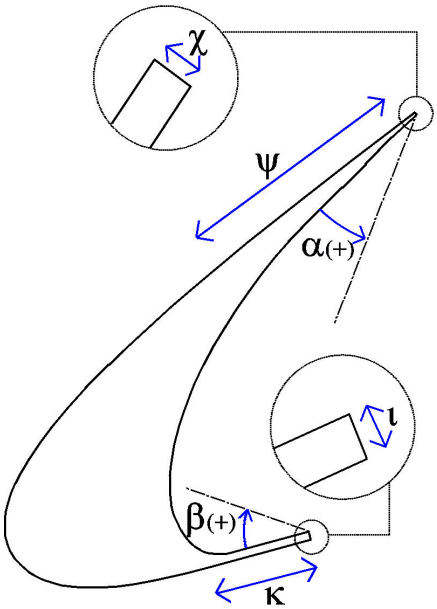

Reference: Author

All values of the angles were measured between the current and baseline configuration and all lengths were calculated in terms of percentage of the same part in the baseline configuration.

3.4.1 Variations in the cusp length

Variations in the cusp length were applied towards modifications in the main shear layer trajectory and length, and therefore, the reattachment in the upper slat surface. The cusp length values showed in Figure 35 are given in percentage of the baseline cusp length. The maximum cusp length ($\kappa = 191\%$) was established to be aligned with the slat trailing edge.

Figure 35: Modifications in the cusp length

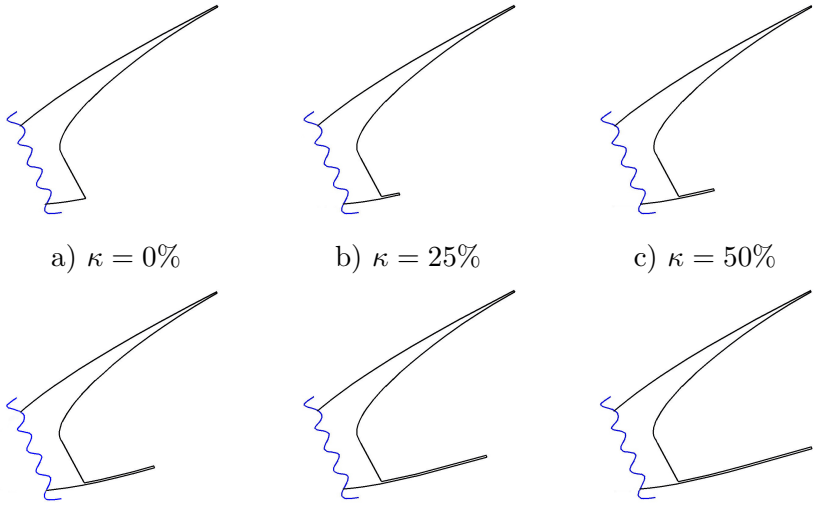

a) $\kappa = 0\%$ b) $\kappa = 25\%$ c) $\kappa = 50\%$

a) *Baseline* b) $\kappa = 150\%$ c) $\kappa = 191\%$

Reference: Author

3.4.2 Variations in the trailing edge angle

The angle of the trailing edge was modified towards a reduction in the resonance of the slat cove and a turbulence change in the trailing edge region. α ranged from -5^o to 20^0 with a 5^o increment. The minimum value was established for the minimum trailing edge thickness allowed by the CAD program and the maximum value was limited for the curvature of the slat cove, i. e., angles larger than 20^o eliminate the slat cove curve. Figure 36 shows the geometries obtained after the variation in the trailing edge angle.

Figure 36: Modifications in the angle of the trailing edge

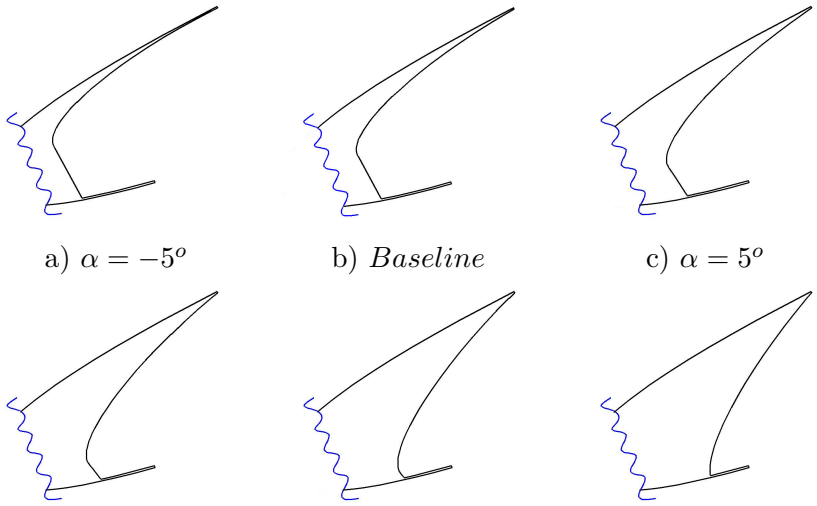

a) $\alpha = -5^o$ b) *Baseline* c) $\alpha = 5^o$

a) $\alpha = 10^o$ b) $\alpha = 15^o$ c) $\alpha = 20^o$

Reference: Author

3.4.3 Variations in the trailing edge length

Variations in the trailing edge length (Figure 37) were applied, since some authors (PAGANI; SOUZA; MEDEIROS, 2017) argue modifications in the gap and overlap of the slat change the noise. However, this change also could be obtained by modifying the length of the trailing edge with no variation in the gap and overlap.

Figure 37: Modifications in the trailing edge length

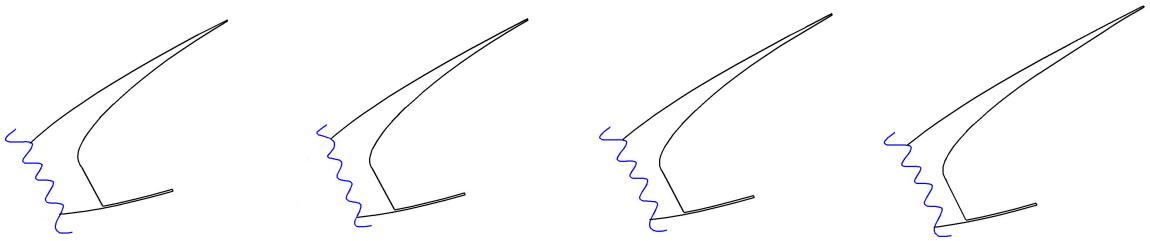

a) $\psi = 50\%$ b) *Baseline* b) $\psi = 150\%$ c) $\psi = 250\%$

Reference: Author

3.4.4 Variations in the trailing edge thickness

Some authors agree the broadband noise is generated by the action of the trailing edge as a dipole (IMAMURA et al., 2007) and (TAKEDA; ZHANG; NELSON, 2004). Therefore, an increment in the trailing edge thickness can modify this behavior and reduce the broadband noise. As a thicker trailing edge increments the turbulence in its region, a deeper study with this parameter must be conducted towards detecting its effect on the slat noise. Variations that reduce and increase the thickness of the trailing edge are shown in Figure 38. The values are given in percentage of the baseline trailing edge thickness.

Figure 38: Modifications in the trailing edge thickness

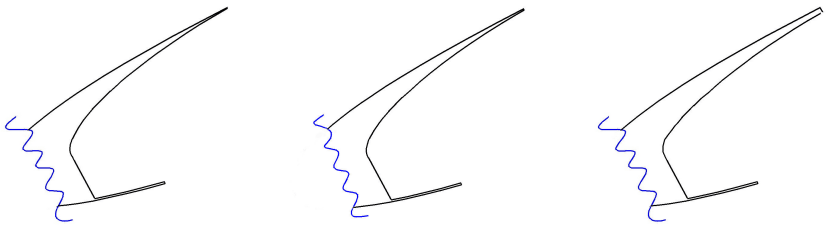

(a) $\chi = 50\%$ b) *Baseline* (b) $\chi = 400\%$

Reference: Author

3.4.5 Variations in the cusp thickness

The cusp thickness was modified towards changing the turbulence in both cusp region and shear layer, once variations in the main shear layer properties can modify the slat noise. The different configurations of cusp thickness are shown in Figure 39. The distances are given in percentage of the baseline cusp thickness.

Figure 39: Modifications in the cusp thickness

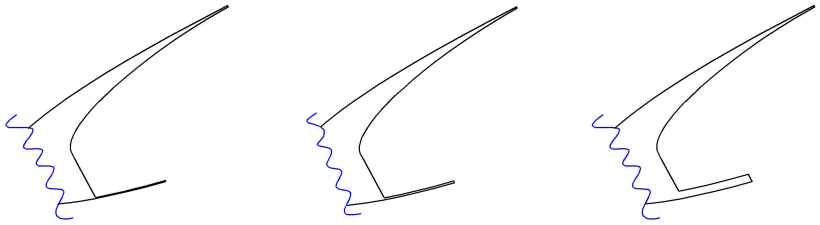

a) $\iota = 50\%$ b) *Baseline* b) $\iota = 400\%$

Reference: Author

3.4.6 Variations in the cusp angle

The cusp angle was varied aiming at a change in the shear layer trajectory and the turbulence around the cusp. The modifications applied are shown in Figure 40. The minimum angle was established for the minimum cusp thickness allowed by the CAD program.

Figure 40: Modifications in the cusp angle

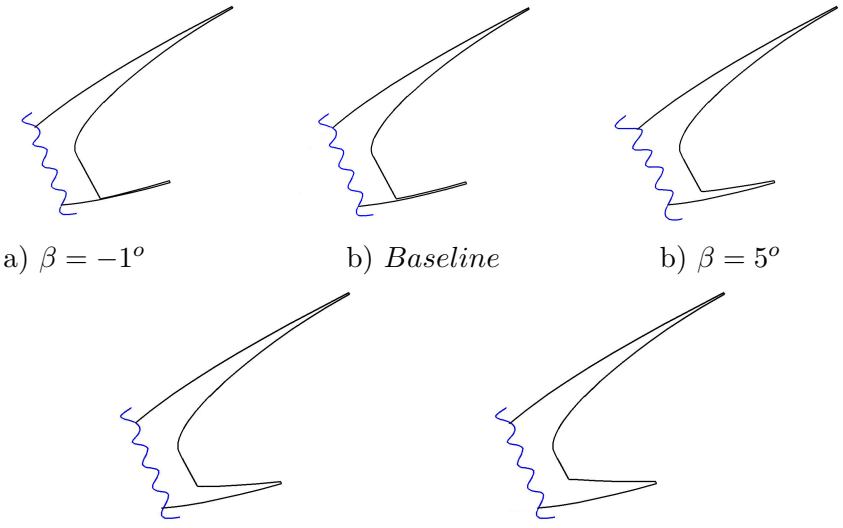

a) $\beta = -1^o$ b) *Baseline* b) $\beta = 5^o$

d) $\kappa = 150\%$ e) $\kappa = 191\%$

Reference: Author

4 RESULTS

4.1 Validation case

The numerical setup was validated through the comparison of aerodynamic and aeroacoustic numerical and experimental results of the baseline configuration, shown in dimensionless values. No values are displayed in the y-axis of the graphs for confidentiality issues.

Aerodynamic comparisons were performed through the analysis of the pressure coefficient distribution. As addressed in the previous subsection, experimental measurements of pressure coefficient were taken by a ScaniValve ZOC33/64PxX2 of ± 0.15% accuracy.

ScaniValve measures the differential pressure between the static pressure in each model tap and wind tunnel static pressure, and c_p is calculated dividing such a differential pressure by the wind tunnel dynamic pressure (Equation 4.1), which is the difference between the total and static pressure in the free-stream. The calculation of the pressure coefficient involves two different measurements, each of them with an uncertainty. Assuming a constant uncertainty of 0.15% in each measurement and following the procedure of propagation of uncertainty proposed by Fox, McDonald and Pritchard (1998), each C_p value shows 0.21% uncertainty, which represents a 0.00212 difference in C_p, for the most critical case (the suction peak at 12^o angle of attack).

$$C_p = \frac{P_{tap}}{P_{ref}} \tag{4.1}$$

Figure 41 displays the numerical and experimental pressure coefficient (c_p) distributions for $0^o, 2^o, 4^o, 6^o$ and 8^o Angles of Attack (AoA). The comparison showed a shift in the angle of attack in the wing main element in the experiments of 4^o, i.e., comparisons were made between 0^0 angle of attack in numerical results and 4^o in experimental results. After the correction of the effective angle of attack, the pressure distributions obtained numerically and experimentally were in agreement, and simulations well captured the suction peak and the short bubble in the main wing element. As expected, the numerical results over-predicted the suction peak in the flap, and experimental results showed an earlier separation than that detected by the numerical results. However, the analysis of the differences in the flap was hampered by the lack of pressure taps.

Figure 41: Pressure coefficient distribution at various angles of attack

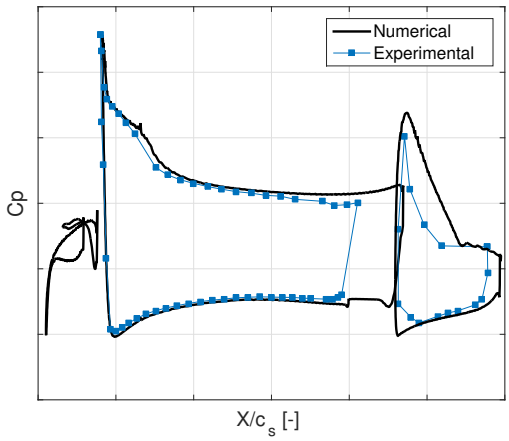

(a) AoA = 0^o

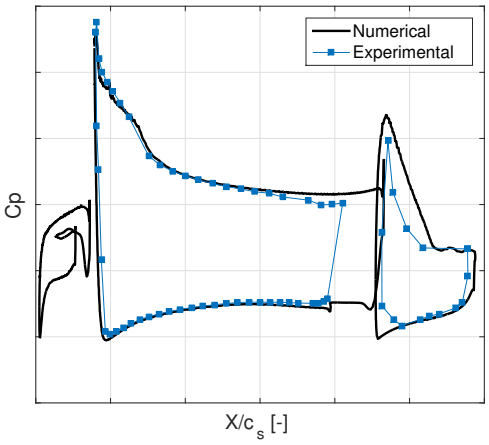

(b) AoA = 2^o

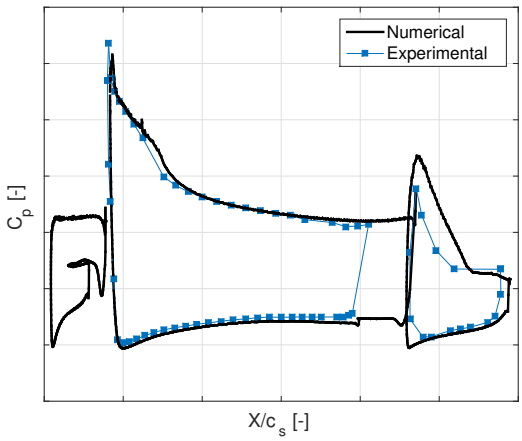

(c) AoA = 4^o

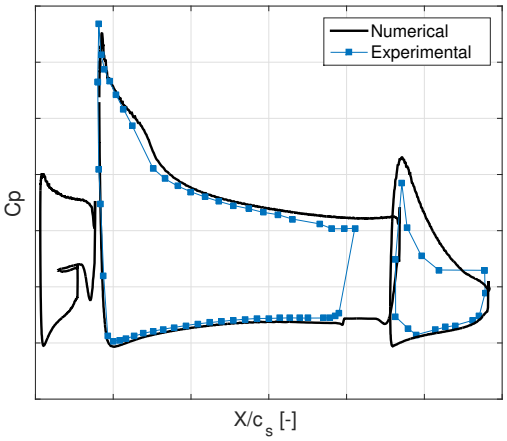

(d) AoA = 6^o

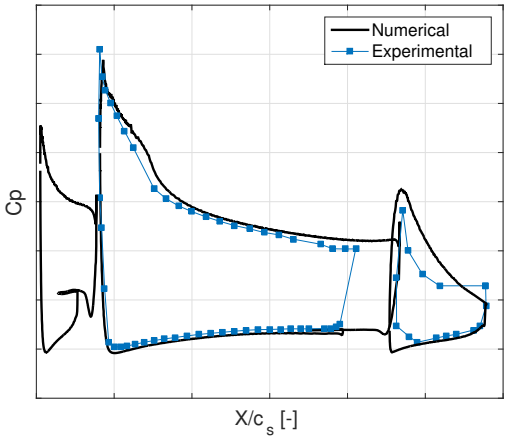

(e) AoA = 8^o

Reference: Author

The difference in the angle of attack in the main wing element can be attributed to several reasons. The first reason is related to 3D effects; although the wind tunnel has

the suction system in the walls, apparently it is not sufficient for the total elimination of the 3D effects. The second reason is related to differences in the flap deflection, which modify the circulation in the wing main element; the last reason refers to the effect of the brackets, which significantly reduces the suction on the wing main element.

Despite the difference in the angle of attack on the wing main element, the slat is well positioned in comparison with numerical simulations, since the slat noise and the reattachment point of the slat shear-layer calculated numerically and experimentally are better comparable with the same angle of attack. The good agreement in the slat region is due to the 3D effects are minor in the slat, since the slat aspect ratio is approximately 5 times larger than the element aspect ratio. On the other hand, the slat is not affected by the brackets and the effects caused by variations in the flap deflection are also minimal. Furthermore, comparisons of the skin friction made by Pereira et al. (2018a) at different slat positions also showed a well agreement at the same angle of attack. As a conclusion, comparisons between numerical and experimental results in the slat region were performed at the same angle of attack.

The reattachment point refers to the region where the main shear layer impinges the slat surface and part of the unsteady flows over the slat trailing edge and the other part recirculates in the slat cove. Such a region may be associated with the generation of mid-frequency tones in the slat spectra. The comparison between the reattachment point found numerically and experimentally was used for the analysis of the similarity of the flow around the slat; however, it will be related to the noise generation in the next sections. In numerical simulations, the reattachment point was detected through streamlines in the slat surface, as shown in Figure 42 (a), whereas in the experiments, it was detected through the calculation of the minimum coherence of the pressure fluctuation measured by several hot-film sensors located in the slat trailing edge region, as reported in Pereira et al. (2018b). Figure 42 (b) displays the reattachment points found by the two methods for the same 0^o to 8^o angles of attack; the values were divided by the slat chord and distances were measured from the slat leading edge. The numerical results agreed with the experimental ones in all AoA and are within the error range of the experimental results, which demonstrates the recirculation in the slat cove by both methods is similar.

The Power Spectral Density (PSD) versus Strouhal number obtained numerically and experimentally is shown in Figure 43 for 0^o, 4^o, and 8^o angles of attack. Experimental results, achieved by Beamforming CLEAN SC methodology, are shown, and the numerical results are displayed with both full and reduced spans, i.e., 1300 and 250 mm at $AoA = 0^o$. Although both simulations have the same FW-H span, the shortest computational domain overpredicted the noise in approximately 3 dB from $St = 20$ due to the blockage effect of the solid walls on the acoustic waves, since the distance between the FW-H measurement region and the walls is shorter, i.e., $0.294c_s$ in comparison to $6.47c_s$ in the full span case.

However, the behavior of the computational results was the same in all frequency range. Pagani, Souza and Medeiros (2016) used $0.17c_s$ and $0.255c_s$ distances between the wall and the measurement region and obtained good comparisons with experimental results.

Figure 42: Shear-layer reattachment

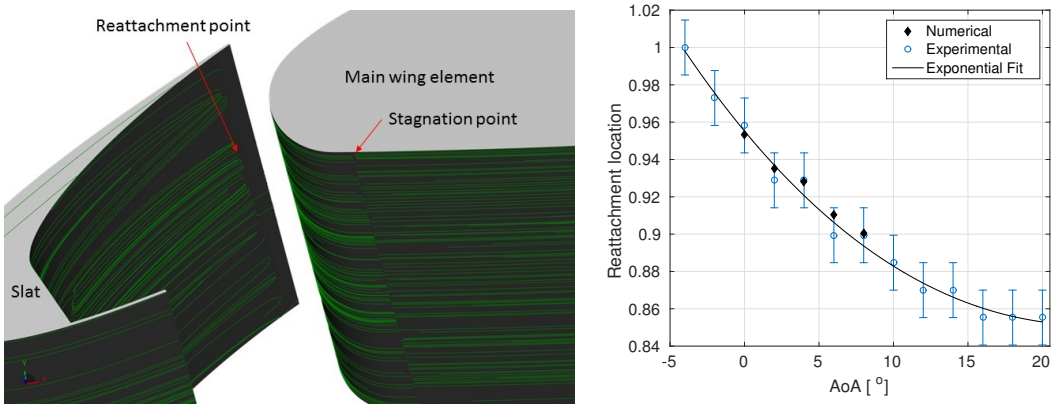

(a) Streamlines in the slat surface (b) Reattachment location

Reference: Author

The numerical results well predicted the tones frequency and level mainly in $AoA = 0^o$. For 4^o and 8^o AoA, they showed tones of higher values. After St 5, the numerical and experimental results showed the same slope up to $St = 40$ in $AoA = 0^o$ and 30 for $AoA = 4^o$ and 8^o. Above these values, the numerical results revealed a larger drop in the power spectrum in function of Strohual number, probably due to the loss of coherence in the phased array antenna and dissipation of numerical results.

The overall pressure level for acoustic fluctuations was calculated between St 1 and 60 and the results are provided in Table 2. The experimental value at $AoA = 0^o$ was uses as a reference. Numerical simulations calculated the OSPL with 4 dB precision for $AoA = 0^o$ and 1 dB precision for the others AoA. Moreover, no difference was detected in the OSPL for the different span dimensions used.

As shown in section 3.2, the numerical results are affected by the element size and FW-H measurement region, however, these limitations exerted an acceptable effect on the results. The numerical and experimental results were in agreement in most part of the spectra. Both frequency and amplitude of mid-frequency peaks and the level and drop of the PSD in function of the frequency of the broadband component were well captured by the experiment and simulations.

Figure 43: PSD at several angles of attack

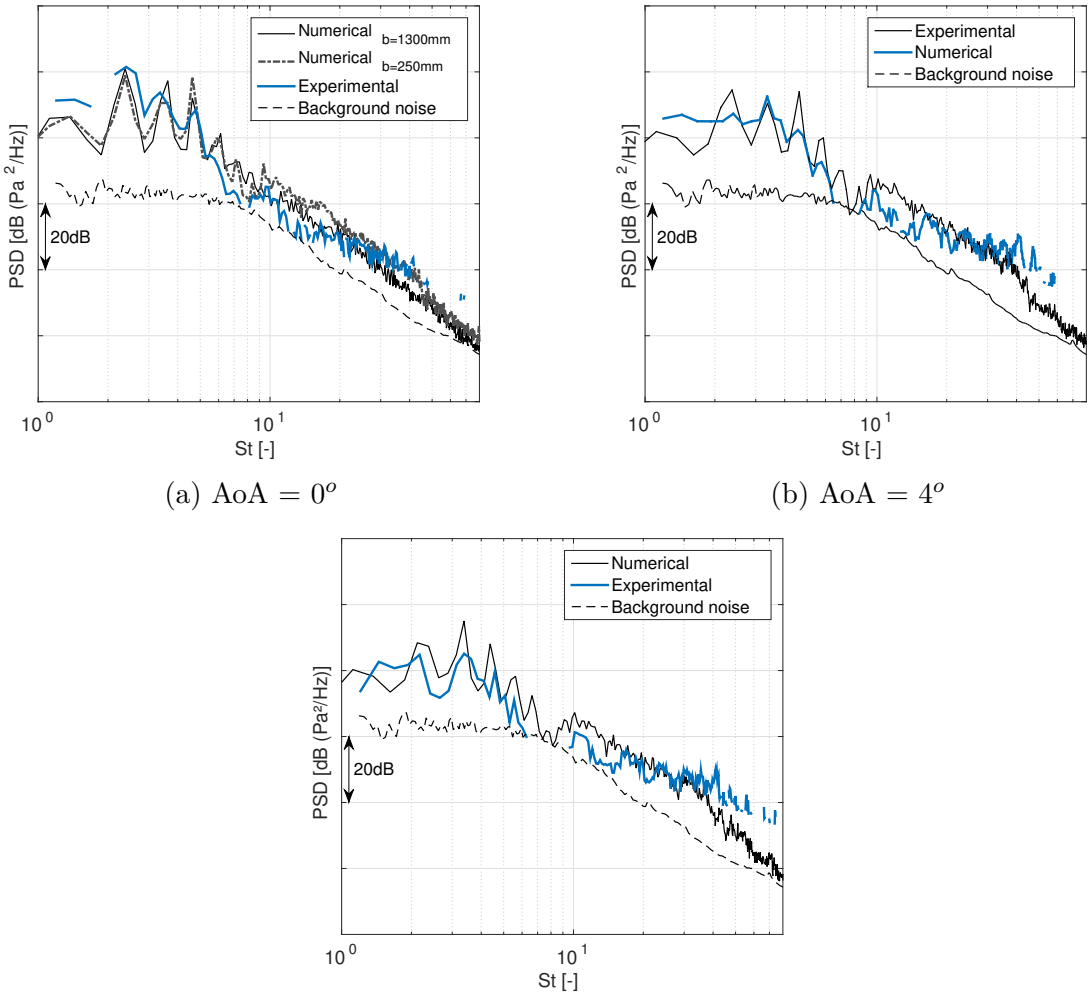

(a) AoA = 0^o

(b) AoA = 4^o

(c) AoA = 8^o

Reference: Author

Table 2: OSPL for acoustic fluctuations between St 1 and 60 for experimental and numerical results at different AoA

AoA [^{o}]	Experimental	Numerical
0	0	4
4	-0.1	-1.56
8	-3.44	-4.67

Reference: Author

4.2 Baseline configuration

4.2.1 Chord-wise unsteady flow analysis

One of the most important aerodynamic characteristics of the slat is instability associated with the development of the shear-layer and its interaction with the main

element and the slat cove. The shear layer is formed along the cusp and, when separated from it, 2-dimensional Kevin-Helmholtz (K-H) instabilities are assembled along the entire span (as shown in Figure 44). They are developed along the shear layer, complete the transition to 3-Dimensional turbulent flow, and finally impinge on the slat upper wall. Some of the vorticity structures at the reattachment location are re-injected into the main recirculation bubble formed in the slat cove, whereas the others flow towards the trailing edge and interact with it, thus causing a high-turbulence region. The figure shows the vortical structures using the λ_2 criterion, which determines for any point in the fluid whether this point is part of a vortex core. A vortex is now defined as a connected region for which every point inside this region is part of a vortex core.

Figure 44: Instantaneous $\lambda_2 = -3000$ iso-surface in the slat cove

Reference: Author

Figure 45 (a) shows the dissipation of the high vorticity generated in the cusp along the shear layer and how it increases when the flow impinges on the slat surface at the reattachment point. Figure 45 (b) displays the time-average streamlines colored by the velocity magnitude, that show the formation of the recirculation region inside the slat-cove and the main shear layer can be distinguished. A remarkable difference is observed between the internal and external velocities; its relation to the broadband noise is addressed in the next sections.

The analysis of pressure fluctuations on the surface aims at the understanding of the flow-surface interaction. Figure 46 displays the root mean square (RMS) wall pressure coefficient in the slat cove. The peak exhibited at $X/c_s = 0.955$ is highly related to the main shear layer reattachment point and has been associated with the generation of tonal noise (CHOUDHARI; KHORRAMI, 2006; TERRACOL; MANOHA; LEMOINE, 2015).

The evolution of the fluctuations of velocity components and turbulent kinetic energy (TKE) along the shear layer is shown in Figure 47, where s is the position along

Figure 45: Gap flow characteristics

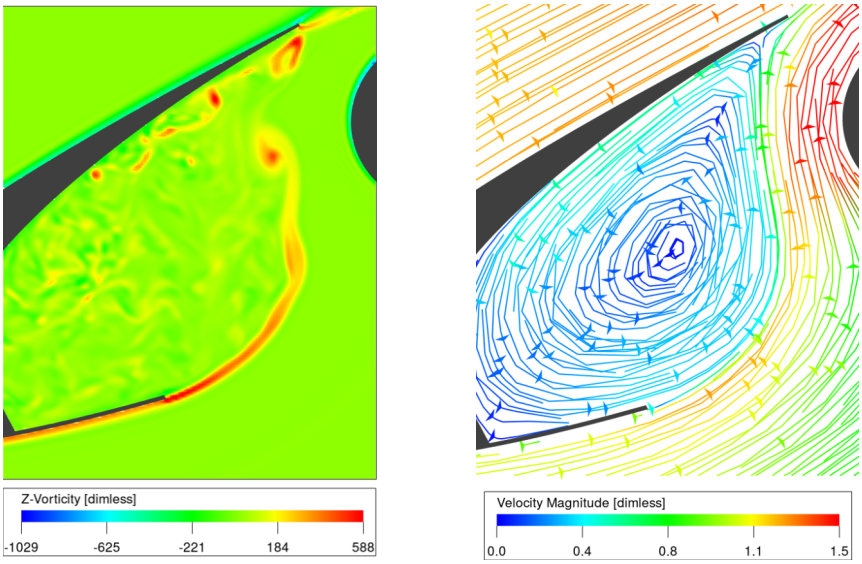

(a) Instantaneous span-wise vorticity (b)Time-average streamlines

Reference: Author

Figure 46: RMS wall pressure coefficient

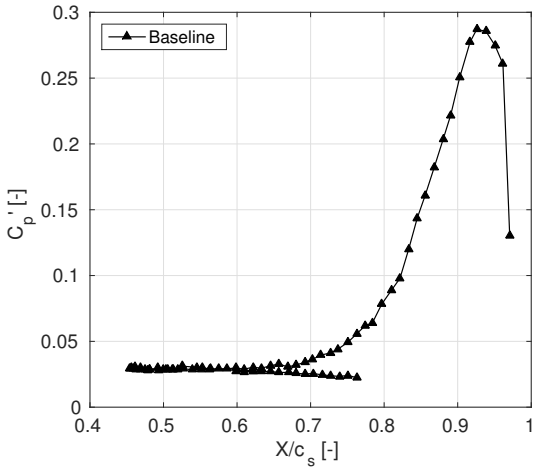

Reference: Author

the shear-layer, $s = 0$ is in slat cusp and $s = 1$ is in the reattachment point. The plane velocity fluctuations (u' and v') are maximal upstream the reattachment and rapidly decay, whereas span-wise velocity fluctuations (w') increase continuously until the reattachment point, probably as a result of changes in the mean flow velocities in the x-y plane. TKE fluctuations ($TKE' = [0.5(uu + vv + ww)]'$) (Figure 47 (b)) are maximal at 62% of the shear layer and might be linked to the maximum value of u'. Similar results were found by Choudhari and Khorrami (2006).

Figure 48 displays the points used for the analysis of the shear-layer behavior and Figure 49 (a,b,c) shows the evolution of the velocity components in comparison with a

Figure 47: Evolution of the shear layer properties

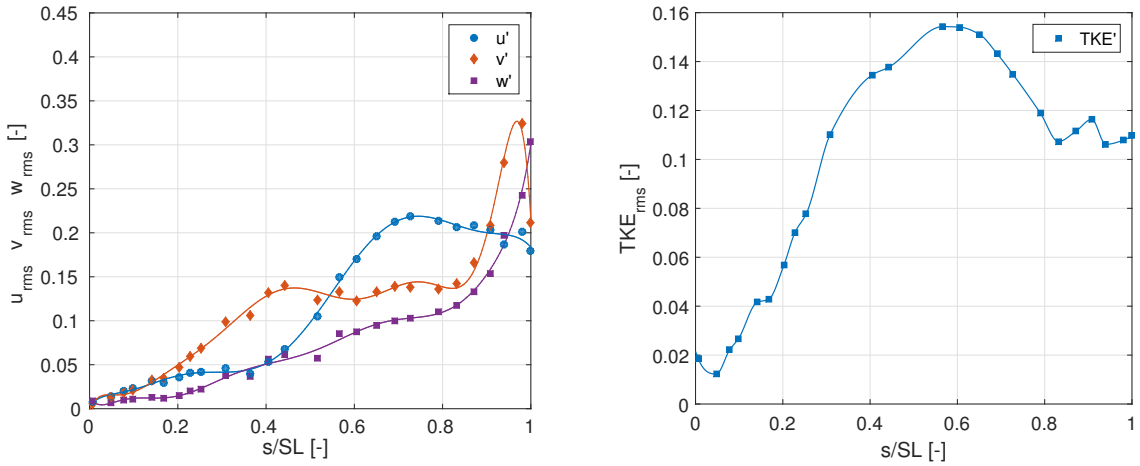

(a) RMS velocity components

(b) RMS turbulence kinetic energy

Reference: Author

drop-off of $f^{-\frac{5}{3}}$, which represents a Kolmogorov spectrum of turbulence on the inertial scale (ZAKHAROV; L'VOV; FALKOVICH, 2012). The turbulence is developed and increased along the shear layer and near the reattachment point exhibited a drop-off close to the Kolmogorov scale up to $St = 20$. Figure 49 (d) illustrates the evolution of the pressure spectra along the shear layer. The hump at the beginning of the shear layer ($s/SL = 0.1$) at $St = 11.5$ is associated with the development of initial K-H instabilities and the frequency at which it occurs is known as the main amplified frequency in the slat mixing layer (TERRACOL; MANOHA; LEMOINE, 2015) and can be estimated as the Strohual number by Equation 4.2, where U_1 and U_2 are the velocities of the parallel flows of the mixing layer (obtained from Figure 17) and δ_w is the vorticity thickness calculated in subsection 3.2.4. The main amplified Strouhal number (9.78) was calculated with the values in Table 3 and is equivalent to that detected in the pressure spectra graph in the shear layer (St = 11.5). Mid-frequency tones are observed in the first stage of the shear layer and are reduced along it. The last stage shows a spectrum with only a broadband component with some remnants of mid-frequency peaks. The cavity of the slat cove causes a resonance with the generation of the tones and therefore they are exhibited in the spectrum of the pressure fluctuation, whereas the spectrum of fluctuations of the velocity components are dominated by turbulence.

$$St_0 = \frac{1}{2}\left(\frac{U_1 + U_2}{7 \times \delta_w}\right) \times \left(\frac{c_s}{U_\infty}\right) \tag{4.2}$$

Figure 48: Points used for the analysis of the shear-layer spectra development

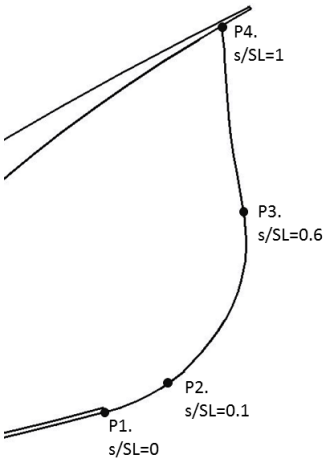

Reference: Author

Table 3: Values used for the calculation of the main amplified frequency

$\frac{U_1}{U_\infty}$	$\frac{U_2}{U_\infty}$	δ_w
1.35	0.16	0.00074

Reference: Author

4.2.2 Span-wise unsteady flow analysis

The interaction of the fluid-structure in the slat in the span-wise direction was analyzed through the calculation of the pressure fluctuations coherence at both trailing edge and reattachment point. Points were spaced $\Delta z = 0.06c_s$ up to $z_{max} = 7c_s$ and $\Delta z = 0.01c_s$ up to $z_{max} = 1c_s$.

The results of the coherence in the trailing edge are provided in subsection 3.2.5 and were used for the determination of the FW-H measurement region length. Figure 50 shows the results of the coherence in the reattachment point. For all cases, the Strouhal numbers shown refer to the peaks determined in the far-field noise spectra and a high-frequency Strouhal number ($St = 97.5$). The coherence length, defined mathematically as the coherence integrated above all distances, represents the distance in which there is a significant coherence between the points.

Figure 50 also shows the Gaussian curve, calculated by Equation 4.3, provided in Lockard and Choudhari (2009). The coherence lengths used in each case are shown in Figure 50 (e). According to Pascioni, Cattafesta and Choudhari (2014), the coherence in the span-wise direction does not attune well to the Gauss curve, especially for tonal peaks, since the coherence level does not tend to zero in the Z-range covered, as in the

Gauss curve. On the other hand, at the broadband frequency, it approaches zero in a short distance for both cases (Gauss and calculated coherence).

Figure 49: Velocity and pressure spectra along the shear layer

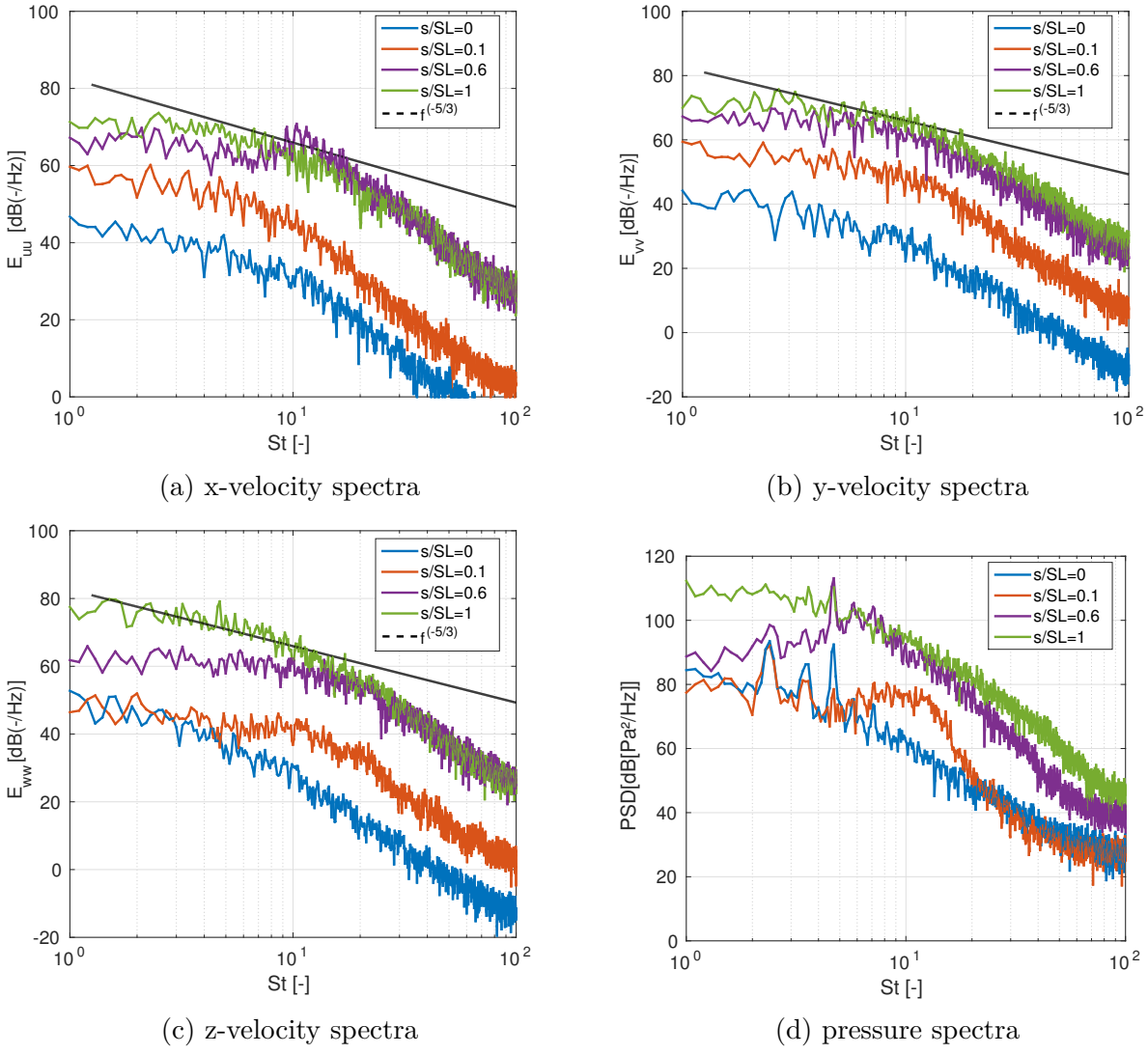

(a) x-velocity spectra

(b) y-velocity spectra

(c) z-velocity spectra

(d) pressure spectra

Reference: Author

$$\gamma^2 = e^{-(\frac{\Delta Z}{L_c})^2} \tag{4.3}$$

In all Strouhal numbers, the coherence at the reattachment is higher than that at the trailing edge and in both locations, the third peak exhibited the highest coherence, which is almost constant at all points until $z_{max} = 1c_s$, and then decays for longer distances. The first peak provided the highest coherence for $z_{max} = 7$, whereas the second showed a larger drop in function of the distance in both locations. The broadband noise (highest Strouhal number) showed the largest drop because of the poor relation of the broadband noise generation and the span-wise correlation. Differently from the case of $z_{max} = 7c_s$, for $z_{max} = 1c_s$, the behavior of the coherence is not cyclic, , probably because the span of the

loop generated between the cusp and the reattachment (or trailing edge) is greater than $1c_s$.

Figure 50: Analysis of span-wise fluid-surface interaction

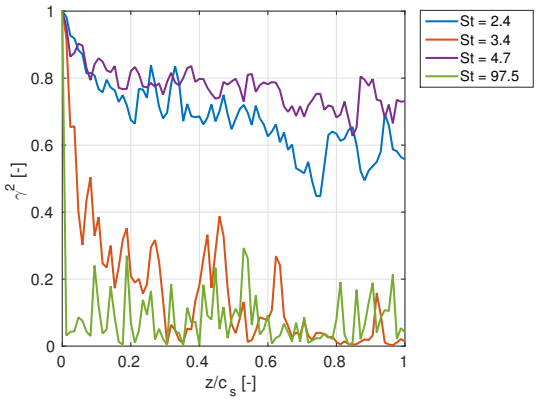

(a) Span-wise coherence at reattachment with $\Delta Z/c_s = 0.01$

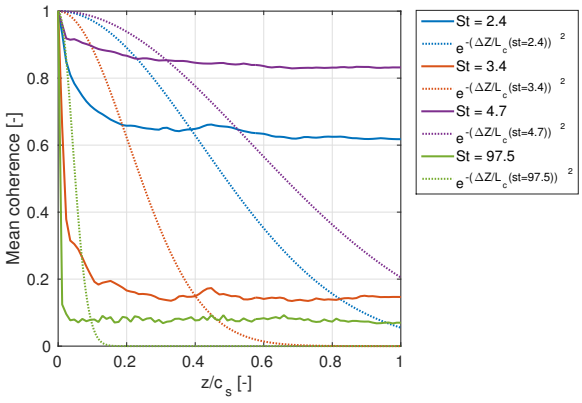

(b) Span-wise mean coherence at reattachment with $\Delta Z/c_s = 0.01$

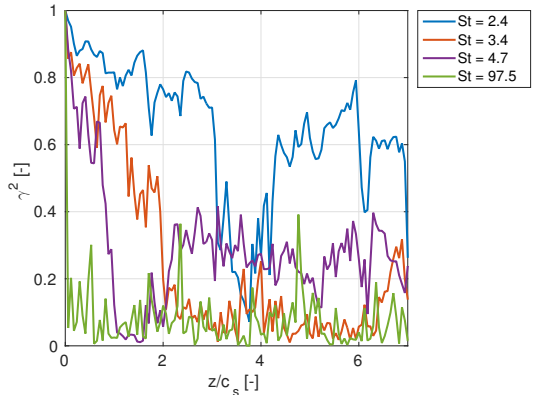

(c) Span-wise coherence at reattachment with $\Delta Z/c_s = 0.06$

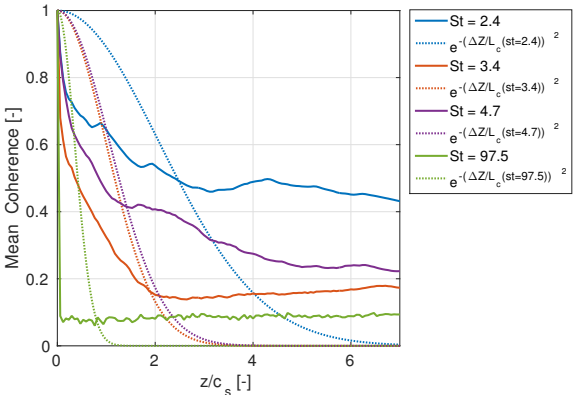

(d) Span-wise mean coherence at reattachment with $\Delta Z/c_s = 0.06$

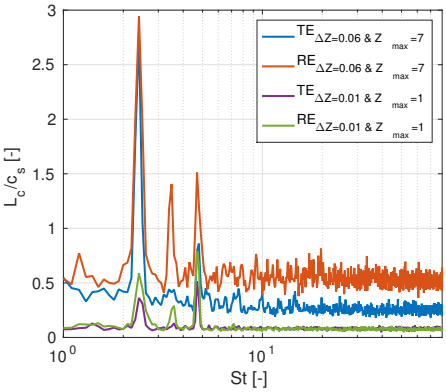

(e) Coherence length

Reference: Author

Figure 50 (e) shows the coherence length non-dimensionalized by the slat chord for the pressure fluctuations of the three cases addressed. As observed by Pascioni, Cattafesta and Choudhari (2014), Lockard and Choudhari (2009) and Pagani, Souza and Medeiros

(2016), the coherence length showed higher values at the same frequencies of the mid-frequency tones detected in the far-field. On the other hand, in the reattachment location, it showed the main three mid-frequency tonal peaks, whereas at the trailing edge, only the first and third peaks were exposed. Furthermore, the coherence length at peaks is greater in the reattachment than in the trailing edge, which leads to the supposition the loop is created between the cusp and the reattachment, and not between cusp and trailing edge. The tones intensity may be related to the coherence length, since larger coherence lengths produce more intense tones.

4.2.3 Far-field analysis

As expected, at $AoA = 0^o$, the slat far-field noise spectrum obtained numerically (Figure 43) is composed of three main mid-frequency tones at $St = 2.34,\ 3.4$ and 4.5, of which the first showed the maximum value of PSD, a low-intensity narrow-band component around St 8-10, and a broadband noise that decreases constantly in function of the St with a 1.01 $[dB/St]$ slope. The tonal peaks have been analyzed in two different ways. First, they were attributed to laminar effects, i. e., a feedback loop between the acoustic waves and Tollmien-Schlichting waves generated in the slat boundary layer. Under this assumption, they should disappear at full scale or be significantly reduced by trip devices. However, according to Kolb et al. (2007a), Pott-Pollenske, Alvarez-Gonzales and Dobrzynski (2003), and Terracol, Manoha and Lemoine (2015), tonal components are still present in the slat spectra, despite the use of them. The second theory establishes tones are related to the existence of a feedback loop between the acoustic waves generated by the reattachment of the main shear layer on the upper slat surface and the mixing layer originated from the slat cusp, as in cavity flows. The theory has been widely accepted and is related to the functionality of slat-covers, since a suppression of the main shear layer significantly reduces the tonal peaks (IMAMURA et al., 2007; KOLB et al., 2007a; ROGER; PÉRENNÈS, 2000; TERRACOL; MANOHA; LEMOINE, 2015). The broadband noise is attributed to the turbulence generated in the trailing edge region (IMAMURA et al., 2007; TAKEDA; ZHANG; NELSON, 2004).

Figure 51 shows the filtered-PSD contour on the slat and wing main element surfaces. The Strouhal numbers showed are those of the far-field's tonal components and a higher Strouhal number ($St = 18$) associated with the broadband noise. Two points of view are shown for each St. The first displays the slat cove and the second exhibits the slat suction side, cusp and WME leading edge. Notably, the highest fluctuations occur in the trailing edge and reattachment region for all Strohual numbers. Regarding the peaks, the noise is highly propagated and higher fluctuations are observed in the leading edge of the WME.

Figure 51: PSD filtered contour on the Slat surface

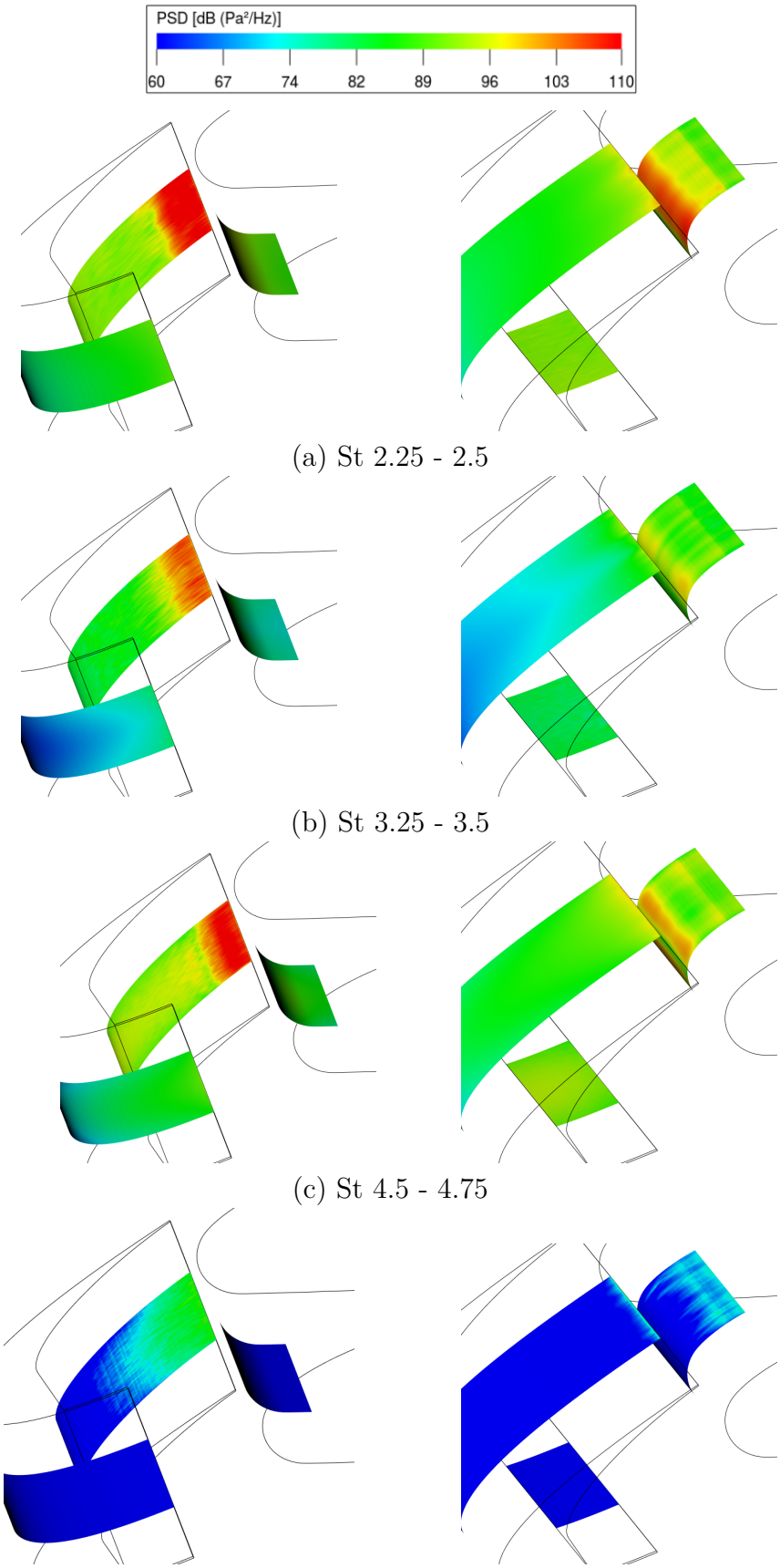

(a) St 2.25 - 2.5

(b) St 3.25 - 3.5

(c) St 4.5 - 4.75

(d) St 18 - 18.25

Reference: Author

Furthermore, for high frequencies, the region of highest fluctuations grows towards the slat cove. The higher pressure fluctuations observed in the upper surface of the slat trailing edge at $St = 18 - 18.25$ (Figure 51 (d)) may be associated with the dipole generated in the trailing edge responsible for the broadband noise. On the other hand, at that frequency, fluctuations in the suction region of the main element are also detected and probably caused by the high and turbulent wake of the slat.

Figure 52 (a) and (b) show the SPL integrated over all frequencies and the effect of the Strouhal number on the slat directivity, respectively. As expected, the noise is more efficiently radiated in the $\phi = 120^o$ direction, following the slat angle (30^o). At low frequencies, the slat exhibited a dipole-like behavior due to the lighter interference of the main element surfaces, whereas at high frequencies (short wavelengths), the main element highly influences the noise propagation and most of the energy is dissipated on the upper side in the $\phi = 330^o$ direction.

Figure 52: Slat directivity

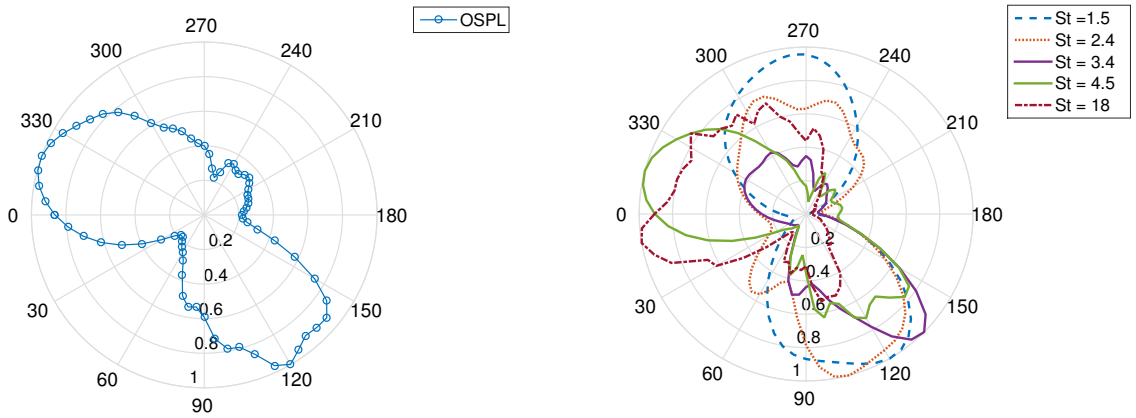

(a) OSPL directivity

(b) Directivity change with St

Reference: Author

4.2.3.1 Effect of the angle of attack

According to Figure 53, the angle of attack exerts a small influence on the broadband noise and the drop of the PSD in function of the Strouhal number is almost constant along all AoA from $St = 10$. On the other hand, the angle of attack influences the mid-frequency tones intensity. The tonal components of the spectra decrease as the angle of attack increases and the maximum tone moves towards higher Strouhal numbers. Nevertheless, the Strohual of each peak decreases as the angle of attack increases. The narrow-band component at approximately St 8-10 is observed in all angles of attack.

Figure 54 displays how the shear-layer trajectory changes and the reattachment point moves through away the trailing edge in function ofthe angle of attack. The analysis of the reattachment location and main shear layer trajectory and length reveals their possible relation to the noise generation, and their modification may reduce the slat noise. Figure 55 shows the variation of the main shear layer (MSL) length and reattachment location (measured from the leading edge) as the AoA increases; both results are divided by the slat chord. As the angle of attack increases, the reattachment moves away from the trailing edge, and the main shear layer decreases. Both, the reattachment location and the shear-layer length follow a quadratic relation with the angle of attack. A lower intensity of mid-frequency tones can be related to longer distances between the trailing edge and reattachment point, as in $AoA = 8^o$.

Figure 53: Far-field noise variation in function of AoA

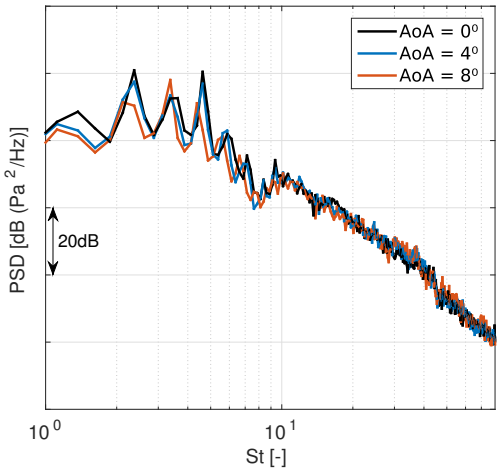

Reference: Author

Figure 54: Main shear layer trajectory for $AoA = 0^o$ and 8^o

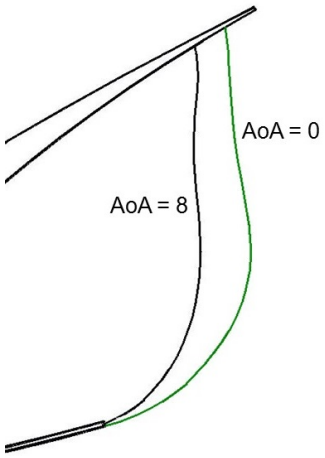

Reference: Author

Although according to Figure 49 (d) the PSD is composed of an unique broadband component in the last stage of the shear layer (near the reattachment), the spectrum of pressure fluctuation in the reattachment point still exhibited mid-frequency tones (Figure 56) related to mid-frequency tones in the far-field. In agreement with Pagani, Souza and Medeiros (2016), the PSD at the reattachment point decreases as the angle of attack increases in all frequency range, however, in the trailing edge, the PSD in the St range greater than 20 is increased as the angle of attack increases. This phenomenon may be due to the greater turbulence behind the slat (near the trailing edge) for higher AoA, which increases the pressure fluctuations in the slat surface at high-frequency.

4.2.4 Analytical derivation of mid-frequency tones

Terracol, Manoha and Lemoine (2015) derived an equation from the phenomenon shown in Figure 57 for analytically calculating tonal frequencies. The vortices originated in

the slat cusp are convected along the main shear layer until the reattachment point, where acoustic waves are generated and propagated inside the slat cove along the acoustic path (straight line between the reattachment point and slat cusp). When one of them reaches the cusp. A new vortex is generated in the main shear layer. Such a loop has multiple numbers of harmonics and the frequency can be estimated by Equation 4.4, where n_h is the number of harmonics, U_∞ is the free-stream velocity, L_a is the linear distance from the cusp to the reattachment, α_l is the ratio between L_a and L_v (main shear layer distance) and κ_v is the ratio between U_v (velocity of the main shear layer) and U_∞.

Figure 55: Variation of shear-layer in function of AoA

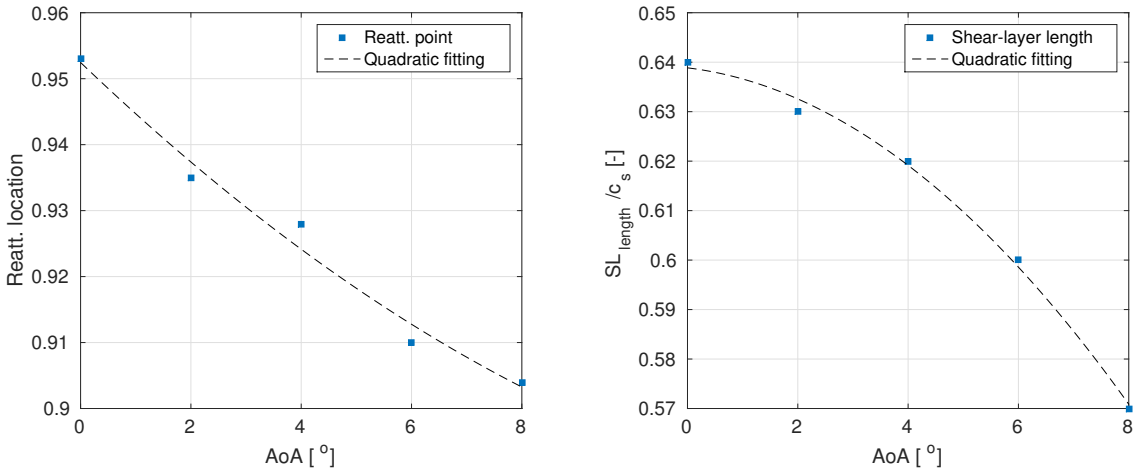

(a) Reattachment (b) Shear-layer length

Reference: Author

Figure 56: PSD at slat surface

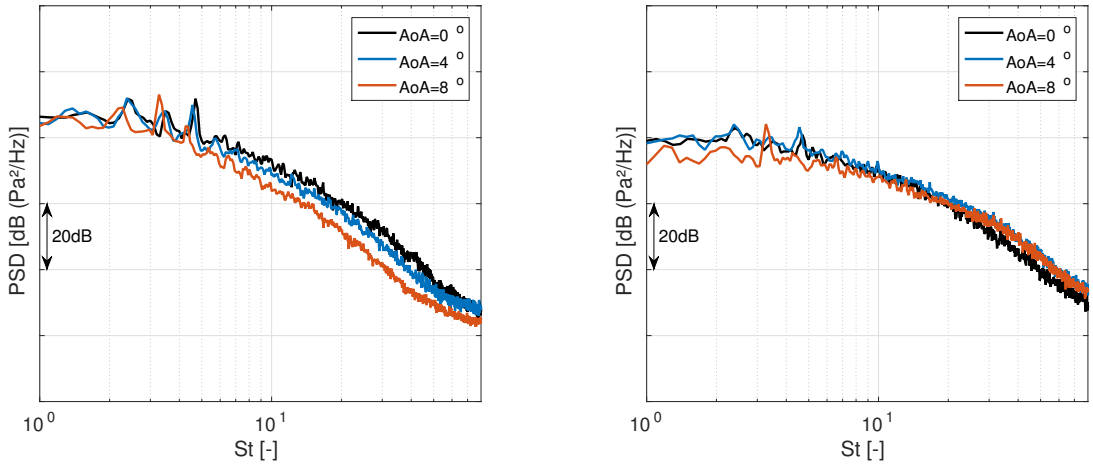

(a) Reattachment (b) Trailing edge

Reference: Author

$$f_n = n_h \frac{U_\infty}{L_a} \left(\frac{1}{M + \frac{\alpha_l}{\kappa_v}} \right) \tag{4.4}$$

Figure 57: Schematic representation of the aeroacoustic feedback loop inside the slat cove. Left: time t_0; right: time $t_0 + t'$

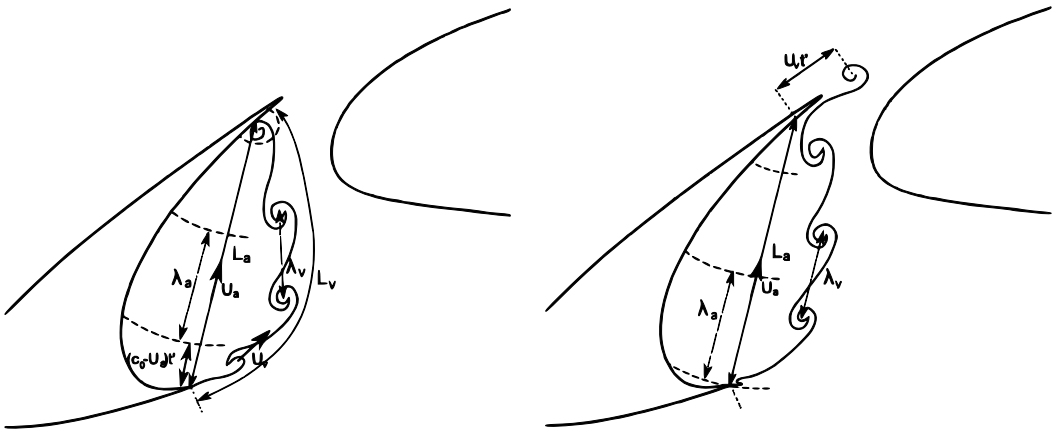

Reference: Terracol, Manoha and Lemoine (2015)

According to Equation 4.4, the frequency of the peaks tends to increase, as the angle of attack increases, since the velocity in the shear layer and L_a reduces. On the other hand, experimental and numerical results showed the frequency decreases as the AoA increases, therefore, an additional analysis was conducted. The loop responsible for the tonal component was assumed created between the trailing edge, rather than the reattachment, and the slat cusp and the vortices are convected until the reattachment and further flow towards the trailing edge. Under this assumption, L_a would be the distance between the trailing edge and slat cusp (constant among all AoA) and L_v would be the main shear layer distance plus the distance between the reattachment and the trailing edge.

Figure 58 shows the Strouhal numbers of the three main tones of the slat calculated analytically (using values in Table 4) and found experimentally and numerically. For lower angles of attack, both analyses (which considered reattachment and trailing edge as noise sources) revealed St values approximated to those obtained experimentally and numerically. However, as the angle of attack increases, the estimation that considers the loop with the reattachment point exhibits a tendency different from the experimental and numerical results. On the other hand, the analysis that considers a loop between the trailing edge and slat cusp provided more coherent results, i.e., the frequency slightly decays, as the angle of attack increases. Analyses at others AoA must be carried out for more precise conclusions.

Table 4: Values used for the analytical calculation of the frequency of tones

AoA	κ_v	α_L (Reattachment)	α_L (Trailing edge)
0	0.82	1.095	1.11
2	0.8	1.11	1.13
4	0.79	1.11	1.13
6	0.79	1.19	1.13
8	0.76	1.05	1.08

Reference: Author

Figure 58: Strohual number obtained numerically, experimentally and analytically

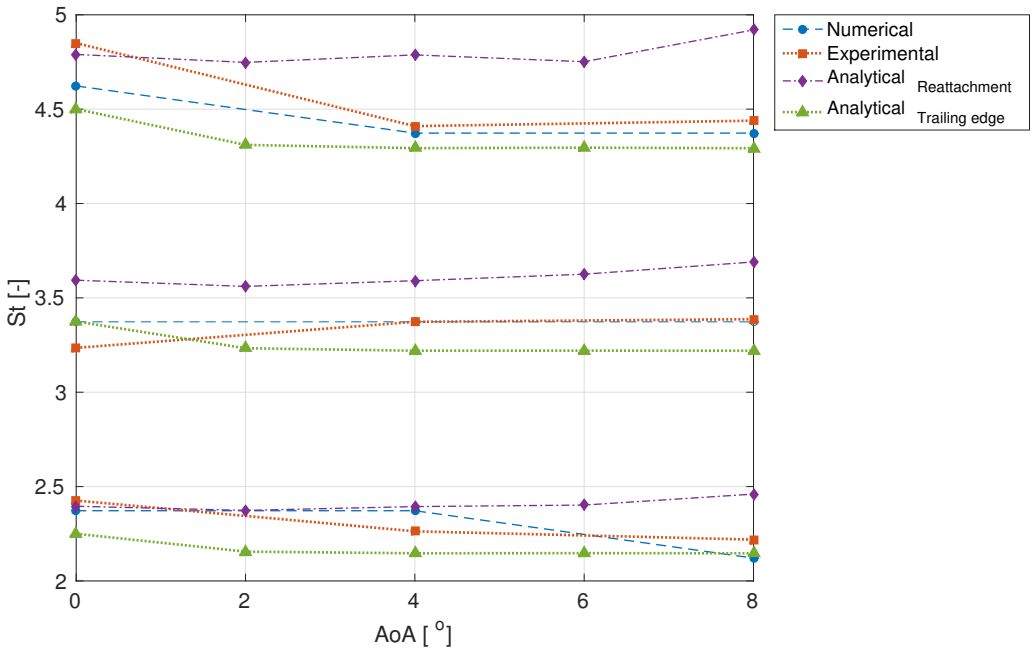

Reference: Author

4.3 Effect of the cusp length

Five modifications in the cusp length (κ) were simulated towards determining its effect on the noise generation. An analysis of the aerodynamic effect of each geometry variation must be conducted prior to the study of the acoustic effect, since, as addressed elsewhere, reductions in C_L result in an increment in velocity, which increases the overall noise at a 6^{th} power.

Table 5 shows the fluctuation of the lift and drag coefficients of the complete element (slat, WME and flap) in function of κ variation. The major variation of the

C_L was a 3% increment in conf. κ191 (191% of the baseline cusp length), related to the increment in the suction peak in the slat and WME (Figure 59); the increment of the suction peak in the WME is because it is affected by the acceleration caused by a longer cups. The drag coefficient (C_D) was reduced by cusp lengths shorter than that of the baseline configuration and increased by longer ones. A 2% reduction in C_D in conf. κ50 and a 13% increment in conf. κ191 were obtained. The increment in the drag coefficient in configurations with a longer cusp is associated with the larger slat wake and the slat main shear-layer is mixed with the boundary layer in the MWE leading edge. Figure 59 shows variation in the pressure distribution for extreme modifications. Differences in the slat and WME suction peaks were obtained, whereas no differences in the flap were perceived among the configurations.

Table 5: Lift and drag coefficients of different κ

Conf.	C_L variation [%]	C_D Variation [%]
κ0	0.96	-0.07
κ25	1.43	-0.19
κ50	1.017	-2.1
Baseline	0	0
κ150	1.92	7.96
κ191	2.90	13.54

Reference: Author

Figure 59: Pressure coefficient distribution at midspan of different κ

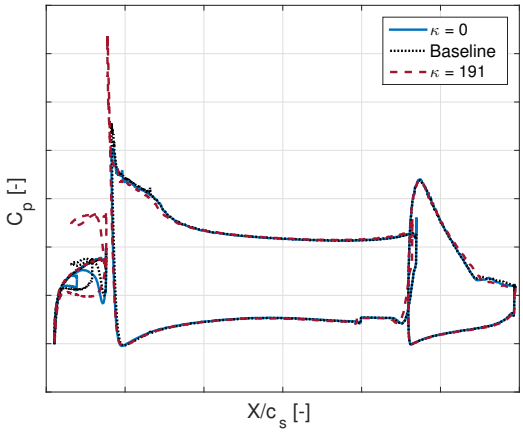

Reference: Author

Figure 60 displays the PSD of the different cusp length configurations propagated to the central microphone of the antenna shown in Figure 23 (a). According to the results, longer cusps cause more tonal and broadband noise than shorter ones.

Figure 60: PSD of different κ

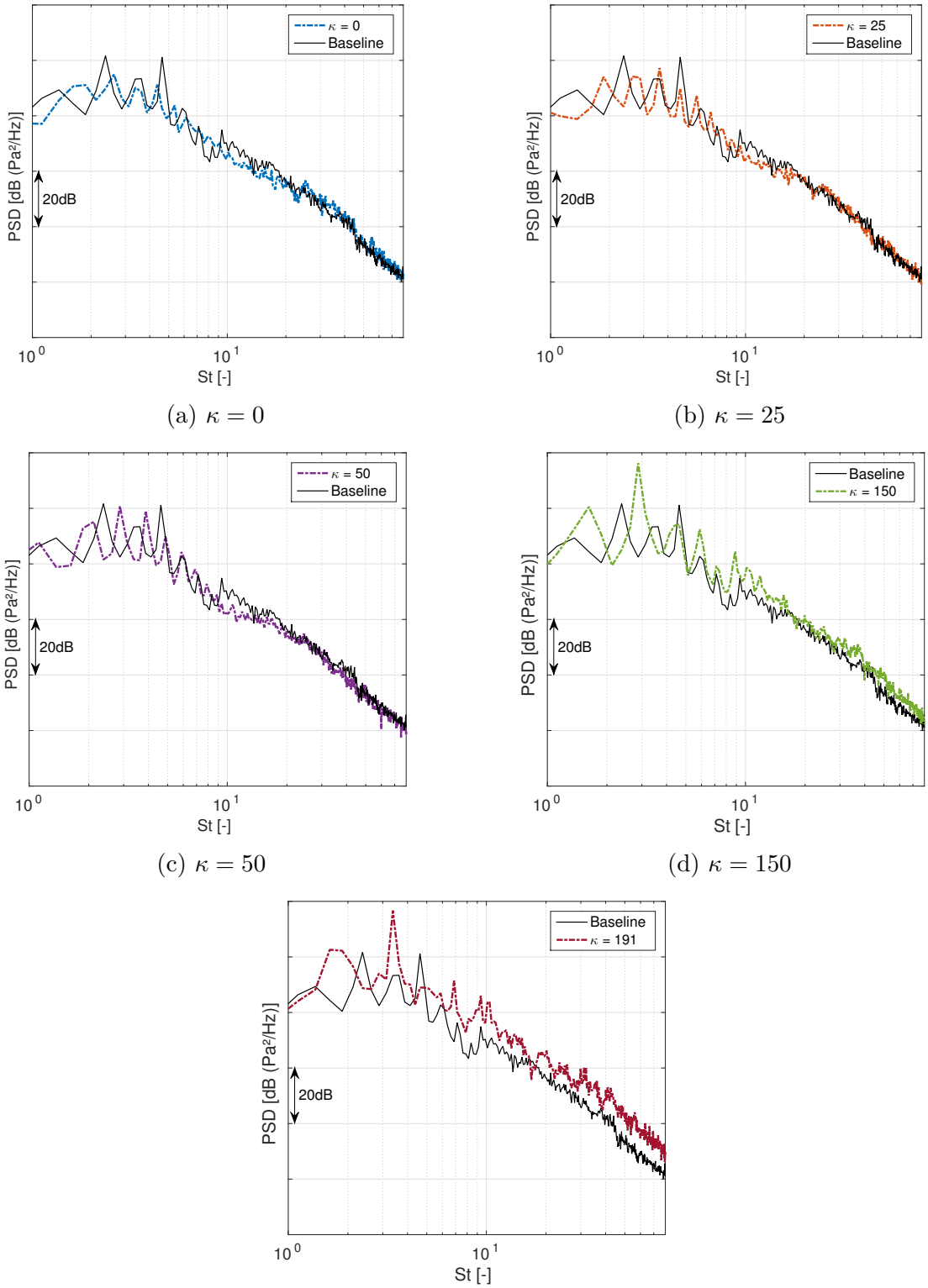

(a) $\kappa = 0$ (b) $\kappa = 25$

(c) $\kappa = 50$ (d) $\kappa = 150$

(e) $\kappa = 191$

Reference: Author

Configuration $\kappa 0$ reduced the mean discrete mid-frequency tones up to 10 dB and 6 dB the broadband noise until $St = 18$. Configuration $\kappa 25$ reduced the tonal noise up to

7 dB and 5 dB the broadband noise until $St = 18$. Configuration $\kappa 50$ did not reduce the tonal noise significantly and, as in previous configurations, reduced in 6 dB the broadband noise until $St = 18$. Configurations $\kappa 150$ increases up 15 dB the mid frequency tones and in 4 dB the broadband noise until $St = 18$ and $\kappa 191$ significantly increased (up to 15 dB) the discrete tones and in 9 dB the broadband noise in all frequency range. Furthermore, all configurations modified the mid-frequency tones' Strouhal number, due to the differences in the shear-layer length and the acoustic path. Table 6 shows the Overall Sound Pressure Level (OSPL) integrated between $St = 1.8$ to 50; an 11 dB difference was detected between confs. $\kappa 191$ and $\kappa 0$. The Maximum peak showed a 6.7 dB reduction in conf. $\kappa 0$ and 14 dB increase in conf. $\kappa 191$ in the baseline configuration.

Table 6 also shows the main shear layer (MSL) length from the cusp to the reattachment point and the distance from the leading edge to the reattachment point for all κ configurations. Both distances were divided by the slat chord. Longer distances between the trailing edge and the reattachment point cause lower tonal noise and longer distances of the main shear layer reduce the broadband noise. Configurations of cusp length shorter than that of the baseline show a shear-layer trajectory with a nearly constant curvature, except in the reattachment region. However, the trajectory of the shear layer of configurations $\kappa 150$ and $\kappa 191$ exhibits an almost-perfect circle until the middle and, then, becomes almost straight until the reattachment point, as shown in Figure 61.

Table 6: OSPL for acoustic fluctuations between St 1.8 and 50 and shear layer characteristics of different κ

Conf.	Δ OSPL [dB]	Maximum peak [dB]	MSL length	Reattachment
$\kappa 0$	-2.7	-6.7	0.820	0.926
$\kappa 25$	-1.5	-4.43	0.80	0.934
$\kappa 50$	-0.8	-1	0.73	0.946
Baseline	0	0	0.64	0.953
$\kappa 150$	6.5	14.6	0.59	0.966
$\kappa 191$	7.9	15	0.58	0.979

Reference: Author

Figure 62 displays the RMS wall pressure coefficient distribution inside the slat cove for confs. $\kappa 0$, $\kappa 191$ and baseline. All configurations exhibited a peak at $X/c_s \approx 0.95$, associated with the reattachment of the main shear layer on the upper surface of the slat. Configuration $\kappa 191$ showed higher values of RMS wall pressure in the slat cove and a significant difference in the peak region associated with the increase in the mid-frequency tonal noise.

The analysis of the difference between the velocities of the mixing layer can be related to the turbulence and instability in the flow along the slat cove. Figure 63 shows the velocity magnitude in function of the streamwise position near the cusp ($s/SL = 0.1$)

Figure 61: MSL trajectory

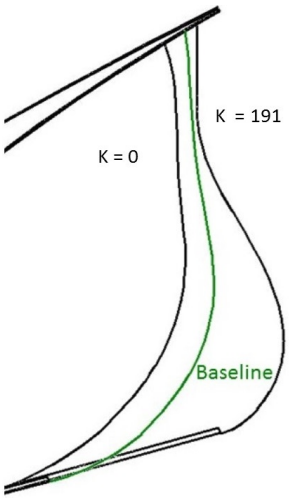

Reference: Author

Figure 62: c_p' distribution inside the slat cove of different κ

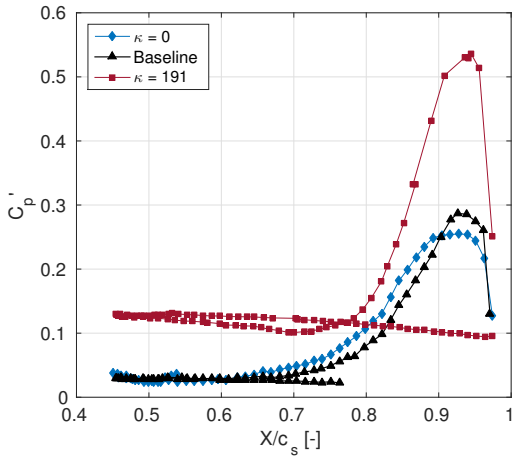

Reference: Author

and its derivative in the streamwise direction for confs. $\kappa 0$, $\kappa 191$ and baseline. The zero point in the X-axis in both graphs refers to the MSL location. Configuration $\kappa 191$ shows the major difference between the velocities that, combined with a shorter distance traveled by the MSL, generate a more intense instability in the flow, hence, an increment in the turbulence after the reattachment and broadband noise.

Figure 63: Tangential velocity profile (a) and its derivative in the streamwise direction (b) at $\frac{s}{SL} = 0.1$ of different κ

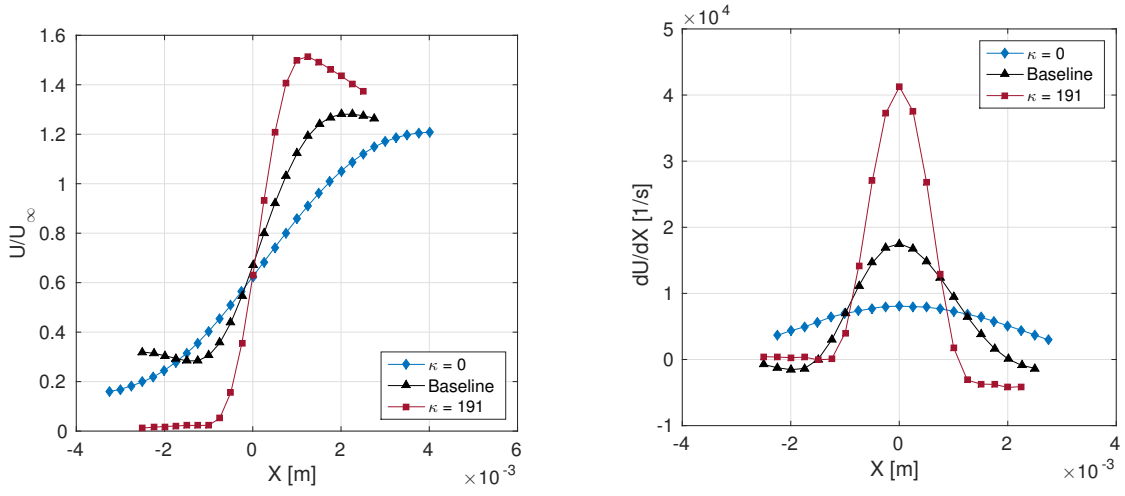

(a) (b)

Reference: Author

Figure 64 shows the instantaneous turbulent kinetic energy (TKE) of configurations $\kappa 0$, $\kappa 191$ and baseline. Configuration $\kappa 0$ shows less turbulence and the vortices are dissipated along the shear layer, whereas the baseline and $\kappa 191$ configurations exhibit an

MSL trajectory with constant and high TKE, i. e., the flow is continuously supplied with turbulence energy.

Figure 64: Instantaneous dimensional-less Turbulent kinetic energy of different κ

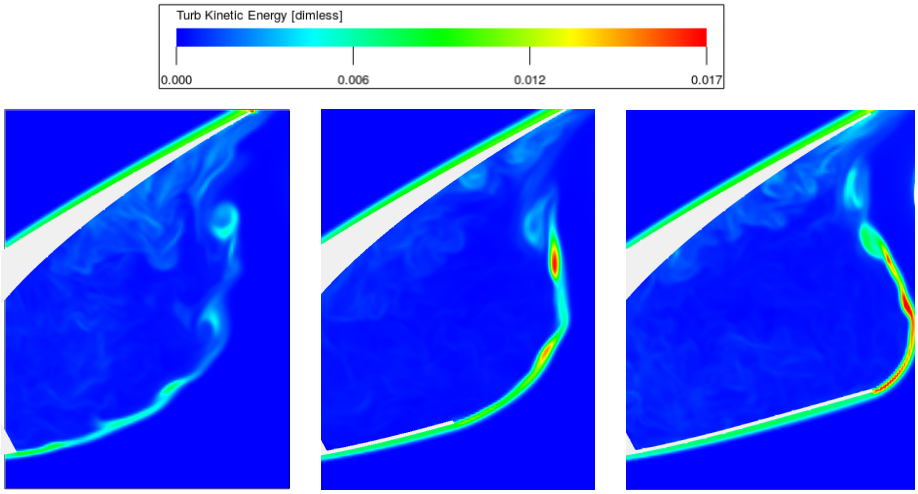

a) κ0 b) Baseline c) κ191

Reference: Author

Figure 65 displays the PSD at midspan in the reattachment point, trailing edge and cusp of the same configurations. The cusp point shows the least PSD at all frequencies in all configurations, hereby, the mid-frequency peaks are more visible on the cusp than on the other points.

Figure 65: PSD at slat surface at midspan of different κ

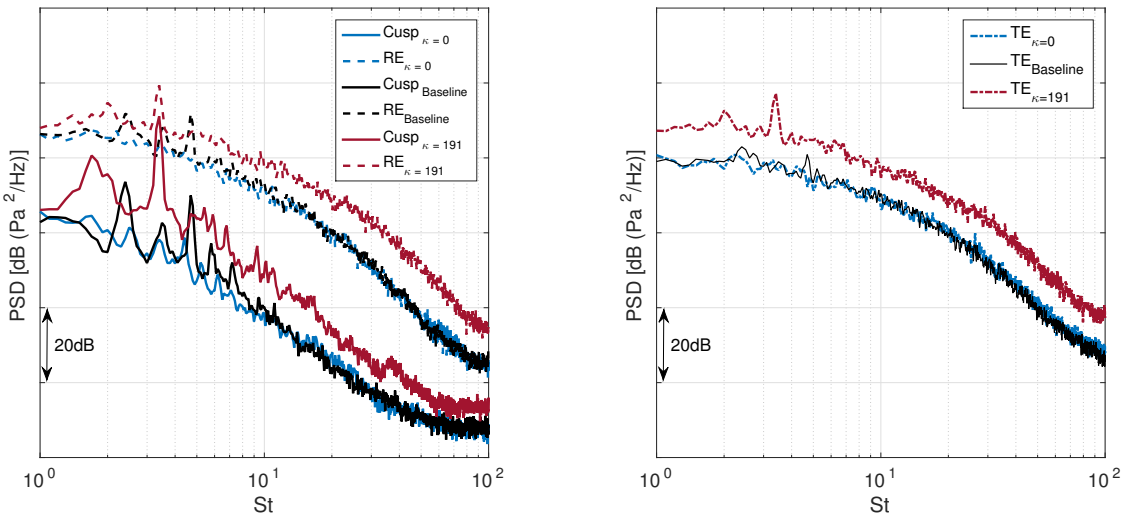

(a) Reattachment and cusp (b) Trailing edge

Reference: Author

The spectra in the trailing edge and reattachment are governed by the turbulence in those regions, however, the baseline and κ191 configurations still show the peaks in

both points, i. e., the noise level is higher than the turbulence level. The reduction in the tonal components in conf. $\kappa 0$ is probably due to the loop between the trailing edge and the cusp is weakly formed due to the extremely large main shear layer trajectory and the dissipation of turbulence.

4.3.1 Experimental results

Configurations $\kappa 0$ and $\kappa 150$ were tested in the wind tunnel for validating the numerical results and checking whether the simulations could identify the tendencies in the noise generation. Such configurations were chosen because they showed contrary results, i.e., conf. $\kappa 0$ reduced the noise, whereas conf. $\kappa 150$ increased it. Furthermore, they can be attached to the WME with the same brackets of the baseline model. Configuration $\kappa 191$ was not tested because the longer cusp is more difficult to prototype and could cause structural problems.

The slat models of both configurations were 3D-printed in Acrylonitrile Butadiene Styrene (ABS) material and reinforced by an aluminum stringer throughout the span, as shown in Figure 66 (a). A zig-zag trip located in the same position of the baseline was also set for each configuration. Figure 66 (b) displays the $\kappa 0$ configuration mounted in the wind tunnel and attached to the WME through four steel brackets, similarly to the baseline configuration.

Figure 66: 3D-printed slats

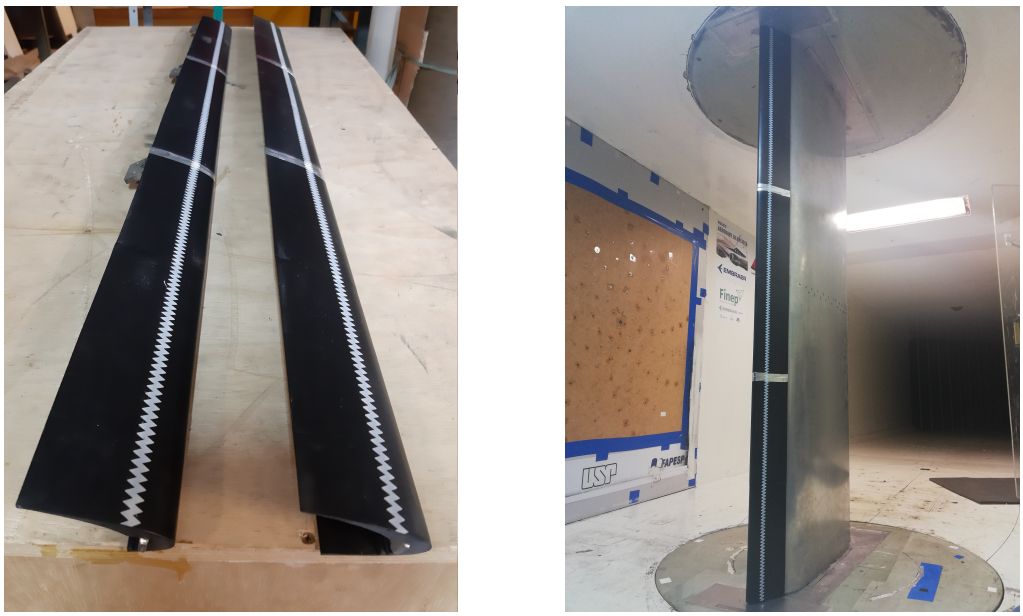

(a) Prototyped models and zig-zag trip (b) $\kappa 0$ model mounted in the wind tunnel

Reference: Author

Figure 67 shows the comparison between the numerical and experimental results of the pressure coefficient distribution of confs. $\kappa 0$ and $\kappa 150$. As in the baseline configuration,

the wing main element exhibited a 4^o shift in the angle of attack, therefore, the comparisons are shown at 0^o and 4^o AoA in the numerical and experimental cases, respectively. Both methodologies exhibited the same behavior between the configurations, i.e., conf. $\kappa 0$ reduced the suction peak of the WME in comparison with the baseline configuration, whereas conf. $\kappa 150$ increased it. The numerical simulations did not detect changes in the flap, however, the experimental results showed conf. $\kappa 0$ also decreased its suction peak and conf. $\kappa 150$ increased it.

Figure 67: Comparisons of pressure coefficient distributions

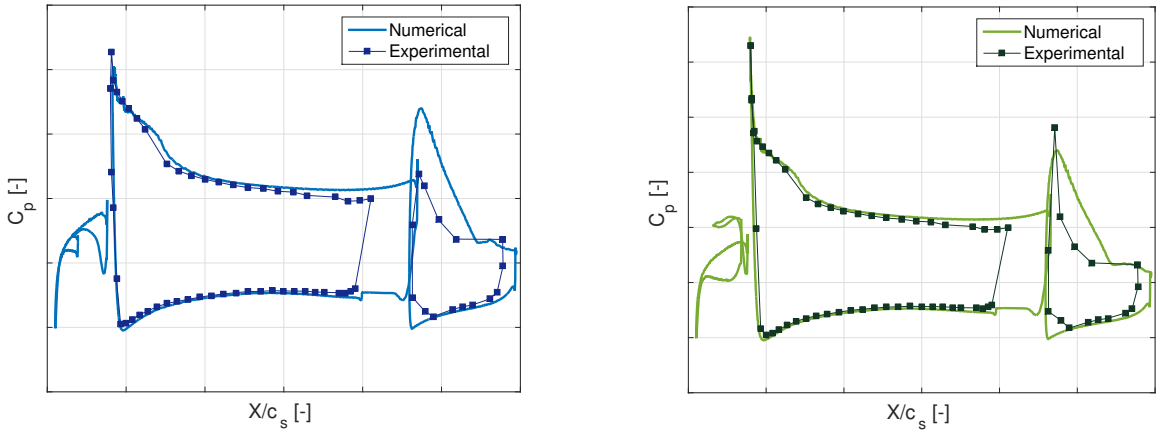

(a) $\kappa = 0$ (b) $\kappa = 150$

Reference: Author

Figure 68 shows the spectra of both configurations obtained numerically and experimentally, experimentally it is calculated through the beamforming CLEAN SC and numerically the noise was propagated to the central micrphone of the array. The results are in agreement up $St = 40$, above which the numerical results exhibited a larger drop of the PSD in function of St number, as in the baseline configuration. Conf. $\kappa 0$ showed a better comparison between the methodologies than conf. $\kappa 150$, since it generates more unsteadiness loads in the shear-layer, and probably a more refined grid or more acquisition time is necessary for more accurate results. Figure 69 shows the behavior of the configurations was the same as those in the experiments and simulations, i. e., conf. $\kappa 0$ reduced the mid-frequency tones, whereas conf. $\kappa 150$ increased the second peak and reduced the others and increased the broadband noise.

Figure 69 also shows the noise obtained experimentally at 4^o AoA. For such an angle of attack, conf. $\kappa 0$ reduced the noise more than at 0^0 AoA in all frequency range. Although conf. $\kappa 150$ still increases the broadband noise and the second peak, the difference between this configuration and the baseline is lower than in 0^o AoA. As the angle of attack increases, conf. $\kappa 0$ exerts a stronger effect, whereas conf. $\kappa 150$ reduces it. it is important to note that at $AoA = 4^o$. conf. $\kappa 0$ produces less noise than the wind tunnel in 4-30 Strouhal

range. For comparisons of only experimental results, a ROI of throughout all span was used.

Figure 68: Comparisons of far-field noise

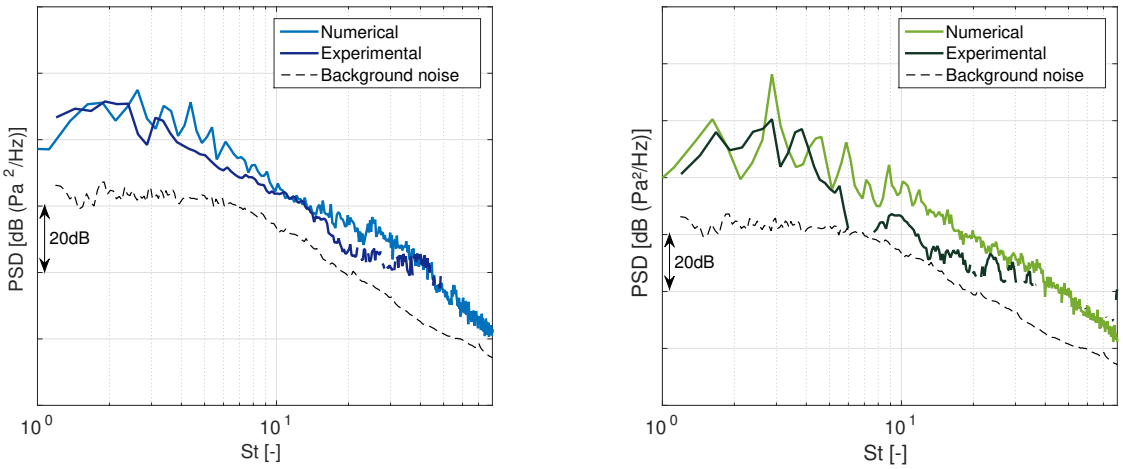

(a) $\kappa = 0$ (b) $\kappa = 150$

Reference: Author

Figure 69: PSD obtained experimentally at different AoA.

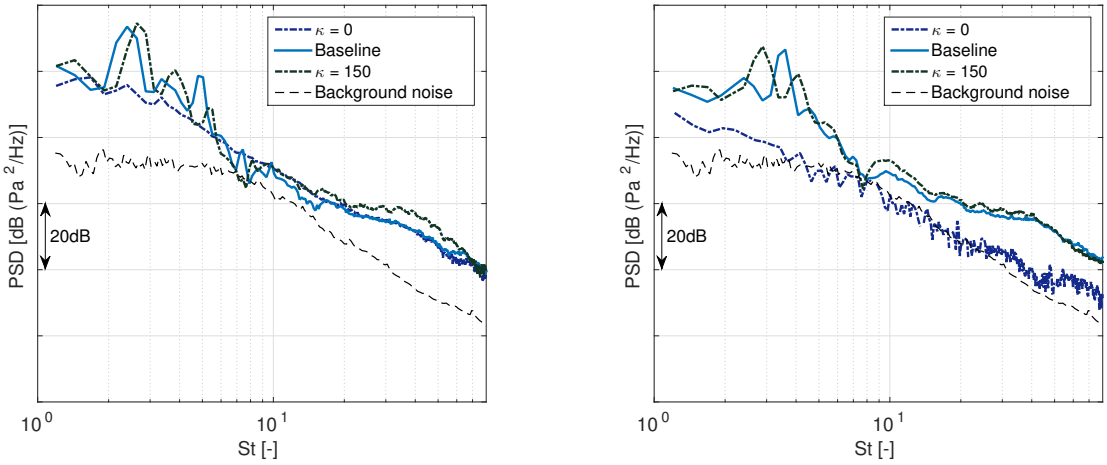

(a) $AoA = 0^0$ (b) $AoA = 4^0$

Reference: Author

Despite the difference between numerical and experimental results, both aerodynamic and aeroacoustic results exhibited the same pattern between the configurations in both techniques. Therefore, we can conclude the numerical simulations can detect the effect of the slat modifications on the aeroacoustics and aerodynamics of the wing.

4.4 Effect of the trailing edge angle

Five modifications in the trailing edge angle (α) were simulated towards the understanding of their relationship with the slat noise. Similarly to variations in the cusp length, they did not affect the lift coefficient of the wing (Table 7), since all variations were lower than 1.5%. The drag coefficient increased, as the angle of the trailing edge increased, and reached a 4.54% increment in conf. $\alpha 20$. No differences in the pressure coefficient distribution were detected among the configurations (Figure 70).

Table 7: Lift and drag coefficients of different α

Conf.	C_L variation [%]	C_D Variation [%]
$\alpha - 5$	0.69	0.96
Baseline	0	0
$\alpha 5$	0.72	0.98
$\alpha 10$	1.31	2.04
$\alpha 15$	1.412	1.18
$\alpha 20$	1.32	4.54

Reference: Author

Figure 70: Pressure coefficient distribution at midspan of different α

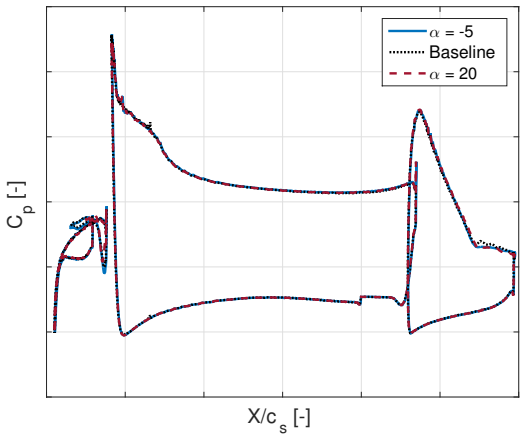

Reference: Author

Figure 71 shows the PSD versus Strouhal number for all α configurations. Smaller angles of trailing edge increase the mid-frequency tonal noise, due to they preserves the coherent structures. Conversely, larger angles of trailing edge reduce the mid-frequency tonal noise and increase the broadband noise, once a thick trailing edge fills part of the slat cove and reduces the cavity resonance. The increment in the broadband noise is related to the increment in the turbulence in the trailing edge region.

Figure 71: PSD of different α

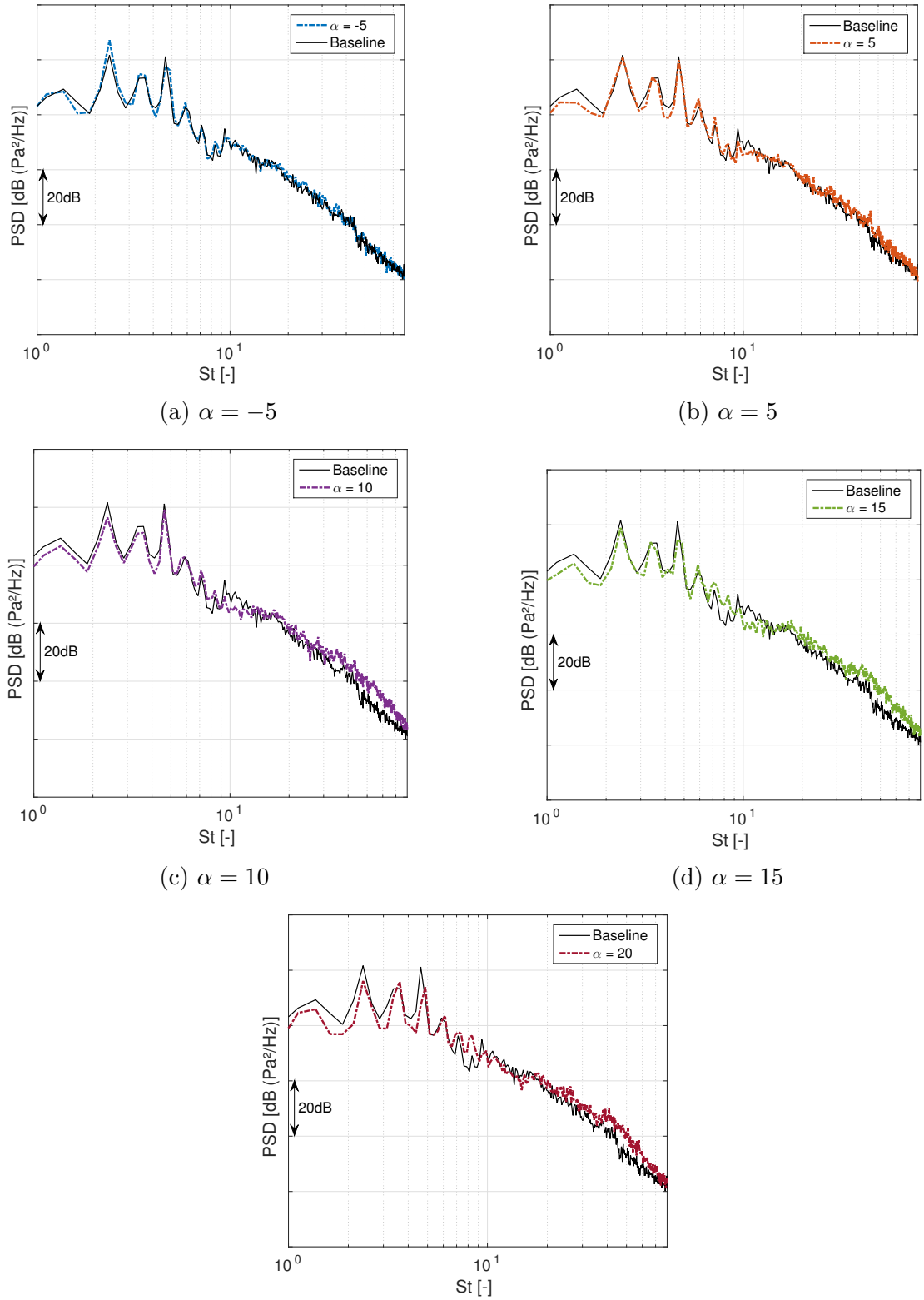

(a) $\alpha = -5$

(b) $\alpha = 5$

(c) $\alpha = 10$

(d) $\alpha = 15$

(e) $\alpha = 20$

Reference: Author

The configuration of the 20^0 trailing edge angle ($\alpha 20$) reduced the first and third

peaks in 5 dB and 8 dB, respectively, and increased approximately 5 dB the broadband noise in all Strohual numbers above 17, in comparison with the baseline configuration. On the other hand, conf. $\alpha - 5$ increased 5 dB the first peak and 3 dB the fourth and fifth, and did not affect the broadband noise.

The OSPL integrated from $St = 1.8$ to 50 and the maximum peak for each configuration are shown in Table 8. It decreases as the angle of the trailing edge increases. Furthermore, conf. $\alpha - 5$ increases the maximum peak in 6 dB, whereas conf. $\alpha 20$ reduces the maximum peak by 5 dB in comparison with the baseline configuration. Table 8 also shows the MSL length from the cusp to the reattachment and the distance between the leading edge and the reattachment point (divided by the slat chord) of each trailing edge configuration. As in variations in the angle of attack and cusp length, larger distances between the trailing edge and the reattachment point decrease the tonal noise levels and shorter distances of the MSL cause stronger broadband noise. No differences were found in the MSL trajectory among the configurations.

Table 8: OSPL for acoustic fluctuations between St 1.8 and 50 and shear layer characteristics of different α

Conf.	Δ OSPL [dB]	Maximum peak [dB]	MSL length	Reattachment
$\alpha - 5$	1.5	6.5	0.65	0.967
Baseline	0	0	0.65	0.953
$\alpha 5$	-0.5	0	0.64	0.940
$\alpha 10$	-1.7	-1.7	0.62	0.939
$\alpha 15$	-1.1	-2.1	0.61	0.927
$\alpha 20$	-2.2	-4.6	0.59	0.917

Reference: Author

The RMS wall pressure in the slat cove for confs. $\alpha - 5$, $\alpha 20$ and baseline is shown in Figure 72. Configuration $\alpha 20$ exhibits a lowest c'_p peak, associated with the lower mid-frequency noise radiated.

Figure 73 displays the velocity profile in the streamwise direction on the main shear layer near the cusp ($s/SL = 0.1$) for confs. $\alpha - 5$, $\alpha 20$ and baseline. Configuration $\alpha 20$ showed a larger difference between the velocities through the mixing shear layer, which increases the broadband noise in conjunction with a shorter MSL length, as in conf. $\kappa 191$. The instantaneous TKE in both shear layer and trailing edge region of conf. $\alpha 20$ is greater than that of the other configurations (Figure 74).

Figure 75 shows the PSD at the trailing edge, reattachment, and cusp of configurations $\alpha - 5$, $\alpha 20$ and baseline at midspan. Such configurations did not show significant differences in the spectra in the trailing edge and reattachment. However, some differences in the cusp spectra were detected for the different configurations. As calculated by the

Figure 72: c_p' distribution inside the slat cove of different α

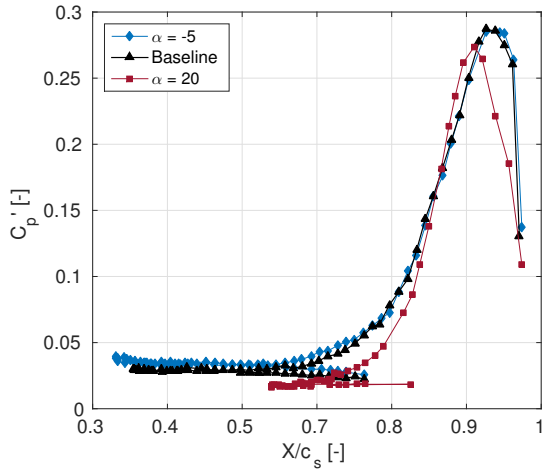

Reference: Author

Figure 73: Tangential velocity profile (a) and its derivative in streamwise direction (b) at $\frac{s}{SL} = 0.1$ for different α

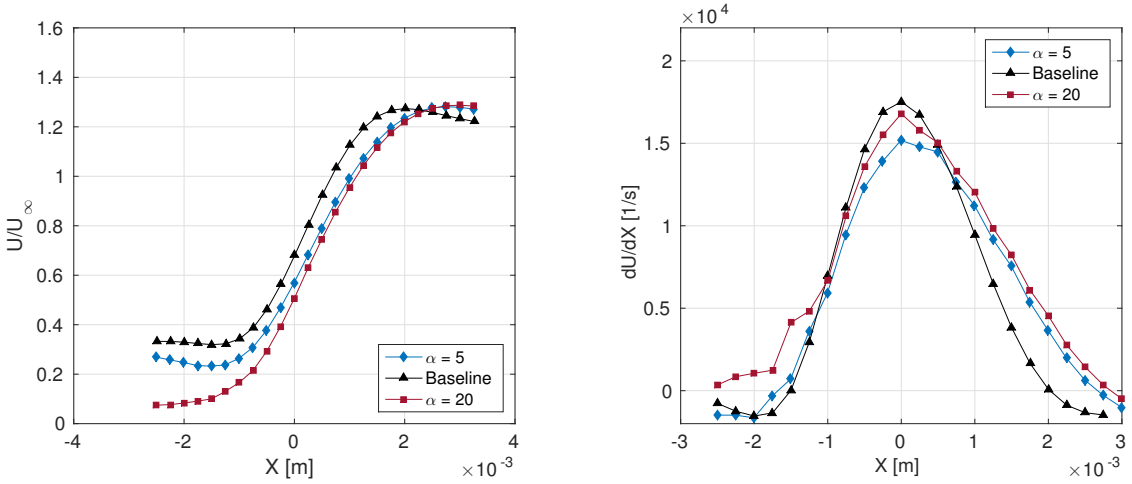

(a) (b)

Reference: Author

FW-H analogy, the spectra on the cusp show conf. $\alpha - 5$ increases the mid-frequency peaks, whereas conf. $\alpha 20$ reduces them and increases the broadband noise.

Figure 74: Instantaneous TKE of different α

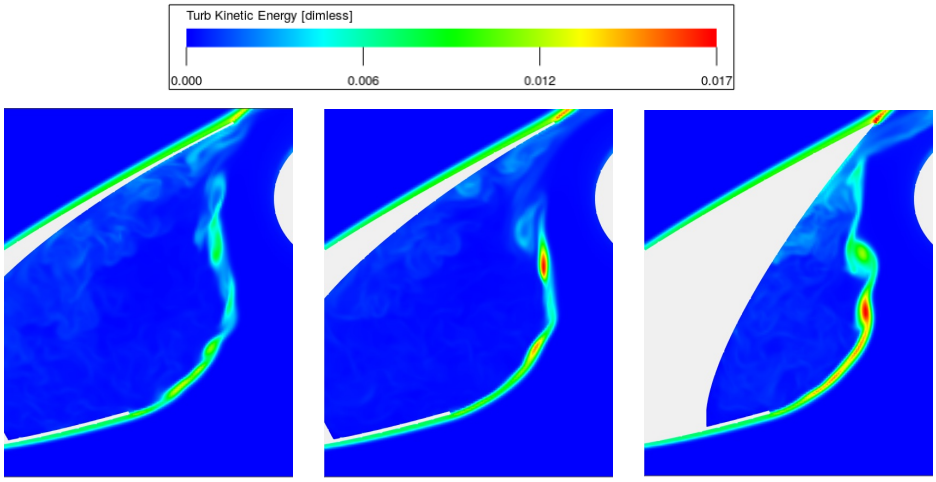

a) $\alpha - 5$ b) Baseline c) $\alpha 20$

Reference: Author

Figure 75: PSD at slat surface at midspan of different α

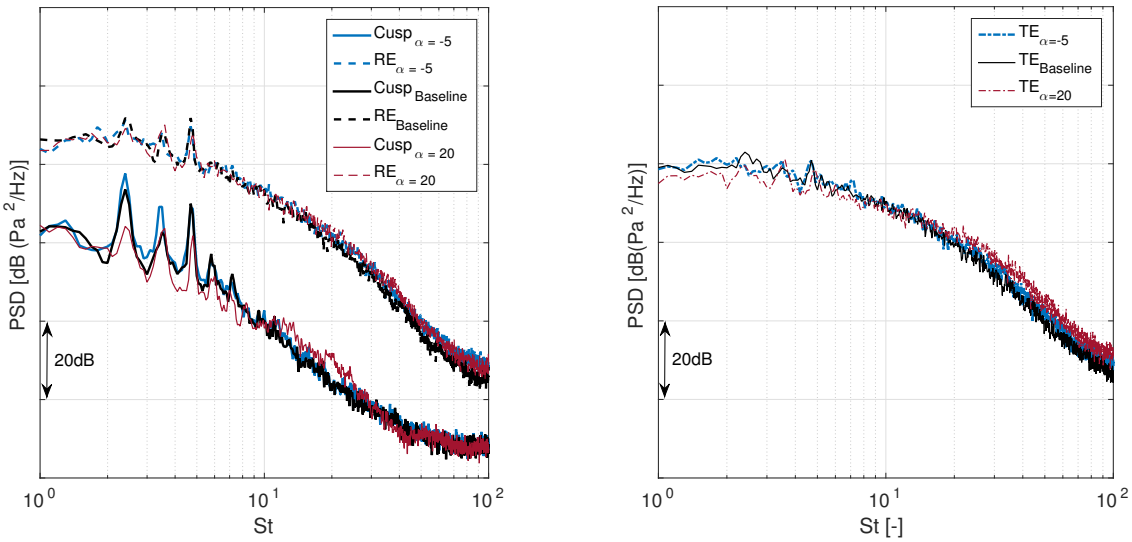

(a) Reattachment and cusp (b) Trailing edge

Reference: Author

4.5 Effect of the trailing edge length

The geometry of the different trailing edge length (ψ) modifications was designed as follows. The region between the reattachment point and trailing edge is mostly straight, and this "straight line" is extended or shortened in each case. Consequently, the leading edge of the slat is moved forward or backward for maintaining the same gap and overlap, as in previous modifications. The calculation of the percentage of the trailing edge length variation is based on the straight part of the baseline configuration. The procedure for the

obtaining of conf. ψ150 is shown in Figure 76, where the black and continuous line refers to the final configuration and the red and dashed line denotes the baseline configuration. The figure also displays the value in milimeters of the trailing edge length and the geometry that are taken as the baseline. Although the slat chord is modified in each case, the chord of the baseline is used for all dimension-less calculations. Table 9 shows the ratio between the slat chord of each modification and the slat chord of the baseline configuration.

Modifications in the slat trailing edge length did not cause significant variations in the lift and drag coefficients (See Table 9). The 2.5% increment in the drag coefficient of conf. ψ250 is due to the increment in the skin friction, since the area and slat wake are larger. Another important characteristic of such a configuration is the center of the entrapped eddy vortex is located downstream the slat cusp, as shown in Figure 77. Although conf. ψ75 increases the suction peak of the WME (Figure 78), the slat area is smaller, therefore, conf. ψ250 showed a greater increment in the lift coefficient. Furthermore, the suction peak of the wing main element increases as the trailing edge length decreases.

Table 9: Lift and drag coefficients of different ψ

Conf.	chord	C_L variation [%]	C_D Variation [%]
ψ75	0.946	0.85	0.62
Baseline	1	0	0
ψ150	1.032	0.74	-1.94
ψ250	1.14	1.25	2.46

Reference: Author

Figure 76: Design of configuration ψ150

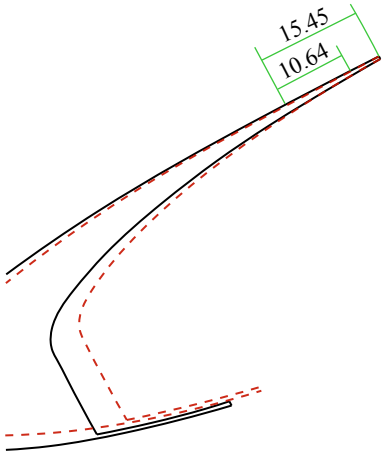

Reference: Author

Figure 77: Streamlines in the slat cove of configuration ψ250

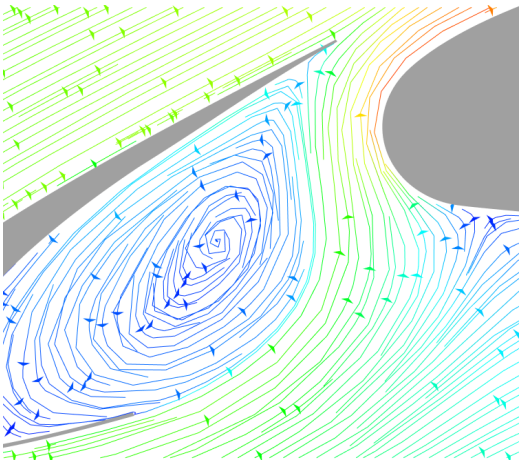

Reference: Author

The effect of the slat trailing edge length on the far-field noise is shown in Figure 79. The frequencies of mid-frequency tones were modified in all configurations. According to the equation established by Terracol, Manoha and Lemoine (2015) (Equation 4.4), the

Figure 78: Pressure coefficient distribution at midspan of different ψ

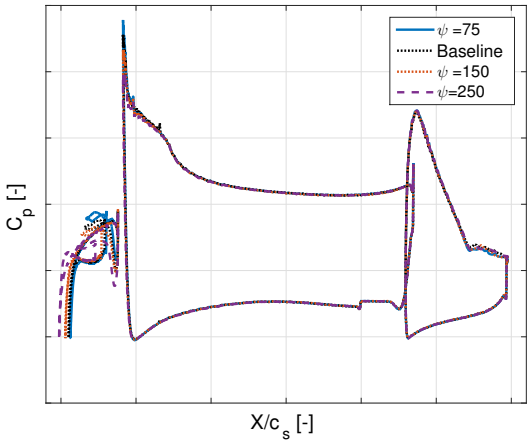

Reference: Author

frequency of each tone, in confs. $\psi 250$ and $\psi 150$, is reduced because the acoustic path (L_a in the equation), i.e., the distance between the reattachment and cusp, is increased, whereas in conf. $\psi 75$, the frequency is increased because L_a is reduced. This parameter yielded interesting results, since it highly influences the tones formation. Although in all cases the maximum peak was increased, only one peak reached higher values - the others were reduced.

Configuration $\psi 75$ exhibited the highest peak (8 dB above the baseline configuration), however, it significantly reduced the first and third peaks and increased 2.1 dB the OSPL integrated between $St = 1.8$ and 50. Configuration $\psi 150$ increased the first peak and reduced the others and the broadband noise in 1 dB in the $St = 10$ to 40 range. Finally, conf. $\psi 250$ also increased the first peak and reduced the others and the broadband noise in 4 dB up $St = 40$, which resulted in a 2.4 dB reduction in the OSPL.

As the location of the leading edge is different for each ψ modification, the measurements between the leading edge and the reattachment revealed higher fluctuations between each configuration than in the other modifications (Table 10). Configuration $\psi 250$ exhibited a value higher than 1 because the chord of this configuration is longer than the baseline's. Although no configuration reduced the mid-frequency tones, conf. $\psi 75$ showed a significant reduction in the first and third peaks, which might also be associated with a longer distance between the slat trailing edge and reattachment point.

As in previous variations, the broadband noise is reduced in conf. $\psi 250$ due to a larger trajectory of the main shear-layer (Table 10) and a smaller difference between the velocities through the mixing layer (Figure 80). Such relations are also present in conf. $\psi 150$.

Figure 79: PSD of different ψ

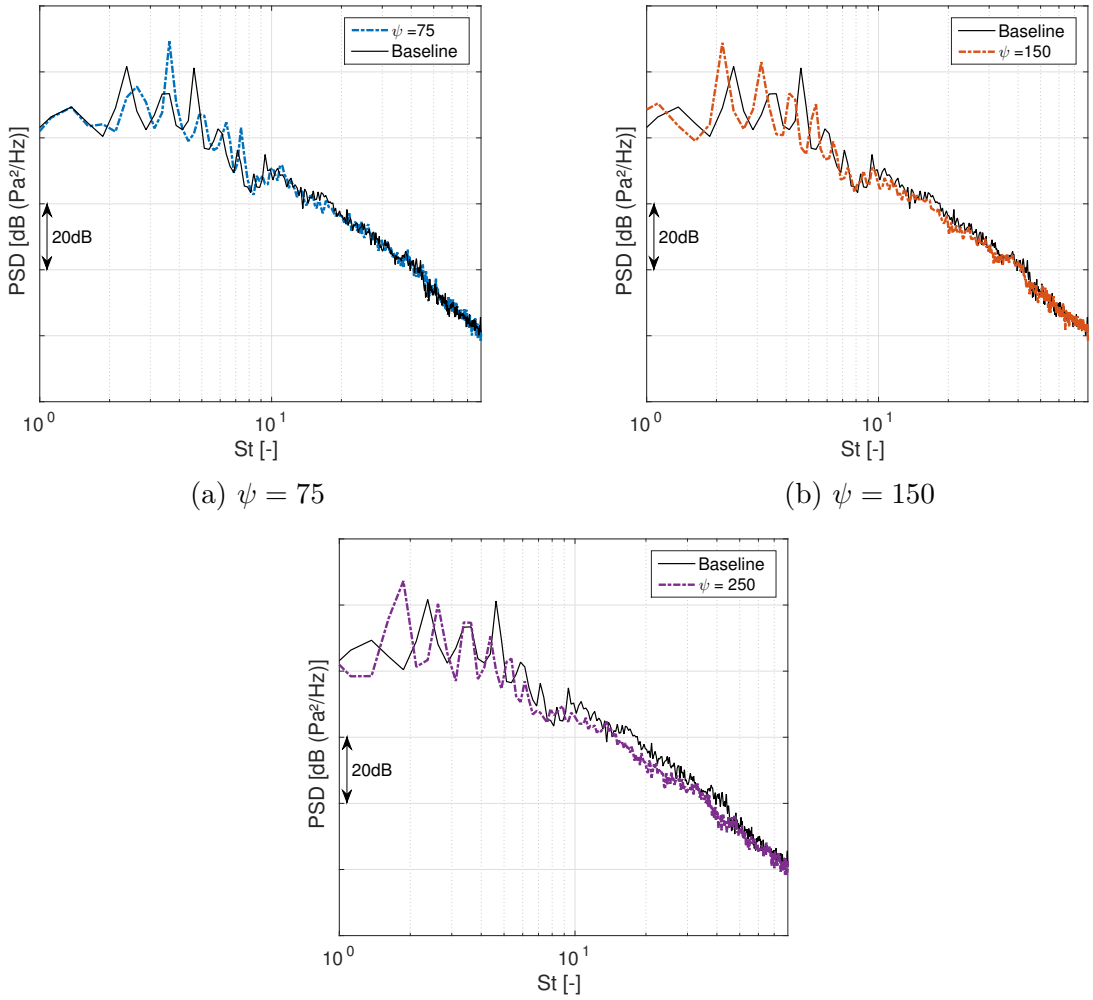

(a) $\psi = 75$ (b) $\psi = 150$

(e) $\psi = 250$

Reference: Author

Table 10: OSPL for acoustic fluctuations between St 1.8 and 50 and shear layer characteristics of different ψ

Conf.	Δ OSPL [dB]	Maximum peak [dB]	MSL length	Reattachment
ψ75	2.1	8	0.61	0.902
Baseline	0	0	0.64	0.953
ψ150	0.9	7.8	0.68	0.977
ψ250	-2.4	6.3	0.79	1.08

Reference: Author

The power spectral density of pressure fluctuations in the cusp of different ψ configurations (Figure 81) did not show other differences than those observed in far-field spectra. However, the lower values exhibited by conf. ψ250 in the reattachment and trailing edge points are related to the reduction in broadband noise and turbulence. Similarly, the peak of the RMS pressure coefficient value (Figure 82) in conf. ψ250 was reduced.

Figure 80: Tangential velocity profile (a) and its derivative in the streamwise direction (b) at $\frac{s}{SL} = 0.1$ of different ψ

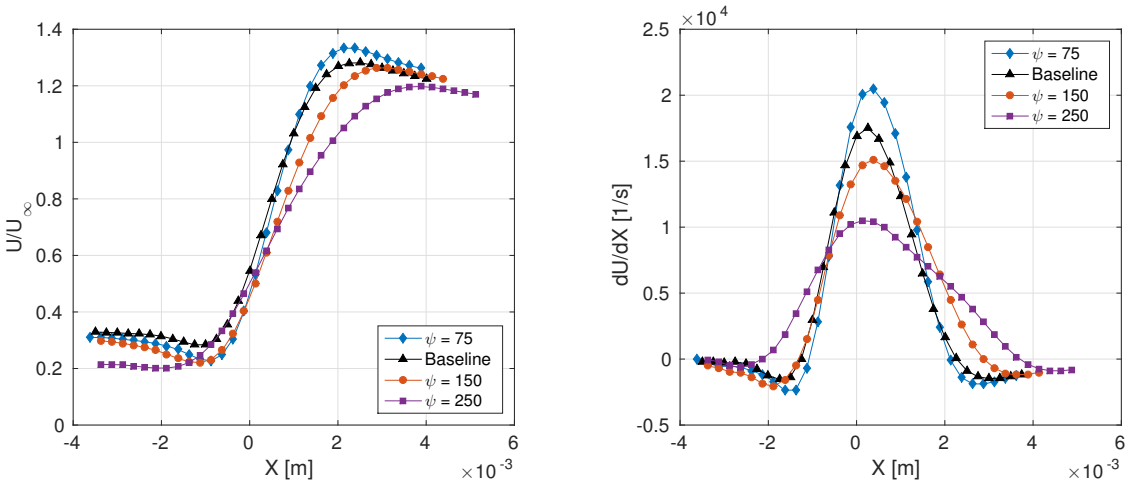

(a) (b)

Reference: Author

Figure 81: PSD at slat surface at midspan of different ψ

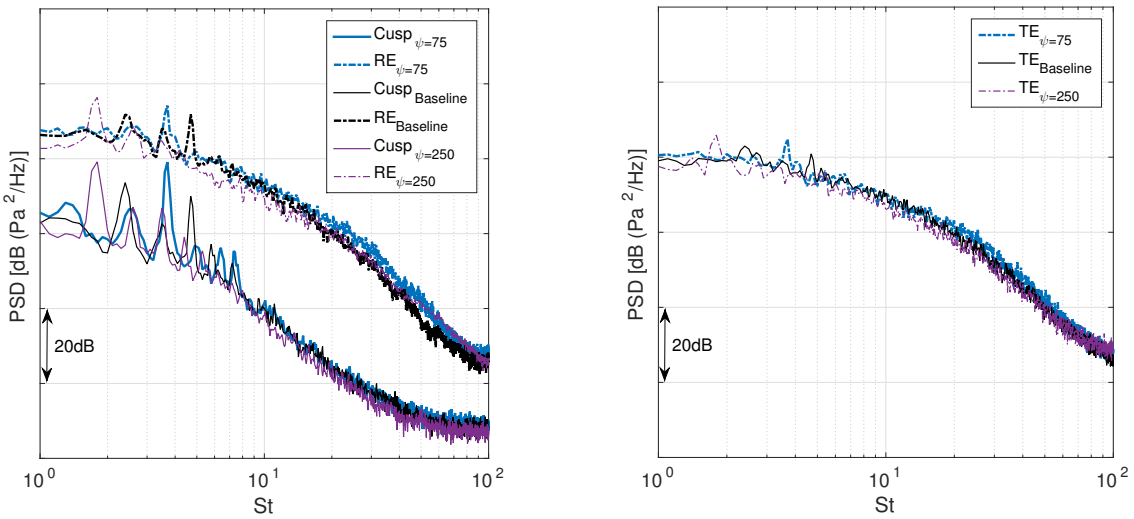

(a) Reattachment and cusp (b) Trailing edge

Reference: Author

4.6 Effect of the trailing edge thickness

A more refined mesh was used in the analysis of the effect of trailing edge thickness (χ) for capturing its variation, since the original mesh was coarse in the trailing edge in comparison with its thickness ($\delta x_{min} = 1.44$ baseline's trailing edge thickness). Therefore, only two modifications were introduced.

The slat trailing edge thickness did not influence the aerodynamics of the wing, since the lift and drag coefficients (Table 11) and the pressure coefficient distribution

Figure 82: c_p' distribution inside the slat cove of different ψ

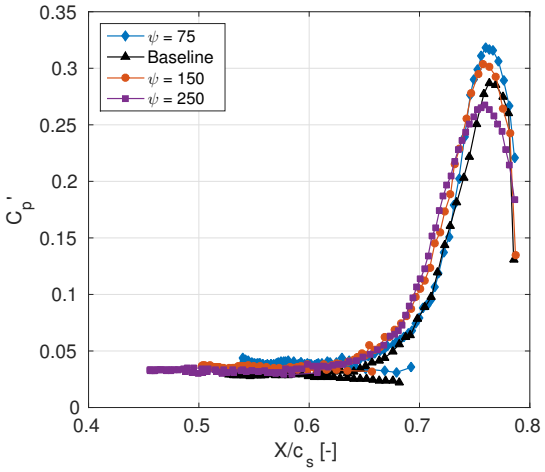

Reference: Author

(Figure 83) were constant for all cases of χ. The reattachment point was also constant for all configurations (Table 11), which can be associated with no variations in the mid-frequency tones in far-field spectra (Figure 84).

Table 11: Lift and drag coefficients and reattachment of different χ

Conf.	C_L variation [%]	C_D Variation [%]	Reattachment
χ50	-0.0066	1.40	0.949
Baseline	0	0	0.943
χ400	0.24	1.55	0.941

Reference: Author

Initially, variations in the trailing edge thickness were simulated with the same mesh of previous cases. However, as shown in Figure 84, the far-field spectra did not exhibit any variation for the different trailing edge thickness configurations because the minimum element size on the original mesh (0.25 mm) was greater than the trailing edge thickness of the baseline configuration. The simulation with this mesh did not detect the changes in the geometry of the trailing edge.

Consequently, three refinement regions (VR) were created in the trailing edge region and the minimum element size was reduced 8 times (for keeping the same element size of all cases in the FW-H measurement region). The new minimum element size was 0.03125 mm, which demanded a time discretization of 4.9×10^6 timesteps for 0.25 s physical time. Figure 85 shows the results of the far-field spectra obtained with the new mesh.

Figure 83: Pressure coefficient distribution of different χ

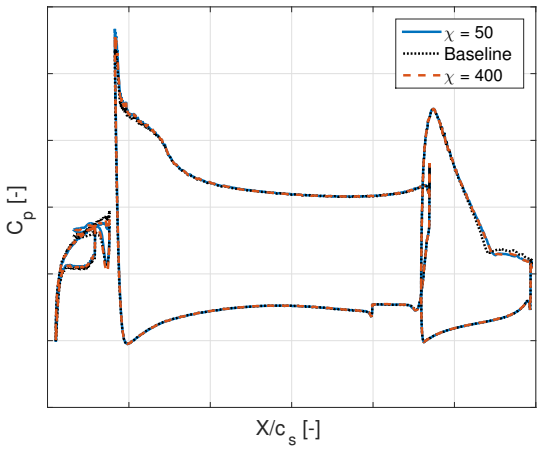

Reference: Author

Figure 84: PSD of different χ configurations. Coarser mesh

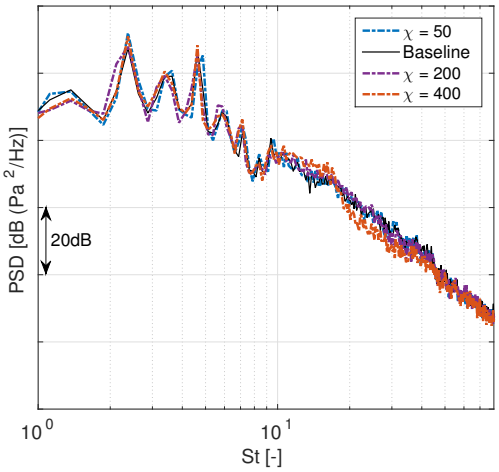

Reference: Author

Figure 85: PSD of different χ

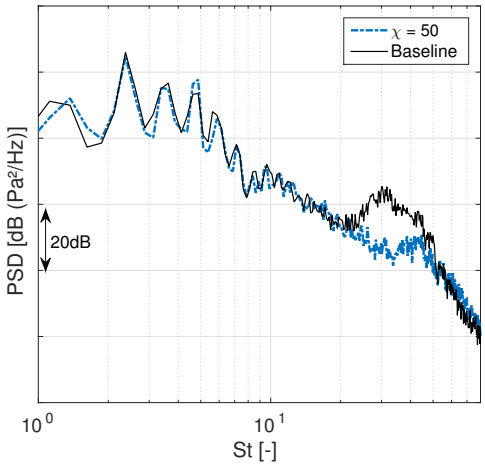

(a) $\chi = 50$

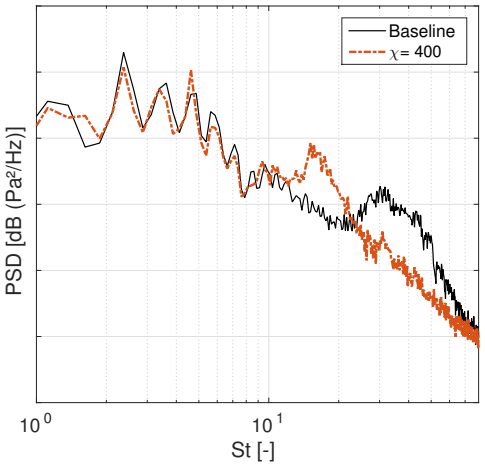

(b) $\chi = 400$

Reference: Author

The three cases (including the baseline configuration) exhibited a hump at high frequency related to the blunt trailing edge (as reported in the literature (IMAMURA et al., 2007)), whose frequency decreases as the trailing edge thickness increases. Before and after the hump, the behavior of the three spectra was the same, i. e., the mid-frequency tones and broadband noise showed no changes and the OSPL was constant among the configurations.

The hump was not present in the previous simulations because of the poor mesh, which was unable to model the vortex shedding behind the slat trailing edge, as obtained and explained by Pagani, Souza and Medeiros (2016). Furthermore, the experiments did not show the high frequency peak, probably because the flow was not laminar in the

trailing edge and the vortex shedding had not been completely formed.

According to Imamura et al. (2007), the hump at high frequency is related to the trailing edge thickness and the dominant frequency is consistent with the vortex shedding frequency behind the slat. Such vortices are governed by the Karman vortex, which became a dipole of a specific frequency, represented by a single peak. Figure 86 shows the vortex shedding process behind the trailing edge of the baseline configuration; $dt = 1.6 \times 10^{-5}$ s. Two vortices are highlighted in the slat trailing edge, i.e., one behind the upper side and the other from the lower side (which is more intense) with 180^o phase shift between them.

Figure 86: Pressure time derivative at the baseline slat trailing edge

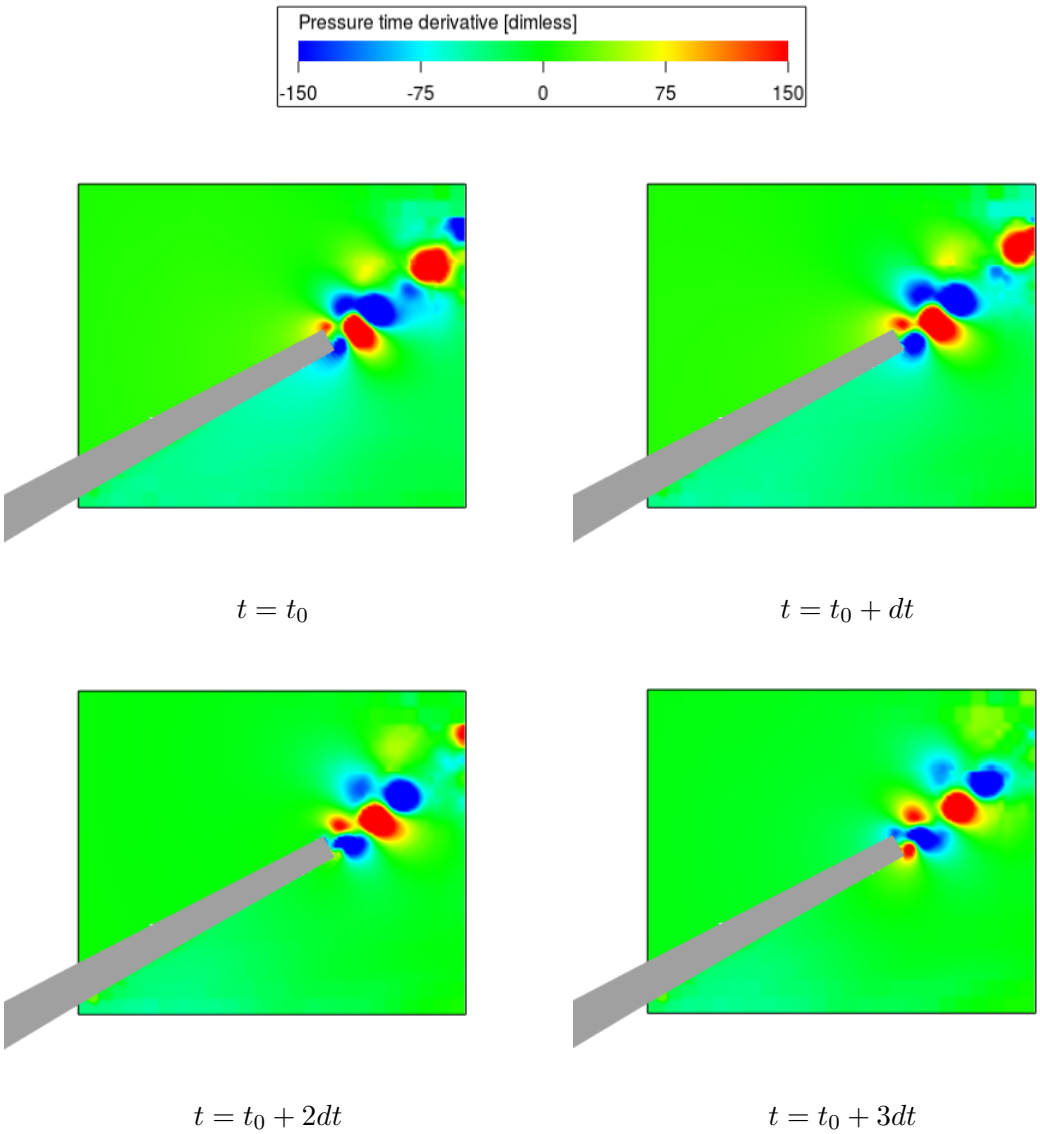

Reference: Author

All configurations exhibited the vortex shedding behind the slat at different frequencies, which were consistent with those observed in the far-field. Table 12 (first column) shows the dominant Strouhal number of the hump observed in the far-field spectra and

the second column shows the dimensional-less frequency (Strohual number) calculated as the inverse of the time between two maximum pressure time derivative in the same wake point. Figure 87 shows the Power Spectral Density in function of the Strouhal number calculated in the lower vortex core of all configurations. All cases exhibited a hump at high frequency, as expected and reported in the literature (DHIRAJ; KAMAL, 2015); however, the Strouhal number of the peak (Table 12 column 3) is not consistent with that observed in the far-field spectra.

Bauer (1961) demonstrated the effective length for the calculation of the Strouhal number of vortex shedding for a thin plate similar to the slat trailing edge is $h = (d + 2\delta^*)$ (d is the plate height - in this case, the slat trailing edge thickness - and δ^* is the ideal Blasius boundary-layer displacement thickness). Therefore, the frequency of the hump in the far-field spectra and the boundary layer displacement thickness were used for the calculation of the Strouhal number of the vortex shedding.

Table 12: St of vortex shedding and slat spectra

Conf.	$St_{far-field}$	$St_{vortex\ shedding}$	$St_{vortex\ core\ spectrum}$
χ50	43.875	43	59.91
Baseline	31.375	31.15	45.73
χ400	16.375	18.25	19.43

Reference: Author

Equation 4.5 obtained the boundary layer displacement thickness; the integration was made in the wake of the slat trailing edge at 0.17 times the baseline trailing edge thickness behind them (Figure 88). The figure also displays each slat trailing edge located according to its wake.

$$\delta^* = \int_{-x}^{x} 1 - \frac{u(y)}{U_\infty} \tag{4.5}$$

Table 13 shows the boundary layer displacement thickness used for the calculation of the Strouhal number (also shown in the table). For all cases, the Strouhal number was close to 0.4, which could be considered characteristic of all slat trailing edge vortex shedding.

Table 13: Boundary layer displacement thickness and characteristic Strouhal number

Conf.	δ^* [mm]	St
χ50	0.75	0.3875
Baseline	1.08	0.4004
χ400	2.074	0.3996

Reference: Author

Figure 87: PSD in the vortex core

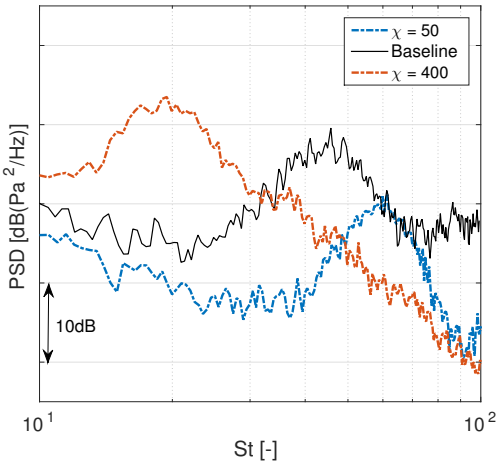

Reference: Author

Figure 88: Slat wake velocity profile

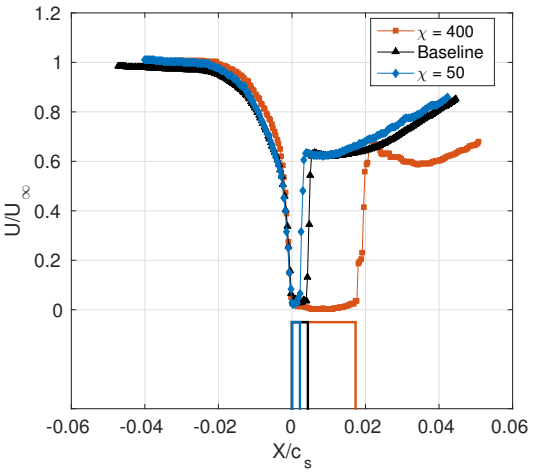

Reference: Author

Imamura et al. (2007) also observed a relation between the high-frequency peak and the dipole created in the trailing edge calculating the PSD in the fluid around the slat trailing edge. Figure 89 shows such PSD around the slat at the far-field hump frequency in each case and at the frequency of first tone. Higher PSD levels were detected behind the tips of the slat trailing edge, which revealed the existence of a dipole of a specific frequency.

Figure 89: PSD contours around the slat trailing edge

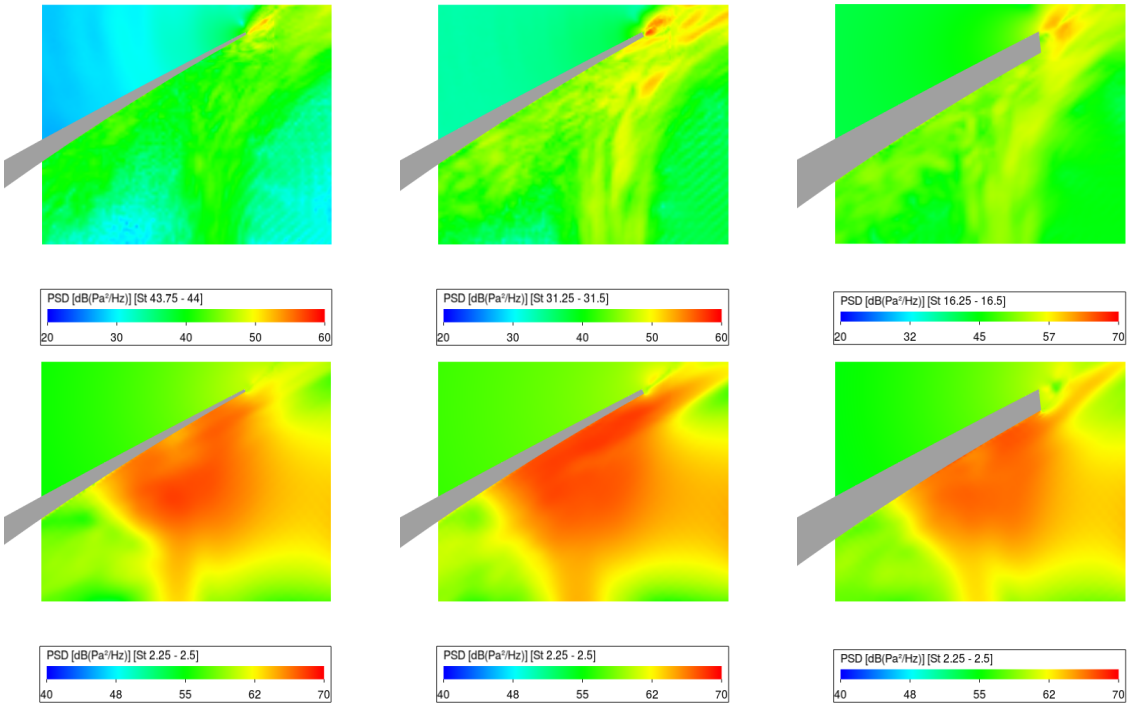

a) $\chi = 50$ b) Baseline c) $\chi = 400$

Reference: Author

On the other hand, at the frequency of the first tone of the far-field spectra, higher levels of pressure fluctuations are observed in the reattachment region. According to the authors (IMAMURA et al., 2007), higher pressure fluctuations at a low frequency around reattachment cause high-frequency fluctuations in the trailing edge. Figure 90 shows the PSD at the cusp, reattachment and trailing edge at midspan of the three χ configurations. Although all configurations exhibited the same values in the frequency range, the hump at a high frequency at the cusp and trailing edge is exhibited for the baseline and conf. χ400. Configuration χ50 showed no high-frequency hump, since at that specific frequency, the turbulence generates pressure fluctuations greater than those related to the vortex shedding.

Figure 90: PSD at slat surface at midspan of different χ

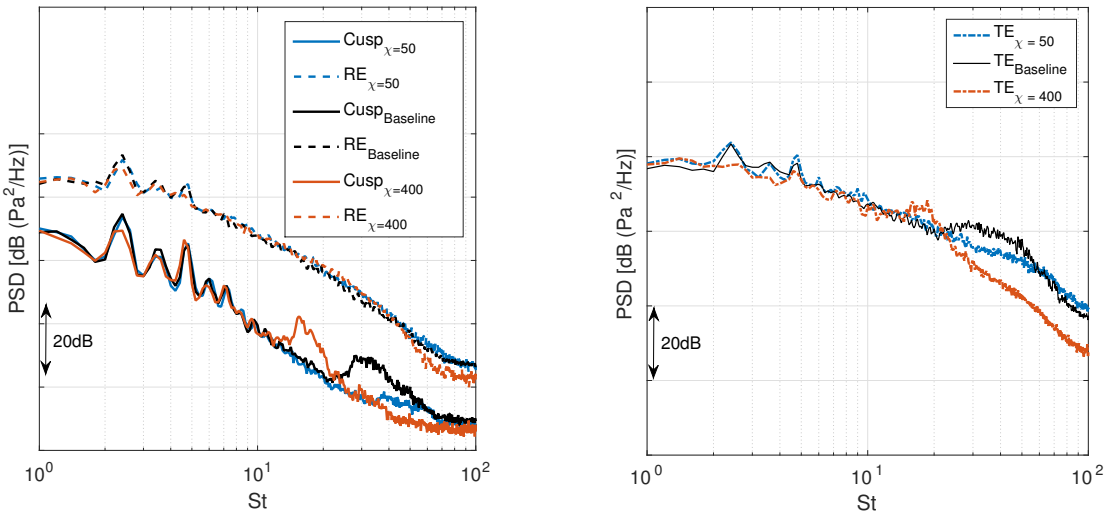

(a) Reattachment and cusp

(b) Trailing edge

Reference: Author

4.7 Effect of the cusp angle and thickness

Differently from the other cases, the angle and thickness of slat cusp exert a small influence on the aerodynamics and aeroacoustics of the wing. Table 14 shows the lift and drag coefficients for the different configurations of angle of cusp. The lift coefficient did not vary significantly in function of the variation in the angle and thickness of cusp, however, as the angle of cusp increased, the drag coefficient also increased.

Figure 91 displays the PSD for different cusp angle configurations. No changes were detected in the mid-frequency peaks and broadband noise. Configuration β15 showed a 1 dB reduction in the OSPL between $St = 1.8$ and 50. The reattachment point of all cusp angle configurations is located approximately 0.955 from the leading edge and no differences were detected in the shear layer trajectory, length and spectra at different points of the slat surface.

Table 14: Lift and drag coefficients of different β

Conf.	C_L variation [%]	C_D Variation [%]
$\beta - 1$	0.53	-0.42
Baseline	0	0
$\beta 5$	0.62	0.502
$\beta 10$	0.15	0.99
$\beta 15$	0.92	3.19

Reference: Author

Figure 91: PSD of different β

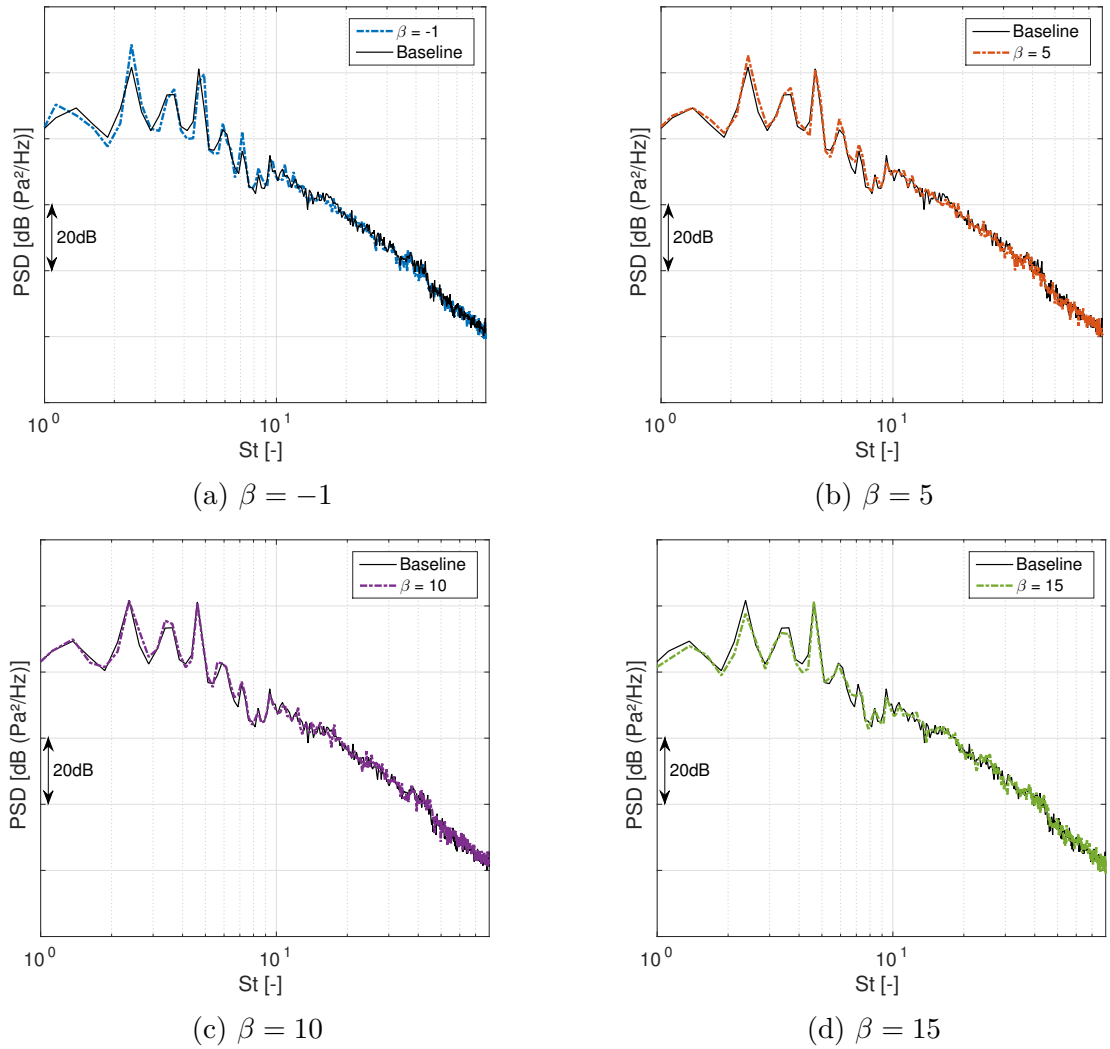

(a) $\beta = -1$ (b) $\beta = 5$

(c) $\beta = 10$ (d) $\beta = 15$

Reference: Author

For the analysis of the effect of cusp thickness (ι) the same mesh methodology used for the simulations of trailing edge thickness was used, i.e., three refinement regions were added in the cusp region and the minimum element size was reduced in 8 times, for

maintaining the same element size in the FW-H measurement region. As the cases are more expensive computationally, only two modifications were simulated.

The lift and drag coefficients did not vary in function of slat thickness, the major variation was an 1 % increment of drag coefficient in configuration $\iota 400$. Figure 92 shows the Power Spectral Density for the two variations in the cusp thickness. As in variations in the angle of cusp, there are no differences in all slat spectrum range and neither in the OSPL integrated from $St = 1.8$ and 50.

Figure 92: PSD of different ι

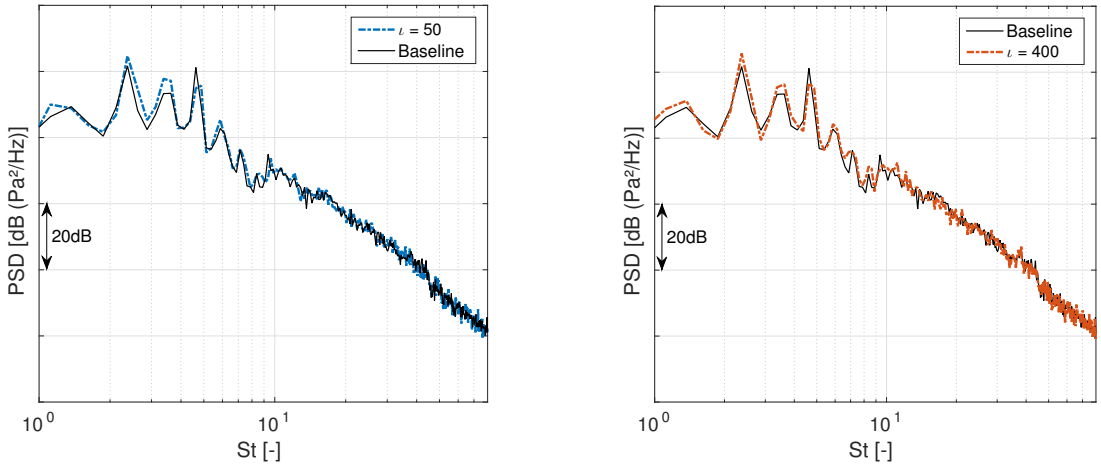

(a) $\iota = 50$ (b) $\iota = 400$

Reference: Author

Finally, although the cusp length exerts the major influence on noise generation, its angle and thickness does not influence the slat noise because actually modifications were completed in the internal part of the cusp (for maintaining the external initial geometry) and the flow only passes through it when the noise generation process is almost ended, i.e., the boundary layer of the slat separates in the cusp and creates the main shear layer and the noise generation phenomena occurs when it impinges the upper slat surface and part of flow flows over to slat trailing-edge, whereas the other part creates a recirculation inside the slat cove and at the end of such a recirculation, the flow has contact with the intern side of the slat cusp. Therefore, the angle and the thickness of cusp does not cause any influence in the flow around slat responsible for the slat noise.

4.8 Summary

The effect of the slat geometry and angle of attack in the slat noise generation could be summarized in Table 15. The table shows the effect if the characteristic is increased in both tonal and boradband components. The relations of the table are also valid in the wrong way.

Table 15: Summary of geometry effect

Characteristic	Tonal component	Boradband noise
AoA	↓	↓
Cusp length	↑	↑
Angle of trailing edge	↓	↑
Trailing edge length	↑	↓
Trailing edge thickness	-	-
Angle of cusp	-	-
Cusp thickness	-	-

Reference: Author

5 CONCLUDING AND REMARKS

Aeroacoustic experimental and numerical analyses of a 2D high-lift wing of a convectional and commercial aircraft were conducted at various angles of attack. Numerical analyses were performed on PowerFLOW 5.3 software, which uses the Lattice Boltzmann method to solve the fluid dynamics and Ffowcs William-Hawking to solve the acoustic far-field, and experimental analyses were carried out in a closed section wind tunnel at the LAE laboratory of the São Carlos School of Engineering. A phased microphone array was used for the measurements and the convectional Beamforming and CLEAN SC techniques was employed for the post-processing. Both analyses were performed at 34 m/s, which corresponds to a 1.01×10^6 Reynolds number based on the stowed chord and 0.098 Mach number.

The good agreement between numerical and experimental results of the different configurations and angles of attack validated the simulation methodology and demonstrated the capability of PowerFLOW software to resolve airframe noise acoustic problems. The experiments revealed a 4^o shift on the angle of attack in the wing main element, probably caused by the three-dimensional effects not present in the slat. On the other hand, differences detected in the far-field noise at high frequencies were related to the loss of coherence in the phased array antenna and dissipation in the numerical results. Nevertheless, the numerical results captured the mid-frequency tones and noise up to $St = 40$ and also the suction peak and pressure coefficient distribution in the wing main element.

As reported in the literature, the slat noise is composed of mid-frequency tones, a broadband component and a high-frequency single tone exhibited in some cases. The mid-frequency tones are caused by a feedback loop created between the vortex generated in the slat cusp that travels through the main shear-layer and the acoustic waves generated when it reaches the slat upper surface. They have a direct relationship with the coherence in the spanwise direction in both reattachment point and trailing edge and exhibit coherence lengths of up to 3 times the slat chord. Such tones cause high fluctuations and instabilities in the surface and flow in the reattachment region, which are represented by a peak in the RMS pressure coefficient distribution in the slat cove. The peaks intensity is related to the distance between the trailing edge and the reattachment point,since if such a distance increases, the level of the peaks decreases. On the other hand, the tones frequency can be associated with the distance between the reattachment point and the cusp, i.e., if it increases, the frequency of each tone decreases. The broadband noise is caused by the instabilities and dipole formed at the slat trailing edge. Differently from the tones, this noise showed no spatial coherence and its level may be associated with the main shear layer length and difference between the velocities through it. As the distance traveled by

the main shear-layer increases and the delta of the velocities decreases, the broadband noise decreases. The high-frequency hump is caused by the blunt slat trailing edge and the vortex shedding formed behind it. The frequency of such a hump exhibited in the far-field corresponds to the vortex shedding frequency. The characteristic Strouhal number for the high-frequency hump is 0.4 and should be calculated using the boundary layer displacement thickness as the characteristic length.

A parametric analysis of the influence of slat geometry on the noise generation was also conducted. 21 slat modifications of six different parts were simulated, i.e., 5 in the cusp length, 5 in the trailing edge angle, 3 in the trailing edge length, 2 in the trailing edge thickness, 4 in the angle of cusp and 2 in the cusp thickness. The cusp length strongly impacted the noise generation process and characteristics of the fluid around the slat, whereas the angle and thickness of the cusp did not show any effect on the aerodynamics and noise of the wing.

The most relevant associations detected between the geometry parts and the noise were an increase in both tonal components and broadband caused by an increase in the cusp length, and a reduction in the tones and increase in the broadband noise due to an increase in the trailing edge angle. An increase in the trailing edge length (or the slat chord) decreases the broadband noise, frequency of each tone and frequency of the maximum among all spectra. Finally, as the trailing edge thickness increases, the frequency of the high-frequency hump decreases.

5.1 Future works

This section addresses some recommendations for complementing this research and better understand the different phenomena that involve the slat noise generation process.

The results showed the effect of a specific parameter can be increased or decreased in function of the angle of attack. Therefore, analyses should be conducted at other angles of attack towards determining if the behaviour of reducing the noise is maintained and at what AoA a specific configuration is optimal, or promotes the highest noise reduction.

This study analyzed modifications made only in the slat; however, each of them modifies the wing main element, since the slat must fit the wing when stowed. A study of the slat modifications combined with the respective modifications in the wing main element should be conducted for checking whether modifications in the wing main element leading edge do not reduce the benefits achieved for a specific slat modification. Moreover, possible significant noise reductions should be analyzed through the combination of the best modifications in each parameter.

Experimental analyses with other measurement devices, as particle image velocimeter (PIV), pressure transducers and hot-film anemometers can promote a better

understanding of the physical phenomena around a deployed slat, validate the relations of fluid characteristics and noise generation found numerically, and correlate the near-field data with the far-field spectrum of the different slat configurations.

Finally, the slat prediction model designed by Guo (2012) can be applied to each slat modification, since such a model has four numerical constants that vary for each slat. Therefore, a study of the relations between the numerical constants and noise level with the flow and slat characteristics of each case should be conducted.

5.2 Dissemination

The first part of this research, which involves the analysis of the baseline configuration and comparisons with experimental results has been published in the conference paper entitled: "Experimental and Numerical Analysis of the Aerodynamic and Aeroacoustic Properties of a 2D High-LiftWing Model" (PEREIRA et al., 2018a) and was presented in the 24th AIAA/CEAS aeroacoustics conference, held in Atlanta, Georgia, in June 2018.

The analysis of the effect of some modifications has been published in the conference paper entitled: "Parametric Analysis of the Influence of Slat Geometry on Acoustic Noise" (BOTERO et al., 2018) and and was presented in the 24th AIAA/CEAS aeroacoustics conference, held in Atlanta, Georgia, in June 2018.

The analysis of the high-frequency hump and the vortex shedding behind the slat has been accepted in the Inter-Noise 2019 congress and will be presented in June, 2019. The paper is entitled: "Numerical analysis of the instabilities behind a blunt slat trailing-edge"

BIBLIOGRAPHY

AIRBUS. Aircraft noise - technologies and operations. **Airbus operations S.A.S**, Blagnac cedex, 2015.

ALLEN, C. S. et al. Aeroacoustic measurements. **Springer Science & Business Media**, New York, 2013.

BAUER, A. B. Vortex shedding from thin flat plates parallel to the free stream. **Journal of the Aerospace Sciences**, v. 28, n. 4, p. 340–341, 1961.

_____. Impedance theory and measurements on porous acoustic liners. **Journal of Aircraft**, American Institute of Aeronautics and Astronautics, v. 14, n. 8, p. 720–728, 1977.

BERTSCH, E.-L. **Noise prediction within conceptual aircraft design**. 2013. Thesis (PhD) — German Aerospace Center - DLR, 2013.

BOTERO, L. et al. Parametric analysis of the influence of slat geometry on acoustic noise. In: **2018 AIAA/CEAS Aeroacoustics Conference**. Atlanta, Georgia: American Institute of Aeronautics and Astronautics, 2018. p. 3593.

CASALINO, D. et al. Aircraft noise reduction technologies: a bibliographic review. **Aerospace Science and Technology**, Elsevier, v. 12, n. 1, p. 1–17, 2008.

_____. Towards numerical aircraft noise certification: Analysis of a full-scale landing gear in fly-over configuration. In: **18th AIAA/CEAS Aeroacoustics Conference (33rd AIAA Aeroacoustics Conference)**. Colorado Springs, Colorado: American Institute of Aeronautics and Astronautics, 2012. p. 2235.

_____. Lattice–boltzmann aeroacoustic analysis of the lagoon landing-gear configuration. **AIAA journal**, American Institute of Aeronautics and Astronautics, v. 52, n. 6, p. 1232–1248, 2014.

CATALANO, F. The new closed circuit wind tunnel of the aircraft laboratory of university of sao paulo, brazil. In: **24TH International Congress of the Aeronautical Sciences ICAS**. Yokohama, Japan: International Congress of the Aeronautical Sciences, 2004.

CHEN, H. et al. Extended boltzmann kinetic equation for turbulent flows. **Science**, American Association for the Advancement of Science, v. 301, n. 5633, p. 633–636, 2003.

CHEN, S.; DOOLEN, G. D. Lattice boltzmann method for fluid flows. **Annual review of fluid mechanics**, Annual Reviews, v. 30, n. 1, p. 329–364, 1998.

CHOUDHARI, M.; KHORRAMI, M. Slat cove unsteadiness: Effect of 3d flow structures. In: **44th AIAA Aerospace Sciences Meeting and Exhibit**. Reno, Nevada: American Institute of Aeronautics and Astronautics, 2006. p. 211.

CHOUDHARI, M. M. et al. Aeroacoustic experiments in the nasa langley low-turbulence pressure tunnel. **NASA technical reports**, National Aeronautics and Space Administration, Hampton, Virginia, 2002.

CHOW, L.; MAU, K.; REMY, H. Landing gears and high lift devices airframe noise research. In: **8th AIAA/CEAS Aeroacoustics Conference and Exhibit**. Breckenridge, Colorado: The American Institute of Aeronautics and Astronautics, 2002. p. 2408.

CHOW, L. C.; LEMPEREUR, P.; MAU, K. Aircraft airframe noise and installation effects—research studies. **Air & Space Europe**, Elsevier, v. 3, n. 1, p. 72–75, 1999.

CROUSE, B. et al. Fundamental aeroacoustic capabilities of the lattice-boltzmann method. In: **12th AIAA/CEAS Aeroacoustics Conference (27th AIAA Aeroacoustics Conference)**. Cambridge, Massachusetts: American Institute of Aeronautics and Astronautics, 2006. p. 2571.

DHIRAJ, K.; KAMAL, P. Effect of tip vortices associated with a finite circular cylinder. In: **Hong Kong International Conference on Engineering and Applied Science**. Hong Kong: HKICEAS, 2015. p. 1.

DOBRZYNSKI, W. Almost 40 years of airframe noise research: what did we achieve? **Journal of aircraft**, American Institute of Aeronautics and Astronautics, v. 47, n. 2, p. 353–367, 2010.

DOBRZYNSKI, W. et al. Airframe noise studies on wings with deployed high-lift devices. In: **4th AIAA/CEAS Aeroacoustics Conference**. Toulouse, France: The American Institute of Aeronautics and Astronautics, 1998. p. 2337.

DOBRZYNSKI, W.; POTT-POLLENSKE, M. Slat noise source studies for farfield noise prediction. In: **7th AIAA/CEAS Aeroacoustics Conference and Exhibit**. Maastricht, Netherlands: American Institute of Aeronautics and Astronautics, 2001. p. 2158.

DOWLING, A. P.; WILLIAMS, J. F. Sound and sources of sound. **Horwood**, Chichester, United Kingdom, 1983.

EASA. European aviation environmental report. **European Aviation Safety Agency reports**, Cologne, Germany, 2016.

EXA COMPANY. The technology behind simulia powerflow: Lattice boltzmann-based physics: Turbulence modeling using cfd. **DassaultSystems Simulia**, 2009. Available from Internet: <https://exa.com/en/company/exa-lattice-boltzmann-technology>. Cited: 4th oct. 2018.

_____. Powerflow user's guide. **Exa Company manuals**, Burlington, MA, 2015.

FARASSAT, F. Derivation of formulations 1 and 1a of farassat. **NASA technical reports**, National Aeronautics and Space Administration, Hampton, Virginia, 2007.

FARES, E.; CASALINO, D.; KHORRAMI, M. R. Evaluation of airframe noise reduction concepts via simulations using a lattice boltzmann approach. In: **21st AIAA/CEAS Aeroacoustics Conference, AIAA AVIATION Forum**. Dallas, Texas: American Institute of Aeronautics and Astronautics, 2015. p. 2988.

FEDERAL AVIATION ADMINISTRATION. Noise regulations - noise stantard. **Federal Aviation Administration - FAA**, Washington, DC, 2017. Available from Internet: <www.faa.gov>. Cited: 10th mar. 2017.

FILIPPONE, A. Aircraft noise prediction. **Progress in Aerospace Sciences**, Elsevier, v. 68, p. 27–63, 2014.

FINK, M. R. Airframe noise prediction method. **UNITED TECHNOLOGIES RESEARCH CENTER EAST HARTFORD CT**, Defense Technical Information Center, Washington, DC, 2002.

FONSECA, W. D. et al. A different approach to archimedean spiral equation in the development of a high frequency array. **SAE Technical paper**, SAE, Brazil, 2010.

FORD, H. Unites States, 1914.

FOX, R. W.; MCDONALD, A. T.; PRITCHARD, P. J. Introduction to fluid mechanic. **John Wiley**, Hoboken, New Jersey, 1998.

GLEINE, W.; MAU, K.; CARL, U. Aerodynamic noise reducing structure for aircraft wing slats. **NASA Ames Research Center**, n. US 6,394,396, may 2002.

G.R.A.S. Gras 46bd 1/4" ccp: Pressure standard microphone set. **G.R.A.S Sound & Vibration**, Holte, Denmark, 2018. Available from Internet: <https://www.gras.dk>. Cited: 20th june 2018.

GUO, Y. Slat noise modeling and prediction. **Journal of Sound and Vibration**, Elsevier, v. 331, n. 15, p. 3567–3586, 2012.

HE, X.; DOOLEN, G. D.; CLARK, T. Comparison of the lattice boltzmann method and the artificial compressibility method for navier–stokes equations. **Journal of Computational Physics**, Elsevier, v. 179, n. 2, p. 439–451, 2002.

HOGBOM, J.; BROUW, W. The synthesis radio telescope at westerbork. principles of operation, performance and data reduction. **Astronomy and Astrophysics**, v. 33, p. 289, 1974.

ICAO. Environmental report 2016. **Aviation and climate change**, International Civil Aviation Organization, v. 2016, 2016.

IMAMURA, T. et al. Simulation of the broadband noise from a slat using zonal les/rans hybrid method. In: **45th AIAA Aerospace Sciences Meeting and Exhibit**. Reno, Nevada: American Institute of Aeronautics and Astronautics, 2007. p. 226.

KHORRAMI, M.; LOCKARD, D. Effects of geometric details on slat noise generation and propagation. In: **12th AIAA/CEAS Aeroacoustics Conference (27th AIAA Aeroacoustics Conference)**. Cambridge, Massachusetts: American Institute of Aeronautics and Astronautics, 2006. p. 2664.

KHORRAMI, M. R.; FARES, E.; CASALINO, D. Towards full aircraft airframe noise prediction: lattice boltzmann simulations. In: **20th AIAA/CEAS Aeroacoustics Conference, AIAA AVIATION Forum**. Atlanta, Georgia: American Institute of Aeronautics and Astronautics, 2014. p. 2481.

KOLB, A. et al. Aeroacoustic wind tunnel measurements on a 2d high-lift configuration. In: **13th AIAA/CEAS Aeroacoustics Conference (28th AIAA Aeroacoustics Conference)**. Rome, Italy: American Institute of Aeronautics and Astronautics, 2007. p. 3447.

_____. Aeroacoustic wind tunnel measurements on a 2d high-lift configuration. In: **13th AIAA/CEAS Aeroacoustics Conference (28th AIAA Aeroacoustics Conference)**. Rome, Italy: American Institute of Aeronautics and Astronautics, 2007. p. 3447.

KOTAPATI, R. et al. The lattice-boltzmann-vles method for automotive fluid dynamics simulation, a review. **SAE Technical Paper**, SAE, Burlington, Vermont, 2009.

LI, Y.; JAMMALAMADAKA, A. Exploring an lbm-vles based cfd approach for predictions of aero-thermal flows in generic turbo-machinery devices. In: **51st AIAA/SAE/ASEE Joint Propulsion Conference**. Orlando, Florida: American Institute of Aeronautics and Astronautics, 2015. p. 4128.

LIGHTHILL, M. J. On sound generated aerodynamically i. general theory. In: **Proceding of the Royal Society London A**. London, United kingdom: The Royal Society, 1952. v. 211, n. 1107, p. 564–587.

LOCKARD, D.; CHOUDHARI, M. Noise radiation from a leading-edge slat. In: **15th AIAA/CEAS Aeroacoustics Conference (30th AIAA Aeroacoustics Conference)**. Miami, Florida: American Institute of Aeronautics and Astronautics, 2009. p. 3101.

MAU, K.; DOBRZYNSKI, W. Flexible airflow separator to reduce aerodynamic noise generated by a leading edge slat of an aircraft wing. **NASA Ames Research Center**, n. US 6,789,769, September 2004.

MAXWELL, J. C. On the stability of the motion of saturn's rings. **Macmillan and Co.**, Cambridge, United Kingdom, 1959.

MOHAMAD, A. A. Lattice boltzmann method: fundamentals and engineering applications with computer codes. **Springer Science & Business Media**, London, United Kingdom, 2011.

MORGAN, H. G.; HARDIN, J. C. Airframe noise-the next aircraft noise barrier. **Journal of Aircraft**, The American Institute of Aeronautics and Astronautics, v. 12, n. 7, p. 622–624, 1975.

PAGANI, C. C.; SOUZA, D. S.; MEDEIROS, M. A. Slat noise: aeroacoustic beamforming in closed-section wind tunnel with numerical comparison. **AIAA Journal**, American Institute of Aeronautics and Astronautics, v. 54, n. 7, p. 2100–2115, 2016.

_____. Experimental investigation on the effect of slat geometrical configurations on aerodynamic noise. **Journal of Sound and Vibration**, Elsevier, v. 394, p. 256–279, 2017.

PASCIONI, K.; CATTAFESTA, L. N.; CHOUDHARI, M. M. An experimental investigation of the 30p30n multi-element high-lift airfoil. In: **20th AIAA/CEAS Aeroacoustics Conference**. Atlanta, Georgia: American Institute of Aeronautics and Astronautics, 2014. p. 3062.

PEREIRA, L. T. L. et al. Experimental and numerical analysis of the aerodynamic and aeroacoustic properties of a 2d high-lift wing model. In: **24th AIAA/CEAS Aeroacoustics Conference**. Atlanta, Georgia: American Institute of Aeronautics and Astronautics, 2018. p. 3458.

_____. Experimental slat noise assessment through phased array and hot-film anemometry measurements. In: **2018 AIAA Aerospace Sciences Meeting**. Kissimmee, Florida: American Institute of Aeronautics and Astronautics, 2018. p. 0758.

POPE, S. B. Turbulent flows. **IOP Publishing**, 2001.

POTT-POLLENSKE, M.; ALVAREZ-GONZALES, J.; DOBRZYNSKI, W. Effect of slat gap on farfield radiated noise and correlation with local flow characteristics. In: **9th AIAA/CEAS Aeroacoustics Conference and Exhibit**. Hilton Head, South Carolina: American Institute of Aeronautics and Astronautics, 2003. p. 226.

RION CORPORATION. Nc-74 sound calibrator, data sheet. **RION Sound and vibration; web-support**, Yokohama, 2003.

ROGER, M.; PÉRENNÈS, S. Low-frequency noise sources in two-dimensional high-lift devices. In: **6th Aeroacoustics Conference and Exhibit**. Lahaina, Hawaii: American Institute of Aeronautics and Astronautics, 2000. p. 1972.

SANTANA, L. D. et al. The update of an aerodynamic wind-tunnel for aeroacoustics testing. **Journal of Aerospace Technology and Management**, Scielo Brasil, v. 6, n. 2, p. 111–118, 2014.

SCANIVALVE CORPORATION. **ZOC 33/64Px—Electronic pressure scanning module, instruction and service manual**. Oxford, England, 2003. Available from Internet: <https://scanivalve.com/media/28028/zoc33_1603.pdf>. Cited: 20th june 2018.

SCHOLTEN, W. D. et al. Development and analysis-driven optimization of superelastic slat-cove fillers for airframe noise reduction. **AIAA Journal**, American Institute of Aeronautics and Astronautics, v. 54, n. 3, p. 1078–1094, 2015.

SIJTSMA, P. Clean based on spatial source coherence. **International journal of aeroacoustics**, SAGE Publications Sage UK: London, England, v. 6, n. 4, p. 357–374, 2007.

SMITH, M.; CHOW, L.; MOLIN, N. Attenuation of slat trailing edge noise using slat gap acoustic liners. In: **12th AIAA/CEAS Aeroacoustics Conference (27th AIAA Aeroacoustics Conference)**. Cambridge, Massachusetts: American Institute of Aeronautics and Astronautics, 2006. p. 2666.

SPERRY, W. C. Aircraft noise evaluation. FEDERAL AVIATION ADMINISTRATION WASHINGTON DC OFFICE OF NOISE ABATEMENT, Washington, DC, 1968.

STREETT, C. et al. Aerodynamic noise reduction for high-lift devices on a swept wing model. In: **44th AIAA Aerospace Sciences Meeting and Exhibit**. Reno, Nevada: The American Institute of Aeronautics and Astronautics, 2006. p. 212.

SUCCI, S.; BENZI, R.; HIGUERA, F. The lattice boltzmann equation: A new tool for computational fluid-dynamics. **Physica D: Nonlinear Phenomena**, Elsevier, v. 47, n. 1-2, p. 219–230, 1991.

TAKEDA, K.; ZHANG, X.; NELSON, P. Computational aeroacoustic simulations of leading-edge slat flow. **Journal of sound and vibration**, Elsevier, v. 270, n. 3, p. 559–572, 2004.

TERRACOL, M.; MANOHA, E.; LEMOINE, B. Investigation of the unsteady flow and noise generation in a slat cove. **AIAA Journal**, American Institute of Aeronautics and Astronautics, v. 54, n. 2, p. 469–489, 2015.

WILLIAMS, J. F.; HAWKINGS, D. L. Sound generation by turbulence and surfaces in arbitrary motion. **Philosofical Transactions of the Royal Society London A**, The Royal Society, v. 264, n. 1151, p. 321–342, 1969.

ZAKHAROV, V. E.; L'VOV, V. S.; FALKOVICH, G. **Kolmogorov spectra of turbulence I: Wave turbulence**. Berlin, Germany: Springer Science & Business Media, 2012.

Annex

AIAA AVIATION Forum
June 25-29, 2018, Atlanta, Georgia
2018 AIAA/CEAS Aeroacoustics Conference

10.2514/6.2018-3593

Parametric Analysis of the Influence of Slat Geometry on Acoustic Noise

Laura Botero-Bolívar*, Lourenço T. L. Pereira†, Daniel Acevedo-Giraldo‡, and Fernando M. Catalano.§
São Carlos School of Engineering, University of São Paulo (EESC-USP), São Carlos, Brazil

Danillo C. Reis¶ and Eduardo L. C. Coelho.‖
EMBRAER, São José dos Campos, Brazil

This article addresses variations in different parameters of the slat internal geometry for the establishment of their relation with noise generation. Studies were carried out through a numerical method on the commercial version of PowerFLOW 5.3®. Numerical results of the baseline configuration were compared with experiments conducted in a closed section wind tunnel at the Laboratory of Aerodynamics (LAE) of the São Carlos School of Engineering - University of São Paulo (EESC-USP), Brazil. The agreement between numerical and experimental results of both aerodynamic and aeroacoustic tests validated the numerical methodology. The parameters modified were cusp length, angle of cusp and angle of trailing edge. Cusp length and angle of trailing edge highly influenced the slat noise; the angle of the cusp showed a small relation with noise generation.

I. Nomenclature

α	=	Angle of trailing edge [^{o}]
β	=	Angle of cusp [^{o}]
δx_{min}	=	Minimum element size [mm]
δ_w	=	Vorticity thickness [m]
κ	=	Cusp length [$\%\kappa_{Baseline}$]
γ^2	=	Coherence [-]
AoA	=	Angle of attack [^{o}]
a	=	Velocity of sound [m/s]
b	=	Span [mm]
C_D	=	Drag Coefficient [-]
C_L	=	Lift Coefficient [-]
C_p	=	Pressure coefficient [-]
c	=	Chord of stowed element [m]
c_s	=	Slat chord [m]
FW-H	=	Ffowcs William - Hawking
LBM	=	Lattice Boltzmann Method
M	=	Mach Number ($\frac{U_\infty}{a}$) [-]
OSPL	=	Overall Sound Pressure Level [dB]
PSD	=	Power Spectra Density [dB (Pa²/Hz)]
Re	=	Reynolds number ($\frac{U_\infty c}{\nu}$)[-]
RMS	=	Root Mean Square
ROI	=	Region of Interest
St	=	Strouhal number ($\frac{c_s f}{U_\infty}$) [-]
U_∞	=	Free-stream velocity [m/s]

*MSc student, Aeronautical Engineering Department, EESC-USP, laura.boterobol@usp.br.
†MSc student, Aeronautical Engineering Department, EESC-USP, lourenco.tercio@gmail.com.
‡MSc student, Aeronautical Engineering Department, EESC-USP, daniel.acevedogi@usp.br.
§Professor, Aeronautical Engineering Department, EESC-USP, catalano@sc.usp.br.
¶Noise and Vibration Engineer, R&T department, EMBRAER, danillo.reis@embraer.com.br.
‖Noise and Vibration Engineer, R&T department, EMBRAER, eduardo.capucho@embraer.com.br.

II. Introduction

In recent years, concerns about the noise generated by aircraft, mainly around airports, have been the focus of several studies and tighter regulations, since aircraft noise reduction enables an increase in airplane traffic without negative effects on neighboring communities [1]. Certification entities regulate aircraft noise levels through international standards established in conjunction with the International Civil Aviation Organization (ICAO), which are applied when the aircraft is requesting its airworthiness certification [2].

Aircraft noise can be divided into two components, namely engine noise, and airframe noise. Engine noise refers to the noise generated by the components of the aircraft propulsion system, whereas airframe noise is generated by the structure as it moves through the air. When aircraft noise first came to the forefront, engines were the main source and the focus of noise reduction. However, in the past few decades, they have become significantly quieter, mainly in long-range aircraft, due to technological advances of the components and materials used [3]. Airframe noise has thus become increasingly important; nowadays it is estimated that approximately half of the total noise during the landing approach is caused by engines, while the other half is generated by the aircraft structure [4]. Airframe noise can be divided into three components, namely slat, side-edge flap and landing gear and the rank of such sources highly depends on the geometry and operational conditions of each aircraft. However, the slat is considered one of the major noise components, due to the complex boundary layer formed in its cavity [1, 5, 6].

Figure 1 shows the flow around a typically deployed slat. The fluid along the gap formed between the slat and the main element is accelerated due to the slat concave geometry and the curvature of the main-element leading edge. Such an acceleration causes the formation of an entrapped eddy vortex along the concave rear surface of the slat and is continuously supplied with more energy from the adjoining gap airflow. Turbulence cells are formed along the boundary between the eddy vortex and the gap flow, which generate and radiate acoustic noise along the entire span of the slat, especially when they separate and flow over the trailing edge of the slat [7, 8].

Slat spectrum is characterized by mid-frequency tones, broadband in medium frequencies (which decrease with the frequency), and high-frequency hump [9]. Tonal peaks are attributed to the cavity resonance in the slat cove in combination with the adjacent wing leading edge. Although broadband noise does not have a specific definition, Dobrzynski, W. and Pott-Pollenske, M. [10] modeled it as an acoustic dipole normal to the slat surface near the trailing edge. High-frequency tones are usually caused by the formation of laminar separation bubbles [11]. Some authors have studied the velocity effect on slat noise and established the velocity power law U^{5-6} [3, 10, 12–14].

This article reports on numerical analyses of slat noise and the influence of the slat internal geometry on the noise generated. Numerical simulations were performed on commercial software PowerFLOW®, which uses Lattice Boltzmann Method (LBM) as a solver method and Ffowcs Williams-Hawking acoustic analogy for the analysis of the far-field. Results of the baseline configuration were compared with wind-tunnel test results for validating the simulation methodology. Wind tunnel tests were conducted at the Laboratory of Aerodynamics (LAE) of the São Carlos School of Engineering - University of São Paulo (EESC-USP), Brazil, at 1.16×10^6 Reynolds number (Re) and 0.098 Mach. Measurements were taken by a microphone phased array and the post-processing was carried out through conventional beamforming technique. Both studies, numerical and experimental, were carried out in a three-element high-lift wing, namely flap, main wing element, and flap.

III. Geometry Variation

This research aimed at a parametric study on the internal geometry of the slat for a better understanding of its influence on the noise generation. Figure 2 shows the parameters to be modified in a representative slat geometry, namely cusp length (κ in Fig. 2), cusp angle (β in Fig. 2) and angle of the trailing edge (α in Fig. 2). The same gap and overlap of the baseline configuration were maintained in all configurations for keeping the same aerodynamic properties of slat.

Table 1 shows the values of the parameters modified in the geometry. The angles were measured between the current configuration and the baseline configuration and the cusp length was calculated in terms of percentage of the baseline cusp length.

Modifications were applied in the cusp, i. e. its length was varied for changing both main shear layer trajectory and reattachment point, and therefore, breaking down the loop between the reattachment and the cusp (cause of mid-frequency tones), in the angle of cusp, for modifying the main shear layer behavior and the reattachment, and in the angle of trailing edge, for modifying the resonance on the slat cove and turbulence in the trailing edge region.

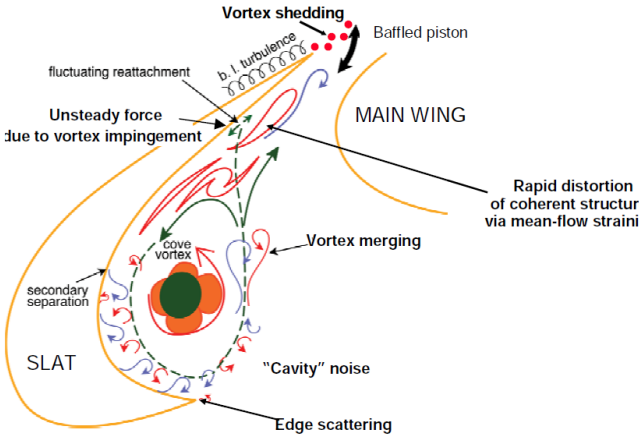

Fig. 1 Flow around slat [8]

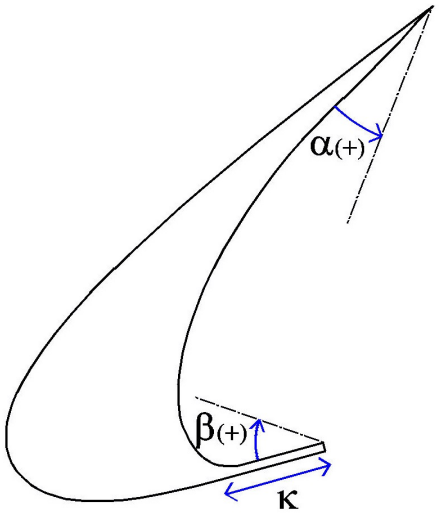

Fig. 2 Parameters of the slat geometry

Table 1 Values of geometry modifications

Parameter	Modifications				
cusp length (κ)	0 %	25 %	50 %	150 %	191 %
cusp angle (β)	-1^o	5^o	10^o	15^o	-
Trailing edge angle (α)	-5^o	5^o	10^o	15^o	20^o

IV. Numerical Approach

Numerical simulations were conducted on the commercial version of PowerFLOW 5.3®, which uses LBM as fluid solver. Such a method is based on the resolution of a Boltzmann equation in discrete lattice cells of appropriate symmetries. The lattice equation is essentially the kinetic equation resulting from the ensemble-averaging of the discrete dynamics of the Frisch-Hasslacher-Pmeau (FHP) cellular automation supplemented with the assumption of molecular chaos [15].

Conventional numerical solvers, e. g. Navier-Stokes (NS) equations, are based on the discretization of macroscopic continuum, whereas LBM incorporates the physics of microscopic processes [16], therefore, the fluid is replaced by fraction particles, according to a distribution function that considers the behavior of a collection of particles a unit. Such a characteristic enables LBM to accurately capture the aerodynamics of high Reynolds number flows and pressure fluctuations due to separated and reattached flows (main airframe noise source). Furthermore, LBM handles complex geometries without grids defined by complex analytical functions [17, 18]. The program discretizes the Lattice-Boltzmann equation temporarily and spatially. It divides the computational domain into 3D-cells, in which particles can move in 18 directions to the neighboring cells besides the 0-vector.

A. Turbulence Model

As a fluid turbulence model, PowerFLOW uses the $\kappa - \epsilon$ RNG equations with extensions, equivalent to time-accurate very large eddy simulations (VLES). The effects of the unresolved (sub-grid) scale-flow properties on the resolved large scale are exerted via eddy viscosity and turbulent Prandtl numbers. PowerFLOW also uses the universal Law of the Wall velocity profile to assume the velocity of the elements closest to the surface and coupled with the wall model pressure gradient extension for determining the local skin friction.

B. Numerical Set-up

The dimensions of the computational domain were 1.3 *m* x 1.7 *m* x 5 *m* for replicating the wind tunnel dimensions and avoid corrections in the effective angle of attack. The length is greater for enabling the full flow development.

The Boundary conditions used in the simulations were the same as those of the wind tunnel. The Velocity inlet was set at 34 m/s, which corresponds to a 0.098 Mach number and 1.16×10^6 Reynolds number (Re), based on the stowed chord; the turbulence level was set at 0.21% (wind tunnel turbulence level [19]) with a 1 *mm* turbulence length scale. The outlet condition was imposed with no pressure gradient. The computational domain, which is delimited by solid walls were set as non-friction and model walls were set as standard wall with automatic transition model. The outer region was modeled as a high viscosity fluid, or anechoic layer, for avoiding the reflection of waves approaching to the computational domain. Such a condition is necessary for simulations even if the wind tunnel does not have any anechoic region because, otherwise, simulations would take long and their completion would be inviable.

Ten refinement regions (VR) were established. The finest elements (VR9) were located in the same region of FW-H measurements and four minimum element size was simulated ($\delta x_{min} = 0.18, 0.20, 0.25$ and 0.28 *mm*). According to Terracol et al [20], a good indicator of the adequacy of the grid for properly resolving the main shear layer dynamics is based on the local ratio between the characteristic lengths of the shear layer and the local grid resolution in each flow direction. In a mixing layer between two parallel flows of velocities U_1 and U_2 (the main shear layer of a slat can be considered a mixing layer), the most-unstable wavelengths in the stream-wise (X-axis), span-wise (Z-axis) and shear directions (Y-axis) are $\lambda_x = 7\delta_w$, $\lambda_z = \frac{14}{3}\delta_w$, and $\lambda_y = \delta_w$, where δ_w is the local vorticity thickness, calculated by Equation 1, where n is the shear-normal direction.

$$\delta_w = \frac{|U_1 - U_2|}{max(\frac{dU}{dn})} \tag{1}$$

Terracol et al [20] also demonstrated the vorticity thickness increases along the shear layer, therefore, it was calculated at the beginning of the shear layer (most critical case), i. e., $\frac{s}{SL} = 0.1$, for the determination of the grid resolution. Figure 3 shows the velocity profile around the shear layer and its normal-shear derivative. The values of U_1, U_2 and $max(\frac{dU}{dn})$ shown in the graph lead to a 7.4×10^{-4} m vorticity thickness, which corresponds to a $\lambda_x/\delta x_{min} = 29, 26, 21$ *and* 18, for the minimum element sizes simulated.

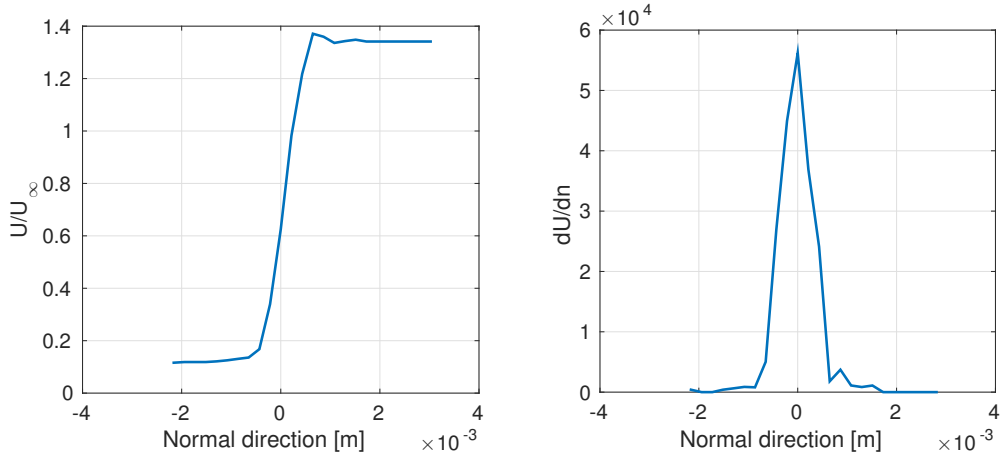

Fig. 3 Tangential velocity profile and associated shear-normal derivative at $\frac{s}{SL} = 0.1$

Figure 4 shows the variation of the PSD and the pressure coefficient distribution using different minimum element sizes. All cases detected the main mid-frequency peaks and only for a $\lambda_x/\delta x_{min} = 29$ a change in the slope of the broadband noise is observed for St above 20. The maximum difference in the OSPL integrated from $St1.6$ to 100 was 0.8 dB between $\lambda_x/\delta x_{min} = 29$ and 18. The pressure distribution in the slat and main element are not sensible for the element size as only differences are found in the predicted separation in the flap, however, they are not significant for the flow in the slat region. No variation in the lift and drag coefficients were detected for different minimum element size. All simulations were completed using $\lambda_x/\delta x_{min} = 21$ (0.25 *mm*) and approximately 3.2×10^8 elements were created. Simulations were performed in approximately 30240 CPU hours for 851000 timesteps (0.34 s in real time).

Only the baseline configuration was simulated with all span (for comparing the results to the wind tunnel) for reducing computational costs. The other slat configurations were simulated with a 250 *mm* span, and the same computational

set-up and FW-H measurement region were maintained. Such simulations have 8.5×10^7 elements and took 9035 CPU hours for 851000 timesteps.

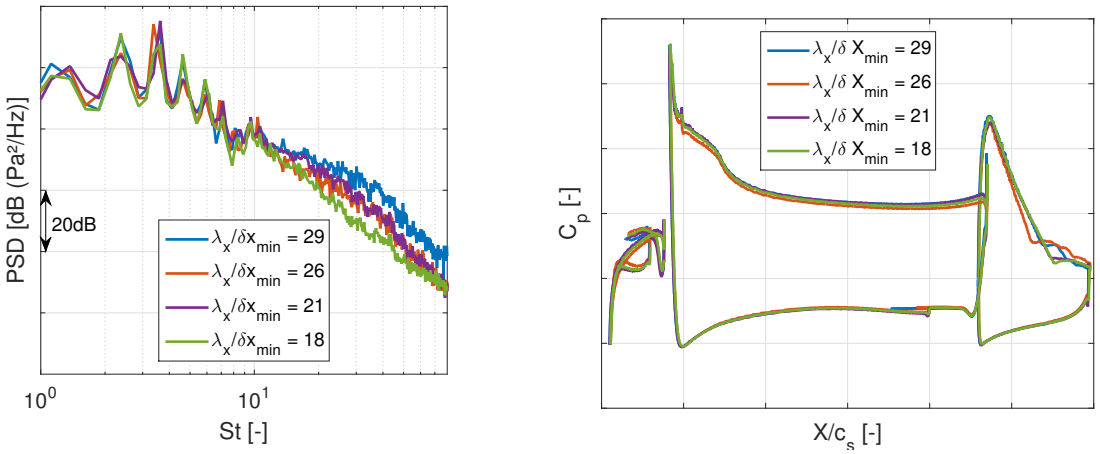

Fig. 4 PSD and pressure coefficient distribution variation with the variation of the minimum element size.

C. Far-field Analysis

The far-field was calculated by the Ffowcs Williams-Hawking (FW–H) acoustic analogy [21], included in PowerACOUSTICS 3.1b post-processing tool. For the standardization, power spectrum values were normalized by the frequency. The FW-H analogy used by PowerFLOW uses pressure fluctuations in a surface and converts them to a noise in the far-field. The surface pressure measurements for the analogy calculation were taken from a $3.5c_s \times 4.7c_s \times Z$ crop in the middle of the span. Figure 5 shows a bottom view of the model and the FW-H measurement region.

A study of convergence was carried out for the establishment of the appropriate dimension in the span-wise direction of the FW-H measurement region, once different measurement regions can cause differences in the noise perceived in the far-field. $0.90c_s$, $2.35c_s$ $3.5c_s$ and $4.7c_s$ span-wise direction dimensions of the FW-H measurement region were simulated and the results are shown in Figure 6 as power spectral density versus Strouhal number. The PSD values were standardized adding the Fig. 2 for each FW-H length case. A significant variation in the mid-frequency tones and broadband intensity was observed between FW-H length of $0.95c_s$ and $2.35c_s$, whereas no significant variations were detected between $2.35c_s$, $3.5c_s$ and $4.7c_s$, which indicates a convergence of the predicted noise in function of the FW-H length.

The capability of the region to detect changes in the geometry or angle of attack was analyzed through simulations varying the angle of attack. Figure 7 shows the noise at $AoA = 0^o$ and 4^o for FW-H lengths of $0.95c_s$ and $2.35c_s$. A $0.95c_s$ FW-H length caused no difference between the values of angle of attack, therefore, such a length is not sufficient to capture the noise generation phenomena. On the other hand, a $2.35c_s$ FW-H length shows a noise variation with the AoA in agreement with theoretical and experimental results (Fig. 12). The low capacity for a $0.95c_s$ FW-H length to predict the noise is due to coherence length related to the noise reaches values greater than the FW-H domain.

$$10log(\frac{b}{FWH_{length}}) \tag{2}$$

A study of the coherence of the pressure fluctuations on the trailing edge was conducted for $AoA = 0^o$ for determining the length in which the correspondence is associated with the noise. The coherence was calculated for each point (i) and they were spaced $\Delta z = 0.06c_s$ from each other. Figure 8 shows the coherence for the peaks Strouhal numbers observed in the slat spectra and for a St of broadband noise ($St = 97.5$). An average of the coherence at each distance for the same St are also provided. As expected, the behavior of the coherence is cyclic, due to the loop created between the cusp and the trailing edge responsible for the tonal noise. The first peak ($St = 2.4$), which is the maximum value in the spectrum, shows a higher coherence than the others For such St the coherence is minimum at a $Z = 3.5c_s$ and the mean coherence at a $Z = 2.35c_s$, which indicates a distance between 2.35 and 3.5 times the slat chord is sufficient for the analyses of the noise generation phenomena. The broadband noise does not correlate between the points.

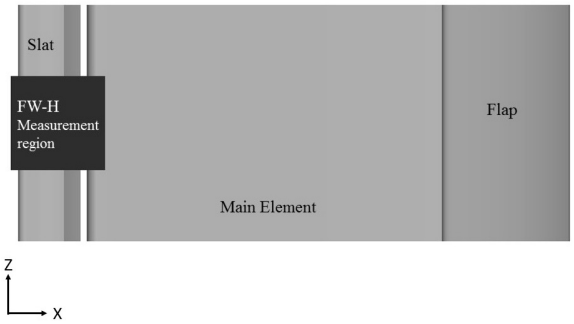

Fig. 5 FWH measurement region

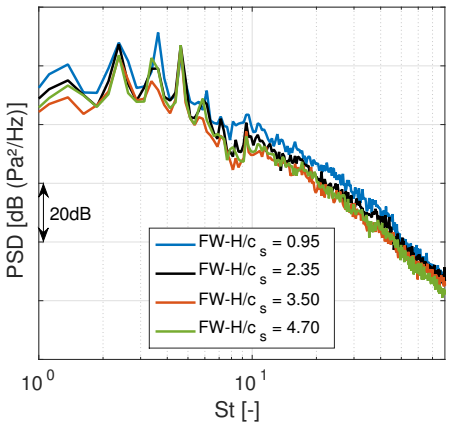

Fig. 6 Influence of the span-direction dimension of the FW-H measurement region ($\delta \mathbf{x_{min}} = \mathbf{0.25}$ mm).

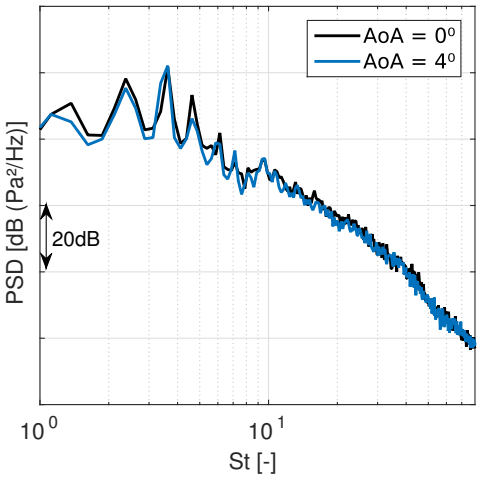

(a) $FW - H_{length} = 2.35c_s$

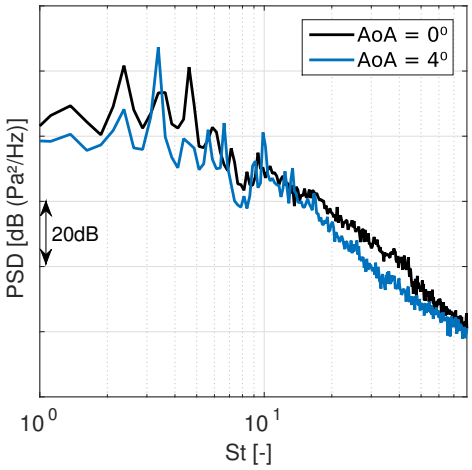

(b) $FW - H_{length} = 2.35c_s$

Fig. 7 Variation in slat spectra with variation in the angle of attack.

FW-H measurements were taken from a crop at the middle of the span of $2.35c_s$ length. Noise was propagated to 61 microphones located at the simulation wall pressure side, which are equivalent to wind-tunnel microphones. Measurements started at 0.147 s at 82 kHz sampling frequency. The results were compared to a Region of Interest (ROI) of all span used in the beamforming post-processing technique. Once the FW-H length in the numerical simulations is different from the ROI used for the beamforming calculation, the expression shown in Equation 2 was added to the numerical results towards standardizing them for the comparison.

D. Near-field Measurements

Fluid measurements were taken after the convergence of lift and drag coefficients. Therefore, the time-average measurements of the fluid were taken with a 71 Hz sampling frequency at each 3D cell and instantaneous measurements with a 10 kHz sampling frequency.

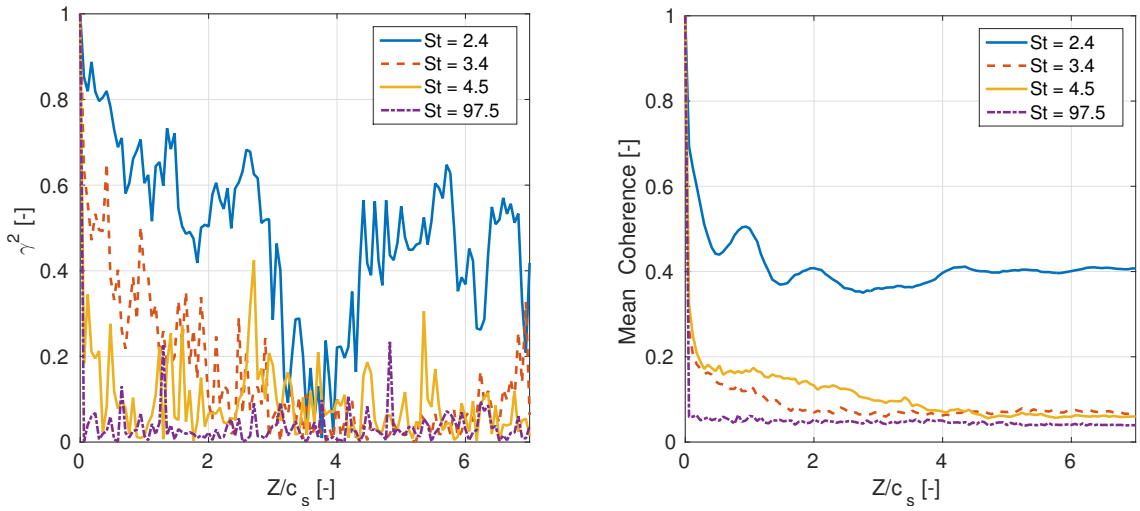

(a) Span-wise coherence

(b) Span-wise main coherence

Fig. 8 Span-wise coherence in the trailing edge in the baseline configuration $\frac{\Delta Z}{c_s} = 0.06$.

V. Experimental Set-up

Experiments were conducted in a closed-circuit subsonic wind tunnel of 1.3 m x 1.7 m x 3 m height, width and length, respectively, and 10 $\frac{m}{s}$ to 45 $\frac{m}{s}$ velocity range. It is driven by an 110 hp electrical motor and an 8-blade fan [22].

The wind tunnel was designed for aerodynamic tests and has been recently adapted for aeroacoustic measurements through different treatments in fan and corner vanes, which reduced the turbulence level from 0.25% to 0.21% at 34 $\frac{m}{s}$ and the overall noise by approximately 4 dB in all velocities [19].

A 2D high-lift wing section model was used. The slat and flaps are attached to the wing main element (WME) by four brackets equally spaced along the span, starting at the border of the model. The model has 500 mm stowed chord and 1300 mm span and is mounted vertically on the wind tunnel by a turn-table that enables 1^0 precision changes in the angle of attack. Two-dimensional flow conditions were improved by a wall boundary-layer suction system placed at the borders of the model.

101 pressure taps were used for aerodynamic measurements and distributed as follows: 57 along the WME chord, 28 along the flap chord and 16 along the WME span. Acoustic measurements were performed with 61 G.R.A.S 46 BD microphones, which include a 26CB preamplifier and provide flat responses up to 70 kHz. They are flush-mounted in the wind tunnel side-wall in an optimized spiral array (Fig. 9), according to Fonseca, W. D. et al [23]. The array has an 850 mm diameter and is located at approximately 835 mm from the pressure side of the model. Figure 10 shows the model mounted at the wind tunnel and the microphones array. The post-processing was carried out through conventional Beamforming calculated in the frequency domain. The region of interest (ROI) used in the beamforming was established in the slat region (similar to the FW-H measurement region) along the entire span. For this case, the brackets were covered with foam to avoid interference of their noise with the slat spectra.

VI. Results

This chapter addresses the aerodynamic and aeroacoustic results of the baseline configuration obtained numerically and experimentally and also the differences in the fluid behavior caused by modifications in the slat internal geometry. Differences in the spectra, shear-layer and turbulence will be analyzed for each case.

A. Comparison with Experimental Results

Aerodynamic comparisons were carried out through the analysis of the pressure coefficient distribution obtained for each technique, shown in Fig. 11. The results agreed in both angles of attack and the experimental and numerical methods showed the same suction peak value and location in the main wing element and flap; differences in the suction

Fig. 9 Microphones array

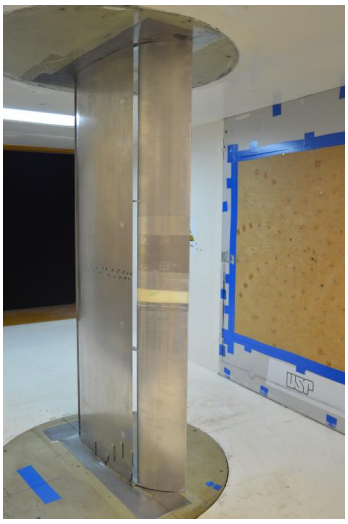

Fig. 10 Wind tunnel and model

region of the main element are probably due to the turbulence model, once the VLES method does not successfully predict the viscosity effects for a small models as this case. Differences in the flap trailing edge are caused by the lack of pressure taps closer to it. The good agreement in the main wing element leading edge supposes similar flow conditions in slat region in both wind tunnel and numerical simulations.

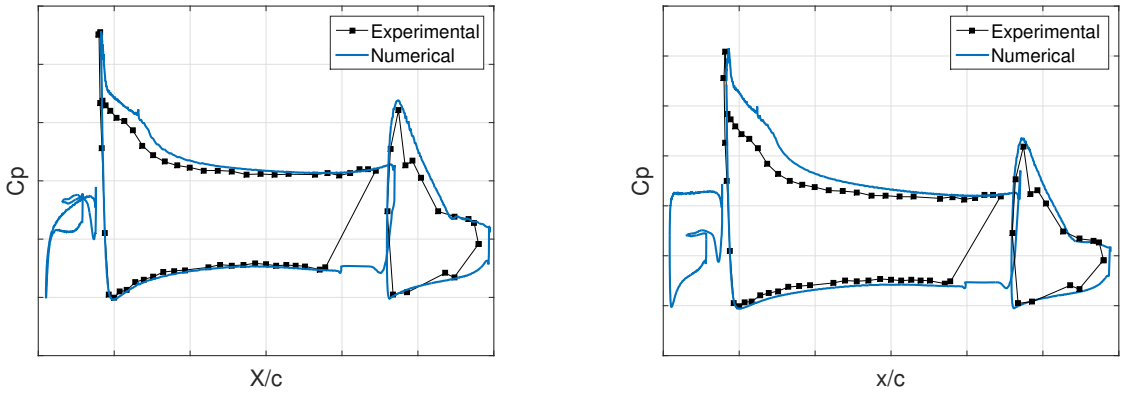

(a) $AoA = 0^o$ (b) $AoA = 4^o$

Fig. 11 Comparison between pressure coefficient distributions of the baseline configuration obtained numerically and experimentally at M = 0.098.

Another comparison was the reattachment point detected numerically and experimentally (Table 2). The reattachment point was estimated in simulations through the visualization of the streamlines on the surface and experimentally through hot-film sensors located in the trailing edge region [24]. Table 2 shows how the shear layer moves towards leading edge in function of the angle of attack.

Figure 12 shows the PSD obtained experimentally and numerically versus Strouhal number. For both AoA, both results exhibited the same maximum intensity and location. Although Numerical results over-predicted the broadband noise in all angles of attack, both techniques exhibited the same slope of PSD versus St up $St = 30$; above such St, numerical results revealed a larger drop of power spectrum in function of St than experimental ones, probably related to the loss of coherence in the phased array antenna and the dissipation of numerical results; furthermore, the slope of the experimental results can be affected by the slope of wind tunnel background noise. In spite of differences, experimental

and simulation results could be considered in agreement in the dominant part of the spectra. Table 3 shows the OSPL for St between 1.6 and 75, numerical results calculated the overall noise within 1.5 dB of precision for $AoA = 0^o$ and 2.3 dB for $AoA = 4^o$

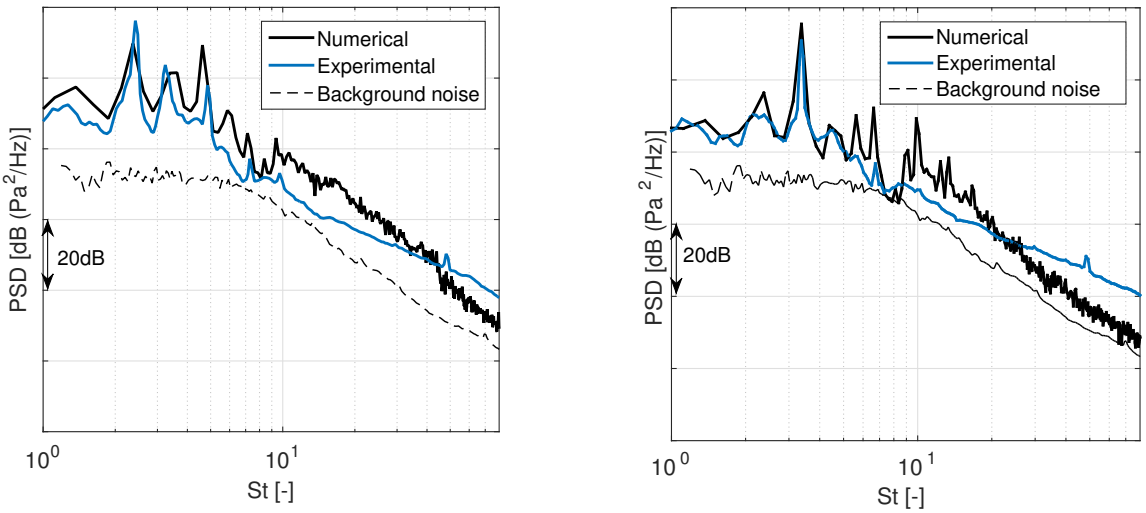

(a) $AoA = 0^o$ (b) $AoA = 4^o$

Fig. 12 Comparison between PSD radiated from the slat in the baseline configuration obtained numerically and experimentally at M = 0.098.

Table 2 Reattachment location in slat chord percentage for the baseline.

AoA [^{o}]	Experimental	Numerical
0	4.2	4.68
4	7.2	7.19

Table 3 OSPL for acoustic fluctuation between St 1.6 and 75

AoA [^{o}]	Experimental [dB]	Numerical [dB]
0	30.2	28.7
4	25.9	28.2

For the analysis of the source of slat noise, the PSD contour on the slat surface at mid-span is shown in Fig. 13. The St showed are those of the main peaks of the slat noise and a broadband noise Strouhal number ($St = 18$). Notably, the great pressure fluctuations occur around the trailing edge and reattachment region, however, in the case of broadband noise (d in Fig. 13) the higher pressure fluctuations region is extended until the slat cove. The same behavior of the slat noise calculated from FW-H analogy is observed, i. e., the first peak is the most intense and the second is the lowest and the noise level decreases in function of St.

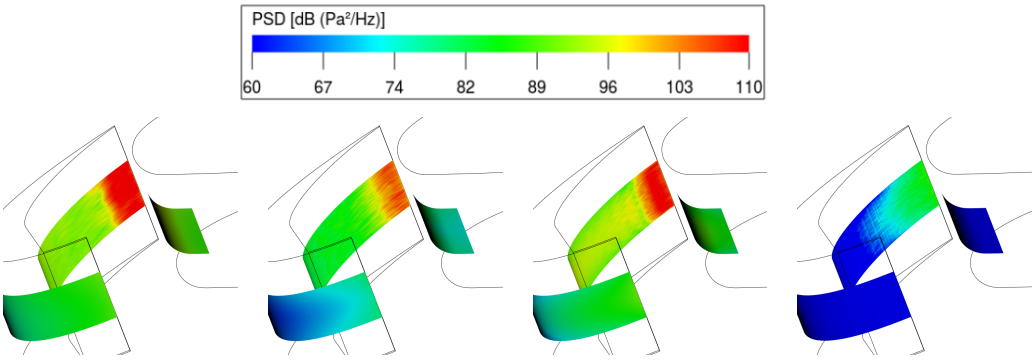

a) St 2.25 - 2.5 b) St 3.25 - 3.5 c) St 4.5 - 4.75 d) St 18 - 18.25

Fig. 13 PSD contour on the Slat surface.

B. Effect of Cusp Length

For determining the effect of the cusp length (κ) in the noise generation, five modifications in it were simulated. The cusp length did not change the lift coefficient (C_L); the major variation was an 1% increment in conf. κ191 (191% of the baseline cusp length) and drag coefficient (C_D) was reduced by cusp lengths shorter than the baseline configuration and increased by longer cusp length; a 5% reduction in C_D in conf. κ50 and a 7% increment in conf. κ191 were obtained. Variations in the pressure distribution for the extreme modifications are shown in Fig. 14. Configuration κ191 increased the suction peak in both slat and main element.

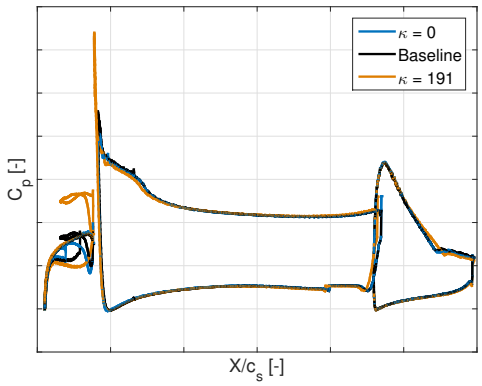

Fig. 14 Pressure coefficient distribution at midspan for configurations κ0, baseline and κ191.

Figure 15 shows the PSD of the different cusp length configurations. According to the results, longer cusps cause more noise than shorter ones in both tonal and broadband noise. Configuration κ0 reduced the mean discrete mid-frequency tones up to 10 *dB* and also the broadband noise until $St = 18$. Configuration κ25 reduced the tonal noise up to 7 *dB* and also the broadband noise until $St = 18$. Configuration κ50 did not reduce the tonal noise significantly, however, it modified the peak frequencies and, as in previous configurations, reduced the broadband noise until $St = 18$. Configurations κ150 and κ191 significantly increased (up 15 *dB*) the discrete tones and the broadband noise in all frequency ranges. Table 4 shows the Overall Sound Pressure Level (OSPL) integrated from $St = 1.8$ to $St = 50$. An 11 *dB* difference is detected between confs. κ191 and κ0. The Maximum peak is reduced in 6.7 *dB* for conf. κ0 and increased in 14 *dB* for conf. κ191 respect to the baseline configuration.

The main shear layer (MSL) trajectory length (from the cusp to the reattachment point) and the distance between the trailing edge and the reattachment are also shown in Table 4 for all κ configurations. Both distances are divided by the slat chord. Larger distances between the trailing edge and the reattachment point cause lower tonal noise and shorter

distances of the main shear layer increase the broadband noise. Configurations of cusp length shorter than that of the baseline showed a shear-layer trajectory with a nearly constant curvature, except in the reattachment region. However, the trajectory of the shear layer of configurations κ150 and κ191 exhibited an almost-perfect circle until the middle and, then, becomes almost straight until the reattachment point, as shown in Fig. 16.

Table 4 OSPL for acoustics fluctuations between St 1.8 and 50 and shear layer characteristics for different configurations of κ

Conf.	OSPL [dB]	Maximum peak [dB]	MSL length	Reattachment
κ0	-2.7	-6.7	0.820	0.074
κ25	-1.5	-4.43	0.80	0.066
κ50	-0.8	-1	0.73	0.054
Baseline	0	0	0.64	0.047
κ150	6.5	14.6	0.59	0.034
κ191	7.9	15	0.58	0.021

Figure 17 shows the RMS wall pressure coefficient distribution inside the slat cove for confs. κ0, κ191 and baseline. All configurations exhibited a peak at $X/c_s = 0.95$, associated with the reattachment of the main shear layer on the upper surface of the slat and represents one of the main sources of slat cove noise [20]. Configuration κ191 showed higher values of RMS wall pressure in all slat cove and a significant difference is observed in the peak region, associated with the increase in the mid-frequency tonal noise calculated in the far-field.

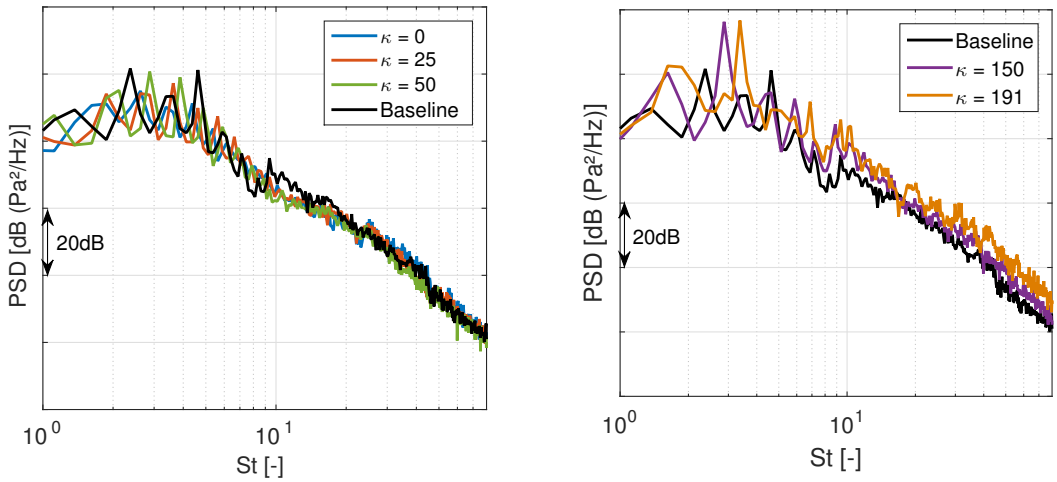

Fig. 15 PSD of different cusp length configurations at M = 0.098 and AoA = 0°.

The analysis of the difference between the velocities of the mixing layer is important, once it can be related to the turbulence and instability in the flow along the slat cove. Figure 18 shows the velocity magnitude in function of the stream-wise position near the cusp ($s/SL = 0.1$) and its derivative in the stream-wise direction for confs. κ0, κ191 and baseline. The zero point in the X-axis in both graphs refers to the location of the MSL. Configuration κ191 shows the major difference between the velocities that combined with a shorter distance traveled by the MSL generates an instability more intense in the flow, which results in an increment in the turbulence after the reattachment and broadband noise.

The instantaneous turbulent kinetic energy (TKE) of configurations κ0, κ191 and baseline is shown in Fig. 19. Configuration κ0 showed less turbulence and it is noted that vortices are dissipated along the shear layer, whereas the baseline and κ191 configurations exhibit an MSL trajectory with constant and high TKE, i. e., the flow is continuously supplied with turbulence energy. Figure 20 displays the PSD at midspan in the reattachment point, the trailing edge and the cusp of the same configurations. The cusp point shows the least PSD at all frequencies in all configurations,

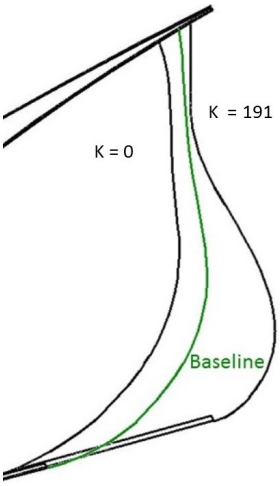

Fig. 16 MSL trajectory

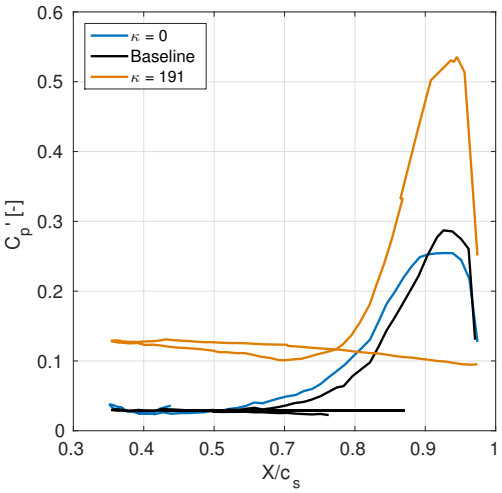

Fig. 17 RMS wall pressure coefficient distribution inside the slat cove for confs. κ0, baseline and κ191.

hereby, the mid-frequency peaks are more visible on the cusp than on the other points. The spectra in both trailing edge and reattachment are governed by the turbulence in those regions, however, the baseline and κ191 configurations still show the peaks in both points, i. e., the noise level is still higher than the turbulence level. Configuration κ0 shows less strong loop between the trailing edge and the cusp (responsible for tonal peaks), once the main shear layer trajectory is extremely large and the turbulence is dissipated along it.

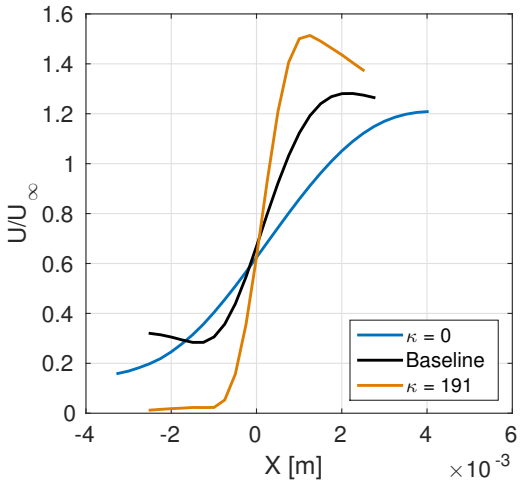

(a)

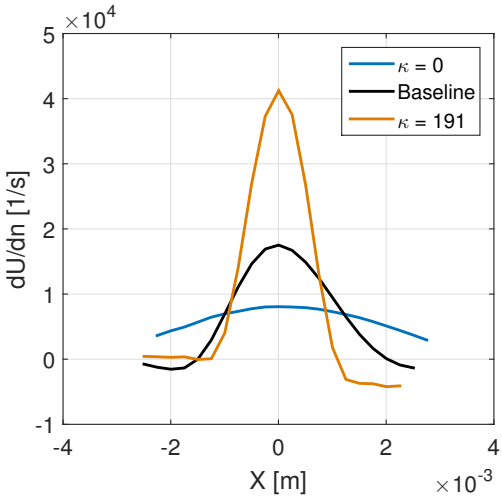

(b)

Fig. 18 Tangential velocity profile (a) and its stream-wise derivative (b) at $\frac{s}{SL}$ = 0.1 for conf. κ0, baseline and κ191

C. Effect of Trailing Edge Angle

Five modifications of the angle of trailing edge (α) were simulated for understanding their relation with the slat noise. The angles were varied 5^o from each other. Similarly to variations in the cusp length, variations in the trailing edge

angle did not affect the aerodynamics of the wing. No changes were observed in the lift coefficient, however, the drag coefficient increases when the trailing edge angle increases. No variations were detected in the C_p distribution (Fig. 21)

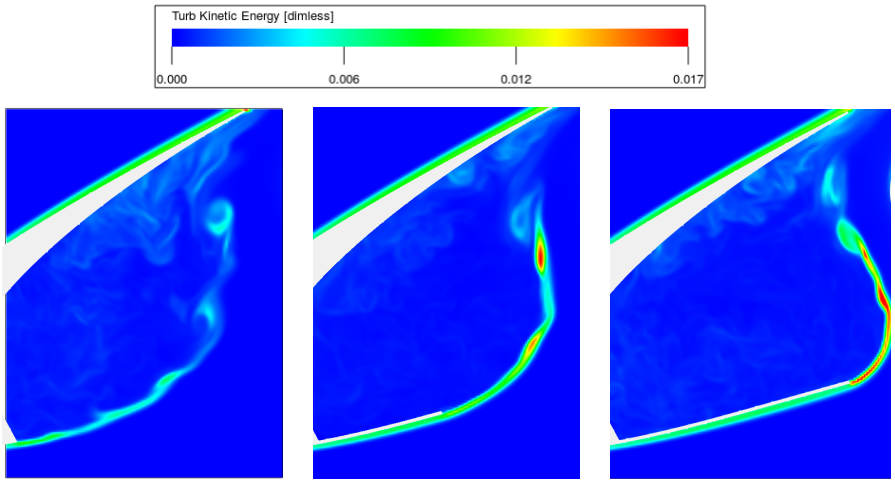

a) $\kappa 0$ b) Baseline c) $\kappa 191$

Fig. 19 Instantaneous dimensional-less turbulent kinetic energy for conf. $\kappa 0$, baseline and $\kappa 191$.

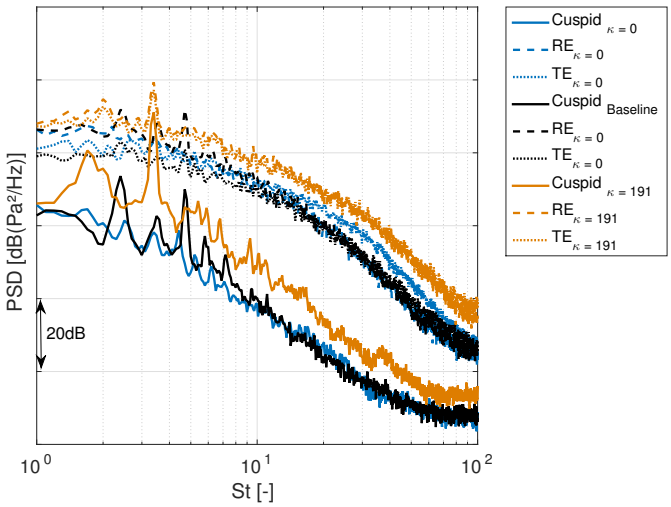

Fig. 20 PSD at cusp , trailing edge and reattachment point at midspan for configurations $\kappa 0$, baseline and $\kappa 191$ at M = 0.098 and AoA = 0°.

The PSD versus the St for all configurations of α is shown in Fig. 22. Angles of trailing edge smaller than that of the baseline increased mid-frequency tonal noise, once thin trailing edges increase the resonance in the slat cove. Conversely, angles of trailing edge larger than of the baseline reduce the mid-frequency tonal noise and increase the broadband noise, once the thick trailing edges fill part of the slat cove and reduce the cavity resonance and the increment in the broadband noise is related to the increment of turbulence in the trailing edge region.

The configuration of the 20^0 trailing edge angle ($\alpha 20$) reduced in 5 dB the first peak and 8 dB the third and increased approximately 5 dB the broadband noise in all Strohual numbers above $St = 17$, in comparison with the baseline configuration. On the other hand, conf. $\alpha - 5$ increased in 5 dB the first peak and 3 dB the fourth and fifth ones, and did not affect the broadband noise. The OSPL integrated from $St = 1.8$ to $St = 50$ and the maximum peak for each

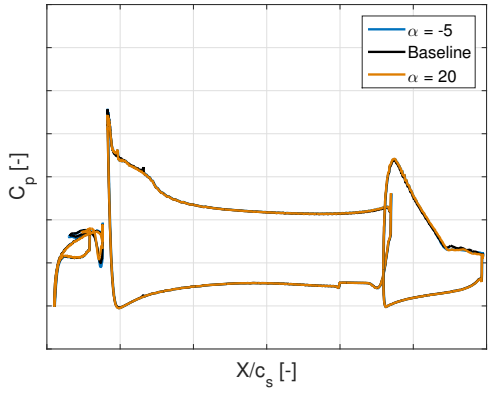

Fig. 21 Pressure coefficient distribution at midspan for configurations $\alpha - 5$, baseline and $\alpha 20$.

configuration are showed in Table 5. The OSPL decreases as the angle of the trailing edge increases; a difference of 3.7 *dB* between the extreme configurations was detected. Configuration $\alpha - 5$ increases the maximum peak in 6 *dB*, whereas conf. $\alpha 20$ reduces the maximum peak in 5 *dB* respect to the baseline configuration.

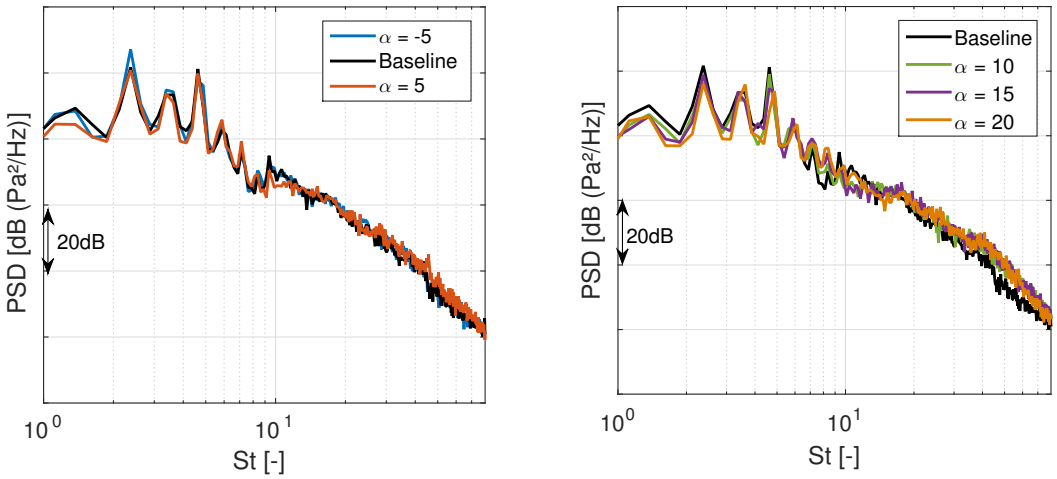

Fig. 22 PSD of different configurations of the trailing edge angle at M = 0.098 and AoA = 0º.

Table 5 also shows the MSL length from the cusp until the reattachment and the distance between the trailing edge and the reattachment point, divided by the slat chord, of each trailing edge configuration. As in variations in the angle of attack and cusp length, larger distances between the trailing edge and the reattachment point cause lower tonal noise levels and shorter distances of the MSL cause higher broadband noise. No differences were found in the MSL trajectory among configurations.

The RMS wall pressure in the slat cove for confs. $\alpha - 5$, $\alpha 20$ and baseline is shown in Fig. 23. Configuration $\alpha 20$ exhibits a lower c'_p peak than the other configurations, associated with the lower mid-frequency noise radiated.

The TKE of conf. $\alpha 20$ in the shear layer and in the region of the trailing edge is greater than that of the other configurations (Fig. 24), which can be related to the larger difference between velocities on the mixing shear layer (Fig. 25). Such characteristics in conjunction with a shorter MSL length increase the broadband noise, as in conf. $\kappa 191$.

Table 5 OSPL for acoustics fluctuations between St 1.8 and 50 and shear layer characteristics for different configurations of α

Conf.	OSPL [dB]	Maximum peak [dB]	MSL length	Reattachment
$\alpha - 5$	1.5	6.5	0.65	0.033
Baseline	0	0	0.65	0.047
$\alpha 5$	0	0	0.64	0.06
$\alpha 10$	-1.7	-1.7	0.62	0.061
$\alpha 15$	-0.9	-2.1	0.61	0.073
$\alpha 20$	-2.2	-4.6	0.59	0.083

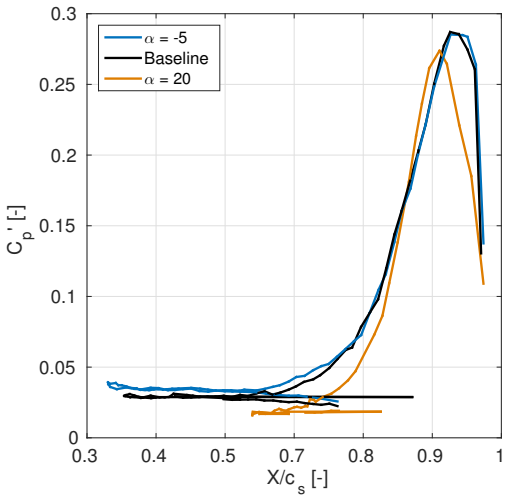

Fig. 23 RMS wall pressure coefficient distribution inside the slat cove for confs. $\alpha - 5$, baseline and $\alpha 20$.

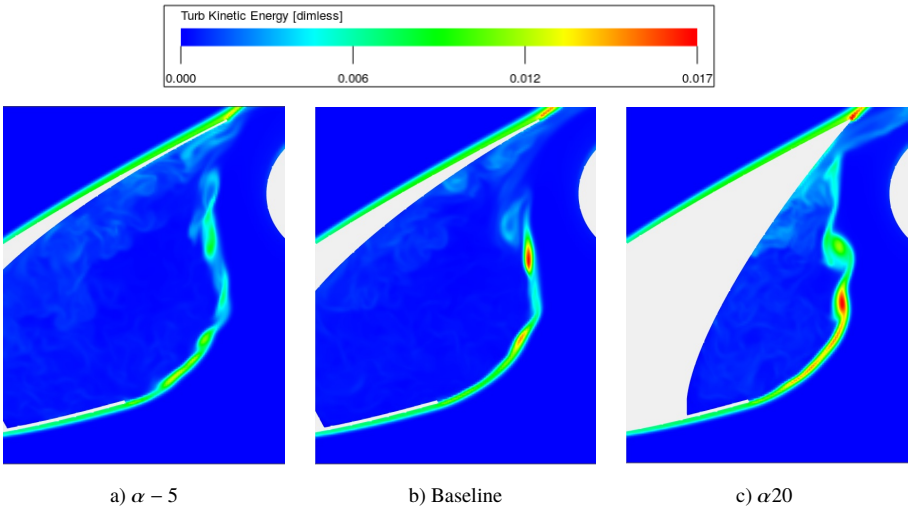

a) $\alpha - 5$ b) Baseline c) $\alpha 20$

Fig. 24 Instantaneous TKE for different configurations of α and baseline.

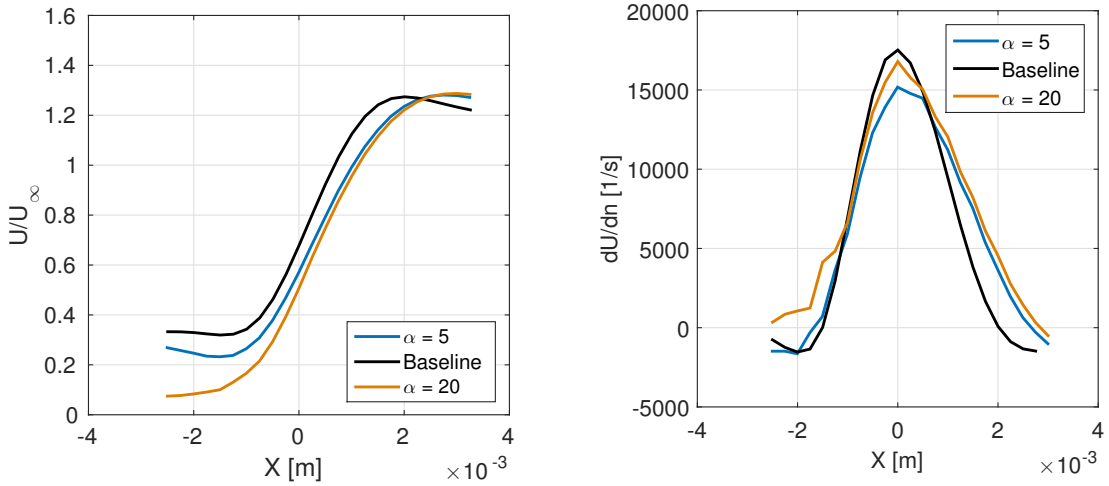

(a) (b)

Fig. 25 Tangential velocity profile (a) and its stream-wise derivative (b) at $\frac{s}{SL} = 0.1$ for conf. $\alpha - 5$, baseline and $\alpha 20$

Figure 26 displays the PSD at midspan at the trailing edge, reattachment and cusp of configurations $\alpha - 5$, $\alpha 20$, and baseline. Such configurations did not show significant differences in the spectra in the trailing edge and reattachment. However, some differences in the spectra were detected on the cusp. As calculated by the FW-H analogy, the spectra on the cusp showed conf. $\alpha - 5$ increases the mid-frequency peaks, whereas conf. $\alpha 20$ reduces them and increases the broadband noise.

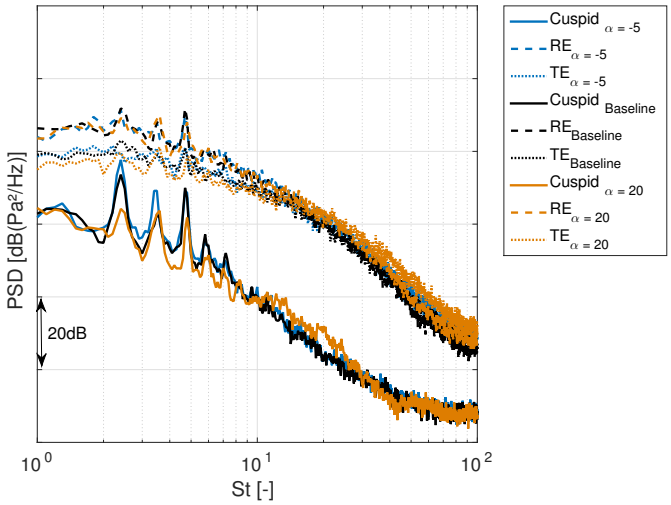

Fig. 26 PSD at cusp, trailing edge and reattachment point at midspan for configurations $\alpha - 5$, baseline and $\alpha 20$ at M = 0.098 and AoA = 0º.

D. Effect of the Angle of the Cusp

Differently from the other cases, the cusp angle does not affect the aeroacoustics and the aerodynamics of the wing. Figure 27 shows the PSD for different configurations of cusp angle. No changes on the mid-frequency peaks

or broadband noise were detected. Configuration $\beta 15$ reduced 1 dB the OSPL integrated from $St = 1.8$ to $St = 50$. The reattachment point of all configurations of cusp angle was located around 0.045 from the trailing edge and no differences in the shear layer trajectory, length and the spectra at different points of slat surface were found.

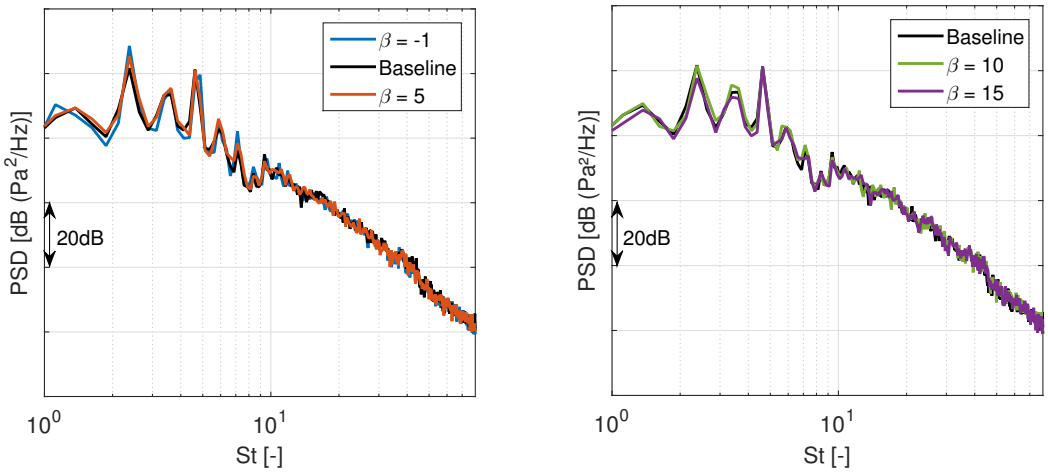

Fig. 27 PSD of different configurations of cusp angle at M = 0.098 and AoA = 0º.

VII. Conclusions

Experiments and numerical simulations (using LBM and FW-H analogy) of a 2D high-lift model at various angles of attack were carried out. The good-concordance between both methods on aerodynamic and aeroacoustic results validated the simulation methodology.

Slat spectrum is characterized by tonal peaks and broadband noise. The tonal components arise due to the feedback loop between the trailing edge and the cusp and are supplied by the main shear layer and the acoustic waves generated when the MSL impinges the upper surface of the slat, similarly to the cavity-noise phenomena. Broadband noise is related to the turbulence on both trailing edge and slat cove, therefore, larger differences between the two velocities of the mixing layer cause louder broadband noise. Simulations showed larger distances between the trailing edge and the reattachment point cause lower tonal noise, whereas larger trajectories of the main shear layer cause lower broadband noise.

The cusp length exerted the major influence on the slat noise generation. A longer cusp increases both tonal and broadband noises, whereas the slat configuration with no cusp reduces noise in all frequencies. Larger angles of trailing edge reduce the tonal noise, however, they increase the broadband noise (due to the increase in the turbulence around the trailing edge), whereas smaller ones increase the mid-frequency tones. The angle of the cusp has a small influence on noise generation. No configuration changes the lift coefficient, however, longer cusp and larger trailing edge angles increase the drag coefficient.

Future studies aim at analyses of other geometrical parameters and verification of possible benefits achieved through combinations of the best configuration of each parameter.

Acknowledgments

The authors acknowledge the Conselho Nacional de Desenvolvimento Científico e Tecnológico (CNPq), Coordenação de Aperfeiçoamento de Pessoal de Nível Superior (CAPES) and A Financiadora de Estudos e Projetos (FINEP) for the financial support provided to this research

References

[1] Dobrzynski, W., Nagakura, K., Gehlhar, B., and Buschbaum, A., "Airframe noise studies on wings with deployed high-lift devices," *4th AIAA/CEAS Aeroacoustics Conference*, 1998, p. 2337.

[2] Federal Aviation Regulation, "www.faa.gov," June 2017.

[3] Chow, L., Mau, K., and Remy, H., "Landing gears and high lift devices airframe noise research," 2002, p. 2408.

[4] Gleine, W., Mau, K., and Carl, U., "Aerodynamic noise reducing structure for aircraft wing slats," , May 2002.

[5] Smith, M., Chow, L., and Molin, N., "Attenuation of slat trailing edge noise using slat gap acoustic liners," *12th AIAA/CEAS Aeroacoustics Conference (27th AIAA Aeroacoustics Conference)*, 2006, p. 2666.

[6] Pascioni, K. A., and Cattafesta, L. N., "Aeroacoustic Measurements of Leading-Edge Slat Noise," *22nd AIAA/CEAS Aeroacoustics Conference*, 2016, p. 2960.

[7] Mau, K., and Dobrzynski, W., "Flexible airflow separator to reduce aerodynamic noise generated by a leading edge slat of an aircraft wing," , 2004.

[8] Choudhari, M. M., and Khorrami, M. R., "Slat Cove Unsteadiness Effect of 3D Flow Structures," 2006.

[9] Pagani, C. C., Souza, D. S., and Medeiros, M. A., "Slat noise: aeroacoustic beamforming in closed-section wind tunnel with numerical comparison," *AIAA Journal*, Vol. 54, No. 7, 2016, pp. 2100–2115.

[10] Dobrzynski, W., and Pott-Pollenske, M., "Slat noise source studies for farfield noise prediction," *7th AIAA/CEAS Aeroacoustics Conference and Exhibit*, 2001, p. 2158.

[11] Dobrzynski, W., "Almost 40 years of airframe noise research: what did we achieve?" *Journal of aircraft*, Vol. 47, No. 2, 2010, pp. 353–367.

[12] Guo, Y., and Joshi, M., "Noise characteristics of aircraft high lift systems," *AIAA journal*, Vol. 41, No. 7, 2003, pp. 1247–1256.

[13] Pott-Pollenske, M., Wild, J., and Bertsch, L., "Aerodynamic and acoustic design of silent leading edge devices," *20th AIAA/CEAS Aeroacoustics conference*, 2014.

[14] Guo, Y., "Aircraft slat noise modeling and prediction," *AIAA paper*, Vol. 3837, 2010, p. 2010.

[15] Succi, S., Benzi, R., and Higuera, F., "The lattice Boltzmann equation: A new tool for computational fluid-dynamics," *Physica D: Nonlinear Phenomena*, Vol. 47, No. 1-2, 1991, pp. 219–230.

[16] Chen, S., and Doolen, G. D., "Lattice Boltzmann method for fluid flows," *Annual review of fluid mechanics*, Vol. 30, No. 1, 1998, pp. 329–364.

[17] Crouse, B., Freed, D., Balasubramanian, G., Senthooran, S., Lew, P.-T., and Mongeau, L., "Fundamental aeroacoustic capabilities of the lattice-Boltzmann method," *AIAA paper*, Vol. 2571, 2006.

[18] He, X., Doolen, G. D., and Clark, T., "Comparison of the lattice Boltzmann method and the artificial compressibility method for Navier–Stokes equations," *Journal of Computational Physics*, Vol. 179, No. 2, 2002, pp. 439–451.

[19] Santana, L. D., Carmo, M., Catalano, F. M., and Medeiros, M. A., "The Update of an Aerodynamic Wind-Tunnel for Aeroacoustics Testing," *Journal of Aerospace Technology and Management*, Vol. 6, No. 2, 2014, pp. 111–118.

[20] Terracol, M., Manoha, E., and Lemoine, B., "Investigation of the unsteady flow and noise generation in a slat cove," *AIAA Journal*, Vol. 54, No. 2, 2015, pp. 469–489.

[21] Bres, G. A., Pérot, F., and Freed, D., "A Ffowcs Williams-Hawkings solver for Lattice-Boltzmann based computational aeroacoustics," *AIAA paper*, Vol. 3711, 2010, p. 2010.

[22] Catalano, F., "The New Closed Circuit Wind Tunnel of the Aircraft Laboratory of University of Sao Paulo, Brazil," *24TH International Congress of the Aeronautical Sciencies ICAS*, 2004.

[23] Fonseca, W. D., Ristow, J. P., Sanches, D. G., and Gerges, S. N., "A different approach to archimedean spiral equation in the development of a high frequency array," Tech. rep., SAE Technical Paper, 2010.

[24] Lima Pereira, L. T., Rego, L. F., Catalano, F. M., Cafaldo Reis, D., and Lobão Capucho Coelho, E., "Experimental Slat Noise Assessment Through Phased Array and Hot-Film Anemometry Measurements," *2018 AIAA Aerospace Sciences Meeting*, 2018, p. 0758.

AIAA AVIATION Forum
June 25-29, 2018, Atlanta, Georgia
2018 AIAA/CEAS Aeroacoustics Conference

10.2514/6.2018-3458

Experimental and Numerical Analysis of the Aerodynamic and Aeroacoustic Properties of a 2D High-Lift Wing Model

Lourenço T. L. Pereira*, Laura Botero-Bolívar†, Matheus T. de Araujo ‡ and Fernando M. Catalano§
University of São Paulo (EESC-USP), São Carlos, Brazil

Danillo C. Reis¶ and Eduardo L. C. Coelho‖
EMBRAER, São José dos Campos, Brazil

Aerodynamic and acoustic measurements of a 2D high-lift wing-section in flap full span deployed and flap side-edge (half span deployed) configurations are investigated both experimentally and numerically to understand the acoustic noise characteristics and the mechanisms of noise generation presented both in the slat and flap side-edge. Experimental analysis is carried out at the LAE-1 closed test section wind-tunnel and measured data includes phased array beamforming results along with steady pressure and hot-film anemometry measurements while numerical analysis using the PowerFLOW® software intends to replicate wind-tunnel conditions with hard-wall boundaries and results from both aerodynamic unsteadiness and far field predictions are presented. The high-lift model is a 2D wing model with single slotted flaps and slats. Tests were conducted both in full deployed flap or in half stowed configuration, for flap side-edge noise analysis. Results provide also comparisons between numerical and experimental data for steady aerodynamic data regarding surface pressure and flap side-edge vortex measurements along with unsteady aerodynamic measurements taken from hot-film anemometry performed at the slat in both chordwise and spanwise directions and far field acoustic noise predictions.

Nomenclature

α	Angle of attack $[^o]$
γ^2	Coherence [-]
c	Reference chord $[m]$
C_P	Pressure coefficient [-]
M	Mach number $\left(\frac{U_\infty}{a}\right)$ [-]
PSD	Power spectral density $[Pa^2/Hz]$
Re	Reynolds number $\left(\frac{\rho U c}{\mu}\right)$ [-]
RMS	Root-mean-square
OASPL	Overall Sound Pressure Level $[Pa^2]$
St	Strouhal number based on element chord $\left(\frac{fc}{U}\right)$ [-]
Subscript	
s	Slat
f	Flap

*MSc student, Aeronautical Engineering Department, EESC-USP, lourenco.tercio@gmail.com.
†MSc student, Aeronautical Engineering Department, EESC-USP, lauraboterob@hotmail.es.
‡PhD student, ICMC, ICMC-USP, matheustozo@gmail.com .
§Professor, Aeronautical Engineering Department, EESC-USP, catalano@sc.usp.br.
¶Noise and Vibration Engineer, R&T department, EMBRAER, danillo.reis@embraer.com.br.
‖Noise and Vibration Engineer, R&T department, EMBRAER, eduardo.capucho@embraer.com.br.

I. Introduction

Airframe noise sources have become more important with the developments in high-bypass turbofan engines and therefore efforts have been focused on comprehending, modeling and mitigating those sources. According to Dobrizinsky [1], airframe acoustic emissions are dominated by landing gears and high-lift devices, specifically trailing-edge of the slats and the side-edges of the flaps.

Slat sources are mainly dominated by the interaction between unsteady flow generated at the slat shear layer and the downstream surfaces, e.g. trailing-edge and wing main element [2]. This generates an spectrum shaped by three possible components, i.e.: i. broadband components, ii. mid-frequency tones and a iii. single high-frequency tone [3]. The first component is characteristic of all slat models and is most probably generated by the shear layer interaction with the downstream elements, mainly the slat trailing edge, whereas the high-frequency tone is related to the vortex shedding behind blunt trailing edges and is therefore not supposed to be observed in flight conditions. The mid-frequency tonal components are doubtful in relation to its Reynolds dependency with some authors describing tonal suppression with increased Reynolds number tests [4, 5] and others witnessing no modification or even higher tonal levels when Reynolds number is increased or tripping devices at the slat pressure side are added [6, 7]. The mid-frequency tones are related to a feedback between the vortices generated at the slat cusp and the acoustic waves at the slat cove.

As for the flap side-edge mechanisms, the forces created at the flap side surface due to vortices in formation and side-edges shear-layers are known to be the most important sources according to Rossignol [8]. The interaction between the vortices formed at the suction side aft-half chord and the flap lateral surface is known to be the main reason for the low-frequency noise while the shear-layer formed at the flap pressure side and its interaction with the side-edge borders in the forward half chord is the main cause for the mid-to-high frequency contents.

In order to assess high-lift noise characteristics, experiments seek acoustic and aerodynamic measurements to understand far field acoustic properties and its correlation with the aerodynamic behaviors responsible for the noise generation. Moreover, computational methods have greatly contributed to the understanding of aeroacoustic sources by providing detailed information about flow unsteadiness beyond what is physically limited to be obtained experimentally.

This study combines the experimental results for a 2D high-lift model in flap full deployed and flap side-edge configuration measuring aerodynamic steady and unsteady characteristics along with acoustic far field data with numerical simulations for the same model configuration, combining therefore the several conditions measured at the wind tunnel with the density of information provided by the CFD/CAA simulations.

II. Model

The high-lift wing model is a 2D airfoil section with slat and single flap and was developed for tests in three configurations, i.e.: stowed flap, flap full deployed and flap side-edge which is obtained using half flap span deployed only. The model has a span of 1.3 m and a stowed chord of 0.50 m. The angle of attack is referenced as 0^o for the flow aligned to the stowed chord line and, by means of a turn-table system that holds the model at the wind-tunnel, the wing is allowed to rotate with 1^o precision. Four equally spaced steel brackets starting at the model ends supports the flap and the slat at the correct overlap, gap and deflection angles.

Fig. 1 shows the model in the two different configurations analysed in this work, i.e.: i. flap full deployed, and ii. flap side-edge.

The model is tested without tripping with the exception of the slat pressure side, where boundary-layer tripping was applied for the assessment of the mid-frequency slat tones. In the experimental study of Pereira et al. [9] it was decided to follow all tests using a sand tripping with 0.5%c maximum height and 23.5%c length located 15 mm apart from the slat cusp.

Due to the high tonal components coming from the slats, tests for the Flap Side-Edge configuration are carried out using slat cove fillers over its entire span. The cove filler geometry was selected to minimally disturb slat flow and maximally suppress mid-frequency slat tones.

III. Experimental Set-up

A. Facility

The campaign was conducted at the LAE-1 wind-tunnel of the São Carlos School of Engineering of the University of São Paulo (EESC-USP). The $1.3 \times 1.7 \times 3.0$ m closed test section wind tunnel was developed for aerodynamic tests[10] and received an acoustic treatment in order to allow aeroacoustic campaigns.

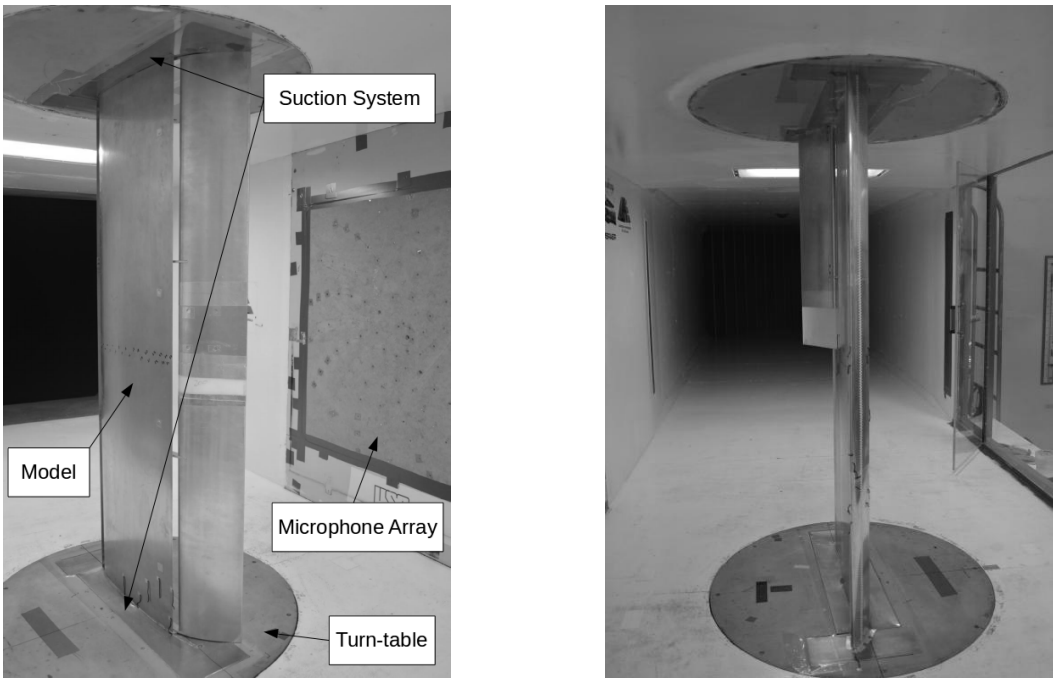

(a) Flap Full Configuration [9]. (b) Flap Side-Edge Configuration.

Fig. 1 SILENCE 2D high-lift model mounted at the LAE-1 wind-tunnel.

Driven by a 110 hp motor with an 8 blade fan, the wind-tunnel reaches velocities of up to 40 m/s with turbulence levels below 0.26% by means of two screens located before the contraction. The acoustic treatment consisted of improvements on the motor insulation and fan tip to wall gap reduction (C), installation of a splitter between the turning-vanes (D) and melamine foam at the wind tunnel walls (A and B), resulting in a total reduction of 4 dB in overall background noise (Ref. [11]) as depicted by Fig. 2 which depicts the regions that received the acoustic treatment.

A wall boundary-layer suction system at the wind-tunnel turn-tables is used to attenuate wall effects over the model and improve flow uniformity over the model span. Suction is applied to the test section walls through a perforated plate with 21% porosity and driven by a 9.2 kW motor. Following the studies from Ref. [9], suction with 50 % of maximum capacity is used in three different locations, e.g.: i. slat leading-edge, ii. wing main-element suction side and iii. flap suction side.

B. Wind-tunnel Instrumentation

Acoustic measurements are performed with a 61 flush mounted microphone array that uses G.R.A.S. 46BD microphones arranged in a modified spiral geometry, optimized to reduce side-lobes in high-frequency maps [12].

The data acquisition is performed with a PXIe system containing a PXIe-8840 controller and 4 PXIe-4497 boards for IEPE microphone acquisition. Although microphones present flat response up to 70 kHz, data is acquired with a sample rate of 102400 Hz and post-processed with conventional beamforming technique (CBF), using Source Power Integration (SPI) technique to integrate the maps and generate acoustic spectrum information.

C. Model Instrumentation

1. Pressure Taps

The model is instrumented with a total of 101 pressure taps that are connected to a ScaniValve ZOC33/64 PX X2 system and distributed as follows:

- 57 taps along the WME chord;
- 28 taps along flap element chord (5 mm) from side-edge;

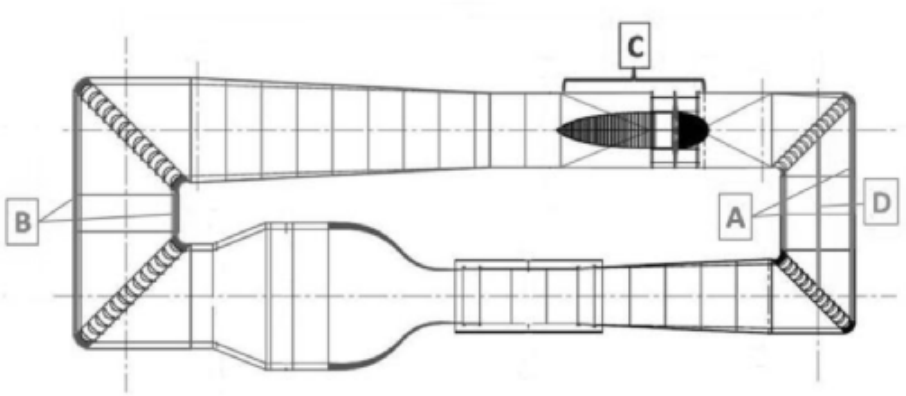

Fig. 2 LAE-1 wind tunnel facility from the São Carlos School of Engineering, University of São Paulo [11].

- 16 taps along the main element span.

WME taps were drilled during the model manufacturing and the flap pressure taps were 3D printed from the PolyJet process. No taps are used on the slat due to difficulties faced in the past with interference of the tubes in the smoothness of the slat cove surface.

2. Hot-Film Sensors

Hot-film sensors were glued to the model at the slat cusp and cove. A single sensor was also used at the slat cusp to assess tripping effects and flow spectrum emerging from the cusp. Senflex®SF93112 patches with 10 sensors spaced by 2.5 *mm* one from each other were installed at the slat cove close to the reattachment region. Also, 6 sensors spaced by 20 *mm* were installed at the spanwise direction close to the shear-layer reattachment location in order to assess spanwise coherence over the model. Anemometry conditioning is performed by a Constant Voltage Anemometry (CVA) system with flat response up to 36 kHz.

IV. Numerical Procedures

Simulations were carried out using the commercial version of PowerFLOW 5.3 ®, which uses the Lattice Boltzmann methodology (LBM). Different from conventional continuum solvers, LBM incorporates the physics of microscopic processes, considering the fluid behaving as fraction particles following specific interaction equations [13]. The solver uses a k-epsilon RNG turbulence model with appropriate extensions that are equivalent to very large eddy simulations (VLES). Near-wall elements are treated by the law of the wall velocity profile.

The dimensions of the computational domain were 1.3 *m* x 1.7 *m* x 5 *m*, replicating the wind tunnel dimensions. Atmospheric conditions used in the simulations were the same as those of the wind tunnel with turbulence levels set to 0.21% (wind tunnel turbulence level according to Ref. [11]) and turbulence length scale of 1 *mm*. The outlet condition was imposed with no pressure gradient and the wind tunnel walls were set as non-friction hard walls. The outermost fluid region was modeled as high viscosity fluid or anechoic layer for the absorption of acoustic waves.

The mesh was defined by 10 refinement regions with minimum size elements of 0.25 *mm* defining all the Ffowcs Williams-Hawkins (FW-H) measurement region, and greater element size was 128 *mm*. Simulations took around 30240 CPU hours for 320 million elements and 851000 time steps (0.34 sec).

FW-H measurements were taken for a crop in the middle of the model span whose dimensions were $3.5c_s \times 4.7c_s \times 2.3c_s$ for the slat and $2.0c_f \times 1.2c_f \times 1.4c_f$ for the flap side-edge, where X is in the stream-wise direction and Z in the span-wise direction. Comparisons with the beamforming results were performed for a microphone at the center of the microphone array and numerical measurements were taken for 0.2 seconds starting after steady convergence, at 0.147 sec, with a sampling frequency of 82 kHz.

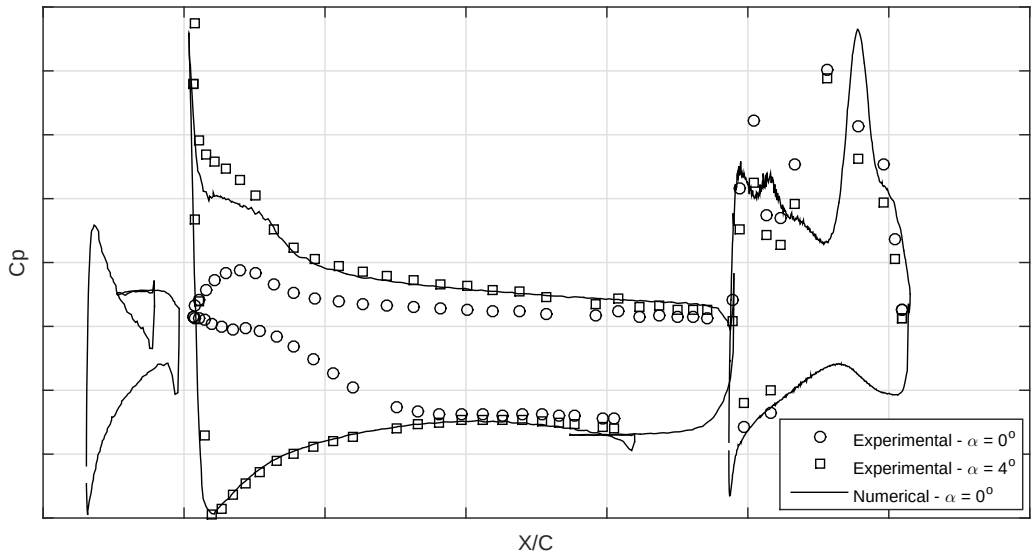

Fig. 3 Comparison between experimental and numerical steady pressure distribution at different angles of attack ($M = 0.11$ and $Re = 1.1 \times 10^6$).

V. Results

A. Flap Side-Edge Configuration

1. Steady Pressure Distribution

Steady pressure distribution over the model (Fig. 3) demonstrates how numerical results compare with the experimental measurements for the side-edge configuration pointing out to a shift in the angle of attack of approximately 4^o at the wing main element (WME) compared to the experiments. At 0^o, the experimental curves depict a situation where the slat is clearly not working properly with no stagnation point formed at the WME while the 4^o case presents a very similar curve to the numerical case at the WME, with the exception of the separation bubble upstream the suction peak, which happens in a lower pressure gradient and smaller length in the experiments.

Also, experimental results reveal a side-edge suction side vortex, characterized by the second low pressure region at the flap measurements, starting upstream from predicted by the numerical results and with lower suction values.

2. Far field Acoustic Noise

Comparisons between results obtained numerically and experimentally (Fig. 4) show still a level discrepancy of about 4 *dB* that is possibly caused by differences between experimental and numerical post-processing, realized by an in-house software and considering the measurements of microphones in different locations and by the PowerFLOW® tools predictions for a single location respectively. Both spectra though present a similar behavior within the frequency range, with a maximum between $St = 5$ (considering the flap chord) and a roll-off with approximately $-15\ dB/dec$.

Looking at the experimental beamforming maps (Fig. 5) it is observed that noise is associated only with the side-edge vortex with no contamination from different sources and almost no side-lobe interference. The source is located close to the flap half chord and matches the region of maximal velocity intensity found by the experimental pressure distribution. It is also interesting to spot that for Strouhal numbers above 30 two visible sources starts to emerge and for the highest Strouhal displayed (100.5) two sources in similar levels are already visible, one close to the middle of the flap side-edge and another close to the flap leading-edge or the middle of the stowed section. Two explanations are possible for these phenomena, a first one considering two important noise sources coming from different shear-layers formed at flap side-edge and another considering the vortex formed at the stowed element as the second noise source.

The filtered spectrum over the flap side-edge from the numerical results and the vortex side-edge vorticity contours (Fig. 6 and 7) reveals how the integrated pressure fluctuations in a range between Strouhal 4.4 and 44 are spread over the

side-edge, suggesting that the interaction between the pressure side vortex and the side-edge surface plays a major role in noise generation while higher Strouhal fluctuations are influenced by the shear-layer over the edges of the model. Two distinct edges of maximum fluctuations are observed due to the shear-layer interactions with the side-edge upper side in the aft-half chord and the lower side at the forward half chord and, together with the smaller beamwidth for the higher frequencies at the beamforming maps, could be the reason behind the observed two sources in the experimental maps.

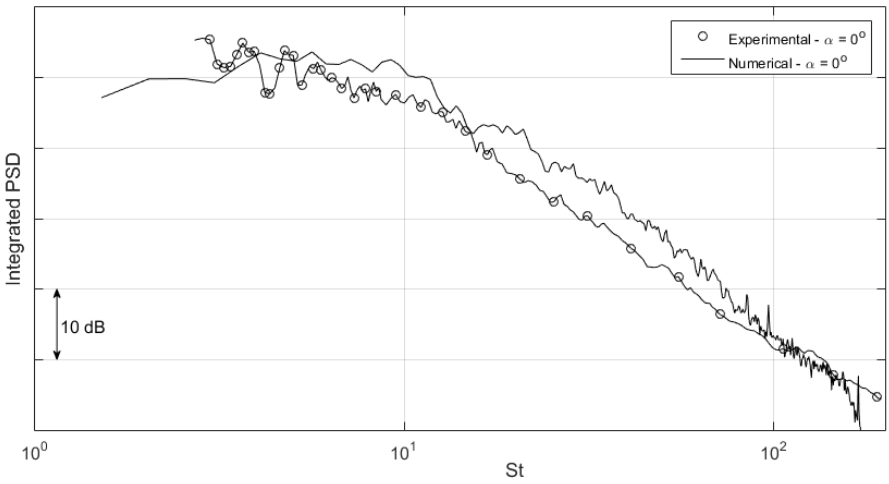

Fig. 4 Comparison between experimental and numerical flap side-edge noise spectrum measured with CBF and single location data respectively ($M = 0.11$, $Re = 1.1 \times 10^6$ and $\alpha = 0^o$).

As observed in the pressure distributions, the angle of attack has a small influence in the flap spectrum (Fig. 8) since circulation is almost unaffected by the changes in the angle of attack, with maximum levels obtained for $\alpha = 4^o$ and a small decrease for $\alpha = 8^o$. A higher level increase is observed at high Strouhal numbers ($St > 50$). The noise directivity presents higher levels in the direction of 30^o for small Strouhal numbers and it moves to 60^o for higher frequencies as the former dipole-like structure changes due to the reflections of the small wavelengths on the model.

As for the Mach and Strouhal number scaling, Fig. 9 and 10 show experimentally how far field flap side-edge noise spectrum is scaled based on the element chord Strouhal and Mach number. Despite the small number of velocities tested, three Mach number variations have demonstrated a better fit for the measurements scaled with the Strouhal number and the Mach to the power of 5.5, also suggested by the Overall Sound Pressure Level scaling (Fig. 10(a)). The variation of the average Mach scale factor with the frequency (Fig. 10(b)) indicates that scaling starts with values close to 6 for low frequencies and decreases for higher frequencies, reaching values close to 5, corroborating to the hypothesis of two different mechanisms for side-edge noise explored by Ref. [8], one related to the pressure fluctuations over the flap surface and a second, for higher frequencies, related to the sound coming from the surface edges (Ref. [14]).

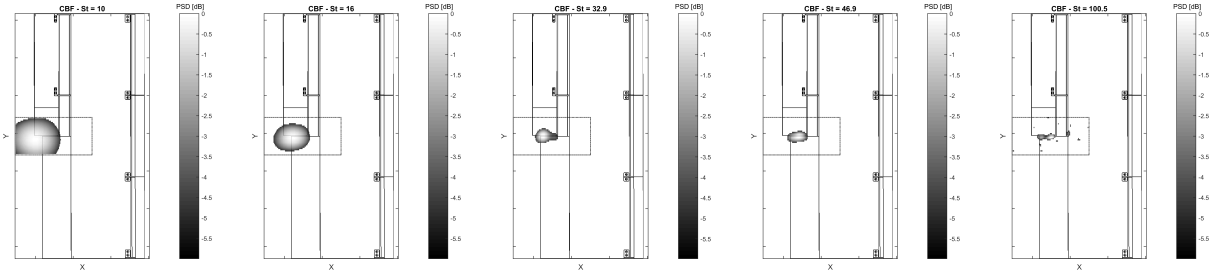

(a) $St = 10.0$ (b) $St = 16.0$ (c) $St = 32.9$ (d) $St = 46.9$ (e) $St = 100.5$

Fig. 5 Beamforming maps obtained for the flap side-edge configuration at $M = 0.11$, $Re = 1.1 \times 10^6$ and $\alpha = 0^o$.

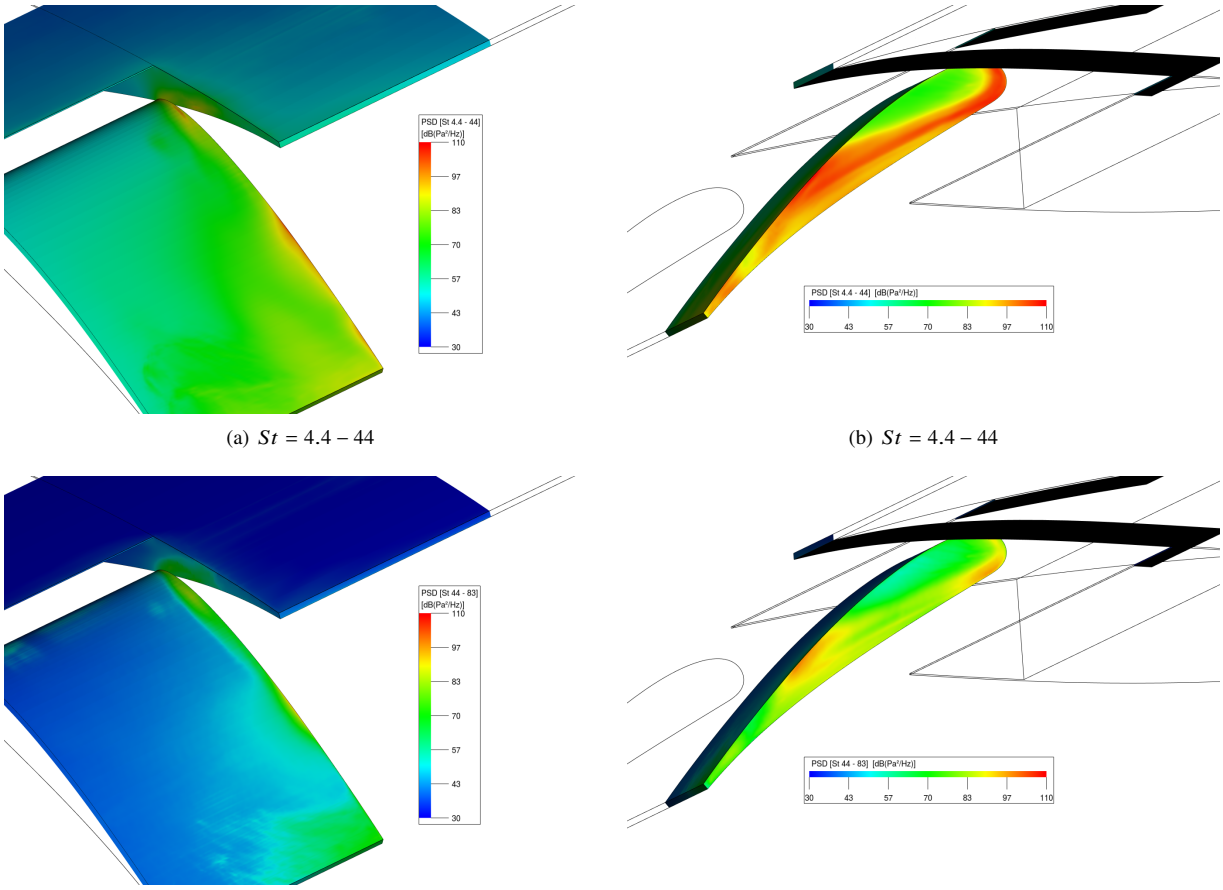

(a) $St = 4.4 - 44$ (b) $St = 4.4 - 44$

(c) $St = 44 - 83$ (d) $St = 44 - 83$

Fig. 6 Filtered pressure spectrum contour over the flap side-edge ($M = 0.11$, $Re = 1.1 \times 10^6$ and $\alpha = 0^o$).

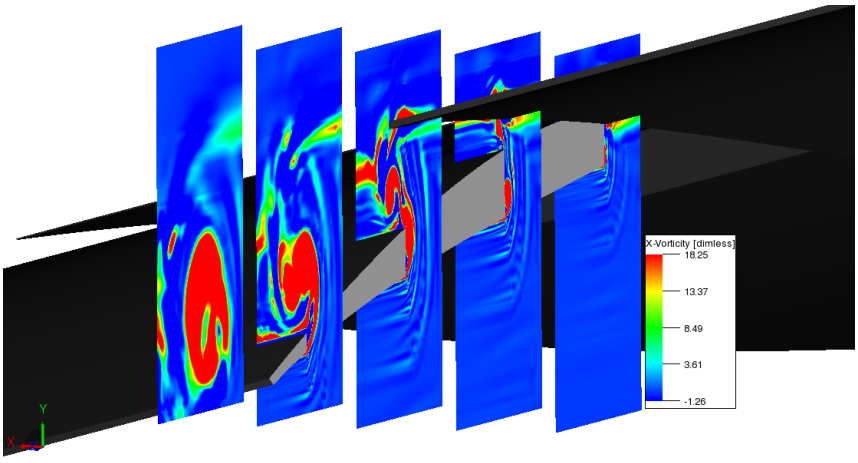

Fig. 7 Numerical visualization of the side-edge vortex formation ($M = 0.11$ and $Re = 1.1 \times 10^6$).

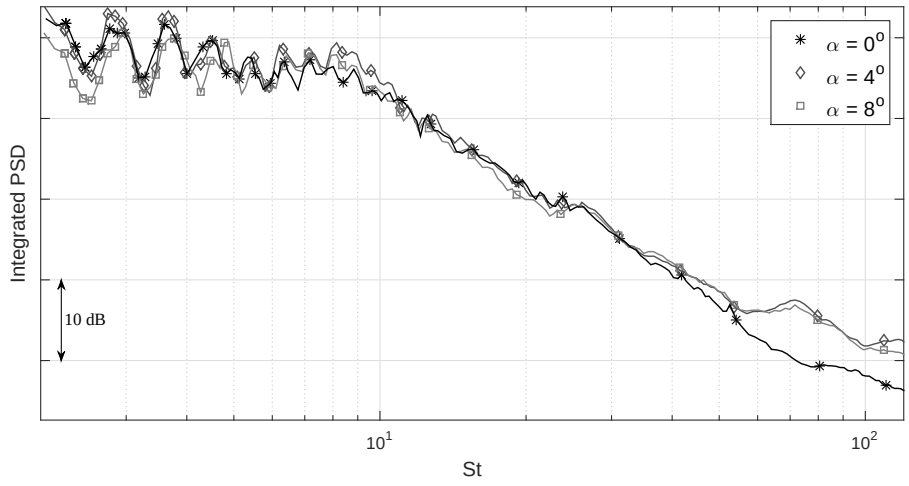

(a)

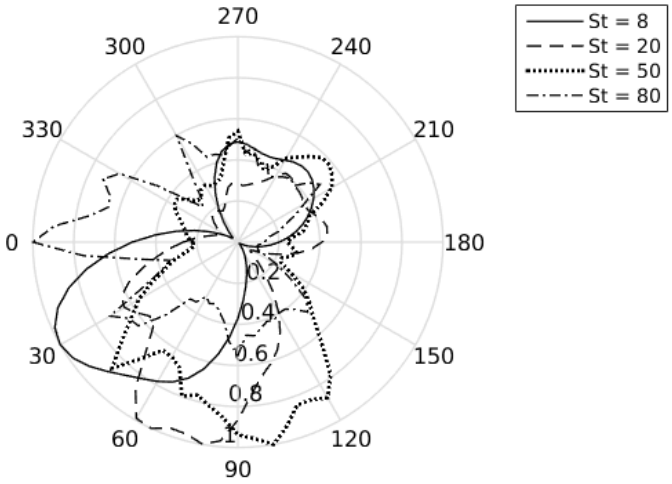

(b)

Fig. 8 Experimental flap side-edge noise spectrum obtained with CBF and SPI methodology at different angles of attack and numerical noise directivity measured for $\alpha = 0^o$ ($M = 0.11$, $Re = 1.1 \times 10^6$).

B. Flap Full Configuration

1. Steady Pressure Distribution

The steady pressure distributions obtained for the full deployed model are firstly used to assess differences between numerical and experimental approaches. Figure 11 shows how pressure over the model compares in different angles of attack. Although the pressure side and the suction peaks are well compared within the same angle of attack the downstream portion of the suction side appears to have a better match by considering again an angle shift of about $\Delta\alpha = 4^o$. This could be related to the difference at the flap circulation which is caused by the separation bubble after its suction peak and the higher separation starting from 50 % of the flap chord that is not captured by the numerical simulations with only a separation starting upstream at the observed experimentally. The agreement observed at the WME leading-edge could indicate that, despite the errors associated to the flap, slat circulations are similar between both analyses.

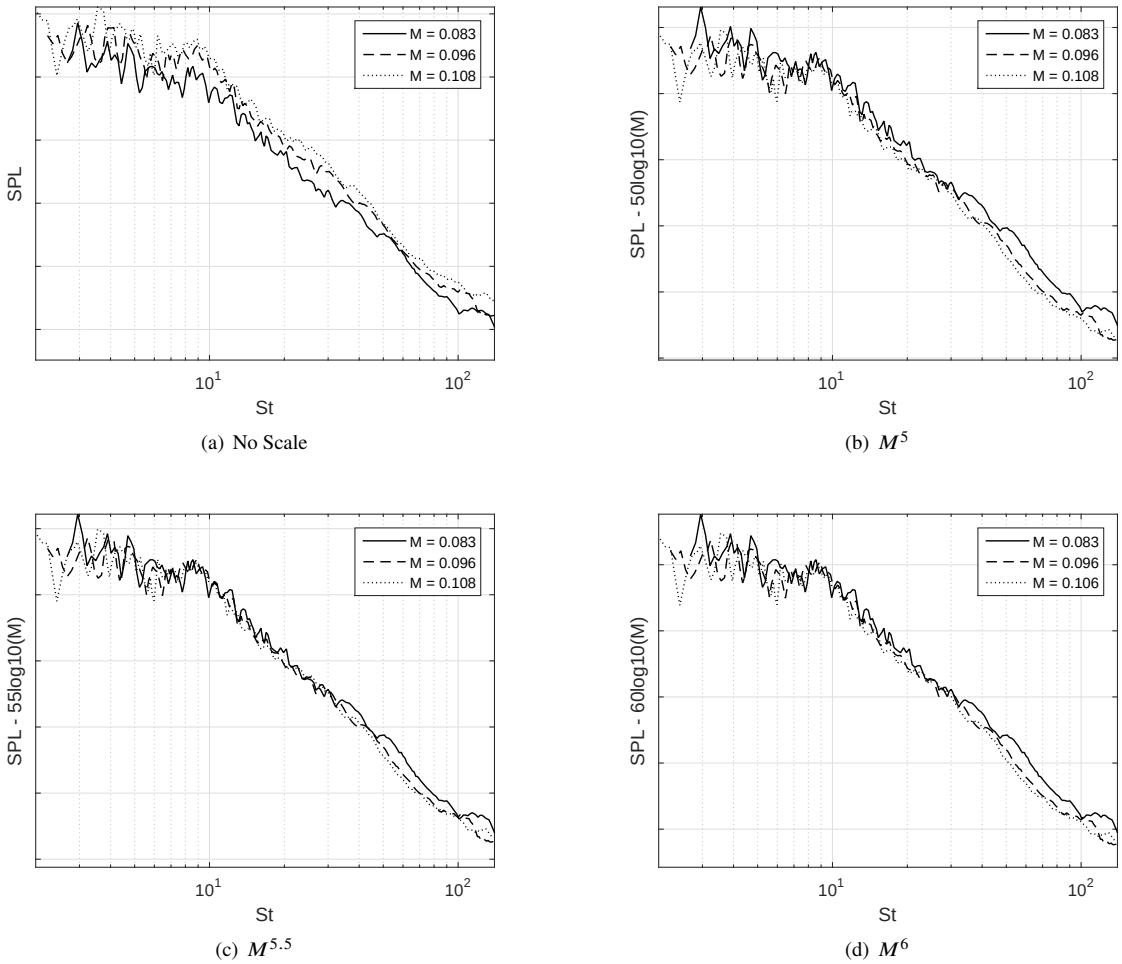

(a) No Scale (b) M^5

(c) $M^{5.5}$ (d) M^6

Fig. 9 Flap side-edge spectrum scaling with Strouhal and Mach number for $\alpha = 0^o$.

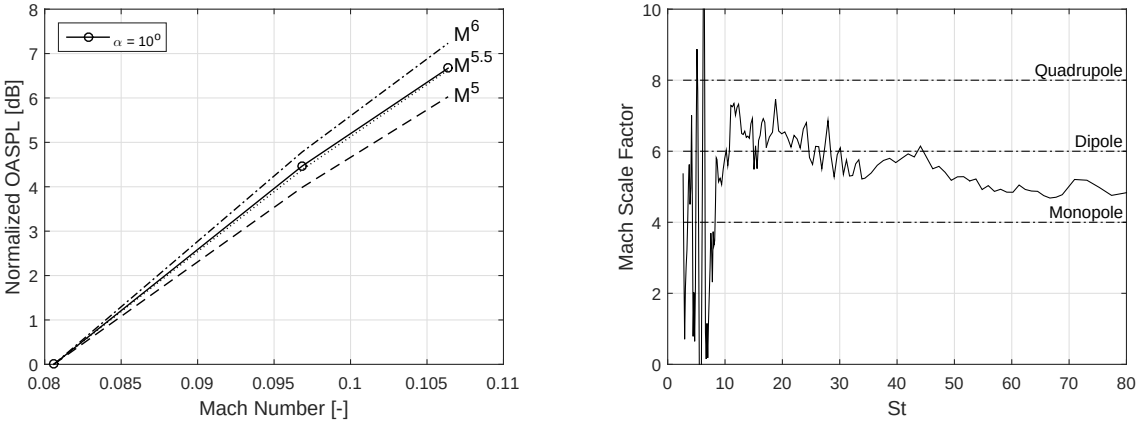

(a) OASPL (b) Spectrum

Fig. 10 Mach number scaling observed for the flap side-edge Overall Sound Pressure Levels and for the entire spectrum ($\alpha = 10^o$).

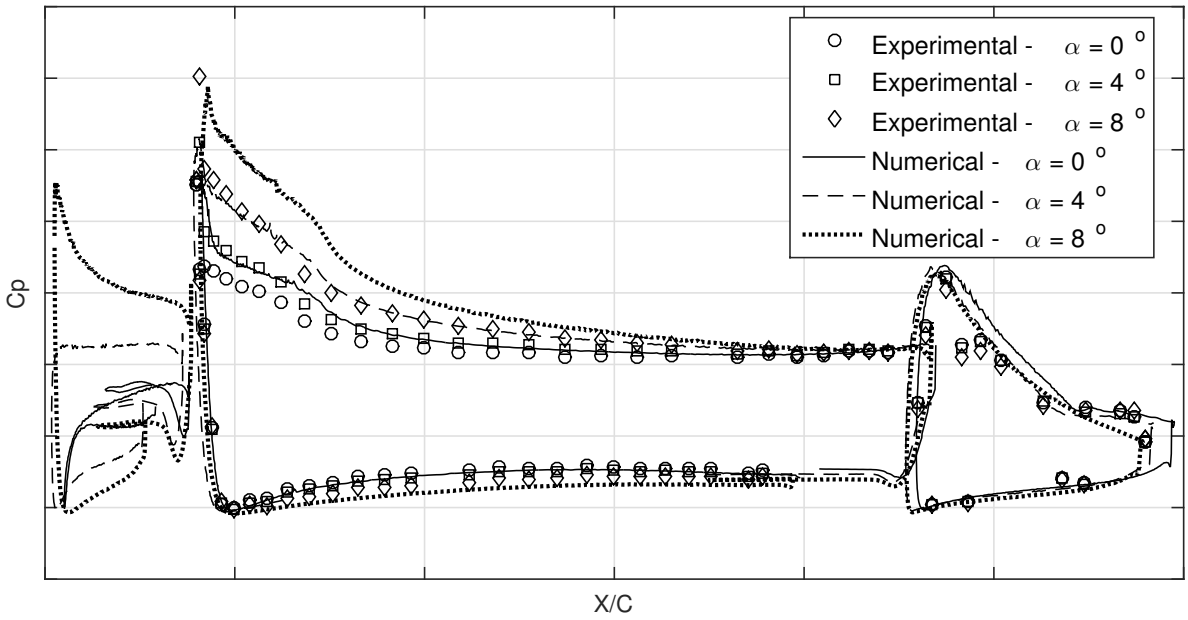

Fig. 11 Comparison between experimental and numerical steady pressure distribution at different angles of attack ($M = 0.11$ and $Re = 1.1 \times 10^6$).

Wing Main Element (WME) pressure distribution depicts a very narrow suction peak region, captured only by a single pressure tap, which induces lower pressures at the slat cusp and could contribute to higher instabilities at the slat shear-layer.

2. Unsteady Aerodynamic

Chowdwise flow behavior: Slat noise is dominated by the unsteady loads generated during the development of the shear-layer at the slat pressure side and its interaction with the slat further elements. In this way, comparisons between measured skin friction over the slat cove and cusp in the chordwise direction are used as a validation process for the unsteady flow predicted by the numerical results.

Comparing the skin friction spectrum measured by the hot-film sensors at the experiment with the numerical simulations (Fig. 12) a similar behavior for the spectrum shape at the reattachment region and at the trailing-edge is observed. Both regions are knowingly important for the broadband noise generation and good comparisons with experimental data are, therefore, prior to far field noise predictions. The similar trends are sustained up to Strouhal 10 when numerical results start to predict lower energies than observed experimentally. It is important to state that there may be still errors in the levels as the hot-film sensors used were not calibrated, and their values are therefore only displayed in Volts.

The numerical results were not able to capture any tonal component while all three experimental results displayed at least the second slat peak. A possible reason for this discrepancy is that hot-films are not only sensitive to skin friction but also to pressure fluctuations that are more affected by the tonal components.

The spectrum at the slat cusp presents a poor comparison with the experiments, what could be associated with the different transition condition imposed by the solver in comparison with the experiments. The higher levels observed for higher Strouhal numbers are probably caused by the tripping device applied 5 *mm* apart from the sensor and, therefore, the turbulence is not fully developed at the measurement locations. Either way, it is interesting to observe that the turbulence developed at the shear layer appears to be almost independent of the upstream turbulence levels and spectrum.

Figure 13 demonstrates how the pressure spectrum is changed from the very beginning of the shear layer until its end. It is interesting to observe how, at the formation of the shear layer, a hump close to Strouhal 10 is observed. This was also depicted by Ref. [15] and is related to the initial formation of Kelvin-Helmholtz instabilities before the turbulent breakdown into 3D vortical structures at the shear-layer. After this first stage, the instabilities grow in scale

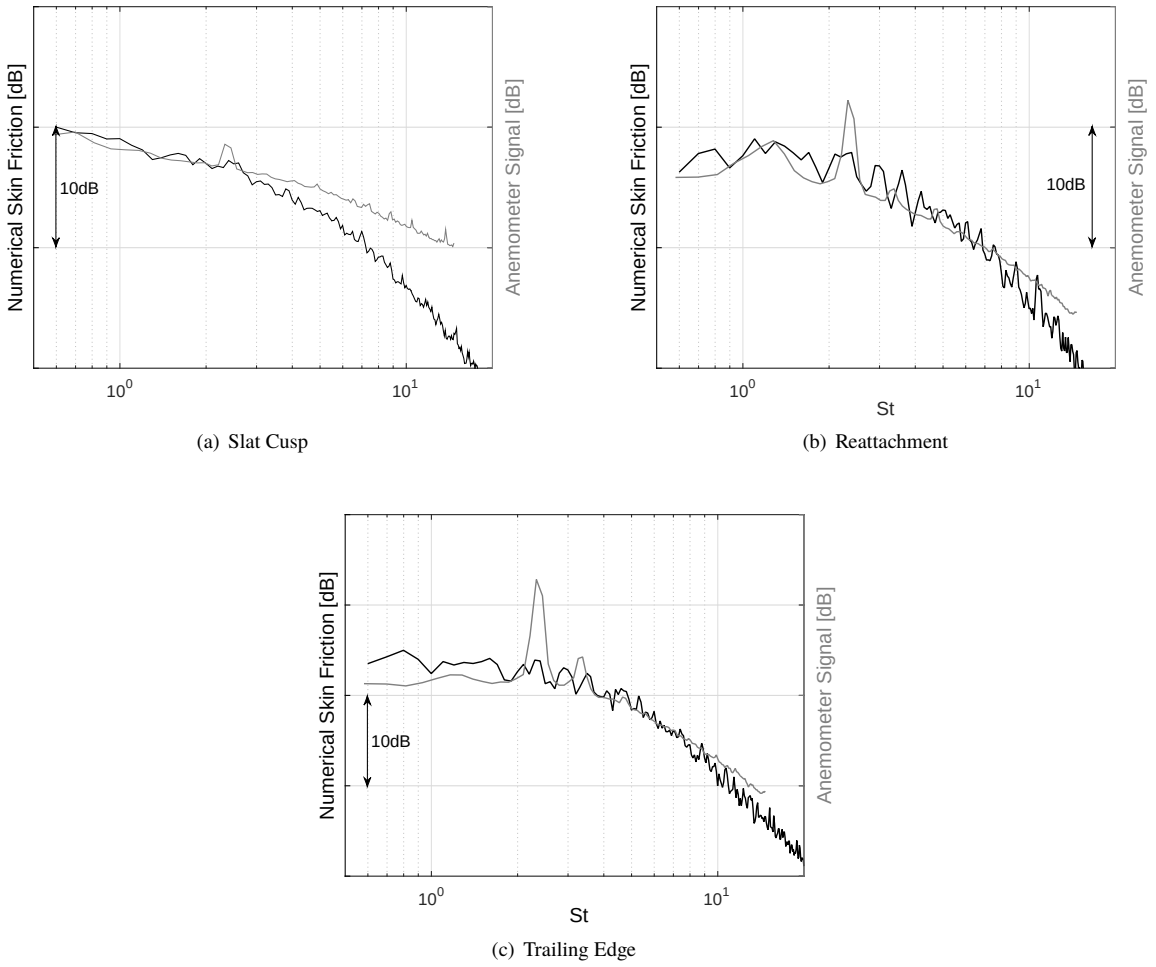

(a) Slat Cusp

(b) Reattachment

(c) Trailing Edge

Fig. 12 Comparison between slat skin friction spectrum obtained at the slat cusp, reattachment and trailing edge for the experimental hot-film measurements and numerical data ($\alpha = 0^o$, $M = 0.11$ and $Re = 1.1 \times 10^6$).

moving towards smaller Strouhal numbers as the band gets broader until the end of the shear layer, where the spectrum is already shaped as the observed slat noise, with higher levels close to Strouhal 3. A numerical estimation of the shear layer vorticity thickness following the work from Terracol et al. (2016) [15] led to a value of 7.4×10^{-4} *mm* and a Strouhal number of approximately 12, matching the expected observed instability frequency close to the slat cusp.

Spanwise flow behavior: Spanwise flow coherence is obtained in order to assess flow coherence length for the broadband components and, especially, for the mid-frequency tones. Due to the reported mechanism involved in the tonal generation, which involves a quasi-2D behavior, it is expected much higher coherence lengths for these frequencies than for the broadband component, which is supposed to behave as compact noise sources and uncorrelated over the span by its nature.

Since the experiments were performed with the hot-film sensors spaced by a minimum of 20 *mm* from each other, therefore not allowing comparisons for the broadband components, first tests pursued a coherence validation for the numerical results. Figure 14 enlightens the reasons behind the differences at the far field tonal levels observed in Section 3. Coherence lengths are higher at the experimental results for the second and fourth tonal component and smaller for the third component, which reflects on the far field observed behavior, with higher levels at the far field predictions for both the numerical and experimental results.

Also, the coherence lengths demonstrate that tonal elements have coherence lengths as big as 250 *mm*. This indicates

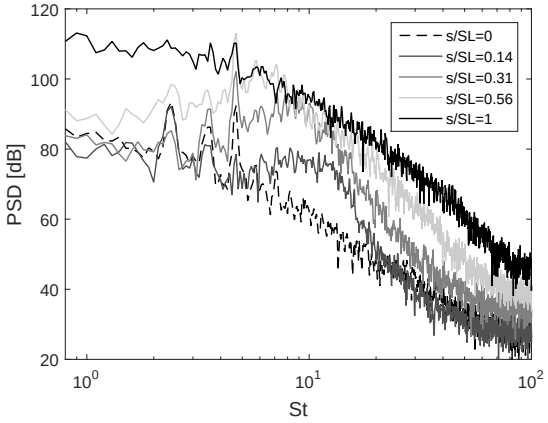

Fig. 13 Evolution of the pressure spectrum along the slat shear layer obtained numerically ($\alpha = 0^o$, $M = 0.11$ and $Re = 1.1 \times 10^6$).

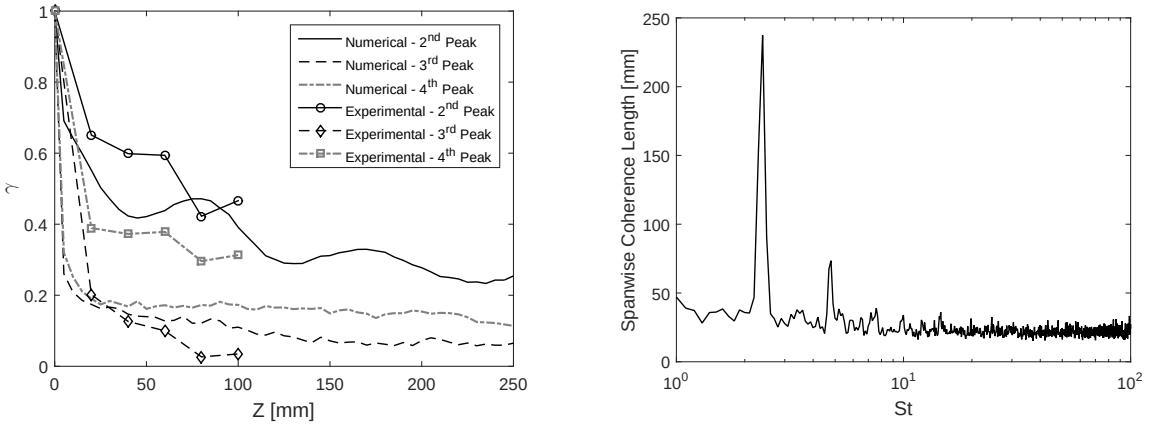

(a) Spanwise coherence

(b) Spanwise coherence length

Fig. 14 Comparison between spanwise coherence at tonal frequencies for the experimental hot-film measurements and numerical data close to the reattachment ($\alpha = 0^o$, $M = 0.11$ and $Re = 1.1 \times 10^6$).

some minimum spanwise length necessary for the FW-H region to completely represent the experimental results. Figure 15 demonstrates how noise predicted by two different angles of attack changes for two different FW-H box in the span length. From that, it is noticeable that the 80 *mm* box cannot predict the same noise variations predicted by the 200 *mm* box, with bigger variations observed along the tonal levels and some modifications on the broadband.

3. Far field Acoustic Noise

Far field acoustic slat noise spectra are shown in Fig. 16 comparing numerical and experimental results. Results reveal how levels differ between each other although both presents a maximum at Strouhal numbers based on the slat chord close to 3 and a further decrease with approximately 18 dB/dec. Numerical results overpredicted the broadband levels, specially for $\alpha = 0^o$ and for Strouhal numbers smaller than 30. Above this Strouhal value, the numerical results decay in a different trend then the experimental one. Tonal frequencies are well predicted by the numerical simulations with some overall trends for the levels also being represented. Higher levels are observed for the numerical $\alpha = 8^o$ case with higher harmonics appearing in the spectrum as well (Strouhal number 5.4). Those higher harmonics could be attenuated with a longer simulation time and could be caused by the absence of statistics to correctly compute their levels.

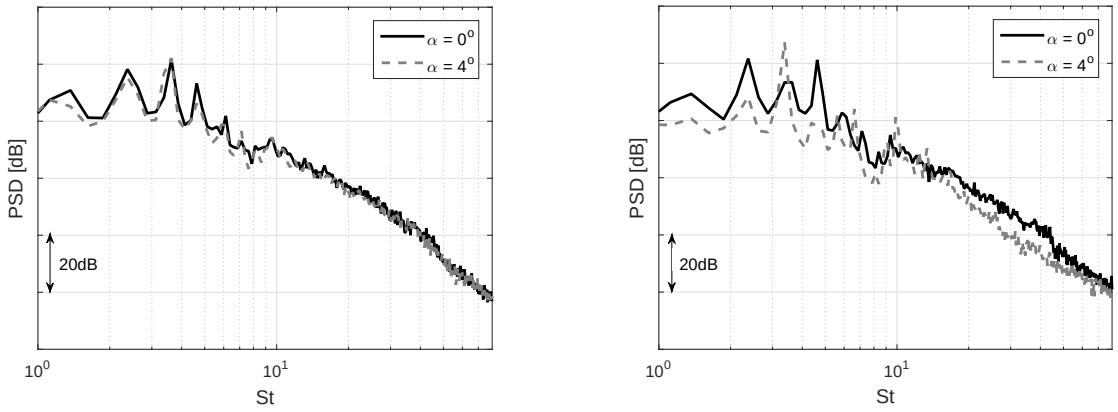

(a) 80 mm span FWH box

(b) 200 mm span FWH box

Fig. 15 Comparison between noise predicted for two different angles of attack for different FWH box dimensions over the span ($M = 0.11$ and $Re = 1.1 \times 10^6$).

Both results also present a narrowband component close to Strouhal 10. These components follow the graphs presented for the Mach variation (Fig. 19) and does not scale with the Strouhal number, possibly indicating some flow excitation of the Slat cavity.

Some beamforming maps obtained from the Conventional Beamforming methodology are presented in Fig. 17 representing one tonal Strouhal number ($St = 2.1$) and four other broadband frequencies. The broadband figures depict the distributed noise sources expected for the slat noise. Some higher levels are still observed close to the slat brackets, although the levels are not very different from the noise between the brackets. The tonal map does not present the expected distributed source since, as a coherently distributed noise source, it is not well computed by the conventional beamforming methodology.

Experimental results are used to observe slat spectrum variation with angle of attack (Fig. 18 (a) and (b)). For very small angles of attack ($\alpha < -4^o$) spectrum presents a completely different shape with no tonal components and with no maximum level for the broadband noise, only a decreasing curve, probably related to the lost of slat functionality at small angles of attack with only separated flow developed between the Slat-WME gap. After $\alpha = -4^o$, spectrum has its expected shape with maximum levels close to $St = 3$ and multiple mid-frequency tones. The peaks reach a level limit at angles between $\alpha = -2^o$ and 5^o with further decrease until it is covered by the broadband component, what happens at angles above 16^o.

Figure 18(c) also depicts computational source directivity observed for different Strouhal numbers. As expected, noise is radiated more efficiently at angles closed to $\Phi = 120^o$ following the Slat angle. Small Strouhal numbers are less affected by wing surfaces and present a dipole-like directivity while higher Strouhal numbers have wavelengths close to the model size and propagation is therefore interfered, with most of the energy propagating to the upper side of the wing instead.

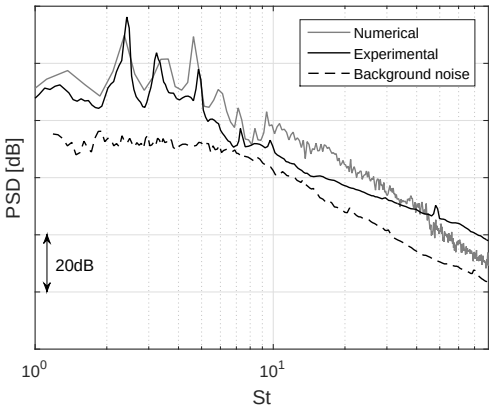

(a) $\alpha = 0^o$

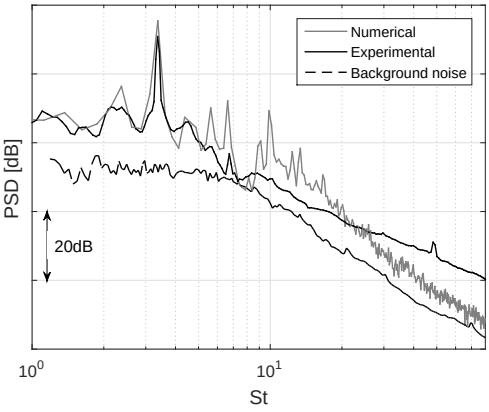

(b) $\alpha = 4^o$

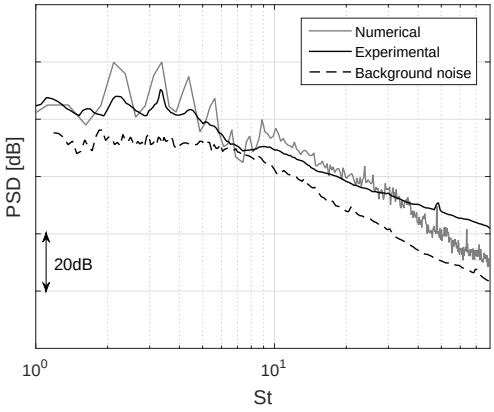

(c) $\alpha = 8^o$

Fig. 16 Comparisons between numerical and experimental slat far field acoustic noise at $M = 0.11$ and $Re = 1.1 \times 10^6$.

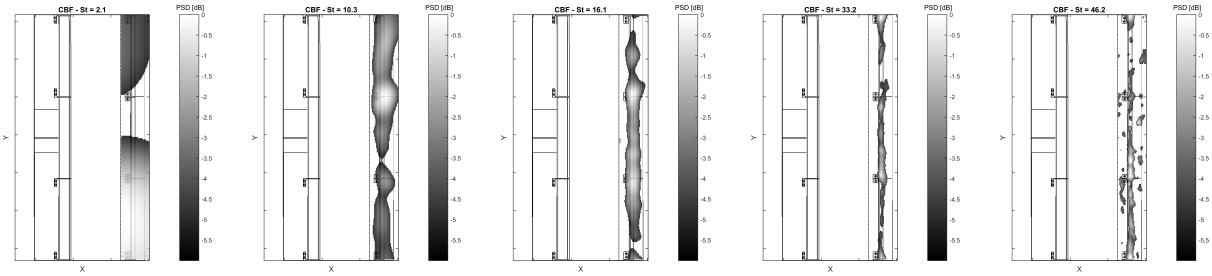

(a) $St = 2.1$ (b) $St = 10.3$ (c) $St = 16.1$ (d) $St = 33.1$ (e) $St = 46.2$

Fig. 17 Beamforming maps obtained for the flap full configuration at $M = 0.11$, $Re = 1.1 \times 10^6$ and $\alpha = 0^o$.

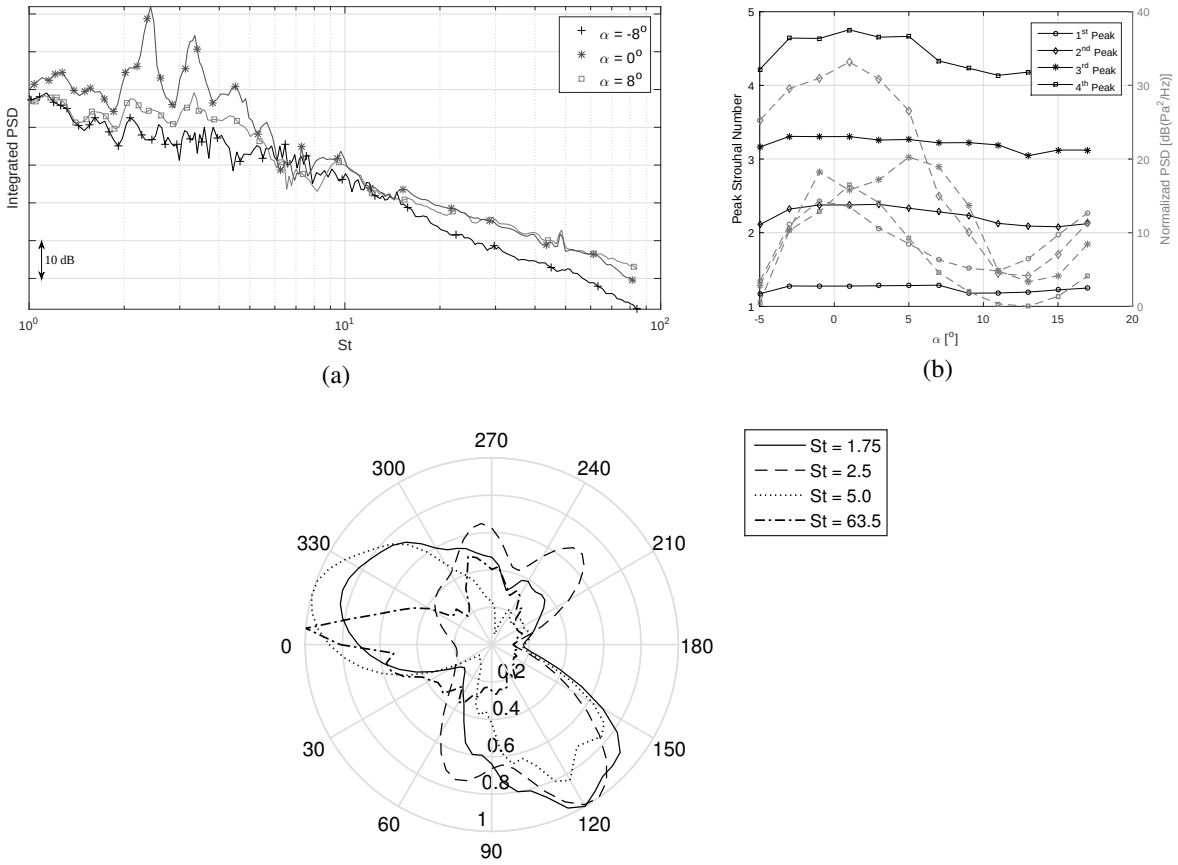

Fig. 18 Flap full deployed acoustic results obtained for $M = 0.11$ and $Re = 1.1 \times 10^6$. (a) Experimental slat acoustic spectra variation with angle of attack obtained with CBF and SPI methodology, (b) Experimental slat tonal component Strouhal number and level variation with angle of attack, (c) Numerical slat noise directivity change with Strouhal number ($\alpha = 0^o$).

Along with Fig. 19, that presents experimental spectra obtained in four different Mach numbers and four different Mach scales for $\alpha = 8^o$, following values proposed by Dobrzynski and Pott-Pollenske (2001) [16], Fig. 20 reveals how the Overall Sound Pressure Level changes with the Mach number and how the Mach scaling is altered along the spectrum for high angles of attack. The higher angles are required in order to avoid the tonal components that, despite good scaling with the Strouhal number, does not seem to present any scaling with the Mach number and, in some cases, it even presents a reduction in levels with increasing velocity, indicating Reynolds dependencies.

Results show a better agreement for a scaling factor between 4 and 4.5 for the broadband noise range. Also, the high-frequency hump close to Strouhal 10 observed does not scale with the Strouhal number, probably suggesting some sort of cavity mode excitation phenomena.

Looking to Fig. 20(b) one can notice that a similar trend is observed for the flap full and flap side-edge configurations, where noise is scaled with higher Mach factor for smaller frequencies (M^5) while higher frequencies are scaled with levels close to M^4 which is attributed by Ref. [16] as the combination of a trailing-edge source (scaling with M^5) and a monopole generated at the gap between the slat trailing-edge and the WME (scaling with M^4).

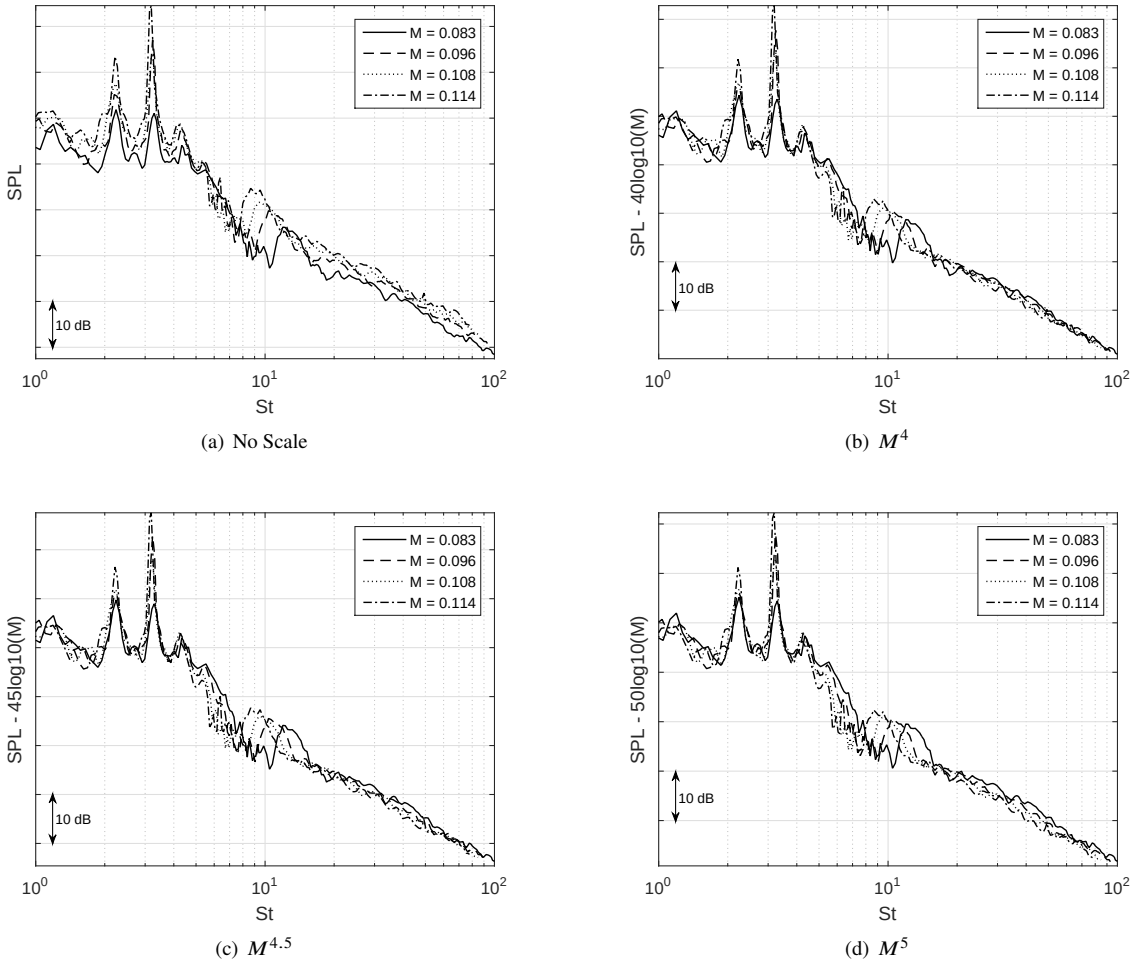

(a) No Scale (b) M^4

(c) $M^{4.5}$ (d) M^5

Fig. 19 Slat spectrum scaling with Strouhal and Mach number for $\alpha = 0^o$.

4. Mid-frequency tones comparisons

The mid-frequency tones are an important issue to be addressed for unswept slat tests. According to Terracol et al., (2016)[15] those tones are generated by the feedback between vortices emerging at the slat cusp and the noise generated at the slat reattachment. This feedback has multiple harmonics and could be estimated by the analytical Equation 1 where n is the harmonic number, L_a corresponds to the distance between the slat cusp and the reattachment location and κ_v and κ_l are respectively the ratio between the shear-layer path and the distance between the slat cusp and the acoustic feedback location and the ratio between the vortex convection mean velocity at the shear layer and the free-stream velocity.

$$f_n = n\frac{U_\infty}{L_a}\left(\frac{1}{M + \frac{\kappa_l}{\kappa_v}}\right). \tag{1}$$

In particular, this equation seems to predict a feedback frequency that increases with the angle of attack, since the reattachment location moves towards the leading-edge and L_a decreases much more significantly than the changes in κ_l. Experimental analysis though [7, 17] have observed a different behavior with slat frequency decreasing with the angle of attack, as was also observed for this model (Fig. 18(b)). Thus, a different estimation could be obtained by considering the feedback with the acoustic waves produced at the slat trailing-edge instead. This assumption also matches the considered model for the broadband noise, with most significant noise sources coming from the slat trailing-edge.

Therefore, vortices generated at the slat cusp are convected through the shear layer until the reattachment and further

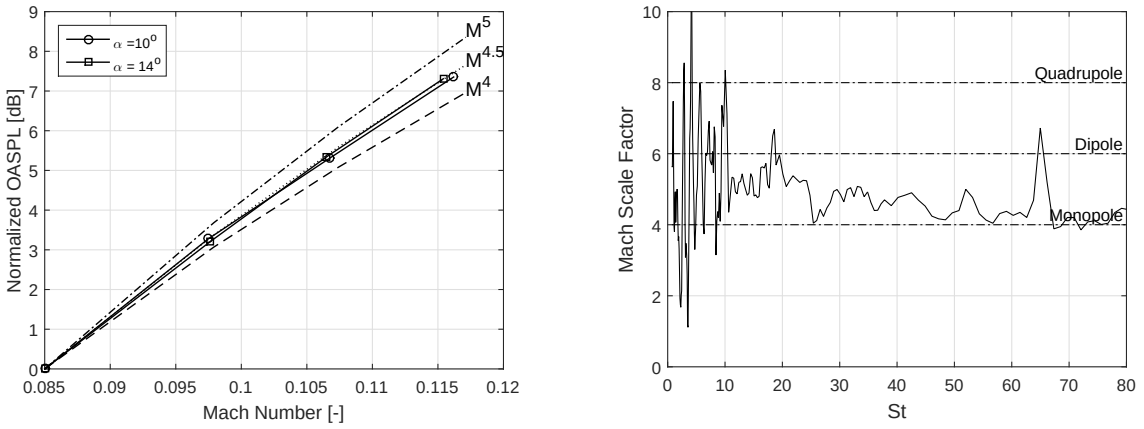

(a) OASPL

(b) Spectrum $\alpha = 10^o$

Fig. 20 Mach number scaling observed for the slat Overall Sound Pressure Levels and for the entire spectrum.

through the slat cove until the trailing-edge where the acoustic waves are formed. Those are propagated in a straight line until the slat cove where the feedback is closed. This possibility could be estimated using L_a as the distance between the slat cusp and the trailing-edge (that does not change with angle of attack) and κ_l as the ratio L_v/L_a, where L_v (the length that the aerodynamic instabilities travel) is now the sum of the shear-layer length and the length between the reattachment location and the trailing-edge.

The slat reattachment location is easily obtained for the numerical analysis, what is not true for the experimental test. This is performed using the hot-film data at the slat cove. It is expected that unsteady contents are divided at the reattachment into the flow that is recirculated at the cove and the one that follows the path until the trailing-edge. Therefore, coherence between hot-film elements should have a minimum at the reattachment region, what can be visualized either with a full coherence matrix or using the coherence between neighbor sensors. The later one is shown in Fig. 21 since more angles of attack could be displayed on the same graph. The figure also presents the position estimated experimental and numerically for the reattachment location, revealing the agreement between both cases at the same angles of attack ($\alpha = 0^o$, 4^o and 8^o).

The constants κ_l and κ_v are both estimated numerically using, respectively, the information about the shear-layer geometry and the shear-layer mean velocity at two angles of attack (0 and 8^o). Table 1 presents the numerical constants estimated for κ_l and κ_v. The constants are linearly fit in relation to the distance between the reattachment position and the slat cusp, that could be estimated both numerical and experimentally. The reattachment cannot be linearly related to the angle of attack and represent the constant that best defines the shape of the shear-layer.

Table 1 Values of the constants κ_v and κ_l estimated numerically for the analytical prediction of the slat tonal frequency.

α [^{o}]	κ_v	κ_L (Reattachment)	κ_l (Trailing Edge)
0	0.82	1.10	1.11
8	0.78	1.05	1.08

With the reattachment position obtained and the constants κ_L and κ_v estimated, slat mid-frequency tones could be predicted analytically and compared to the observed numerical and experimental results. Figure 22 shows how the model appears to follow, both computational and experimentally, the analytical estimation for the feedback considered at the slat trailing edge. The model even predicts the slight Strouhal decrease with increasing angle of attack and reattachment location moving towards the leading-edge.

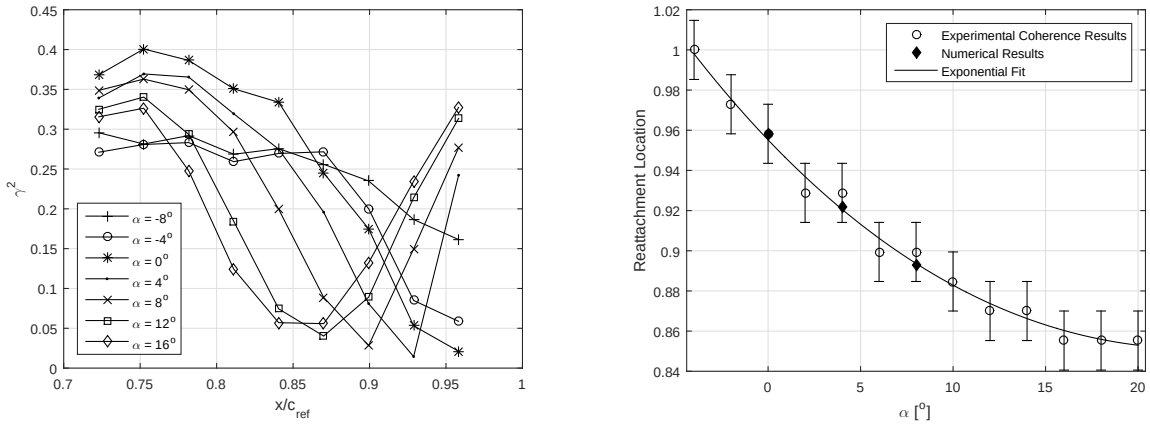

(a) Consecutive Sensor coherence [9]

(b) Reattachment location variation

Fig. 21 Coherence between consecutive sensors and reattachment location estimation with different angles of attack for $M = 0.11$ and $Re = 1.1 \times 10^6$ conditions.

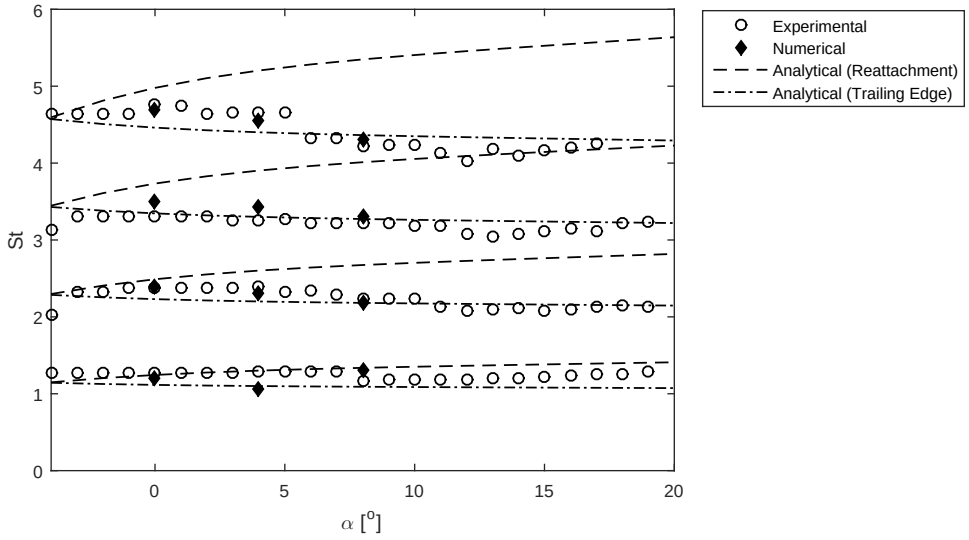

Fig. 22 Comparison between experimental and numerical tonal peaks strouhal numbers based on slat chord and analytical predictions considering a feedback at the reattachment and at the slat trailing-edge ($M = 0.11$ and $Re = 1.1 \times 10^6$).

VI. Conclusions

Acoustic and aerodynamic properties of the high-lift model are assessed both numerical and experimentally. Results presented data of the model far field acoustic properties along with aerodynamic characteristics responsible for the observed behaviors.

Flap full span and flap side-edge pressure measurements were compared and analyzed, providing model steady characteristics and information over numerical and experimental discrepancies that could lead to different unsteady predictions.

Alongside with steady aerodynamic properties, the far field acoustic predictions were obtained for both the experimental and numerical analysis with observed good comparisons of noise spectrum between the experimentally measured beamforming results and the numerically obtained Ffowcs-Williams Hawkins results.

Noise levels, beamforming maps, and directivity estimations were used to identify and characterize each noise source studied at this work, differing the mechanisms observed for tonal and broadband noise and the impacts of the angle of attack and Mach number over the acoustic behaviors.

Flap side-edge noise was observed as a single broadband component with maximums close to Strouhal numbers 5 and Mach scaling following a Mach to the 5.5 power. Beamforming maps have shown noise sources concentrated at the middle of the flap chord with a second source observed at higher frequencies close to the flap leading edge or to the middle of the stowed section, indicating two source mechanisms for higher frequencies related to the shear-layer interaction with the edges on the flap side-edge surface.

Slat noise was investigated more deeply in terms of unsteady aerodynamic measurements. Broadband sound sources are most probably related to the unsteady flow reaching the slat trailing-edge. Slat far field spectrum shape is mostly defined at the shear-layer formation, with almost no impact of the spectrum at the slat cusp or the flow between the reattachment and the trailing-edge. Slat directivity follows the dipole model proposed by Dobrzynski and Pott-Pollenske (2001) [16] with more discrepancies at higher frequencies due to the reflection of the waves on the model. The noise also follows a Strouhal and Mach scaling with Mach to the 4.5 power.

Spanwise coherence analysis has presented the importance of analyzing a slat span compatible with the slat coherence length of the noise produced. The development of the noise along the span, despite very small for the broadband region, can reach lengths of up to 200 *mm* at the mid-frequency tonal components, demonstrating how 2D those structures tend to be along the slat span.

Mid-frequency slat tones were assessed analytical, numerical and experimentally. Estimations of the shear-layer reattachment using the hot-film transducers made possible to compare observed slat tones with analytical and numerical predictions, showing that this model appears to present tones caused by a feedback between vortices generated at the slat cusp and acoustic waves produced at the slat trailing-edge and not at the slat reattachment.

Acknowledgements

The authors acknowledge the financial support from the Brazilian agencies FINEP and CNPq.

References

[1] Dobrzynski, W., "Almost 40 Years of Airframe Noise Research – What did we achieve?" *Journal of Aircraft*, Vol. 47, No. 2, 2010, pp. 353–367. doi:10.2514/1.44457.

[2] Choudhari, M., and Khorrami, M., "Slat cove unsteadiness: Effect of 3d flow structures," *44th AIAA Aerospace Sciences Meeting and Exhibit*, 2006, p. 211. doi:10.2514/6.2006-211.

[3] Imamura, T., Ura, H., Yokokawa, Y., Enomoto, S., Yamamoto, K., and Hirai, T., "Designing of slat cove filler as a noise reduction device for leading-edge slat," *13th AIAA/CEAS Aeroacoustics Conference (28th AIAA Aeroacoustics Conference)*, 2007, p. 3473. doi:10.2514/6.2007-3473.

[4] Ahlefeldt, T., and Quest, J., "Real-Flight Reynolds Number Microphone-Array Measurements on a Scaled Model in ETW," *52nd Aerospace Sciences Meeting*, 2014, p. 1483. doi:10.2514/6.2014-1483\r10.2514/6.2014-1483.

[5] Pott-Pollenske, M., Delfs, J., and Reichenberger, J., "A testbed for large scale and high Reynolds number airframe noise research," *19th AIAA/CEAS Aeroacoustics Conference*, 2013, p. 2260. doi:10.2514/6.2013-2260.

[6] Herr, M., Pott-Pollenske, M., Ewert, R., Boenke, D., Siebert, J., Delfs, J., Rudenko, A., Büscher, A., Friedel, H., and Mariotti, I., "Large-Scale Studies on Slat Noise Reduction," *21st AIAA/CEAS Aeroacoustics Conference*, 2015, p. 3140. doi:10.2514/6.2015-3140.

[7] Murayama, M., Nakakita, K., Yamamoto, K., Ura, H., Ito, Y., and Choudhari, M. M., "Experimental Study on Slat Noise from 30P30N Three-Element High-Lift Airfoil at JAXA Hard-Wall Lowspeed Wind Tunnel," *20th AIAA/CEAS Aeroacoustics Conference*, 2014, p. 2080. doi:10.2514/6.2014-2080.

[8] Rossignol, K.-S., "Flow field measurements to characterize flap side-edge noise generation," doi:10.2514/6.2013-2061.

[9] Lima Pereira, L. T., Rego, L. F., Catalano, F. M., Cafaldo Reis, D., and Lobão Capucho Coelho, E., "Experimental Slat Noise Assessment Through Phased Array and Hot-Film Anemometry Measurements," *2018 AIAA Aerospace Sciences Meeting*, 2018, p. 0758. doi:10.2514/6.2018-0758.

[10] Catalano, F. M., "The New Closed Circuit Wind Tunnel of the Aircraft Laboratory of University of Sao Paulo, Brazil," *24TH International Congress of the Aeronautical Sciences ICAS*, 2004. doi:na.

[11] Santana, L. D., Carmo, M., Medeiros, M. A. F., and Catalano, F. M., "The update of an aerodynamic wind-tunnel for aeroacoustics testing," *Journal of Aerospace Technology and Management*, Vol. 6, No. 2, 2014, pp. 111–118. doi:10.5028/jatm.v6i2.308.

[12] Fonseca, W. D., Ristow, J. P., Sanches, D. G., and Gerges, S. N., "A Different Approach to Archimedean Spiral Equation in the Development of a High Frequency Array," Tech. rep., SAE Technical Paper, 2010. doi:10.4271/2010-36-0541.

[13] Chen, S., and Doolen, G. D., "Lattice Boltzmann method for fluid flows," *Annual review of fluid mechanics*, Vol. 30, No. 1, 1998, pp. 329–364.

[14] Guo, Y., "Aircraft flap side edge noise modeling and prediction," *17th AIAA/CEAS Aeroacoustics Conference (32nd AIAA Aeroacoustics Conference)*, 2011, p. 2731. doi:10.2514/6.2011-2731.

[15] Terracol, M., Manoha, E., and Lemoine, B., "Investigation of the Unsteady Flow and Noise Generation in a Slat Cove," *AIAA Journal*. doi:10.2514/1.J053479.

[16] Dobrzynski, W., and Pott-Pollenske, M., "Slat noise source studies for farfield noise prediction," *7th AIAA/CEAS Aeroacoustics Conference and Exhibit*, 2001, p. 2158. doi:10.2514/6.2001-2158.

[17] Pascioni, K. A., and Cattafesta, L. N., "Aeroacoustic Measurements of Leading-Edge Slat Noise," *22nd AIAA/CEAS Aeroacoustics Conference*, 2016, p. 2960. doi:10.2514/6.2016-2960.

MADRID
inter.noise 2019
June 16 - 19
NOISE CONTROL FOR A BETTER ENVIRONMENT

Numerical analysis of the instabilities behind a blunt slat trailing-edge

Botero-Bolívar, Laura[1]
Acevedo-Giraldo, Daniel
Pereira, Lourenço T.
Catalano, Fernando M.
University of São Paulo
Av. Trab. São Carlense, 400, São Carlos - SP, Brazil

Reis, Danillo C.[2]
Coelho, Eduardo L. C.
EMBRAER
Av. Brigadeiro Faria Lima 2170, São José dos Campos - SP, Brazil

ABSTRACT

Concerns about the noise generated by the structure of aircraft have significantly increased over the past years due to the reduction in the engine noise and tighter regulations established by certifying entities. Slat is one of the most important sources of airframe noise, since it generates a noise spectrum composed of mid-frequency tones, a broadband component, and a high-frequency hump. This article addresses a detailed analysis of the high-frequency tone generation and its relation with the slat trailing-edge thickness. Numerical simulations of a typical three-element airfoil were conducted by PowerFLOW 5.3 software at 1 million Reynolds number and the noise was propagated according to the Ffowcs William-Hawking methodology. The high spatial and temporal resolution in the simulations aimed to capture variations in the slat trailing-edge thickness. The results showed the presence of a strong vortex shedding behind the slat, which is highly related to the high-frequency tone and the blunt slat trailing edge. The frequency of the tone in the far-field spectrum is in agreement with that in the vortex shedding. The Strouhal number calculated with the use of the boundary layer displacement thickness as the characteristic length was constant for all cases and close to 0.4.

Keywords: Airframe Noise, Slat Noise, Vortex Shedding, Computational Aeroacoustics, Slat Trailing Edge
I-INCE Classification of Subject Number: 21
http://i-ince.org/files/data/classification.pdf

[1] laura.boterobol@usp.br
[2] danillo.reis@embraer.com.br

1. INTRODUCTION

Since the 1960's, aircraft noise has become one of the most important topics in aeronautic sciences due to increases in both air traffic and population close to main worldwide airports. As a consequence, tighter regulations, several programs and research have been developed in different aeronautic institutions towards reductions in the aircraft noise [1, 2]. Aircraft noise is composed of engine noise and airframe noise; engine noise refers to the noise generated by the components of the aircraft propulsion system, whereas airframe noise is generated by the fluid-structure interaction [3, 4]. When aircraft noise first came to the forefront, engines were the main source and the focus of noise reduction. However, over the past few decades, they have become significantly quieter due to the incorporation of the high-by-pass technology [4, 5] and engine noise is currently the major contribution to the overall aircraft noise during take-off, when the maximum power is required. On the other hand, airframe noise is the most significant component in the landing approach stage [6].

The main sources of airframe noise are landing gear and high-lift systems (slats and flaps) and their rank highly depends on the geometry and operational conditions of each aircraft. According to Dobrzynski, W. et al (2015) [2], a wing in the high-lift configuration is 10 dB noisier than a wing in the cruise configuration. The slat noise is generated by the complex flow formed in the gap between the slat and the main wing element and the unsteady loads caused by the interaction of such flow with the downstream elements, i. e., slat upper surface and trailing edge and main wing element leading edge (Figure 1a) [5, 7]. Such a phenomenon causes a typical slat spectra (Figure 1b) composed of mid-frequency tones, a broadband component that decrease in function of the frequency, and a high-frequency hump. The mid-frequency tones are attributed to a feedback loop created between the vortices detached from the slat cusp and acoustic waves generated in the reattachment point [10]. The broadband noise is probably due to the interaction of the shear-layer and the wing components [11]. Finally, the high-frequency hump is related to the vortex shedding behind blunt slat trailing edges [12]. Such vortices are governed by Karman vortex, which became a dipole of a specific frequency, represented by a single tone at high frequency.

This paper reports on an analysis of the high-frequency hump and its relation to the vortex shedding and the slat trailing edge thickness. Simulations were performed with varied slat trailing edge thickness of a conventional mid-range aircraft three-element airfoil (slat, main wing element, and flap). The numerical analyses were conducted at 1.1 x 10^6 Reynolds number and 0.101 Mach number on PowerFLOW software, which uses the Lattice Boltzmann Method (LBM) as a fluid solver, and the Ffocws William-Hawking (FW-H) acoustic analogy for resolving the acoustic far-field.

2. NUMERICAL METHODOLOGY

Numerical simulations were conducted on PowerFLOW 5.3® coomercial software. It focuses on aeroacoustic simulations and uses LBM for resolving the flow properties. The method is based on the resolution of the Lattice-Boltzmann equation in discrete cells with appropriate symmetries, which is essentially the kinetic equation resulted from the ensemble-averaging of the discrete dynamics of the Frish-Hasslacher-Pmeau (FHP) cellular automation supplemented with the assumption of molecular chaos [13].

The main feature of LBM is the incorporation of the physics of microscopic processes, since it replaces the fluid by fraction particles according to a distribution function that considers the behaviour of a collection of particles a unit [14]. Consequently, LBM accurately captures the aerodynamics of high Reynolds number flows and pressure

fluctuations due to separated and reattached flows (main airframe noise source) and handles complex geometries without grids defined by complex analytical functions [15]. The program discretizes the Lattice-Boltzmann equation temporarily and spatially; it divides the physical time into timesteps, in which each variable is calculated and divide the computational domain into 3D-cells, in which the particles can move in 18 directions to the neighboring cells besides the 0-vector [15, 16].

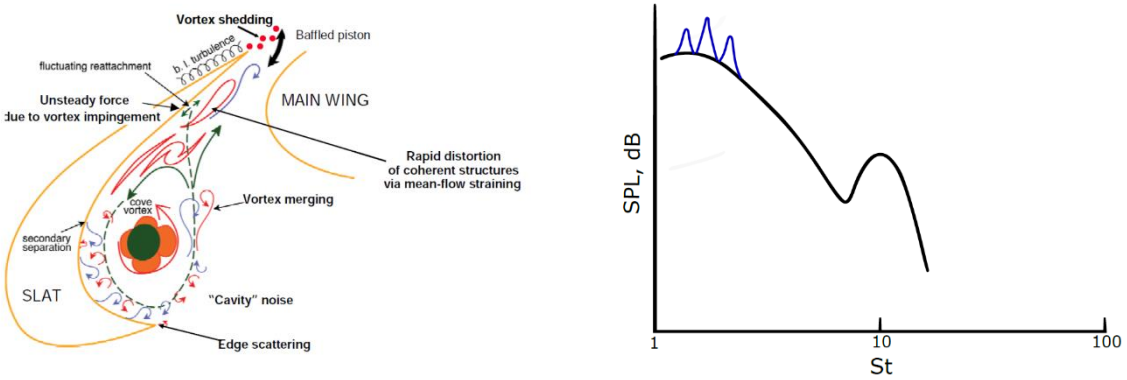

a) Flow around slat [8] *b) Typical slat spectrum [9]*

Figure 1 – Slat noise characteristics

For the analysis of the far-field, PowerFLOW uses the FW-H acoustic analogy supplemented by the 1A formulation [17-20], which is included in the PowerACOUSTICS post-processing tool. Such an analogy propagates pressure fluctuations in the model surfaces in pressure fluctuations in the observer location, in this case, the microphone, assuming the aerodynamic noise as a quadrupole source.

2.1 Model

The model used for numerical studies was a three-element wing composed of a slat, a main wing element and a flap. Both flap and slat were fully extended and the angle of attack was 0^o. The model has 500 mm stowed chord and 250 mm span. Simulations were performed with the wing in an infinite configuration, for avoiding the 3D affects in the wing tips.

2.1 Turbulence model

PowerFLOW uses the κ-ε Re-Normalisation Group (RNG) with extensions, which are equivalent to time-accurate Very Large Eddy Simulations (VLES) as a turbulence model. It also employs the eddy viscosity and Prandtl number to apply the effects of the unresolved (sub-grid) scale-flow properties to the resolved large scale and the universal law of the wall velocity profile coupled with the wall model pressure gradient to resolve the elements closest to the surface and determine the local skin friction.

2.2 Numerical set-up

The computational domain dimensions were 6500 mm x 1650 mm x 250 mm, where X and Z are in the streamwise and spanwise directions, respectively. The atmospheric conditions used in the simulations were: P = 101325 Pa, T=300 K, $\rho = 1.177$ kg/m^3, and $\nu = 1.497 \times 10^{-5}$ m^2/s. The velocity inlet was set at 34 m/s, which correspond to 0.101 Mach number and 1.16×10^6 Reynolds number based on the stowed chord, and turbulence intensity at 0.21% with 1 mm turbulent scale. The outlet condition was set as no pressure gradient. The solid walls of the computational domain were non-frictional

and the model walls were set as standard walls with an automatic transition model (the program calculates the transition).

The mesh on PowerFLOW is defined by refinement regions of different element sizes. Each region increases twice the size of the element of the previous region. The minimum element size was 0.17 times the thinnest slat trailing edge thickness and the finest elements are located around the slat trailing edge (for capturing the effect of the slat trailing edge variations and vortex shedding). The element size in the FW-H measurement region was 0.25 mm, which is sufficient to capture the slat generation noise phenomena, according to Botero-Bolívar, L. et al (2018) [21] and Pereira, L et al (2018) [22]. The maximum element size was 128 mm, near the inlet and outlet walls, where the flow is almost constant. The outer region was modelled as a high viscosity fluid, or anechoic layer, for avoiding the reflection of waves approaching to the computational domain. Such a condition is necessary for simulations since, otherwise, they would take long and their completion would not be viable.

The simulations were discretized into 103.23 x 10^6 elements and 4.9 x 10^6 timesteps, which correspond to 0.25 s in physical time, and took 22700 CPU hours.

2.3 Far-field Analysis

The surface pressure measurements for the FW-H analogy calculation were taken from a $3.5c_s$ x $4.7c_s$ x $2.4c_s$ (c_s is the slat chord) crop in the middle of the span (Figure 2) and propagated to a microphone located 0.65 m from the source. Measurements started at 0.147 s (for eliminating initial transient effects) at 82 kHz sampling frequency.

Power spectral values were normalized by the frequency for standardization and the reference value for the conversion to dB was 2 x 10^{-5} Pa. The time signal was segmented by the Hanning window and the band was a 100 Hz constant-width band both for the calculation of the Fast Fourier Transformation (FFT).

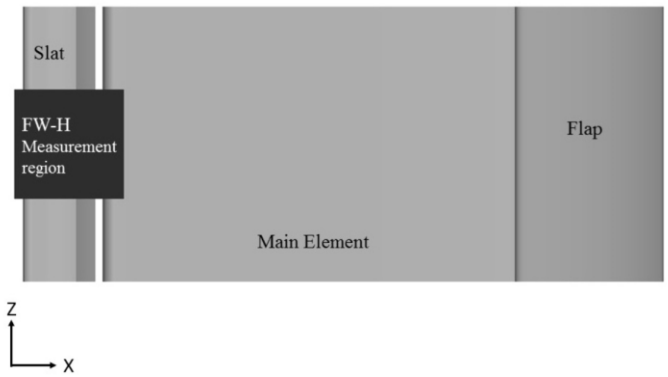

Figure 2 – FW-H measurement region

2.4 Near-field Measurements

Fluid measurements were taken after the convergence of lift and drag coefficients. The time-average measurements of the fluid were taken at 71 Hz sampling frequency and instantaneous measurements were performed at 10 kHz sampling frequency. The latter were also used for the calculation of the Power Spectral Density (PSD) contours around the slat. The PSD was calculated under the same conditions of the far-field slat spectra.

3. RESULTS AND DISCUSSIONS

This chapter addresses aerodynamic and aeroacoustic results of simulations of three different slat Trailing Edge Thicknesses (TET), namely $0.0021c_s$, $0.0042c_s$, and $0.017c_s$. In each case, only the slat trailing edge thickness was modified, whereas the other

geometry characteristics were kept constant. Steady aerodynamic results are composed of comparisons of lift and drag coefficients and pressure coefficient distribution. Unsteady aerodynamic results consist in the transient characteristics of the vortex shedding, and aeroacoustic results are the far-field spectra and PSD contours.

The slat trailing edge thickness does not affect the wing performance significantly, since it influences neither the pressure coefficient distribution (Figure 3) nor the lift and drag coefficients. The major variations were 0.3% and 3% of lift and drag coefficients, respectively, between the thinnest and thickest slat trailing edge configurations, of which the thickest one exhibited higher values.

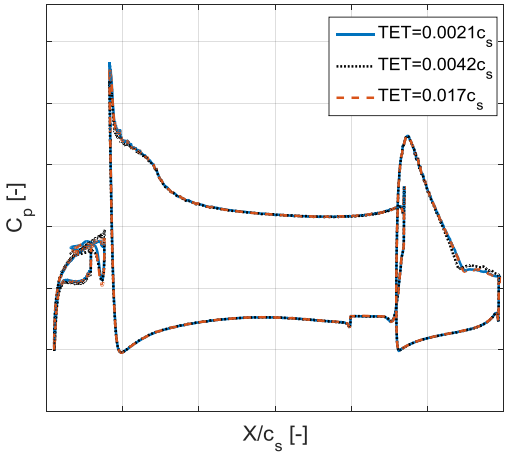

Figure 3 – Pressure coefficient distribution

Figure 4 shows the results of the far-field spectra regarding Power Spectral Density (PSD) in function of Strouhal number (fU/c_s; U is the free stream velocity). The three cases exhibited the typical mid-frequency tones between 2 and 7 Strouhal number and also the hump, whose frequency decreases as the trailing edge thickness increases. Before and after the hump, the behaviour of the three spectra was the same and the Overall Sound Pressure Level (OSPL) was constant among the configurations.

Figure 5 shows the vortex shedding process behind the slat trailing edge of the TET=0.0042c_s configuration (dt = 1.6 x 10^{-5} s). Two vortices are highlighted in the slat trailing edge, i.e., one behind the upper side and the other from the lower side (which is more intense) with 180° phase shift between them.

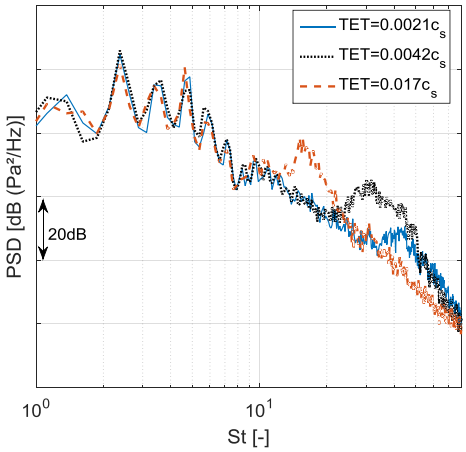

Figure 4 – Far-field spectra

All configurations exhibited the vortex shedding behind the slat at different frequencies, which were consistent with those observed in the far-field. Table 1 (first column) displays the dominant Strouhal number observed in the far-field spectra and the second column shows the dimensional-less frequency (Strouhal number) calculated as the inverse of the period between two maximum pressure time derivatives in the same wake point.

Figure 6 shows the PSD in function of the Strouhal number calculated in the lower vortex core of all configurations. All cases exhibited a hump at high frequency, as reported in the literature [23]; however, the Strouhal number of the peak (table 1, column 3) is not consistent with that observed in the far-field spectra.

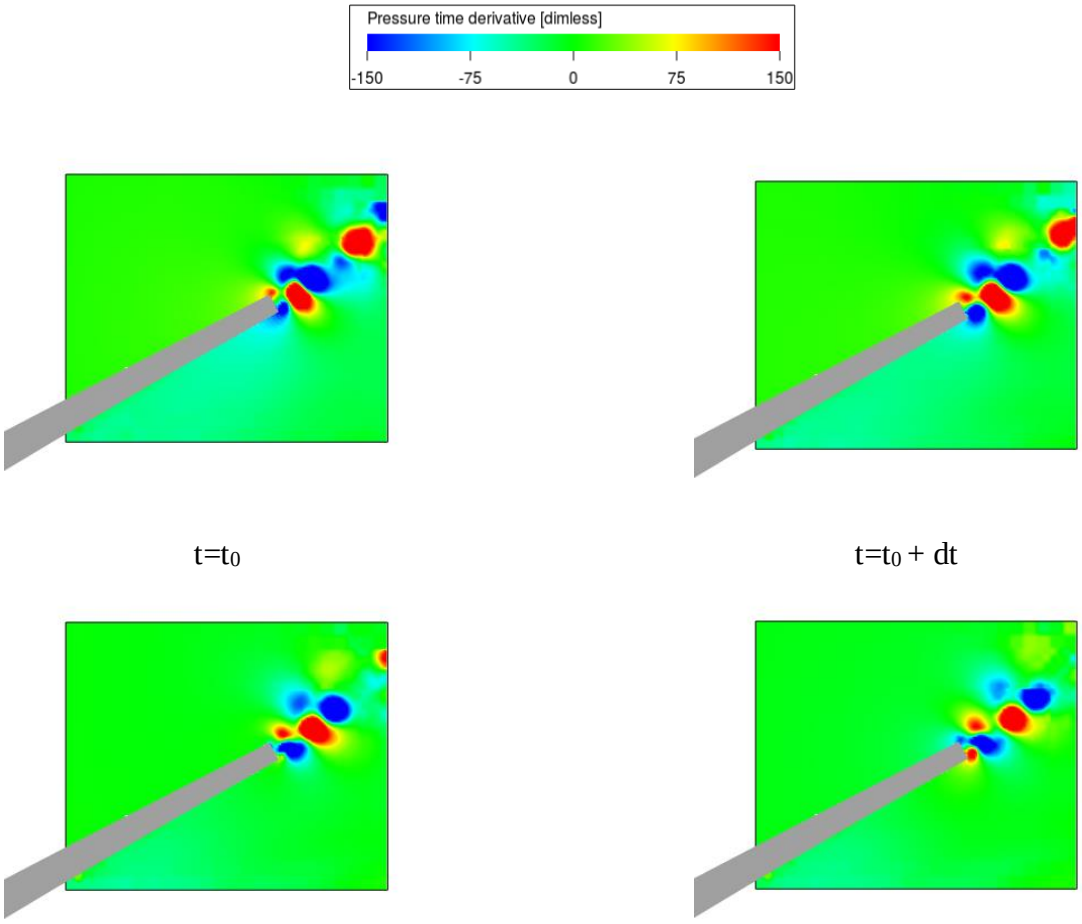

Figure 5 – Pressure time derivative at the slat trailing edge

Trailing edge thickness	$St_{far\text{-}field}$	$St_{vortex\ shedding}$	$St_{vortex\ core\ spectrum}$
$0.0021c_s$	43.87	43	59.91
$0.0042c_s$	31.37	31.15	45.73
$0.0017c_s$	16.37	18.25	19.43

Table 1 – Strouhal number of vortex shedding and slat spectra

Bauer, A. B (1961) [24] demonstrated the effective length for the calculation of the Strouhal number of a vortex shedding for a thin plate (similar to the slat trailing edge) is $h=(d+2\delta^*)$, where d is the plate thickness - in this case, slat trailing edge - and δ^* is

the ideal Blasius boundary-layer displacement thickness. Therefore, the frequency of the hump in the far-field spectra and the boundary layer displacement thickness were used for the calculation of the characteristic Strouhal number of the vortex shedding ($St=fU/\delta^*$).

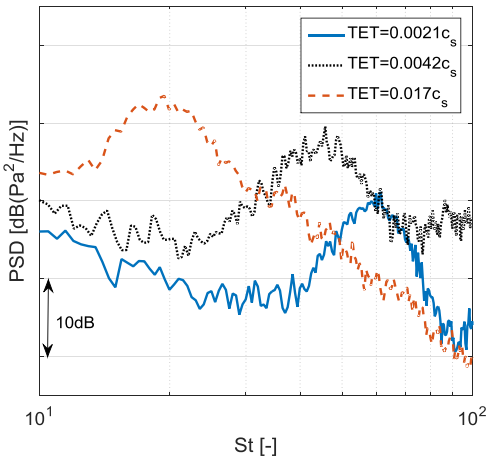

Figure 6 – Power Spectral Density in the vortex core

Equation 1 obtained the boundary layer displacement thickness; the integration was made in the wake of the slat trailing edge at $0.00074c_s$ behind it. Figure 7 displays the velocity profile at each configuration and its respective slat trailing edge. The results of this process are shown in Table 2. The Strouhal number was close to 0.4 for all cases, which could be considered characteristic of all slat trailing edge vortex shedding.

$$\delta^* = \int_{-x}^{x} 1 - \frac{u(x)}{U}$$

Equation 1 – Boundary layer displacement thickness

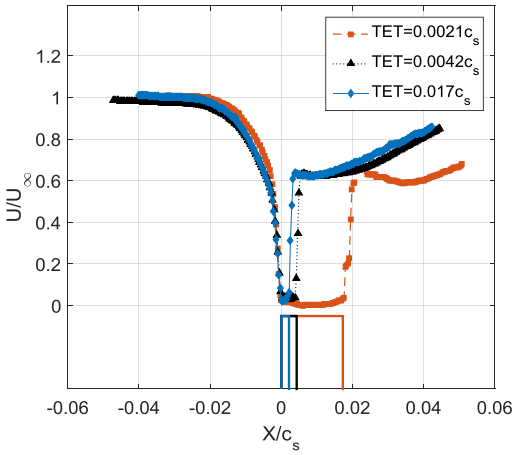

Figure 7 – Velocity profile behind the slat trailing edge

Imamura, T. et al (2007) [12] also observed a relation between the high-frequency hump exhibited in the far-field and the dipole created in the trailing edge calculating the PSD in the fluid around the slat trailing edge at the same frequency of far-field hump (figure 8). Higher PSD levels were detected behind the tips of the slat trailing edge (where the vortex shedding is located), which revealed the existence of a dipole of that specific frequency. On the other hand, Figure 9 shows the PSD at the far-field first tone frequency; higher levels of PSD are observed in the reattachment region. According to the authors

[12], higher pressure fluctuations at a low frequency around reattachment cause high-frequency fluctuations in the trailing edge.

Trailing edge thickness	δ* [mm]	St
$0.0021c_s$	0.75	0.3875
$0.0042c_s$	1.08	0.4004
$0.0017c_s$	2.074	0.3996

Table 2 – Boundary layer displacement thickness and Strouhal number

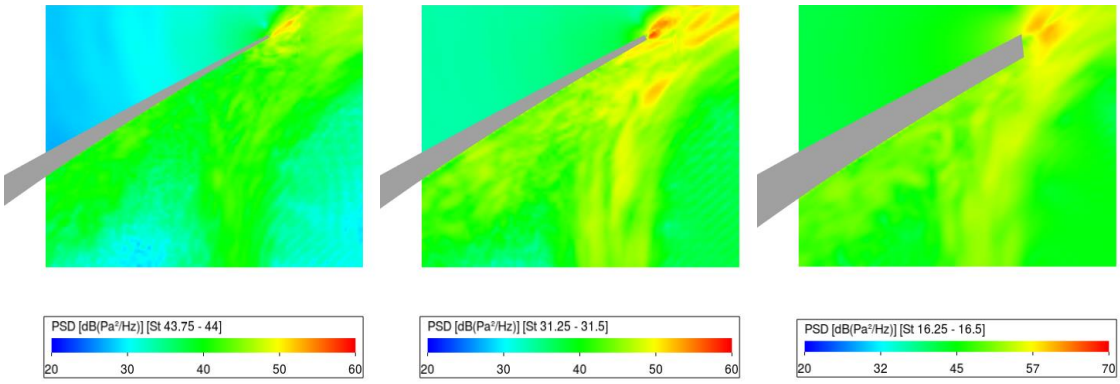

a) TET=0.0021c_s *b) TET=0.0042c_s* *c) TET=0.017c_s*

Figure 8 – Power Spectral Density around slat trailing edge

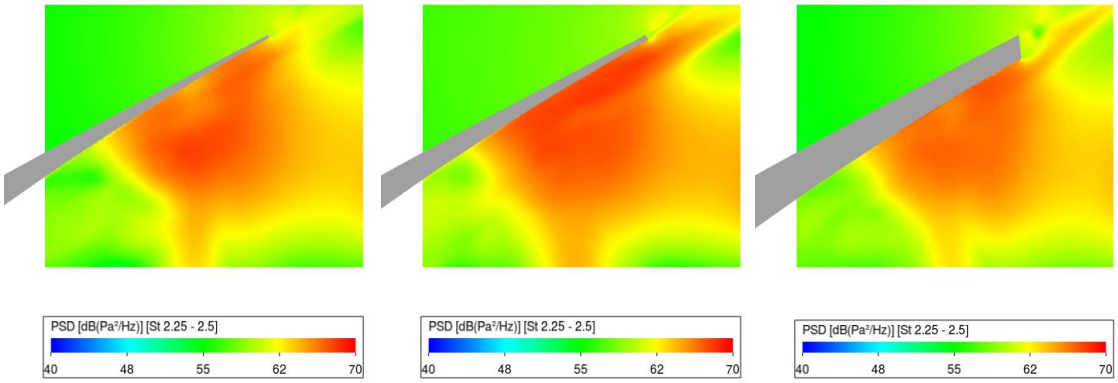

a) TET=0.0021c_s *b) TET=0.0042c_s* *c) TET=0.017c_s*

Figure 9 – Power Spectral Density in the reattachment region

Figure 10 shows the PSD in function of Strouhal number of surface pressure fluctuations at the cusp, reattachment and trailing edge at the mid-span of the three configurations. Although all configurations exhibited the same values in all frequency range, the hump at a high frequency at the cusp and trailing edge is exhibited for the $0.0042c_s$ and $0.017c_s$ trailing edge thickness configurations. The other configuration (TET=$0.0021c_s$) showed no high-frequency hump, since at that specific frequency the turbulence generates pressure fluctuations greater than those related to the vortex shedding.

4. CONCLUSIONS

Simulations of three different slat trailing edge thicknesses of a 2D high-lift airfoil well captured spatially and temporally the vortex shedding in the slat wake in each case and the differences related to the differences in geometry. In the far-field spectrum, all

cases exhibited the same mid-frequency tones (same frequency and intensity values) and a high-frequency hump, whose frequency increases as the trailing edge thickness decreases. The results showed such a hump is highly related to the vortex shedding behind the slat and its frequency is consistent with the vortex frequency, whereas the mid-frequency tones are associated with the interaction of the shear-layer and slat surface in the reattachment region.

In a blunt trailing edge, two vortices are formed with 180^0 phase difference and become a dipole of specific frequency in the far-field. Finally, since the behaviour of the slat trailing edge is similar to a thin plate, the characteristic Strouhal number for the hump is close to 0.4 if the characteristic length is the boundary layer displacement thickness for each case.

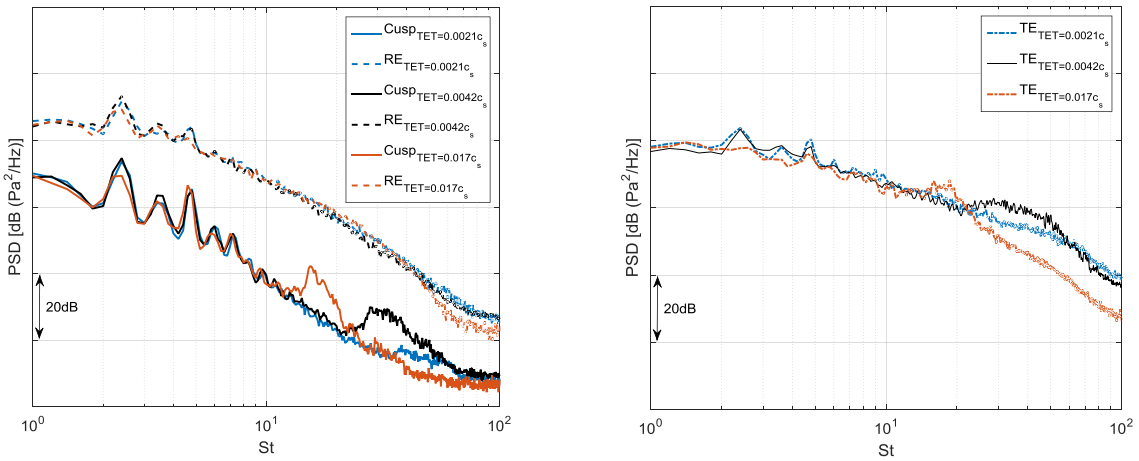

a) Cusp and reattachment *b) Trailing edge*

Figure 10 – Power Spectral Density at surface point at midspan

5. ACKNOWLEDGEMENTS

The authors acknowledge the Conselho Nacional de Desenvolvimento Científico e Tecnológico (CNPq), Coordenação de Aperfeiçoamento de Pessoal de Nível Superior (CAPES) and A Financiadora de Estudos e Projetos (FINEP) for the financial support provided to this research.

6. REFERENCES

1. ICAO, I., "*Environmental report 2013*", Aviation and climate change, Vol. 2013.

2. Dobrzynski, W., Nagakura, K., Gehlhar, B., and Buschbaum, A., "*Airframe noise studies on wings with deployed high-lift devices*" 4th AIAA/CEAS Aeroacoustics Conference (1998)

3. Dobrzynski, W., "*Almost 40 Years of Airframe Noise Research – What did we achieve?*" Journal of Aircraft (2010)

4. Chow, L., Mau, K., and Remy, H., "*Landing gears and high lift devices airframe noise research*" 8th AIAA/CEAS Aeroacoustics Conference & Exhibit (2002)

5. Smith, M., Chow, L., and Molin, N., "*Attenuation of slat trailing edge noise using slat gap acoustic liners*" 12th AIAA/CEAS Aeroacoustics Conference (27th AIAA Aeroacoustics Conference) (2006)

6. Airbus, "*Aircraft Noise - Technologies and Operations*" Tech. rep., Airbus (2007)

7. Pascioni, K. A., and Cattafesta, L.N., "*Aeroacoustic Measurements of Leading-Edge Slat Noise*" 22nd AIAA/CEAS Aeroacoustics Conference (2016)
8. Choudhari, M. M., and Khorrami, M. R., "*Slat Cove Unsteadiness Effect of 3D Flow Structures*" 44th AIAA Aerospace Sciences Meeting and Exhibit (2006).
9. Khorrami, M. R., Fares, E., Casalino, D. "*Towards full aircraft airframe noise prediction: lattice boltzmann simulations*" 20th AIAA/CEAS Aeroacoustics Conference, AIAA AVIATION Forum (2014).
10. Imamura, T., Ura, H., Yokokawa, Y., Enomoto, S., Yamamoto, K., and Hirai, T., "*Designing of slat cove filler as a noise reduction device for leading-edge slat*" 13th AIAA/CEAS (2007)
11. Dobrzynski, W., and Pott-Pollenske, M., "*Slat noise source studies for farfield noise prediction*" 7th AIAA/CEAS Aeroacoustics Conference and Exhibit (2001)
12. Imamura, T. et al. "*Simulation of the broadband noise from a slat using zonal les/rans hybrid method*" 45th AIAA Aerospace Sciences Meeting and Exhibit (2007)
13. Succi, S., Benzi, R., and Higuera, F., "*The lattice Boltzmann equation: A new tool for computational fluid-dynamics*" PhysicaD: Nonlinear Phenomena (1991)
14. Chen, S., and Doolen, G. D., "*Lattice Boltzmann method for fluid flows*" Annual review of fluid mechanics (1998)
15. Crouse, B., Freed, D., Balasubramanian, G., Senthooran, S., Lew, P.-T., and Mongeau, L., "*Fundamental aeroacoustic capabilities of the lattice-Boltzmann method*," Journal of Aircraft (2006)
16. He, X., Doolen, G. D., and Clark, T., "*Comparison of the lattice Boltzmann method and the artificial compressibility method for Navier–Stokes equations*" Journal of Computational Physics (2002)
17. Bres, G. A., Pérot, F., and Freed, D., "*A Ffowcs Williams-Hawkings solver for Lattice-Boltzmann based computational aeroacoustics*" Journal of Aircraft
18. Lighthill, M. J., "*On sound generated aerodynamically i. general theory*" In proceeding of Royal Society London A. London, United kingdom: The Royal Society (1952)
19. Farassat, F., "*Derivation of formulations 1 and 1a of farassat*" (2007)
20. Dowling, A. P., Williams, J. F. "*Sound and sources of sound*" (1983)
21. Botero-Bolívar, Laura et. al., "*Parametric Analysis of the Influence of Slat Geometry on Acoustic Noise*" 2018 AIAA/CEAS Aeroacoustics Conference (2018)
22. Pereira, Lourenco et. al., "*Experimental and Numerical Analysis of the Aerodynamic and Aeroacoustic Properties of a 2D High-LiftWing Model*" 2018 AIAA/CEAS Aeroacoustics Conference (2018)
23. Dhiraj, K and Kamal, P., "*Effect of tip vortices associated with a finite circular cylinder".* Hong Kong International Conference on Engineering and Applied Science (2015)
24. Bauer, A. B., "*Vortex shedding from thin flat plates parallel to the free stream".* Journal of the Aerospace Sciences (1961)